FINAL

TROUT LAKE DAM

STRUCTURAL STABILITY ANALYSIS

Prepared for

Town of Friday Harbor
60 Second Street
P.O. Box 219
Friday Harbor, Washington 98250

January 12, 2010

URS

8181 E. Tufts Ave.
Denver, Colorado 80237
Project 22240846

List of Appendices

List of Tables

List of Figures

URS Corporation would like to acknowledge all of the individuals that were involved in producing this report.

From the Town of Friday Harbor, URS would like to thank Mr. King Fitch, Town Administrator, for hosting site visits, providing answers to numerous questions, sharing information on the project, and collecting data for the analysis.

The following individuals provided information regarding the 1958 modifications to the dam that was helpful in these structural evaluations. Dr. Ark G. Chin was an engineer on the 1958 design team, and was responsible for the arch raise design. Mr. Dick Scheumann was employed by the construction company selected to modify the dam, and supervised the 1958 construction operations. Mr. Roger Loring was on the contractor's work force.

From URS Corporation, Mr. Guy Lund, P.E., project Principal-in-Charge and responsible engineer for the structural stability analysis of Trout Lake Dam. Mr. Chad Gillan, PE, Civil/Structural Engineer, P.E., responsible for project management, finite element model development, structural analysis and evaluation, and report development.

Mr. Howard Boggs, concrete dam consultant, performed peer review of the methods of analysis, parameter assumptions, results from the analysis, and report.

The technical material and data contained in this report were prepared under the supervision and direction of the undersigned, whose seal as professional engineer is affixed below.

Guy S. Lund, P.E.

URS Corporation

Trout Lake Dam is located on San Juan Island, in San Juan County, Washington. The dam is owned and operated by the Town of Friday Harbor. The primary purpose of the dam is to store water for municipal use. Trout Lake dam is a thin concrete arch dam originally constructed in 1928 and raised in 1958.

Trout Lake Dam is a thin concrete arch dam and currently has a height of 36 feet with a crest elevation of 281 feet and crest length of 141. The dam has a constant radius of 60 feet to the extrados (upstream) face. The dam has a crest thickness of 2 feet and a base thickness of 3.25 feet. Adjacent to the dam on the left abutment is a fixed crest weir type spillway with a crest elevation of 279.5 and weir length of approximately 20-feet-long.

Trout Lake Dam is founded in a U-shaped canyon with a flat bottom. The canyon is considered to be made up of metavolcanic rock with a chemical composition between andesite and basalt. The foundation is considered to be strong and massive

URS Corporation (URS) was retained by the Town of Friday Harbor to perform a structural stability analysis of the dam and to evaluate the safety of the dam for the usual (normal), unusual (probable maximum flood [PMF]), and extreme (seismic) loading conditions. The results were evaluated against different failure modes, including concrete overstressing, sliding stability, foundation rock block stability, and rock scour (erodibility) due to overtopping.

The structural analysis used the three-dimensional finite element method of analysis to evaluate the dam. Based on the results from the analysis, the dam is considered to have adequate safety against failure against the failure modes for the assumed usual, unusual, and extreme loading conditions.

1.1 PROJECT DESCRIPTION

Trout Lake Dam is located on San Juan Island, in San Juan County, Washington, and consists of a concrete arch dam, spillway, outlet works, and a downstream embankment (buttress) called the pressure berm. The dam is owned and operated by the Town of Friday Harbor. The primary purpose of the dam is to store water for municipal use.

Trout Lake Dam is a thin, concrete arch dam. The original dam was constructed in 1928, as shown on Figure No. 1 - 1. Modifications were performed to the dam in 1958 to increase of the structural height of the dam for additional water storage, as shown on Figure No. 1 - 2, The drawing on Figure No. 1 - 2 is dated 1947; however, interviews with individuals involved in the design and construction of these modifications (performed during this study) indicated that the dam raise was completed in 1958.

The structural height of the dam is 36 feet with the crest at elevation (El.) 281.0. The length of the crest is 141 feet. *Note, the crest length of 141 feet is based on field measurements taken during the site examination and is different than the length shown on the modification drawing (Figure No. 1 - 2).* The dam has a constant radius of 60 feet, as measured from the center of the arch to the extrados (upstream) face of the dam.

The thickness of the dam varies from 3.25 feet at the base El. 245, to 2 feet at El. 270.0. The thickness of the dam is a constant 2 feet between El. 270.0 and the crest, El. 281.0. The upstream face of the dam is vertical. Similarly, the downstream face is vertical between El. 270.0 and the crest, and sloped between the base and El. 270.0.

The spillway abuts with the arch dam, and is located on the left abutment. The spillway is an uncontrolled fixed crest weir type with the crest at El. 279.5. The weir length is approximately 20-feet-long. The spillway flows travel over the weir and through a concrete lined channel (chute), which discharges downstream of the toe of the dam.

The outlet works consists of two steel pipes through the dam. The outlets are located near the center of the dam, with the centerline of the outlet pipes at El. 248.0. The outlets each consist of a 24-inch diameter intake opening, 2-foot-long transition, and 12-inch diameter steel pipe. One outlet pipe provides the water to the Town of Friday Harbor. The other outlet pipe was originally intended for releases downstream of the dam; however, it is currently presumed to be inoperable.

The downstream buttress, or pressure berm, was constructed as a part of the 1958 modifications and is located on the downstream face of the dam. The top of the berm is at approximately El. 262.0, and is constructed with selected fills consisting primarily of sands and gravels. The pressure berm covers the outlet pipes.

The dam is founded in a U-shaped canyon with a flat bottom. The canyon is considered to be made up of metavolcanic rock with a chemical composition between andesite and basalt. The foundation is considered to be strong and massive.

1.2 ADDITIONAL PERTINENT PROJECT INFORMATION

Some additional information regarding the dam was obtained through discussions with individuals involved in the 1958 modifications and construction. During the site examination, URS engineers had discussions with Mr. Rodger Loring, a resident of San Juan Island. Mr. Loring was part of the contractor work force during the 1958 construction effort. Discussions were also had with Messrs. Dick Scheumann and Ark G. Chin, PhD during the evaluations of the dam. Mr. Dick Scheumann was employed by the company that was retained to construct the modification to the dam in 1958, and supervised the construction effort. Dr. Ark G. Chin, structural engineer, was a member of the design team for the arch dam raise. The following notes summarize pertinent information regarding the project that was learned through the discussions with these individuals:

- The pressure berm was constructed as part of the 1958 modification to raise the crest of the dam. The purpose of the berm was to provide pressure on the downstream foundation. There was only limited foundation data available during the design of the dam raise, and the condition of the foundation under the central section of the dam was unknown. The weight of the pressure berm would counter act any increase in the uplift forces through the foundation material, thus, preventing seepage/piping through the foundation.
- The dam raise was designed using horizontal arch theory, which assumes that the dam is made up of several independent horizontal arches. This assumption neglects any interaction between arches.
- The construction of the dam raise was performed during the summer season. The concrete in the dam raise was constructed in two or three placements. The concrete was placed in horizontal lifts between formed construction joints, which contained waterstops and horizontal reinforcement across the joints. There was also vertical reinforcement at the interface of the original dam and dam raise.
- The concrete was placed with manual labor. Access from the batch plant on the left abutment to the dam was via scaffolds and planks. The concrete was transported to the dam with wheelbarrows and dumped into the forms from above. The concrete was consolidated using vibrators.
- The reservoir was not drained during construction of the dam raise.

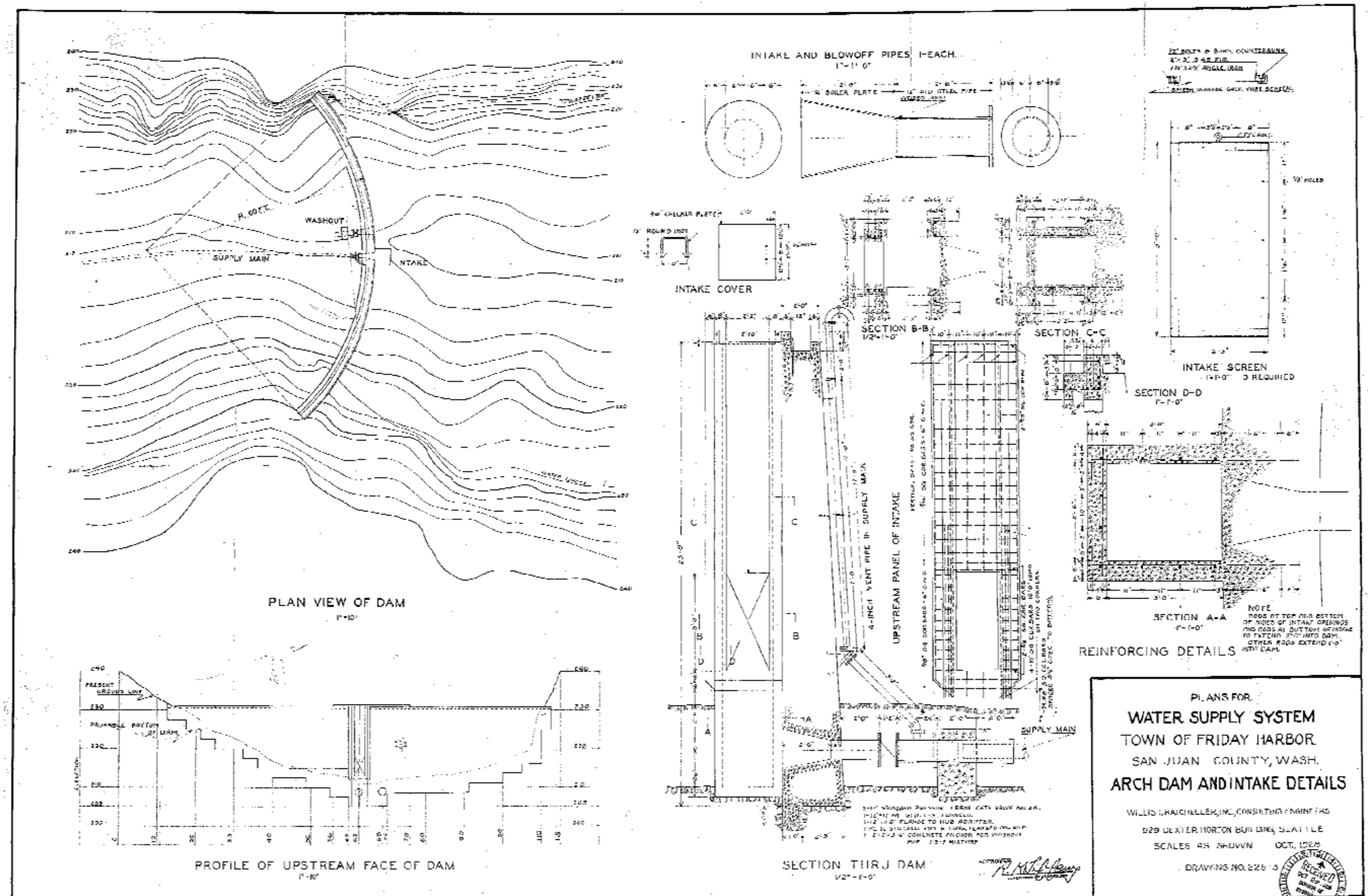

Trout Lake Dam

1928 Construction Drawing

Figure No. 1- 1

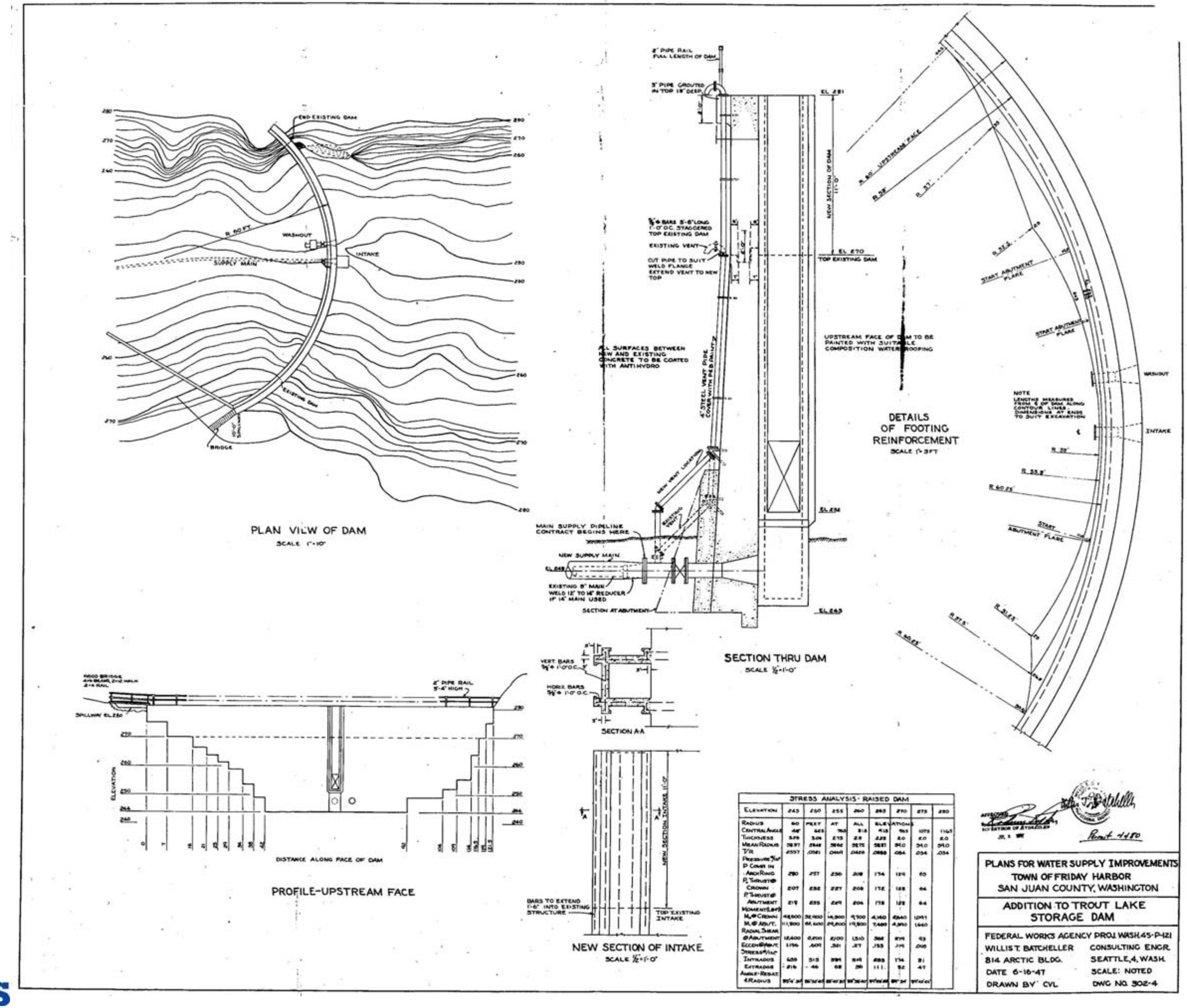

URS

Trout Lake Dam

1958 Construction Drawing

Figure No. 1- 2

2.1 CONCRETE PROPERTIES

The concrete material properties used for the structural analysis of the dam were based on the technical specifications for the construction of the original dam and dam raise and published data for concrete by the United States Bureau of Reclamation (USBR), Federal Energy Regulatory Commission (FERC), and American Concrete Institute (ACI).

2.1.1 Compressive Strength

The technical specifications for original dam constructed in 1928 stated, that the concrete proportions should be approximately one (1) part cement, two (2) parts sand, and four (4) parts gravel with sufficient water to thoroughly hydrate the cement and to produce a workable mixture *[1]*. Although the water content was not specified and the quality of the cement is unknown, these proportions would most likely yield a relatively high concrete strength for that era of construction.

For comparison, Grand Coulee Dam completed in 1942, also located in the State Washington had concrete proportions of 1 part cement, 2.6 parts sand, and 6.8 parts gravel, and was comprised of mostly basalt. The concrete at Grand Coulee Dam had an unconfined compressive strength at 365 days of 5990 lb/in^2 *[3]*. Trout Lake Dam is assumed to also be constructed with the majority of the aggregates being basalt because that is the prominent hard rock in the local area. The mix portions show that Trout Lake Dam had a larger amount of cement than in Grand Coulee Dam. Therefore based on this information, the concrete of the original portion of Trout Lake Dam is conservatively assumed to have an unconfined compressive strength of 4,000 lb/in^2 for these studies.

The technical specifications for the dam raised in 1958 stated that the minimum unconfined compressive strength shall be 3,000 lb/in^2 at 28 days and have a minimum cement content of 5.5 sacks of concrete per cubic yard *[2]*. The technical specifications also stated that trial mixes were to be preformed prior to construction, and test cylinders were to be made and tested to verify that the concrete strengths were greater than the specified minimum strength. Discussions with Mr. Scheumann indicated that these specification requirements were met.

For comparison, Grand Coulee Dam had a cement content of approximately 4.0 sacks of concrete per cubic yard, and again had an unconfined compressive strength at 365 days of 5990 lb/in^2 *[3]*. Therefore based on the minimum cement content of 5.5 sacks per cubic yard, the compressive strength is conservatively assumed to be 4,000 lb/in^2 for these studies.

The results from these structural evaluations showed that the assumed concrete strength did not significantly impact the results of the analysis.

2.1.2 Other Concrete Properties

The other material property parameters were based on published data for mass concrete. The tensile strength of the concrete was based on the modulus of rupture for concrete as published by FERC guidelines *[4]*, and described in more detail in Section 3.1.1. The unit weight and thermal properties of the concrete were estimated based on laboratory tests for concrete from other dams that contained similar aggregate rock *[3]*.

The instantaneous modulus of elasticity for the concrete was computed based on published equations by the ACI *[5]*. The sustained modulus of elasticity, used for the evaluation of the static loads, was assumed equal to 65 percent of the instantaneous value, as recommended by the USBR guidelines *[6]*. Poisson's Ratio for the concrete was based on a recommended value by the USBR guidelines *[6]*.

The concrete material properties are summarized in Table 2-1.

Table 2-1
Concrete Material Properties

Properties	Values	
Unconfined Compressive Strength	4,000	lb/in^2
Tensile Strength	428	lb/in^2
Unit Weight	154	lb/ft^3
Modulus of Elasticity		
Sustained	2,600,000	lb/in^2
Instantaneous	4,000,000	lb/in^2
Poisson's Ratio	0.20	
Thermal Conductivity	1.08	BTU / ft-hr-^{o}F
Specific Heat	0.22	BTU / lb-^{o}F
Coefficient of Thermal Expansion	0.0000045	in / in / ^{o}F

lb/in^2 = pounds per square inch
lb/ft^3 = pounds per cubic foot
BTU/ft-hr-^{O}F = British thermal unit per foot-hour-degree Fahrenheit
BTU/lb-^{O}F = British thermal unit per pound-degree Fahrenheit
in/in/ ^{O}F = inch per inch per degree Fahrenheit

2.2 FOUNDATION PROPERTIES

The foundation at Trout Lake Dam is considered strong and massive. The rock is characterized as strong, extrusive igneous rocks with a fine grained, dark blue-gray groundmass with 3 mm pyroxene phenocrysts and minor amounts of quarts, olivine and biotite. The rock has vesicles that are just barley visible without magnification. The rock is classified as a metavolcanic rock with chemical composition between andesite and basalt.

2.2.1 Joint Sets

There is a primary and secondary joint set. The joint sets are discussed in the 1993 Periodic Dam Safety Inspection Report for Trout Lake Dam *[7]* and in the 1997 Trout Lake Dam Improvement Feasibility Study *[8]*. The primary joint set roughly parallels the trend of the valley and has strike ranging between north 10 to 50 degrees west with a near vertical dip. This primary joint set has a spacing of 20 to 40 feet. The secondary joint set has a strike ranging between north 30 to 55 degrees east with a dip between 25 and 65 degrees to the south. This secondary joint set has a spacing of approximately 29 feet. All the joints are considered to be tight and very rough.

2.2.2 Rock Quality Designation

The rock quality designation (RQD) for the rock mass was based on site observations. The RQD would be expected to be excellent or to range between 95 and 100 percent.

2.2.3 Compressive Strength

The unconfined compressive strength of the rock foundation was estimated using a Terrametrics Point Load Tester, Model No. T-500 on rock samples retrieved from the dam site. A total of 10 point load tests were performed. The unconfined compressive strengths from the point load tests were evaluated using two methods, the Terrametrics Method described in the Terrametrics instruction manual and American Society for Testing and Materials (ASTM) described in ASTM D-5731-08. The unconfined compressive strength of the rock foundation, based on the average of the two methods, was assumed to be approximately 10,100 lb/in^2. Calculations and a more detailed discussion of the test results are shown in Appendix A, Foundation Strength Computations.

2.2.4 Erodibility Index

Water jets that impact the downstream area of a dam with high velocity can develop scour (erosion) unless the rock is extremely hard and quite sound. A study was performed to evaluate the impact that overtopping flows during the probable maximum flood (PMF) event would have on the rock foundation. The analysis used the Erodibility Index method, as described in Chapter 11 of the FERC guidelines *[4]*. The Erodibility Index, which is used to determine the likelihood of erosion, is computed using Equation 1:

Equation 1
Erodibility Index

$$K = M_S \times K_b \times K_d \times J_S$$

where:

K = Erodibility Index
M_S = mass strength number
K_b = block size number
K_d = inter-block bond shear strength number
J_S = ground structure number

Mass Strength Number (M_S)

The M_s was selected based on field observations and the estimated compressive strength of the rock. The rock was very resistant to strikes with a geologist's pick and required many hard blows with the pick to break. The rock strength was estimated to be approximately 10,100 lb/in^2

(70 mega pascal [MPa]). Therefore, based on the rock strength and observed hardness, a mass strength number of 70 was assumed *[4]*.

Block Size Number (K_b)

K_b is equal to the quotient of the estimated RQD of the rock mass and a joint set number (J_n). The J_n for the rock mass was estimated to be approximately 1.83, based on field observations that identified one primary joint set and one secondary joint set *[4]*. The resulting value for K_b was calculated to be approximately 52.

Inter-Block Bond Shear Strength Number (K_d)

The K_d is equal to the quotient of the joint roughness number (J_r) and the joint alteration number (J_a). At Trout Lake Dam the joints were typically observed to be tight, with joint openings ranging from negligible to little. The shape of the joints was very rough and undulating. Therefore, a J_r equal to 3.0 was selected *[4]*.

The J_a was selected based on the condition of the joint wall strength and separation of the joint. The joint walls are typically slightly altered and have separation ranging from 1 mm to 5 mm. Therefore, a J_a equal to 2.0 was selected for slightly altered, non-softening, non-cohesive rock mineral or crushed rock infilling *[4]*.

Using the selected J_r and J_a resulted in a K_d equal to 1.5.

Ground Structure Number (J_s)

The J_s was selected based on the orientation and spacing of joints in the foundation relative to the direction of water flow. The orientation of the primary joint set is near parallel to the direction of flow and the dip is near vertical. The average spacing between both the primary and secondary joint sets is approximately 30 feet; thus, the average J_s would be approximately 1.14 *[4]*.

Summary

Based on the estimated values for mass strength number (M_S), block size number (K_b), inter-block bond shear strength number (K_d), and the ground structure number (J_S) the estimated Erodibility Index for the foundation at the Trout Lake Dam is approximately 6220. Converting the Erodibility Index into units consistent with stream power (which is used in the erodibility evaluation) yields approximately 700 kilowatts per meter (kW/m) *[4]*.

2.2.5 Modulus of Deformation and Poisson's Ratio

The deformation modulus and Poisson's Ratio for the foundation rock mass at Trout Lake Dam were estimated based on published data for rock samples of similar rock type taken from the Grand Coulee dam site, Columbia Basin Project in Washington *[9]*. The average compressive strength for the USBR rock samples at this location was 11,900 lb/in^2, which is similar to the average estimated strength for the rock at Trout Lake Dam. Based on this comparison, it was considered reasonable to assume that the intact modulus of elasticity for the rock at Trout Lake Dam would be similar to the tested values from the intact test samples from the USBR.

The average modulus of elasticity for the USBR intact rock samples was computed to be approximately 5,600,000 lb/in^2 *[9]*. Information by Francois E. Heuze, states that the in-situ foundation deformation modulus generally varies between 20 and 60 percent of the intact laboratory modulus *[10]*. Therefore, the in-situ modulus of deformation for the foundation at Trout Lake Dam could range between 1,120,000 lb/in^2 and 3,360,000 lb/in^2, with a median value of approximately 2,240,000 lb/in^2.

The value for Poisson's Ratio for the rock foundation at Trout Lake Dam was assumed equal to 0.14, which corresponds to the computed average value taken from the USBR intact rock samples *[9]*.

2.2.6 Rock Mass Shear Strength

Trout Lake Dam is situated in a key in the rock foundation, which was excavated to hard, sound rock. Therefore the abutments would have to shear through the rock mass to become unstable. The estimated rock mass shear strength was simulated using the strength parameters computed by the generalized Hoek-Brown failure criterion, as shown in Equation 2 *[11]*.

Equation 2
Generalized Hoek-Brown Failure Criterion for Rock Mass Joints

$$\sigma'_1 = \sigma'_3 + \sigma_{ci} \cdot \left(m_b \cdot \frac{\sigma'_3}{\sigma_{ci}} + s \right)^a$$

where:

σ'_1 = Maximum effective stress at failure (MPa)

σ'_3 = Minimum effective stress at failure (MPa)

σ_{ci} = Uniaxial compressive strength for intake rock

m_b = Hoek-Brown constant for the rock mass

a = 0.5 for rock GSI > 25

s = $\exp\left(\frac{GSI-100}{9}\right)$ for rock GSI > 25

A Mohr envelope for shear strength versus confining pressure was computed for the rock mass using Equation 2. For Trout Lake Dam, the confining stress at the dam/foundation interface was estimated to range between 25 and 300 lb/in^2. Based on the Mohr envelope, a linear relationship was developed to simulate the shear strength of the rock mass within the limits of the expected confining stress. The linear relationship is defined by an effective friction angle, which corresponds to the slope of the line, and apparent cohesion, which corresponds to the Y-intercept of this line.

The results from Equation 2 and the generalized Hoek-Brown criterion indicates that the shear strength of the rock mass can be simulated using an effective friction angle of approximately 58 degrees, and an apparent cohesive strength of approximately 225 lb/in^2. For these evaluations, the apparent cohesive strength of the rock mass was conservatively neglected. The foundation material parameters used for these stability evaluations are summarized in Table 2-2.

Table 2-2
Foundation Material Parameters

Properties	Values
Erodibility Index	6220
Mass Strength Number (M_S)	70
Block Size Number (K_b)	52
Inter-Block Bond Shear Strength Number (K_d)	1.5
Ground Structure Number (J_S)	1.14
Unconfined Compressive Strength	10,100 lb/in^2
Poisson's Ratio	0.14
Modulus of Deformation	
Minimum Estimate	1,120,000 lb/in^2
Median Estimate	2,200,000 lb/in^2
Maximum Estimate	3,400,000 lb/in^2
Rock Mass	
Effective Friction Angle	58 degrees

Notes: lb/in2 = pounds per square inch

3.1 EVALUATION CRITERIA

The structural stability of the dam was evaluated in accordance with Federal Energy Regulatory Commission (FERC) guidelines for the safety evaluation of concrete arch dams, and as summarized below:

- Concrete Overstressing. Compares the computed stresses from the finite element model with the allowable strength of the concrete to determine if the material will crack or crush.
- Abutment Stability. Evaluates the sliding stability at the dam/foundation interface and stability of potential rock block wedges formed by intersecting discontinuities in the foundation rock mass.
- Erosion. Evaluates the potential for rock scour due to water overtopping the dam during a flooding event and the effect that potential scour would have on the overall stability of the dam.

3.1.1 Overstressing Criteria

The structural capacity of the concrete in the dam was evaluated by comparing the calculated stresses from the Finite Element Method (FEM) of the analysis to the allowable tensile and compressive strength of the concrete. Evaluation of the computed tensile stresses from the FEM study requires a basic understanding of the assumptions used in the linear elastic analysis and of the behavioral characteristics of concrete due to the rate of loading.

The studies for Trout Lake Dam used linear elastic assumptions for the material (concrete); however, the concrete actually behaves non-linearly. Figure No. 3 - 1 shows the idealized stress-strain curve for concrete in tension. The tensile stresses in the concrete increase nearly linearly until they approach the maximum tensile strength of the concrete, where the stresses strain relationship becomes highly non-linear, shown as Point B on the curve. The assumption in the FEM analysis computes the concrete stresses using the constant linear slope. This results in the FEM analysis computing the tensile stress at Point A, which corresponds to the strain at the maximum tensile stress of the concrete (Point B). The predicted stress at Point A has been termed the "Apparent Tensile Strength" and should be used to evaluate the computed stresses from a linear FEM analysis for the extreme (seismic) loading conditions, as recommended by FERC *[4]*.

The second characteristic that must be discussed deals with concrete tests that have shown that strength is dependent on the rate of loading. For example, the faster the load is applied to the concrete cylinder, the greater the load required to break the cylinder. This increased strength has been quantified through laboratory tests capable of producing loading rates similar to those that occur during seismic events. These tests have shown that the loading characteristics of the earthquake increased the tensile strength by approximately 50 percent. Therefore, the seismic tensile strength of concrete is equal 150 percent of the static tensile strength, as recommended by FERC *[4]*. Studies have shown that the static tensile strength can be estimated using Equation 3, which is based on the modulus of rupture. The seismic tensile strength can be estimated using Equation 4, which is 150 percent of Equation 3. Finally, the seismic apparent tensile strength of concrete can be estimated using Equation 5 *[4]*.

Equation 3

$$f_t = 1.7 \times f_C^{2/3}$$

Equation 4

$$f_t = 2.6 \times f_C^{2/3}$$

Equation 5

$$f_t = 3.4 \times f_C^{2/3}$$

where: f_c = tensile strength

f_t = compressive strength

The rate of application of the load also has an affect on the compressive strength of the concrete. However, the increase in compressive strength is only approximately 25 percent for the seismic loading conditions. Typically the loads on concrete dams do not infringe on the allowable compressive stress of the concrete; therefore, compressive strength gain due to seismic loads is typically neglected in structural studies.

The static loading conditions (usual and unusual) typically produce tensile stresses in the concrete that are within the elastic portion of the stress-strain curve. Therefore, for the static studies the allowable tensile strength of the concrete is equal to the assumed actual tensile strength of the concrete (Equation 3) divided by the factor of safety for the loading condition, as specified in the U.S. Bureau of Reclamation (USBR) guidelines *[6]*.

The seismic loading conditions commonly result in the concrete tensile stresses to fall within the non-linear portion of the stress-strain curve. The allowable seismic tensile strength of the concrete for the dynamic loading conditions will be computed using Equation 5, as previously discussed. The structural capacity of the concrete in the dam will be evaluated by comparing the calculated maximum stresses from the structural analysis to the allowable tensile and compressive stresses of the concrete. Per the acceptance criteria, the allowable strength of the concrete is equal to the assumed strength divided by the factor of safety for the loading condition. The allowable stresses for the mass concrete are summarized in Table 3-1.

Table 3-1
Allowable Stresses of Concrete

Properties	Values
Overstressing Factors of Safety	
Usual Load Combination	3.0
Unusual Load Combination	2.0
Extreme Load Combination	> 1.0
Allowable Compressive Stress	
Usual Load Combination	1,333 lb/in^2
Unusual Load Combination	2,000 lb/in^2
Extreme Load Combination	< 4,000 lb/in^2
Allowable Tensile Stress	
Usual Load Combination	143 lb/in^2
Unusual Load Combination	214 lb/in^2
Extreme Load Combination	
Seismic Tensile Stress	655 lb/in^2
Apparent Tensile Stress	857 lb/in^2

Notes: lb/in^2 = pounds per square inch
< = less than

3.1.2 Abutment Stability

For the evaluation of Trout Lake Dam, the minimum allowable factors of safety are based on current criteria published by the FERC *[4]*, and summarized in Table 3-2.

Table 3-2
Sliding Stability Factors of Safety

Properties	No Foundation Cohesion
Usual Load Combination	1.5
Unusual Load Combination	1.5
Extreme Load Combination	1.1

The uplift pressures will not be included in the stability computation at the dam/foundation interface, based on USBR guidelines that concluded that the uplift on a thin arch dam is negligible *[6]*. The sliding stability was computed using Equation 6:

Equation 6

$$Q = \frac{F_N \times Tan(\phi_e)}{F_D}$$

where:

Q =	sliding factor of safety
$Tan(\phi_e)$ =	effective coefficient of friction
F_N =	normal force minus uplift force
F_D =	driving force

3.1.3 Rock Scour (Erosion)

The probable maximum flood (PMF) for Trout Lake Dam results in water overtopping of the dam crest. The discharge due to overtopping can result in rock scour if there is enough energy; therefore, the dam was evaluated for potential rock scour on the downstream abutment rock.

The erodibility of the rock mass at the abutments was evaluated using the Erodibility Index method, as described in the FERC guidelines *[4]*. The Erodibility Index method compares the stream power of the overtopping jet with the Erodibility Index, which was discussed in Section 2.2.4. The stream power for the overtopping discharge is computed using Equation 7 *[4]*.

Equation 7
Stream Power

$$E = \frac{q \times \Delta E \times \gamma}{A}$$

where:

E =	rate of energy dissipation due to overtopping
q =	unit discharge
ΔE =	elevation difference (i.e., reservoir and foundation)
γ =	unit weight of water
A =	area of jet at impact

The potential for rock scour was evaluated by comparing the estimated Erodibility Index to the computed stream power. If the Erodibility Index is greater than the stream power, then rock scour is not likely. If the stream power is greater than the Erodibility Index, then rock scour is likely.

3.2 LOADS

The behavior of the dam was analyzed for the static and dynamic loads associated with the usual (normal), unusual (flood), and extreme (seismic) loading conditions. The static loads include gravity, seasonal concrete temperatures, normal and flood reservoir elevations, sediment, and ice. The dynamic loads include the added mass due to the reservoir interaction with the dam and the ground acceleration associated with the Maximum Design Earthquake (MDE). The individual loads are summarized in Table 3-3.

Table 3-3
Individual Loads

Load	Description
Gravity	Dead weight of dam.
Temperature	Loads due to the volumetric changes in the concrete caused by seasonal variations in reservoir and air temperatures.
Reservoir	Hydrostatic water pressure applied to the upstream face of the dam.
Sediment	Additional pressure applied to the upstream face of the dam to simulate sediment in the reservoir.
Tailwater	Hydrostatic water pressure applied to the downstream face of the dam.
Pressure Berm	Additional hydrostatic pressure applied to the downstream face of the dam to simulate the pressure berm at the toe of the dam.
Ice	Additional static load applied at the NWS to simulate force due to ice.
Hydrodynamic Added Mass	Added mass to represent the reservoir/dam interaction during the earthquake.
MDE	Ground accelerations due to the MDE, an event with Peak Ground Acceleration (PGA) of 0.55 g.

Notes: g = Acceleration due to gravity
MDE = Maximum Design Earthquake
NWS = Normal Water Surface

3.2.1 Gravity

The gravity load was based on an assumed unit weight of 154 pounds per cubic foot (lb/ft^3) for the concrete dam. The load was developed in the model using a staged construction analysis, which simulates the actual construction sequencing of the dam and more accurately represents how the weight of the dam was be transferred to the foundation during construction. The gravity loading sequence is described in more detail with Section 3.2.11.

3.2.2 Temperature

There was no data available for the ambient air or reservoir temperatures at Trout Lake Dam; therefore, the necessary information was developed based on published data for similar sites and reservoirs. The ambient air temperatures for the dam site were assumed equal to the published data from the Roche Harbor Airport, Weather Station KWAROCHE, located approximately two miles from the dam site. Based on this data, the average annual ambient air temperature is approximately 50 degrees Fahrenheit (^{o}F).

The reservoir water temperatures were developed based on USBR published data *[12]*. The reservoir temperatures for Trout Lake were assumed equal to the average values for the upper elevations of the Grand Coulee Dam. This reservoir was selected because the average annual air temperature at this USBR dam sites closely matches that of the dam site. A plot of the annual ambient air and reservoir temperature variations is shown on Figure No. 3 - 2.

The temperature fluctuations in the dam were computed using a transient thermal analysis available in the computer program ANSYS. The results from the thermal analysis indicated that the stress-free temperature of the concrete in the dam was approximately 49 ^{o}F. The "stress-free" temperature is defined as the temperature at which there is minimal expansion and/or contraction of the concrete, and typically corresponds to the spring or fall season where the concrete is transitioning between warm and cold weather. The temperature contours at the crown cantilever section of the dam for the winter and summer seasons are shown on Figure No. 3 - 3 and Figure No. 3 - 4, respectively.

3.2.3 Reservoir

The hydrostatic loads corresponding to the normal and PMF reservoir levels were simulated using a fluid density of 62.5 lb/ft^3. The usual (normal) loading condition, assumed that the normal water surface (NWS) is at the crest of the spillway, El. 279.5 feet.

The unusual PMF loading conditions assumed the reservoir level would be at El. 282 feet, which corresponds to the estimated peak reservoir level due to the PMF event *[13]*. The unusual reservoir level overtops the crest of the dam by 1.0 feet.

The hydrologic analysis did not estimate the time of year that the PMF event for Trout Lake Dam would occur *[13]*. As will be discussed later in this report, the more critical temperature load on the dam is the winter condition (compared to the spring, fall, or summer conditions). Therefore, for these structural studies the unusual PMF event was assumed to occur during the winter season.

3.2.4 Sedimentation

The sedimentation in the reservoir was assumed to be at El. 252 feet, which corresponds to the top elevation of the intake screens. The sediment load on the upstream face was simulated assuming a horizontal equivalent fluid density of 85 lb/ft^3 *[4]*.

3.2.5 Tailwater

Tailwater was conservatively neglected for these studies.

3.2.6 Pressure Berm

The downstream pressure berm was assumed to be constructed to approximately El. 262 feet, based on measurements taken during the site examination performed by URS on February 10, 2009. The berm was simulated assuming a horizontal equivalent pressure of soil in an at rest condition equal to 60 lb/ft^3. This pressure assumes a soil density of 120 lb/ft^3 and an at rest soil coefficient of 0.5.

3.2.7 Ice Load

During the winter months the reservoir is assumed to freeze and develop a 6-inches-thick sheet of ice. The ice load due to thermal expansion and wind drag was assumed to be 2,500 pound per linear foot (lb/ft), applied to the upstream face of the dam at the NWS elevation *[4]*.

3.2.8 Hydrodynamic Added Mass

Hydrodynamic loads are the results of the interaction between the reservoir and dam during an earthquake. Additional mass was included on the upstream face of the FEM to simulate the added inertia due to the dam/reservoir interaction. The hydrodynamic masses were computed using the generalized theory for Westergaard's Added Mass *[14]*.

3.2.9 Maximum Design Earthquake (MDE)

URS preformed a site-specific seismic hazard evaluation for Trout Lake Dam. The MDE was based on a return period of 3,000 years with a corresponding peak ground acceleration (PGA) of 0.55 g. The time-history recorded used in the analysis was from the 2001 Nisqually earthquake. The earthquake record was scaled by spectrally matching the record to the natural frequency of Trout Lake Dam. Appendix B contains the Site-Specific Seismic Hazard Evaluation Report.

The U.S. Society of Dams (previously the U.S. Committee on Large Dams [USCOLD]) and the International Congress on Large Dams (ICOLD) endorse a probabilistic approach to developing a MDE. The USCOLD recommends the determining of the MDE be based on a return period between 3,000 and 10,000 years *[15]*. Based on the hazard classification and size of Trout Lake Dam the MDE corresponding to the 3,000 year frequency event is considered adequate. In additional, correspondence between URS and staff with the Department of Ecology, State of Washington, concurred that a return period of 3,000 years is adequate to develop the MDE *[16]*.

The ground motions due to the MDE event were simulated in the finite element model using the three components of acceleration time history: upstream-downstream, cross-canyon, and vertical. The scaled acceleration time-history plots for the three components are shown on Figure No. 3 - 5 through Figure No. 3 - 7. The developed time-history accelerations from the 2001 Nisqually earthquake event contain an initial 19 seconds of zero acceleration, which will not affect the structure. Therefore, the initial 19 seconds of the time history accelerations were excluded in these studies.

3.2.10 Load Combinations

Five load combinations representing the usual, unusual, and extreme loading conditions for the dam were analyzed as summarized below:

Usual Load Combinations (USLC):

USLC-1 **Gravity**, stress-free **temperatures** (spring/fall), NWS **reservoir** El. 279.5 feet, **pressure berm**, and **sediment** El. 252 feet.

USLC-2 **Gravity**, summer **temperatures**, **reservoir** NWS El. 279.5 feet, **pressure berm**, and **sediment** El. 252 feet.

USLC-3 **Gravity**, winter **temperatures**, **reservoir** NWS El. 279.5 feet, **ice**, and **pressure berm**, **sediment** El. 252 feet.

Unusual Load Combination (UNLC):

UNLC-1 **Gravity**, stress-free **temperatures** (spring/fall)**, reservoir** PMF El. 282 feet, and **pressure berm**, **sediment** El. 252 feet.

Extreme Load Combination (EXLC):

EXLC-1 **Gravity**, stress-free **temperatures** (spring/fall), **reservoir** NWS El. 279.5 feet, **pressure berm**, **sediment** El. 252 feet, **hydrodynamic added mass**, and ground acceleration due to the **MDE**.

3.2.11 Loading Sequence

Trout Lake Dam is unique, because of its construction and loading history. Therefore, the load sequence used to evaluate the behavior of the dam was developed to simulate the construction of the original dam, initial reservoir filling, construction of the pressure berm, construction of the dam raise, and final filling of the reservoir. The following steps summarize the load sequence used for these studies:

1. Construction of the original dam – The weight of the original dam was evaluated using a staged construction analysis, which simulates the construction of the dam in lifts. This method more accurately simulates how the weight of the dam is transferred to the foundation during initial construction.
2. Original filling of the reservoir – The hydrostatic pressure was applied to the upstream face of the dam to simulate the initial reservoir filling of the reservoir to El. 270.
3. Construction of the pressure berm – The hydrostatic pressure was applied to the downstream face of the dam to simulate construction of the pressure berm.
4. Construction of the dam raise – The construction of the dam raise was again performed using a stage construction analysis.
5. Final filling of the reservoir – The reservoir load was increased to the NWS and the sedimentation load was applied to the upstream dam face.

After the initial load sequence was performed each of the loading combinations were analyzed.

3.3 METHOD OF ANALYSIS

These analyses used the finite element program ANSYS to perform a structural analysis of Trout Lake Dam. The finite element model was used to determine the stresses, deformations, and overall stability of the dam due to the usual, unusual, and extreme loading conditions. The model included a significant portion of the foundation in addition to the concrete dam. The foundation extends at least one dam height into each abutment and at least one dam height upstream and downstream from the extreme edges (toe and heel) of the dam.

The geometry of the dam and foundation was based on data from record drawings. The dimensions used to define the finite element model are shown on Figure No. 3 - 8. An isometric view of the finite element model is shown on Figure No. 3 - 9.

The global coordinate system for the finite element model is oriented such that the X-axis (i.e., cross-canyon) is positive toward the left abutment, Y-axis (i.e., vertical) is positive upward, and Z-axis (i.e., upstream/downstream) is positive downstream.

3.3.1 Parametric Studies

3.3.1.1 Finite Element Refinement

URS Corporation (URS) performed several studies to verify that a sufficient number of elements had been used in the finite element model. The number of nodes and elements in the model were increased until additional mesh refinement did not result in significant changes in the computed deflection in the model. A plot of the computed crest deflection for various models with different numbers of degrees of freedom (DOF) (i.e., there are a maximum of six DOF per node in the model) as shown on Figure No. 3 - 10. The results show that the model used in the studies has a sufficient number of DOFs.

The final model contains 10,616 nodes, 10,854 elements, and 29,292 DOF. The elements consist of eight-node brick, single-node mass elements, and four-node contact elements. The eight-node brick elements (ANSYS program calls these elements "SOLID185") are used to simulate the behavior of the concrete dam and foundation. The single-node mass elements ("MASS21") are elements distributed to the nodes on the upstream face of the dam to simulate the added inertia during the seismic loads due to the reservoir/dam interaction. The four-node contact elements ("CONTA173") are elements used to simulate the dam/foundation contact, the horizontal plane between the original and raised portions of the dam, and the vertical cracks in the raised portion of the dam.

3.3.1.2 Variable Concrete and Foundation Modulus

Several studies were performed in which the foundation deformation modulus was varied from 1,120,000 lb/in^2 to 3,400,000 lb/in^2. The studies evaluated the effects the different foundation material properties would have on the behavior of the dam.

The horizontal and vertical stresses on the upstream and downstream face of the crown cantilever (maximum section) were used to evaluate the behavior of the dam. Figure No. 3 - 11 shows the cantilever (vertical) and arch (horizontal and tangential to the dam face) stresses in the selected nodes. The results from these studies indicated that there are only minor changes in the behavior of the dam. As the foundation deformation modulus increased, the arch stresses at the crown cantilever decreased. This indicated that the load carried by the arches was reduced, and the load carried by the cantilevers was increased. The increase in the cantilever action of the dam was shown by an increase in the moment (directly related to the increase in the change of cantilever stresses between the upstream and downstream face, shown on Figure No. 3 - 11), which increased as the foundation deformation modulus increased.

In addition, the change in behavior was evaluated by comparing the abutment sliding stability of the dam/foundation interface from the different finite element models. The results indicated that the change in sliding factor of safety was only a couple percentage points for the range of foundation deformation modulus.

Based on the results from these sensitivity studies, it was concluded that the foundation deformation modulus did not significantly influence the behavior of the dam. Therefore, for these studies, the foundation modulus was assumed equal to the mean value for the range, 2,200,000 lb/in^2.

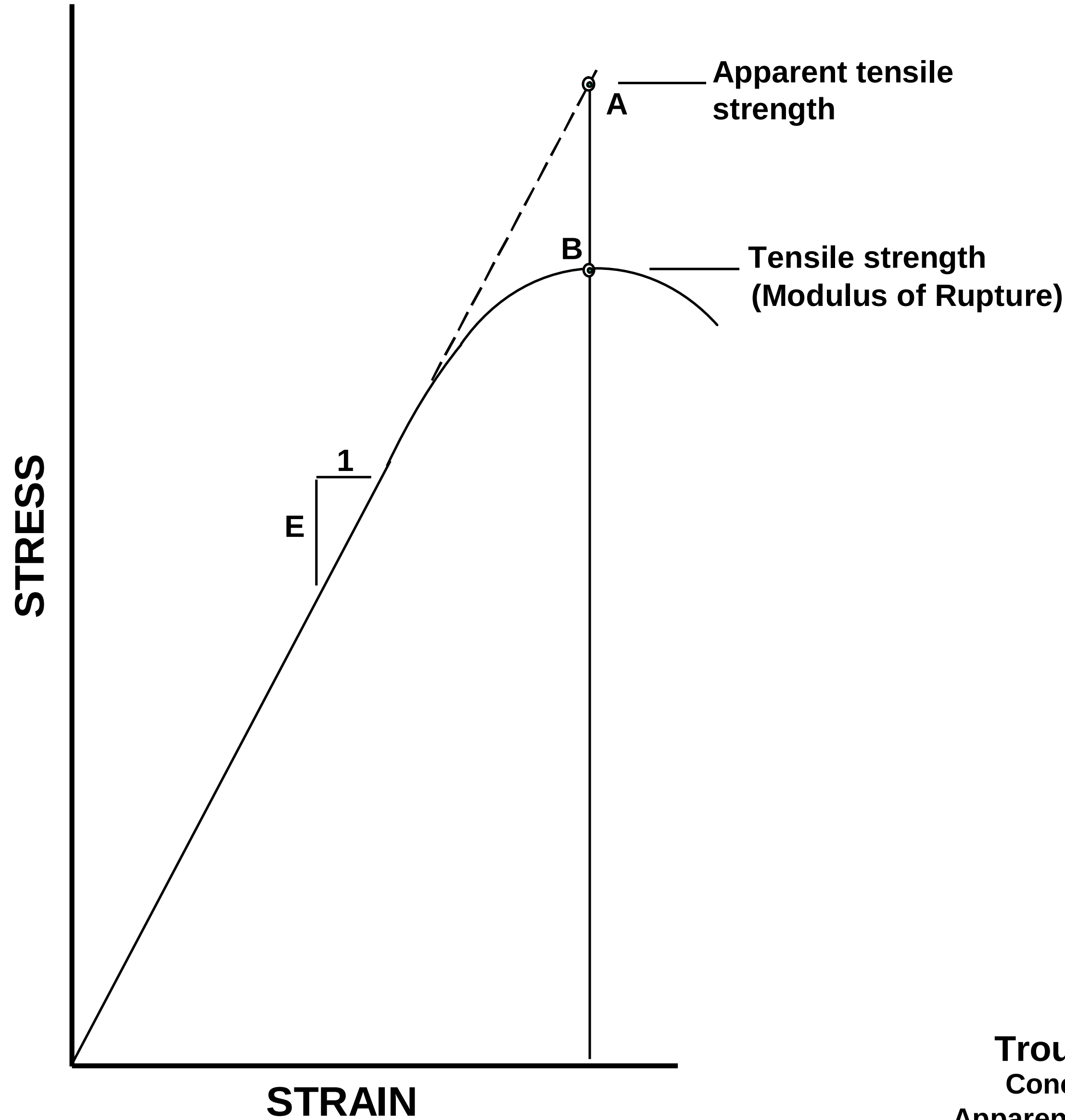

Trout Lake Dam
Concrete Strength
Apparent Tensile Strength

Figure No. 3- 1

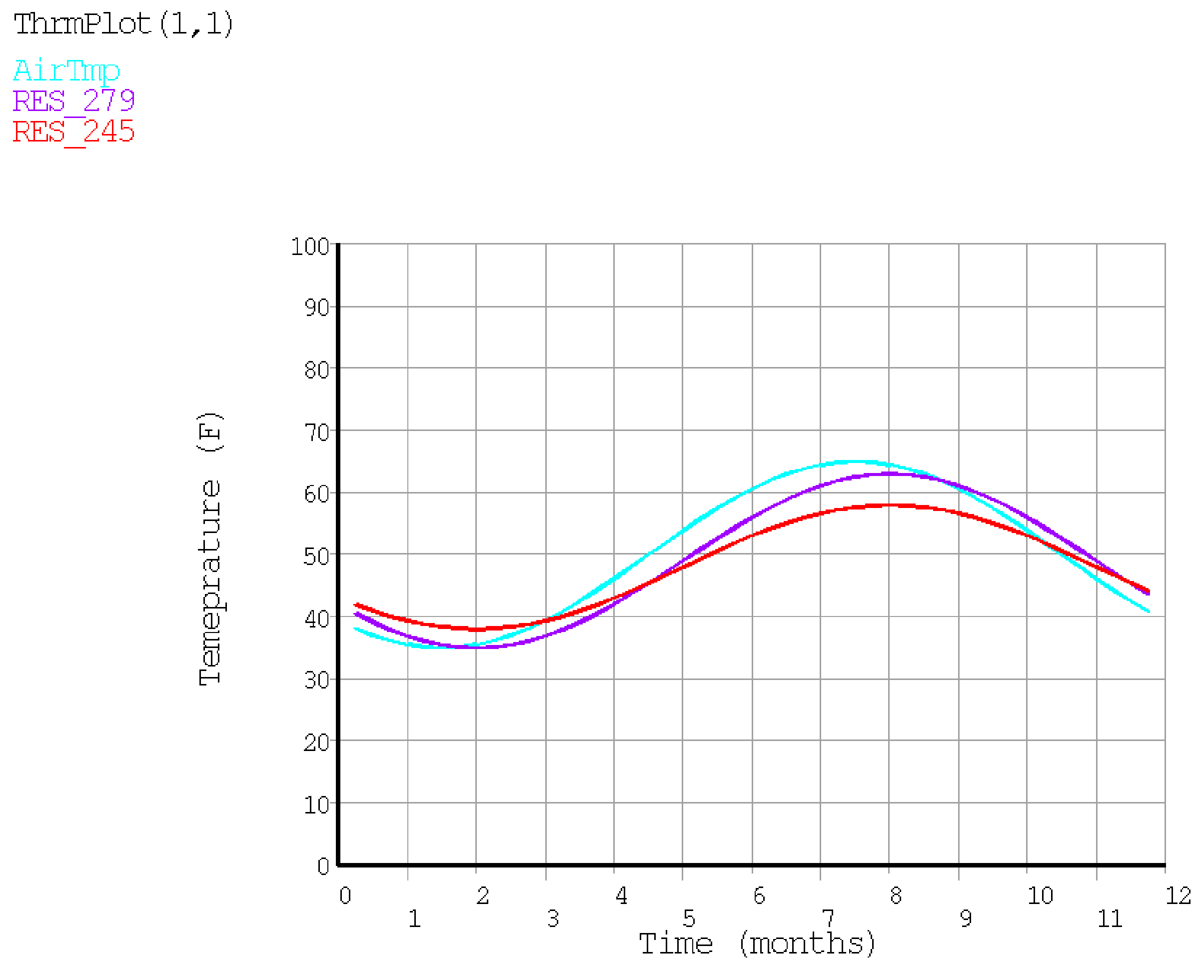

Trout Lake Dam
Thermal Analysis
Variable Air & Reservoir Temperatures
Figure No. 3- 2

URS

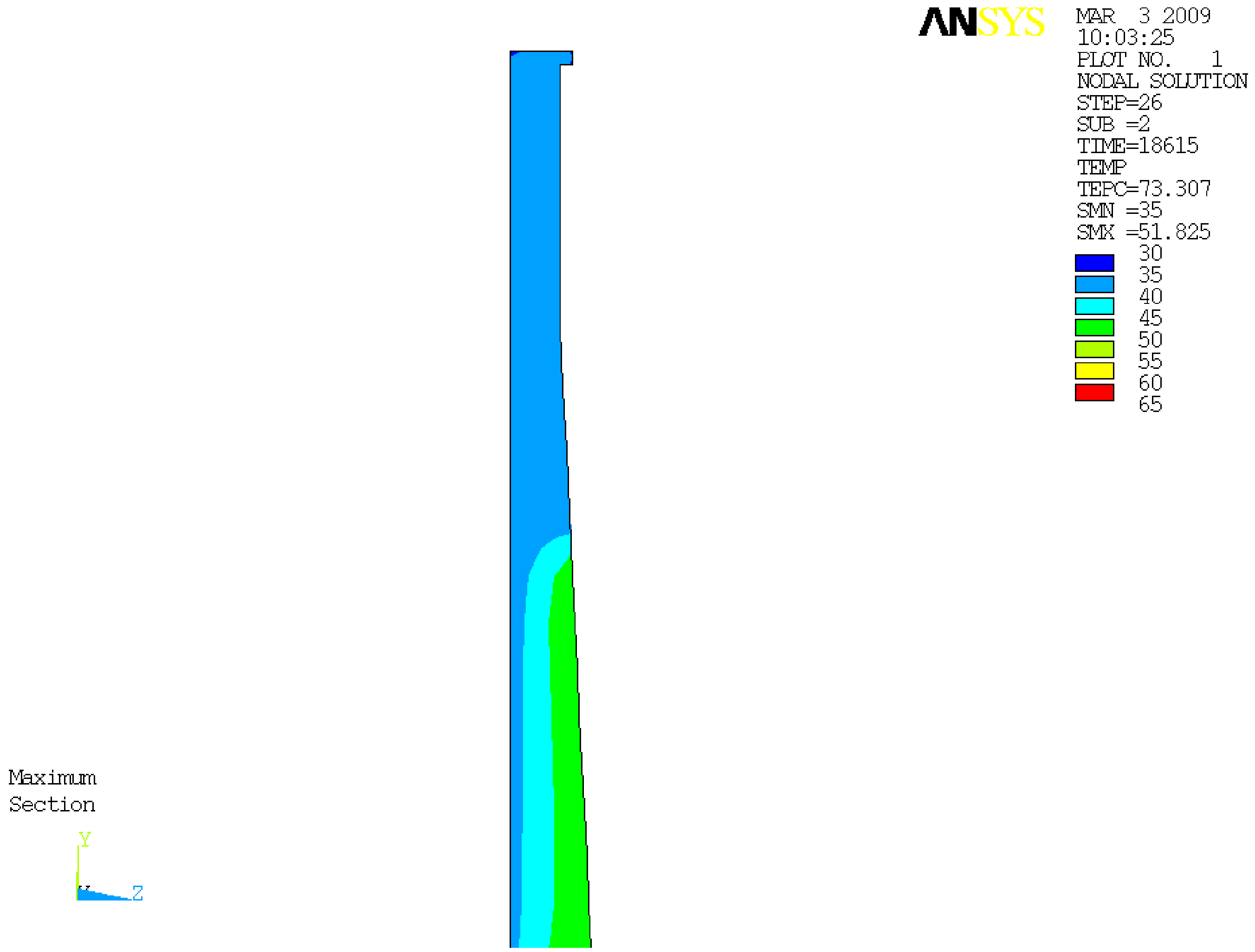

URS

Trout Lake Dam
Thermal Analysis
Winter Temperatures

Figure No. 3- 3

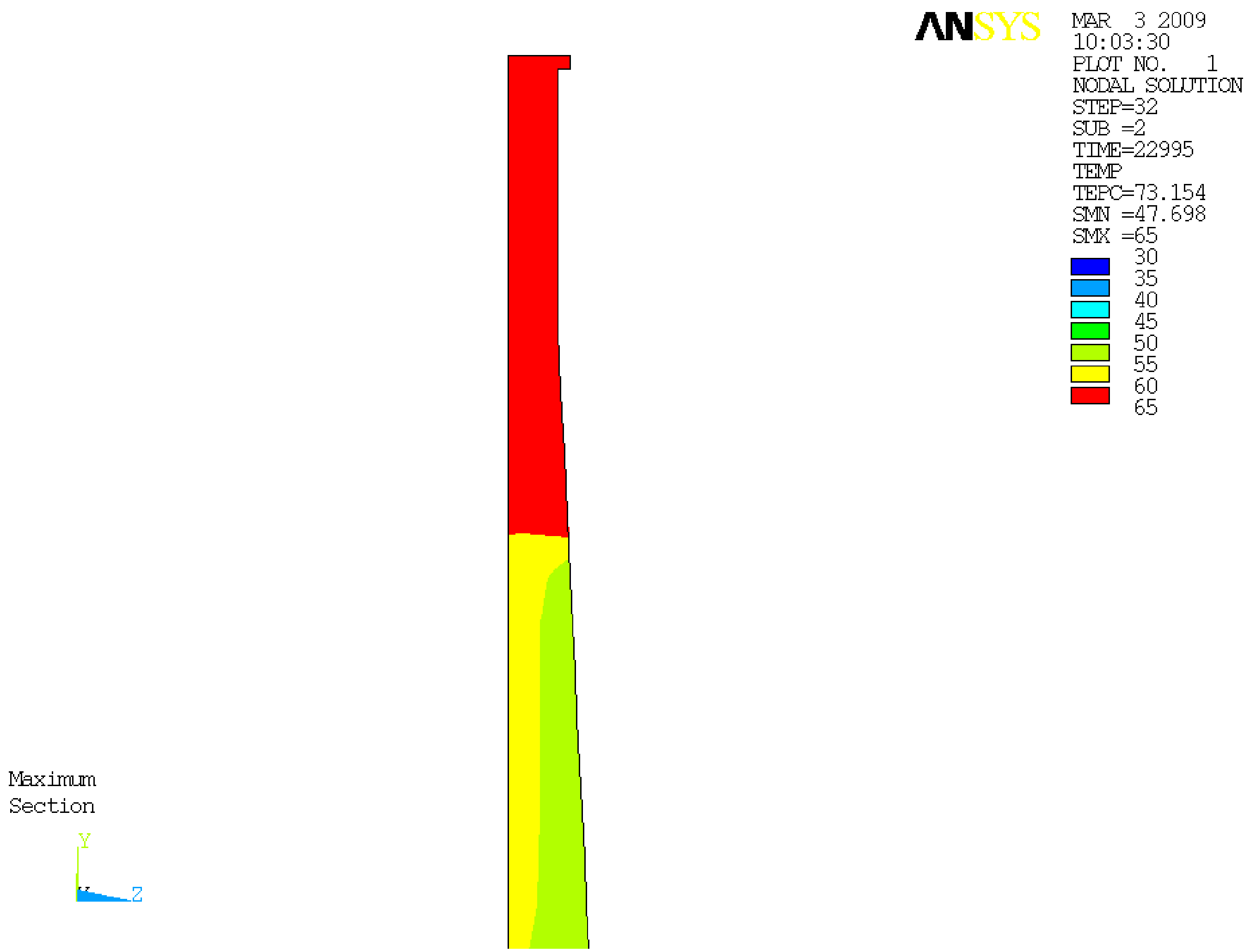

URS

Trout Lake Dam
Thermal Analysis
Summer Temperatures

Figure No. 3- 4

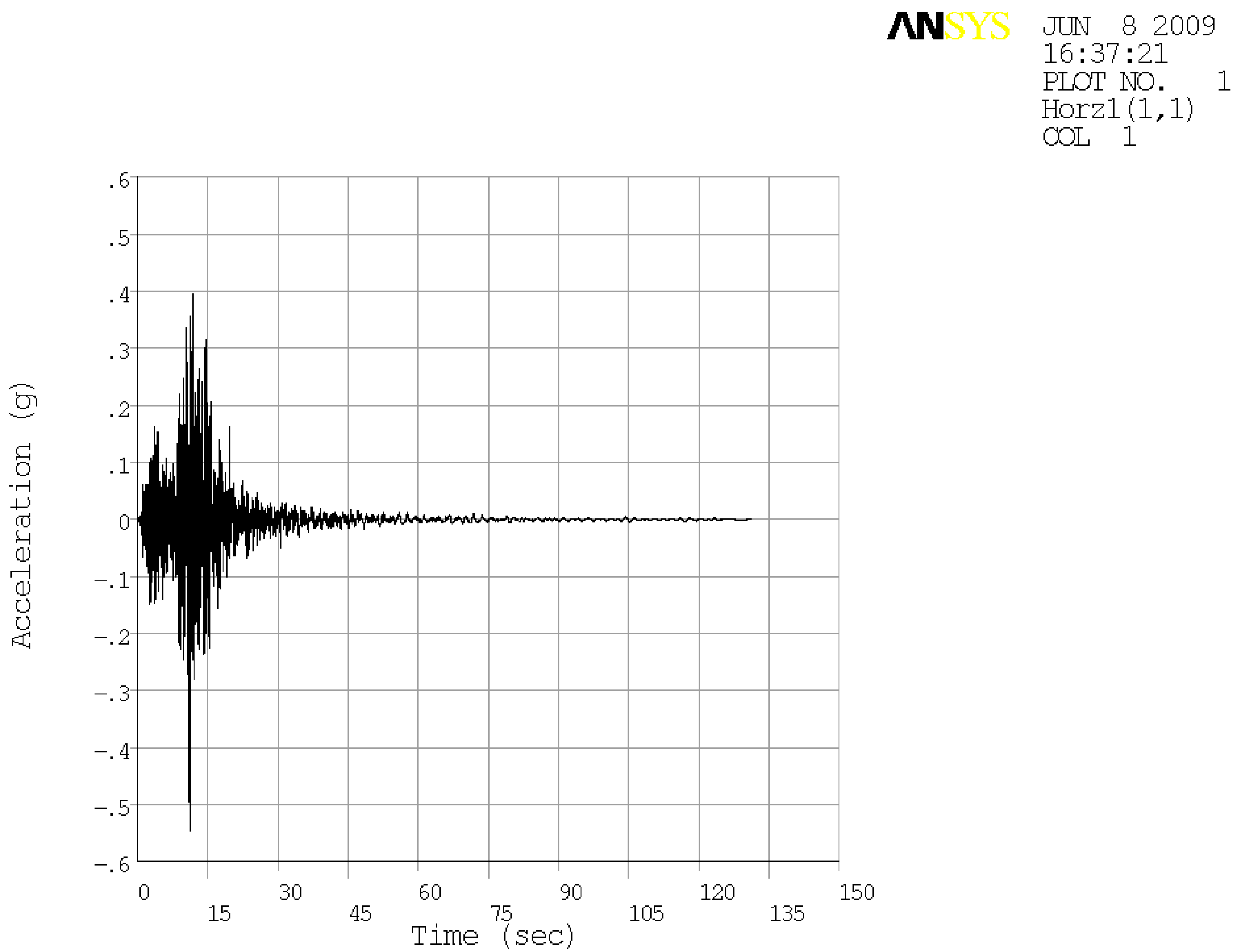

Trout Lake Dam
Seismic Analysis
Upstream-Downstream Acceleration

URS

Figure No. 3- 5

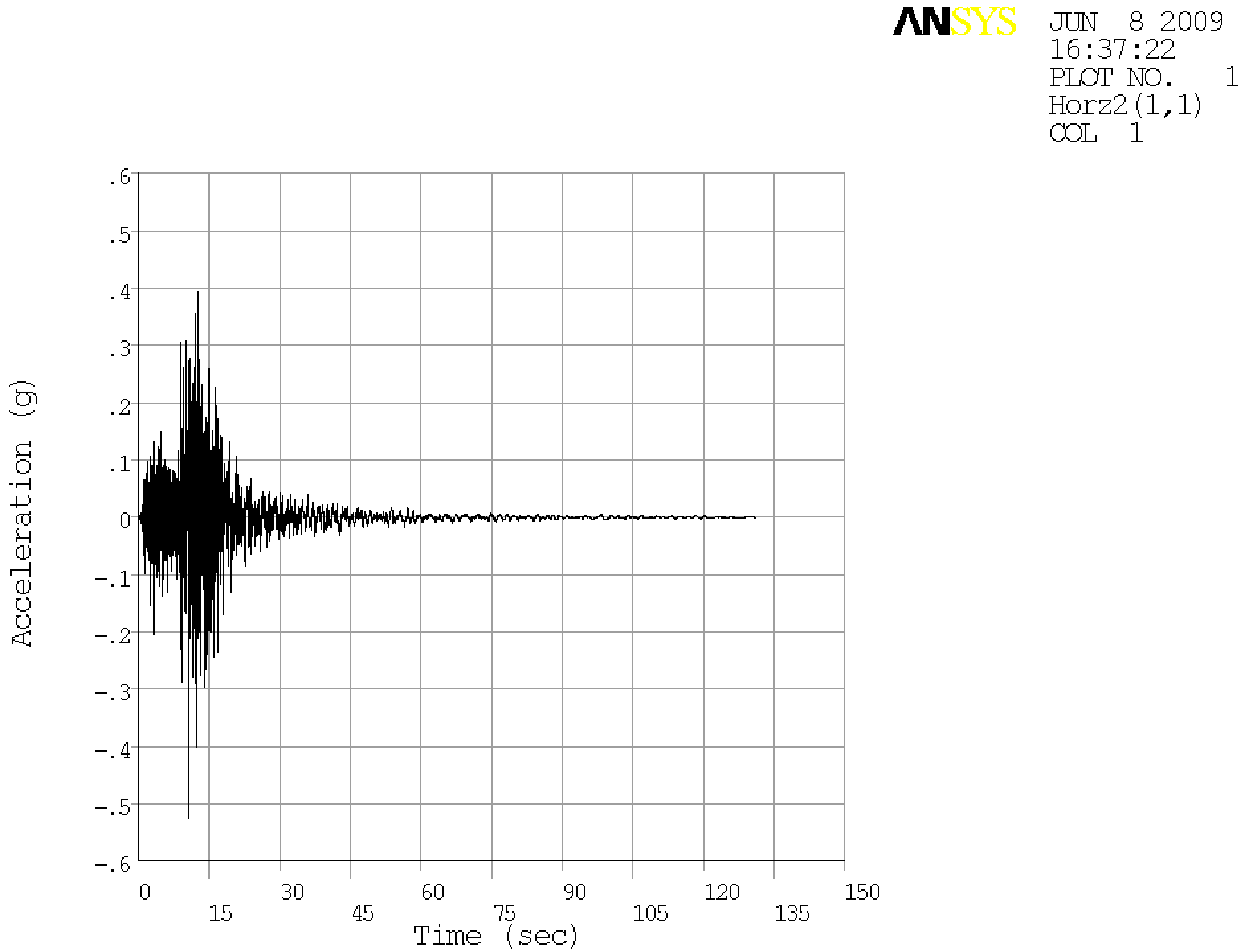

Trout Lake Dam

Seismic Analysis

Cross-Canyon Acceleration

Figure No. 3- 6

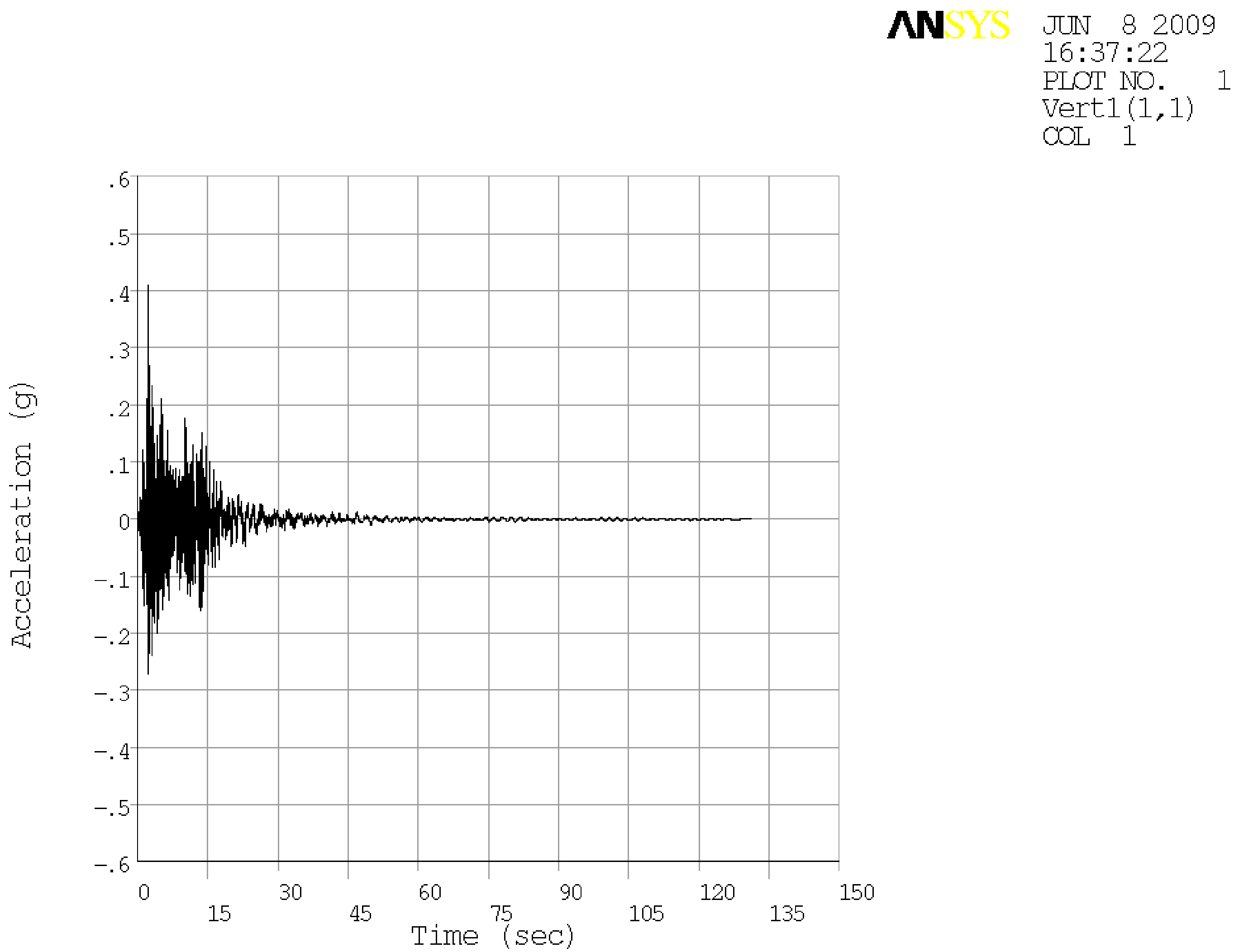

Trout Lake Dam

Seismic Analysis

Vertical Acceleration

URS

Figure No. 3- 7

Measured from the left abutment, intrados length, 2-10-2009			
Crack	Length, ft	Angle, degrees	Distance Between, ft
1	13	12.8	
			19
2	32	31.6	
			16
3	48	47.4	
			23
4	71	70.1	
			16
5	87	85.9	
			15
6	102	100.8	
			20
7	122	120.5	
			19
Right Abut.	141	139.2	

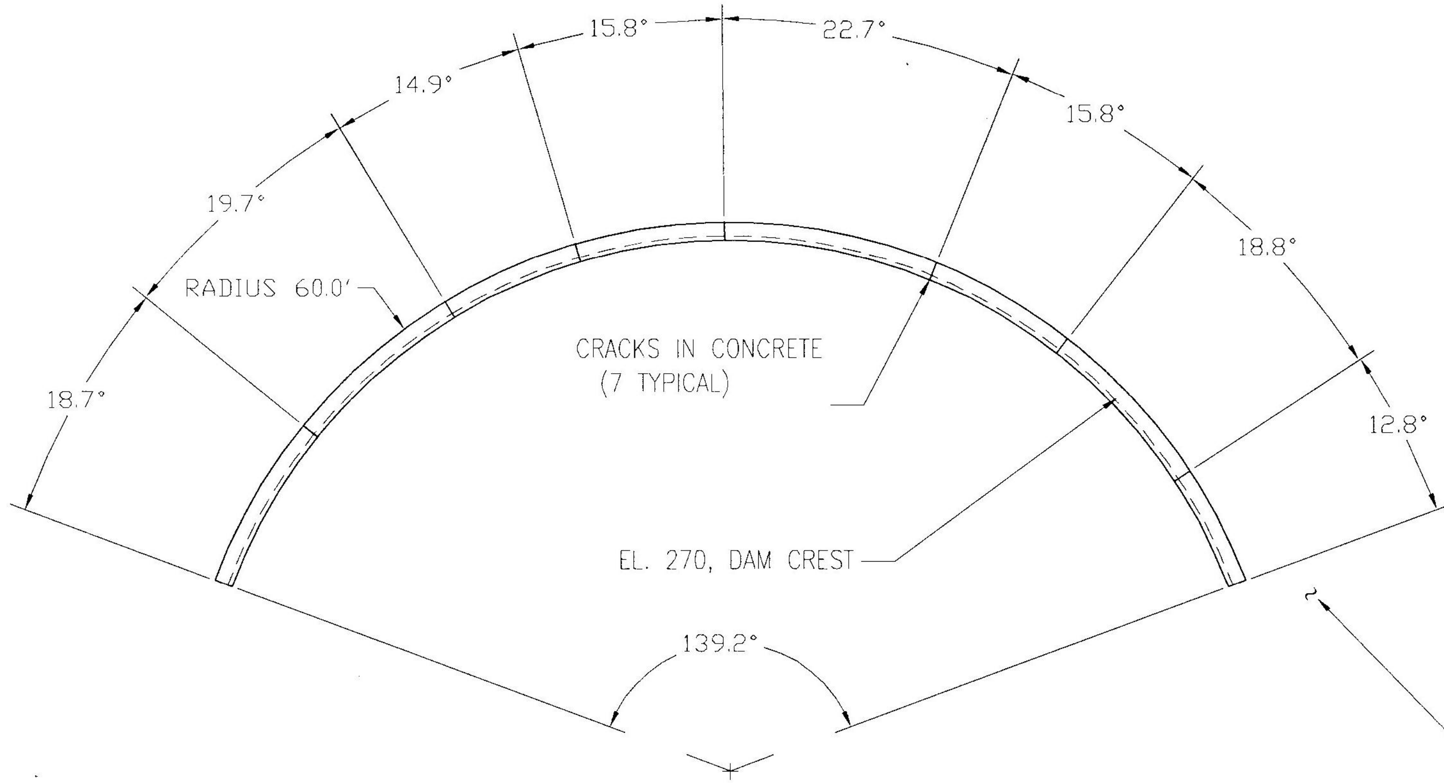

PLAN

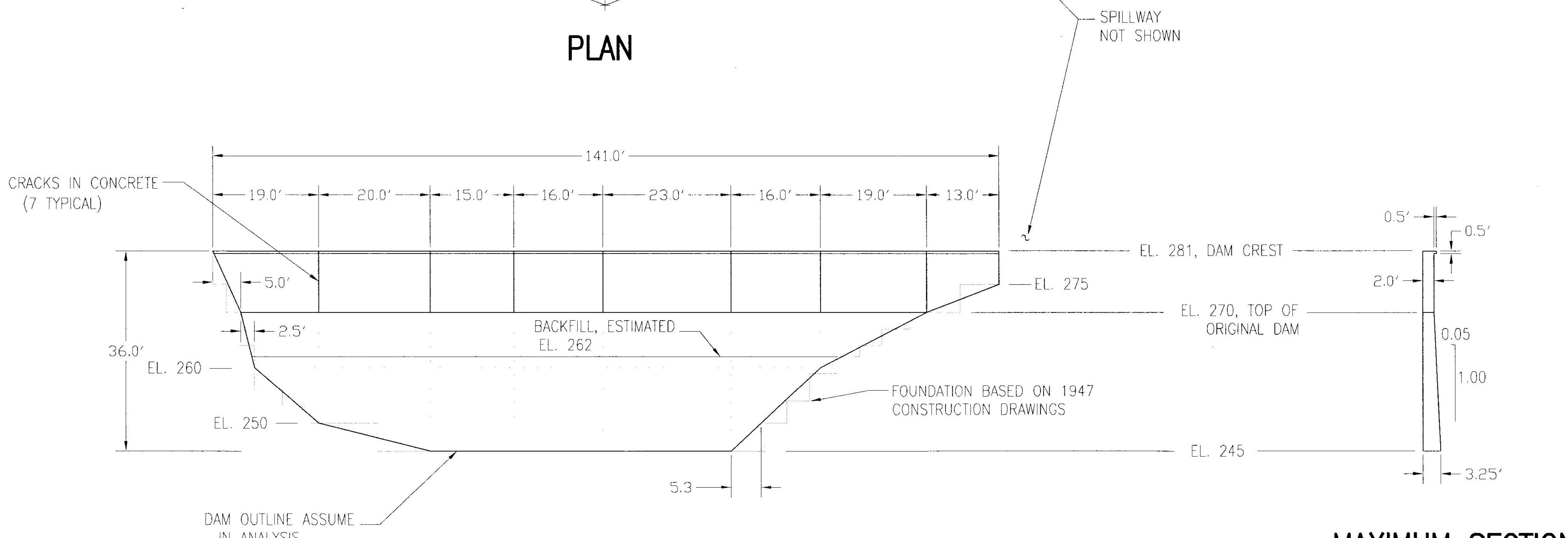

DOWNSTREAM DEVELOPED PROFILE

MAXIMUM SECTION

Trout Lake Dam

Finite Element Model
Assumed Geometry

URS

Figure No. 3- 8

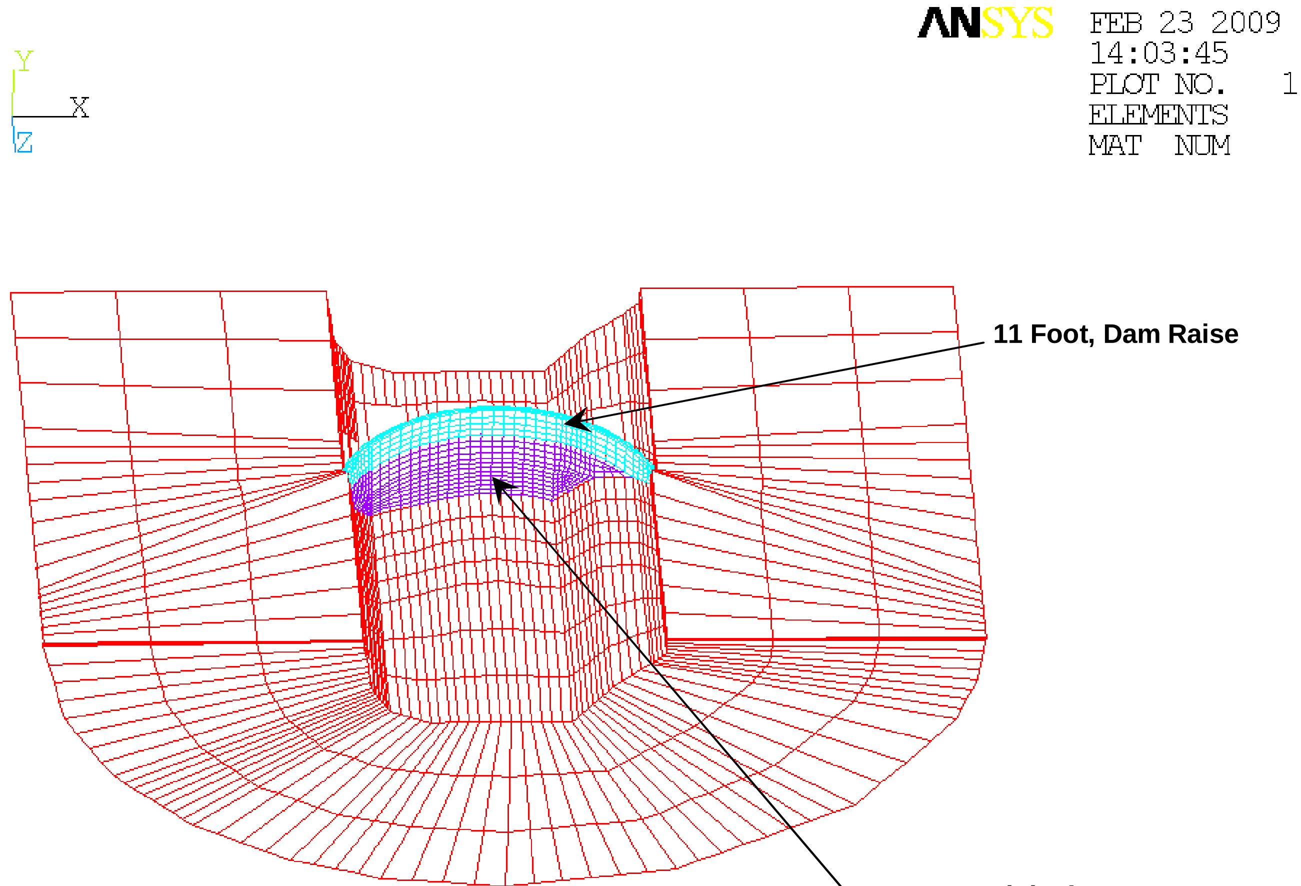

Trout Lake Dam
Finite Element Model
Isometric View

URS

Figure No. 3- 9

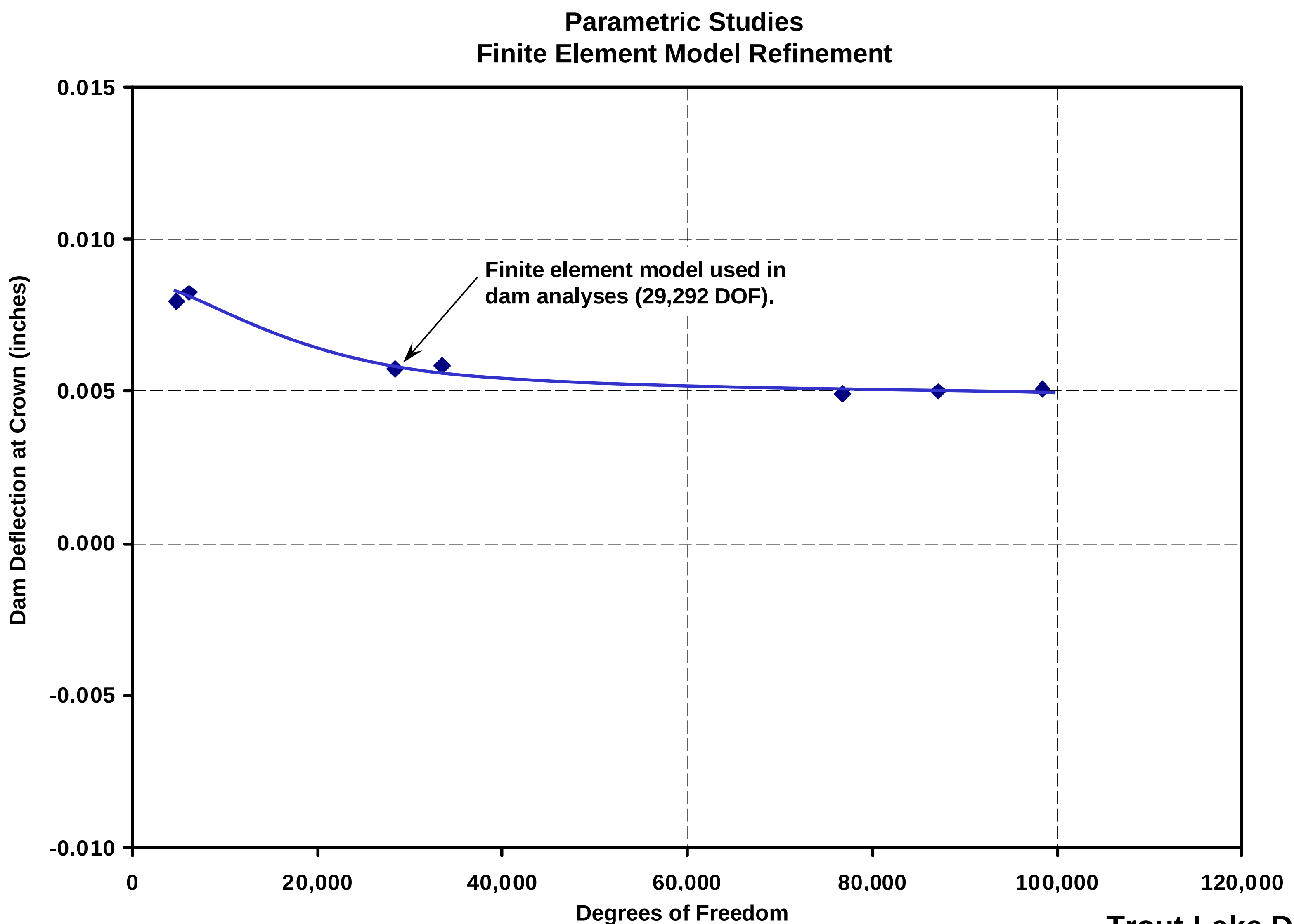

Trout Lake Dam
Parametric Studies
Mesh Refinement

URS

Figure No. 3- 10

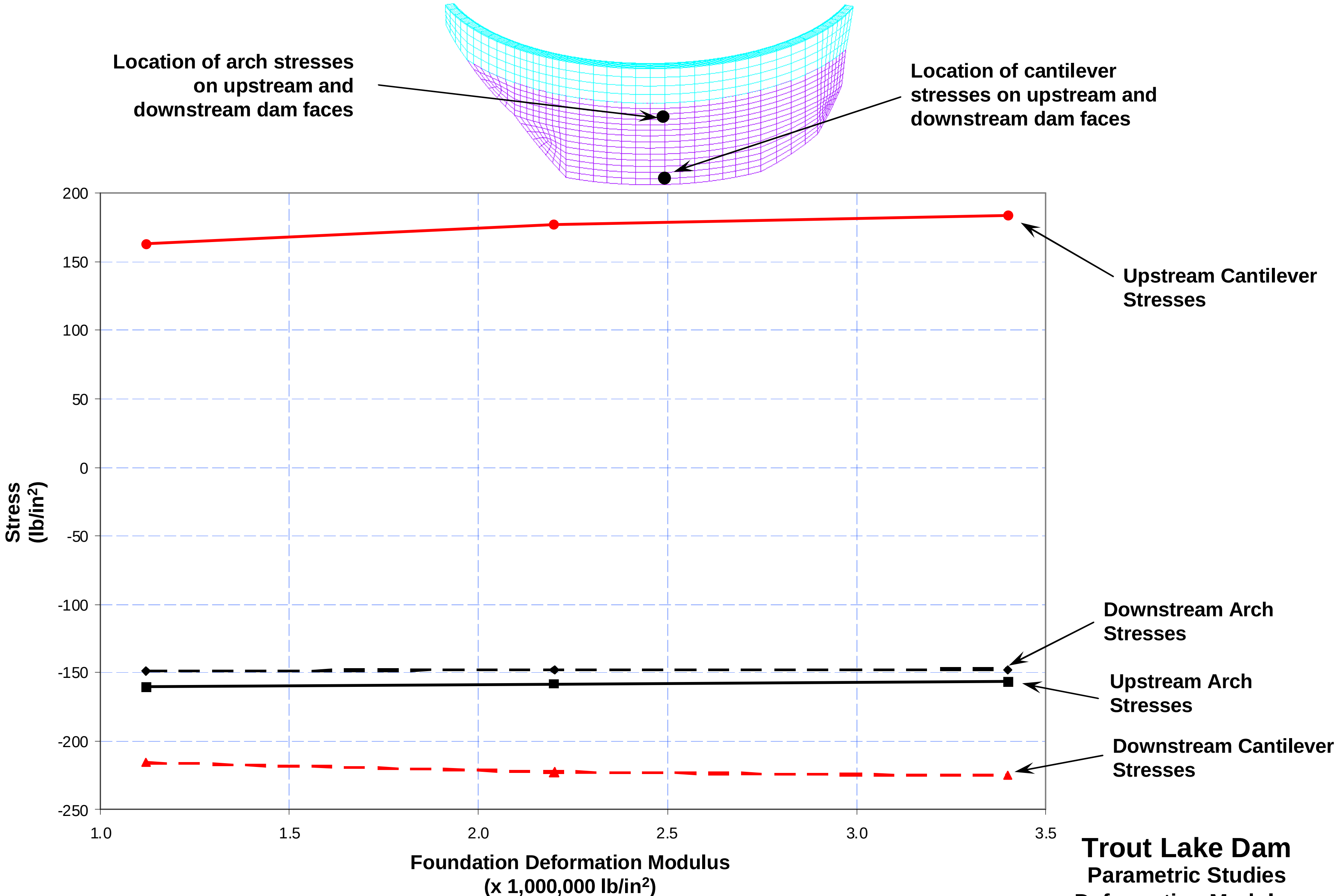

URS

Trout Lake Dam

Parametric Studies
Deformation Modulus
Arch and Cantilever Stress

Figure No. 3- 11

4.1 STRUCTURAL ANALYSIS

Dam Local Coordinate System

The dam was evaluated by transforming the global results into a dam local coordinate system, which is oriented such that the X-axis is normal to the dam axis, Y-axis is horizontal and tangent to the circumference of the arch, and Z-axis is vertical. The stress results were primarily evaluated using the horizontal (i.e., local Y-axis) and vertical (i.e., local Z-axis) stresses, defined as “arch” and “cantilever” stresses, respectively. The stress results are presented in the form of color contour plots, with the contour units shown in pounds per in square inch (lb/in^2). Negative and positive values correspond to compressive and tensile stresses, respectively.

The structural behavior of the dam was also evaluated using the computed deflections from the analysis, which are presented in graphs showing the radial (normal to axis of dam), tangential (tangent to the arch circumference), and vertical deflections along the upstream edge of the dam crest and upstream face of the crown cantilever (maximum section). A positive radial deflection is downstream and normal to the axis of the dam. A positive tangential deflection is towards the right abutment (looking downstream). Vertical deflection is positive in the upward direction.

Dam/Foundation Interface Local Coordinate Systems

The finite element model contains a thin layer of solid elements (defined as “transition elements”) located between the dam and foundation elements. The typical height of these elements is 0.7 percent of the dam height (approximately 3 inches). The transition elements are assumed to have the same material properties as the dam concrete. The sliding stability along the dam/foundation interface was evaluated by transforming the global results into local coordinate systems of the transition elements. The coordinate systems for the transition elements are oriented such that the X-axis is in the plane of the dam/foundation interface and tangent to the upstream face of the dam, Y-axis is in the plane of the dam/foundation interface and normal to the upstream face of the dam (pointing toward the center of the arch), and Z-axis is normal to the slope of the dam/foundation interface. The normal and shearing forces were computed with the local coordinate systems of the transition elements and used to estimate the sliding factor of safety along the interface. In addition, non-linear contact elements were used between the transition and foundation elements to provide the ability of simulating a no tension condition. The no tension condition assumes that cracks may develop between the dam and foundation.

4.2 STATIC ANALYSIS

The initial study for each load combination began with homogeneous, monolithic, and linear elastic assumptions for the dam and foundation. Based on the results from the initial study, the finite element model was modified to evaluate specific behaviors (i.e. separation (cracking) along the dam/foundation interface and horizontal cracks on the downstream face). The following sections discuss the results from the static load combinations.

4.2.1 Usual Load 1

4.2.1.1 Stress Results

This usual loading condition (USLC-1) evaluated the dam for static loads due to gravity, NWS (El. 279.5), pressure berm, spring/fall temperatures, and sedimentation. The spring/fall temperature condition simulates the dam as it transitions from warmer to colder temperatures. This is assumed to be the *"stress free temperature"* when the dam is neither expanding nor contracting, and provides a baseline from which to evaluate other temperature loads. The maximum stresses for USLC-1 are summarized in Table 4-1.

Table 4-1
Usual Load Combination 1,
Maximum Stress

Description	Compression	Tension
	(lb/in^2)	(lb/in^2)
Extrados (upstream) Face		
Arch Stress	-162	46
Cantilever Stress	-79	246*
Intrados (downstream) Face		
Arch Stress	-243	--
Cantilever Stress	-320	52
Allowable Strength	-1,333	143

Notes: Positive stress denotes tension, and negative stress denotes compression.
* The peak tensile stress is isolated to the base of the upstream face, see discussion below.
-- Denotes no tension
lb/in^2 pounds per square inch

The plot of the radial, tangential, and vertical deflections due to USLC-1 along the crest of the dam and crown cantilever (maximum section in the center of the dam) are shown on Figure No. 4- 1 and Figure No. 4- 2, respectively. The results show a maximum radial deflection of 0.035 inches downstream, located approximately 14 feet below the crest of the dam near the crown cantilever, as shown on Figure No. 4- 2. The radial deflection at the crest is less than the deflection lower in the dam because the hydrostatic reservoir pressure increases with depth; therefore, there is significantly less load on the upper arches of the dam and the reduced load results in less deformation at the crest. Note, the arches near the dam crest act like a spring support for the top of the maximum cantilever, as shown on Figure No. 4- 5.

The horizontal arch stress results from the finite element analysis on the upstream and downstream face of the dam are shown on Figure No. 4- 3. The results show that the computed arch compressive and tensile stresses are within the allowable strength range of the concrete for USLC-1.

The cantilever stress results on the upstream and downstream face of the dam are shown on Figure No. 4- 4. The cantilever and arch stresses for the crown section of the dam, along with the exaggerated deformed shape, are shown on Figure No. 4- 5.

The results show that cantilever tensile stresses develop in the model on the upstream face near the base, and at the central portion of the downstream face, as shown on Figure No. 4- 5. The tensile stresses on the upstream face near the base are primarily due to the bending moments caused by the hydrostatic load on the dam. The cantilever tensile stresses on the downstream face are cause by bending between the constrained base and the upper arches (spring support at the crest).

The maximum computed tensile stresses on the upstream face near the base of the dam are greater than the maximum allowable tensile strength of 143 lb/in^2 for the concrete. This indicates that the dam/foundation interface may separate (i.e. crack) to reduce the potential tensile stresses. Similarly, the results show development of cantilever tensile stresses on the downstream face of the dam, as shown on Figure No. 4- 5, which indicates that horizontal cracks on the downstream face may develop to reduce the developments of these tensions. Note: the site examination observed seepage on the downstream face at several lift lines and the contact between the original and raised dam sections. Potential horizontal cracks at the upstream heel and on the downstream face of the dam will reduce the ability of the cantilevers to support load. This would result in the load being redistributed to the arches. Therefore to justify that the dam has adequate safety for the assumed load, an additional analysis that simulates the reduced strength of the cantilevers and increase load on the arches was performed.

4.2.2 Modified Usual Load 1a

The finite element model was modified to simulate cracking along the dam/foundation interface and horizontal cracking on the downstream face. The modulus of elasticity for selected transition elements was reduced to simulate a potential crack along the dam/foundation interface. Additionally, the vertical component of the modulus of elasticity for selected elements on the downstream face of the dam was reduced to simulate development of horizontal cracks. The modified elements in the dam are shown on Figure No. 4- 6.

The modified finite element model was evaluated for the static loads due to gravity, NWS (El. 279.5), pressure berm, spring/fall temperatures, and sedimentation. The load is identified as usual load combination 1a (USLC-1a).

4.2.2.1 Stress Results

The plot of the radial, tangential, and vertical deflections due to USLC-1a along the crest of the dam are shown on Figure No. 4- 7. A comparison of the maximum crest deflection results between USLC-1 and USLC-1a shows only a small increase in the downstream deflection, approximately 0.015 inches. The relatively small increase in radial deflection indicates that the load was already supported by the arches; therefore, modifying the finite element model to simulate the reduced capacity of the cantilevers did not result in any significant load redistribution.

The computed arch stress results from the finite element analysis on the upstream and downstream faces of the dam are shown on Figure No. 4- 8. The comparison of the results between load USLC-1 and USLC-1a (Figure No. 4-3 and 4-8) shows a moderate increase in the maximum compressive stress. The comparison primarily shows an increase in the arch stress magnitude over a larger area on the and downstream faces. A comparison of the arch stresses at the crown cantilever from USLC-1 to USLC-1a is shown on Figure No. 4- 9.

The results from the modified finite element model show that the arches in the dam have sufficient strength to support the redistribution of the load. Based on these results, Trout Lake Dam is considered to have adequate strength against overstressing for USCL-1 and USCL-1a.

4.2.2.2 Stability Results

The results from the finite element analysis were used to compute the normal and shear stress results along the dam/foundation contact. These stresses were then integrated over the area of the contact to estimate the normal and shear forces acting from the dam on the foundation. The normal and shear forces were then used to evaluate the sliding stability along the interface of the dam. The results from these stability computations for each sliding plane are summarized in Table 4-2 and are shown on Figure No. 4- 10.

Table 4-2
Modified Usual Load Combination 1a,
Sliding Factor of Safety

Description	Sliding Plane	Area	Normal Force	Shear Force	Factor of Safety
		(ft^2)	(kips)	(kips)	
Left Abutment	L1	12	25	3	12.3
Left Abutment	L2	28	83	52	2.6
Left Abutment	L3	49	321	274	1.9
Left Abutment	L4	63	621	342	2.9
Right Abutment	R1	24	200	83	3.8
Right Abutment	R2	23	302	54	9.0
Right Abutment	R3	44	397	205	3.1
Minimum Allowable Factor of Safety					1.5

Notes: ft^2 square feet
kips 1000 lbs

The results show that Trout Lake Dam has adequate safety against sliding for the usual load USLC-1a. Only usual load USLC-1a was evaluated because for sliding the increased arch action results in more severe sliding stability factors of safety along the abutments. Since USLC-1a has adequate safety against sliding, the stability factors of safety for USLC-1 would also be adequate.

4.2.3 Usual Load 2

4.2.3.1 Stress Results

This usual loading condition (USLC-2) evaluated the dam for static loads due to gravity, NWS (El. 279.5), pressure berm, summer temperatures, and sedimentation. The maximum stresses for USLC-2 are summarized in Table 4-3.

Table 4-3
Usual Load Combination 2,
Maximum Stress

Description	Compression	Tension
	(lb/in^2)	(lb/in^2)
Extrados (upstream) Face		
Arch Stress	-835	27
Cantilever Stress	-337	110
Intrados (downstream) Face		
Arch Stress	-691	61
Cantilever Stress	-300	260*
Allowable Strength	-1,333	143

Notes: Positive stress denotes tension, and negative stress denotes compression.
* The peak tensile stress is isolated to small area at the top of the berm on the downstream face, see discussion below.
lb/in^2 pounds per square inch

The plot of the radial, tangential, and vertical deflections due to USLC-2 along the crest of the dam and crown cantilever are shown on Figure No. 4- 11 and Figure No. 4- 12, respectively. The maximum radial deflection is approximately 0.06 inches in the upstream direction, and located at the crest of the dam approximately 42 feet towards the left abutment, as shown on Figure No. 4- 11.

The upstream deflection is due to the thermal expansion of the concrete caused by the warmer summer temperature loads. The warmer temperatures increase the length of the arches causing the crest of the dam to move in the upstream direction. The summer temperatures have a greater influence on the upper arches of the dam than the lower arches because the pressure berm insulates the lower portion of the dam from the summer air temperatures. This is why the majority of the upstream deflection is in the arches above the top of the berm. Note, the expansion of the concrete and insulation of the pressure berm also results in an upstream bending of the cantilevers starting near the top of the berm (El. 262), as shown on Figure No. 4- 12.

The computed arch and cantilever stress results from the finite element analysis on the upstream and downstream faces of the dam are shown on Figure No. 4- 13 and Figure No. 4- 14, respectively. The computed cantilever stress results for the crown section are shown on Figure No. 4- 15.

The arch stresses are less than the maximum allowable compressive and tensile strength of the concrete. The computed cantilever compressive stresses are also less than the allowable compressive stress; however, the maximum cantilever tensile stress on the downstream face is greater than the allowable tensile strength of the concrete, which is 143 lb/in^2. The peak cantilever tensile stress is due to the upstream bending due to summer temperature expansion of the concrete and the insulating effect of the berm, as discussed previously.

The cantilever tensile stresses on the downstream face may indicate that minor cracking may develop during this loading condition. If cracking were to develop it is not a concern regarding the safety of the dam during the summer loading condition, because of the restoring hydrostatic pressure from the reservoir.

Based on the results from this analysis, Trout Lake Dam is considered to have adequate strength against overstressing for USCL-2.

4.2.3.2 Stability Results

The results from the finite element analysis were used to compute the normal and shear stress results along the dam/foundation contact. These stresses were then integrated over the area of the contact to estimate the normal and shear forces acting from the dam on the foundation. The normal and shear forces were used to evaluate the sliding stability along the interface of the dam and foundation. The results from these stability computations for each sliding plane are summarized in Table 4-4 and are shown on Figure No. 4- 16.

Table 4-4
Modified Usual Load Combination 2,
Sliding Factor of Safety

Description	Sliding Plane	Area	Normal Force	Shear Force	Factor of Safety	
		(ft^2)	(kips)	(kips)		
Left Abutment	L1	12	280	139	3.2	
Left Abutment	L2	28	107	59	2.9	
Left Abutment	L3	49	263	290	1.5	
Left Abutment	L4	63	500	177	4.5	
Right Abutment	R1	24	276	310	1.4	2.5
Right Abutment	R2	23	386	117	5.3	
Right Abutment	R3	44	369	104	5.7	
Minimum Allowable Factor of Safety					1.5	

Notes: ft^2 square feet
kips 1000 lbs

The results for USLC-2 indicates that sliding plane R1 (located on the upper right abutment) has a computed factor of safety that is less than the minimum allowable of 1.5. The computed safety factor is not a concern, although it does not satisfy the stability criteria. This is because of the three-dimensional interaction that develops in the dam, in which there will be shear transfer within the dam above adjacent sliding planes (i.e. planes R1 and R2). In order for sliding along plane R1 to develop, there must also be sliding along the adjacent sliding plane (R2).

The effect of the interaction within the arch dam is evaluated using a progressive stability analysis (PSA). The progressive stability analysis methodology is summarized in the following list:

- If a sliding plane is evaluated to have a factor of safety that is less than required by criteria, then a PSA is performed.
- Since adjacent sliding planes must interact, the forces from the dam are combined for adjacent sliding places. For example, the total normal force from sliding planes R1 and R2 is computed, along with the total shearing force. These are then used to compute an interacting sliding factor of safety.
- If the combined factor of safety is greater than the required value per criteria, then the combined sliding plane is assumed to have adequate sliding stability. If the combined sliding planes do not satisfy criteria, then the PSA is performed for the combined planes (R1 and R2) plus the next adjacent sliding plane (R3).

The results from the PSA are shown in Table 4-4 and are shown on Figure No. 4- 16.

Based on these results, Trout Lake Dam is considered to have adequate safety against sliding for the usual load USLC-2.

4.2.4 Usual Load 3

4.2.4.1 Stress Results

This usual loading condition (USLC-3) evaluated the dam for static loads due to gravity, NWS (El. 279.5), pressure berm, winter temperatures, ice, and sedimentation. The initial analysis for load USLC-3 used a linear, homogeneous finite element model. The maximum stresses for USLC-3 are summarized in Table 4-5.

Table 4-5
Usual Load Combination 3,
Maximum Stress

Description	Compression	Tension
	(lb/in^2)	(lb/in^2)
Extrados (upstream) Face		
Arch Stress	-239	522*
Cantilever Stress	-106	582*
Intrados (downstream) Face		
Arch Stress	-393	353*
Cantilever Stress	-502	254**
Allowable Strength	-1,333	143

Notes: Positive stress denotes tension, and negative stress denotes compression.
* The peak tensile stress is located near the dam/foundation interface, see discussion below.
** The peak tensile stress is located near the top of the berm, see discussion below.
lb/in^2 pounds per square inch

The plot of the radial, tangential, and vertical deflections due to USLC-3 along the crest of the dam and crown cantilever are shown on Figure No. 4- 17 and Figure No. 4- 18, respectively. The maximum radial deflection is approximately 0.10 inches downstream and located at the crest of the dam approximately 28 feet towards the left abutment, as shown on Figure No. 4- 17.

A comparison between load USLC-1 and USLC-3 shows an increase in the downstream radial deflection at the crest by approximately 0.08 inches. This is due to the contraction of the concrete caused by the colder winter temperatures and the additional load due to the ice. The contraction of the concrete reduces the crest length, which results in an increase in the radial deflection. Similar to the summer loading condition USLC-2, the pressure berm provides insulation for the downstream face of the dam against the colder air temperatures; however, unlike the load USLC-2, the reservoir temperature is cold and overcomes the effect of the berm, which results in a cold concrete temperature and contraction in the lower portion of the dam.

The computed arch and cantilever stress results from the finite element analysis on the upstream and downstream faces of the dam are shown on Figure No. 4- 19 and Figure No. 4- 20, respectively. The computed cantilever stress results for the crown section are shown on Figure No. 4- 21.

The as shown on Figure No. 4- 21 and Figure No. 4- 22 the compressive stresses in the dam are all less than the allowable compressive strength of the concrete; however, there are significant areas of tensile stress on both faces. The maximum tensile stresses are greater than the allowable tensile strength of the concrete.

The tensile stresses on the upstream face are isolated to the dam/foundation contact. These results indicate that separation (cracking) along the dam/foundation interface will develop during this loading condition, which will reduce the magnitude of these tensile stresses.

The tensile stresses on the downstream face, shown on Figure No. 4- 20 are primarily due to the bending of the vertical cantilevers between the constrained base and the upper arches of the dam. This behavior indicates that minor joint opening may develop between the original and raised portion of the dam, or minor horizontal cracking may develop along the downstream face of the dam just above the berm.

As discussed previously, cracking along the dam/foundation interface or on the downstream face of the dam will result in a redistribution of load from the cantilevers to the arches in the dam. Therefore, to show that the dam has adequate safety after the load is redistributed to the arches of the dam the model was again modified.

4.2.5 Modified Usual Load 3a

The finite element model was modified to simulate cracking along the dam/foundation interface and horizontal cracking on the downstream face. Similar to load USLC-1a, the modulus of elasticity for selected transition elements along the upstream face at the dam/foundation interface was also reduced to simulate cracking at the base. Additionally, the vertical component of elastic modulus for selected elements on the downstream face was reduced to simulate development of horizontal cracks. The modified elements in the dam are shown on Figure No. 4- 22.

The modified finite element model was evaluated for the static loads due to gravity, NWS (El. 279.5), pressure berm, winter temperatures, ice, and sedimentation. The load is identified as usual load combination 3a (USLC-3a).

4.2.5.1 Stress Results

The plot of the radial, tangential, and vertical deflections due to USLC-3a along the crest of the dam are shown on Figure No. 4- 23. A comparison of the maximum crest deflection results between USLC-3 and USLC-3a shows only a small increase in the downstream deflection, approximately 0.02 inches. The relatively small increase in radial deflection indicates that the load was primarily supported by the arches before modifications of the finite element model, and therefore, simulating the reduced capacity of the cantilevers to support the load did not result in any significant load redistribution.

A comparison of the arch stress results from load UNLC-1 and UNLC-1a at the crown cantilever of the dam is shown on Figure No. 4-24. The comparison between the results shows only a moderate 14 percent increase in the peak arch compressive stress. The maximum arch stress is less than the allowable compressive strength of the concrete; therefore, based on the results from these analyses the dam is considered to have adequate safety against overstressing for the winter loading condition USLC-3a.

4.2.5.2 Stability Results

The results from the finite element analysis were used to compute the normal and shear stress results along the dam/foundation contact. These stresses were then integrated over the area of the contact to estimate the normal and shear forces acting from the dam on the foundation. The normal and shear forces were used to evaluate the sliding stability along the interface of the dam. The results from these stability computations for each sliding plane are summarized in Table 4-6 and shown on Figure No. 4- 25.

Table 4-6
Modified Usual Load Combination 3a,
Sliding Factor of Safety

Description	Sliding Plane	Area	Normal Force	Shear Force	Factor of Safety	
		(ft²)	(kips)	(kips)		
Left Abutment	L1	12	--	62	--	1.7
Left Abutment	L2	28	100	29	5.5	
Left Abutment	L3	49	440	341	2.1	
Left Abutment	L4	63	660	570	1.9	
Right Abutment	R1	24	215	91	3.8	
Right Abutment	R2	23	315	51	9.9	
Right Abutment	R3	44	437	316	2.2	
Minimum Allowable Factor of Safety					1.5	

Notes: ft^2 square feet
kips 1000 lbs

The results for USLC-3a show that sliding factors of safety for the abutment planes are greater than the required value of 1.5, for all area except area L1 on the left abutment. The factor of safety for sliding plane L1 has a computed factor of safety that is less than the minimum allowable of 1.5. However, as noted previously, in order for plane L1 to slide there must be movement along plane L2. The progressive stability analysis combined the normal and shear forces for plane L1-L2, which results in a sliding factor of safety greater than required.

The results show that Trout Lake Dam has adequate safety against sliding for the usual load USLC-3a.

4.2.6 Unusual Load 1

4.2.6.1 Stress Results

This usual loading condition (UNLC-1) evaluated the dam for static loads due to gravity, PMF (El. 282.0), pressure berm, winter temperatures, and sedimentation. The maximum stresses for UNLC-1 are summarized in Table 4-7.

Table 4-7
Unusual Load Combination 1,
Maximum Stress

Description	Compression	Tension
	(lb/in²)	(lb/in²)
Extrados (upstream) Face		
Arch Stress	-185	560*
Cantilever Stress	-101	622*
Intrados (downstream) Face		
Arch Stress	-446	430*
Cantilever Stress	-548	256**
Allowable Strength	-2,000	214

Notes: Positive stress denotes tension, and negative stress denotes compression.
* The peak tensile stress is located near the dam/foundation interface, see discussion below.
** The peak tensile stress is located near the top of the berm, see discussion below.
lb/in² pounds per square inch

The plot of the radial, tangential, and vertical deflections due to UNLC-1 along the crest of the dam and crown cantilever are shown on Figure No. 4- 26 and Figure No. 4- 27, respectively. The maximum radial deflection is approximately 0.09 inches downstream and located at the crest of the dam approximately 28 feet towards the right abutment, as shown on Figure No. 4- 26.

A comparison between load USLC-3 and UNLC-1 shows a decrease in the downstream radial deflection at the crest by approximately 0.01 inches, which is a 10 percent reduction, even though the reservoir load is increased. The reduction is because there is no ice load applied to the crest of the dam during the PMF event.

The computed arch and cantilever stress results from the finite element analysis on the upstream and downstream faces of the dam are shown on Figure No. 4- 28 and Figure No. 4- 29, respectively. The computed cantilever stress results for the crown section are shown on Figure No. 4- 30.

A comparison between the stress results from USLC-3 and UNLC-1 shows that the maximum arch compressive stress increase by approximately 13 percent, while the allowable strength of the concrete increased by approximately 33 percent. By inspection, this would lead to the conclusion that the dam will have adequate safety due to the PMF loading condition. However, similar to the previous usual loading conditions, additional studies were performed to show that if cracks were to develop at the dam/foundation interface, and on the downstream face of the dam, that the increased load to the arches would not result in overstressing failure mode.

4.2.7 Modified Unusual Load 1a

The finite element model was modified to simulate cracking along the dam/foundation interface and horizontal cracking on the downstream face. The modulus of elasticity for selected transition elements along the upstream face at the dam/foundation interface was also reduced to simulate cracking at the base. Additionally, the vertical component of elastic modulus for selected elements on the downstream face was reduced to simulate development of horizontal cracks. The modified elements in the dam are similar to that shown in Figure No. 4- 22.

The modified finite element model was evaluated for the static loads due to gravity, NWS (El. 282.0), pressure berm, winter temperatures, and sedimentation. The load is identified as unusual load combination 1a (UNLC-1a).

4.2.7.1 Stress Results

The plot of the radial, tangential, and vertical deflections due to USLC-3a along the crest of the dam are shown on Figure No. 4- 31. A comparison of the maximum crest deflection results between UNLC-1 and UNLC-1a shows only a small increase in the downstream deflection, approximately 0.02 inches. The relatively small increase in radial deflection indicates that the load was primarily supported by the arches before modifications of the finite element model, and therefore, simulating the reduced capacity of the cantilevers to support the load did not result in any significant load redistribution.

A comparison of the arch stress results from load UNLC-1 and UNLC-1a at the crown cantilever of the dam is shown on Figure No. 4- 32. The comparison shows negligible change in the maximum arch compressive stresses. The maximum arch stress is less than the allowable compressive strength of the concrete; therefore, based on the results from these analyses the dam is considered to have adequate safety against overstressing for the winter loading condition UNLC-1a.

4.2.7.2 Stability Results

The normal and shear stress results along the dam/foundation contact used to evaluate the sliding stability along the dam/foundation contact. The results from these stability computations for each sliding plane are summarized in Table 4-8 and are shown on Figure No. 4- 33.

Table 4-8
Unusual Load Combination 1a,
Sliding Factor of Safety

Description	Sliding Plane	Area	Normal Force	Shear Force	Factor of Safety	
		(ft^2)	(kips)	(kips)		
Left Abutment	L1	12	--	27	--	
Left Abutment	L2	28	67	95	1.1	1.9
Left Abutment	L3	49	426	287	2.4	
Left Abutment	L4	63	796	606	2.1	
Right Abutment	R1	24	175	96	2.9	
Right Abutment	R2	23	310	61	8.1	
Right Abutment	R3	44	466	382	2.0	
Minimum Allowable Factor of Safety					1.5	

Notes: ft^2 square feet
kips 1000 lbs

The results for UNLC-1a shows that factor of safety for sliding planes L1 and L2 on the left abutment have computed factors of safety that are less than the minimum allowable of 1.5. However, the sliding planes L1 and L2 cannot move without mobilization from the adjacent plane L3. The combined normal and shear forces for sliding planes L1, L2, and L3 were combined and the SFOS then becomes 1.9 for the left abutment. The results for the right abutment show that the sliding factors of safety are all greater than the require value of 1.5.

The results show that Trout Lake Dam has adequate safety against sliding for the usual load UNLC-1a.

4.3 DYNAMIC ANALYSIS

4.3.1 Modal Analysis

A modal analysis was performed on a linear finite element model using the computer program ANSYS to determine the dynamic characteristics of the dam. The dam/reservoir interaction was simulated using mass elements attached to the upstream face of the dam. The mass for these elements was computed using the generalized Westergaard's Theory for added mass on concrete dams during a seismic event *[14]*. The first 15 mode shapes and natural frequencies of the dam were computed. The natural frequencies of the dam are summarized in Table 4-9. The deflected shapes of the dam corresponding to the computed mode shapes 1 through 15 are shown on Figure No. 4- 34, Figure No. 4- 35, and Figure No. 4- 36.

Table 4-9
Modal Analysis Frequencies

Mode Number	Natural Frequency
	(Hz)
1	9.79
2	10.19
3	14.62
4	15.35
5	19.51
6	21.35
7	21.72
8	23.38
9	24.83
10	27.48
11	30.82
12	32.48
13	34.55
14	36.70
15	37.30

Notes: Hz = hertz

4.3.2 Transient Analysis

The dynamic analysis consisted of a full transient non-linear analysis using the acceleration time history described in Section 3.2.9, Maximum Design Earthquake (MDE). The material properties for the concrete and foundation were based on homogeneous, monolithic, and linear elastic assumptions; however, the finite element model included non-linear contact elements to simulate seven vertical cracks in the raised portion of the dam. The contact elements develop compressive stress normal to the element, but opening instead of developing tensile stresses. The non-linear simulation of theses seven cracks was not necessary for static loads, because the results showed that the cracks were effectively in compression for all the static loading conditions.

During an earthquake event there was a concern that the vertical cracks could open with an upstream deflection and a *"free cantilever"* could develop. A free cantilever is a portion of the dam between two open vertical cracks or joints that losses continuity with the rest of the dam. A free cantilever can jeopardize the safety of the dam if during a seismic event the upstream inertia causes vertical joints to open enough so that the free cantilever topples into the reservoir. This is illustrated on Figure No. 4- 37.

4.3.3 Extreme Load Combination 1 (EXLC-1)

4.3.3.1 Stress Results

The extreme loading condition (EXLC-1) considered the dam for normal static loads due to gravity, NWS (El. 279.5), spring/fall temperatures, sedimentation, hydrodynamic effect of the dam/reservoir interaction, and the seismic effects due to ground accelerations caused by the Maximum Design Earthquake (MDE). The maximum stresses for EXLC-1 are summarized in Table 4-10.

Table 4-10
Extreme Load Combination 1,
Maximum Stress

Description	Compression	Time	Tension	Time
	(lb/in^2)	(seconds)	(lb/in^2)	(seconds)
Extrados (upstream) Face				
Arch Stress	-448	11.53	633	11.48
Cantilever Stress	-381	11.53	600	14.62
Intrados (downstream) Face				
Arch Stresses	-710	14.67	452	11.48
Cantilever Stresses	-672	11.16	312	11.49
Allowable Stress:	-4,000			
Seismic Tensile Strength			655	
Apparent Tensile Strength			857	

Notes: See Table 3-1for a complete listing of allowable strengths.
lb/in^2 pounds per square inch

The crest deflections, and arch and cantilever stresses on the upstream and downstream face of the dam are shown on Figure No. 4- 38 through Figure No. 4- 55.

The results from the dynamic analysis show that the maximum upstream deflection is approximately 0.23 inches at 11.49 seconds, as shown as Figure No. 4- 44 and Figure No. 4- 56, and is primarily influenced by the fundamental mode of vibration. (Note: the fundamental mode causes one-half of the dam crest to deflect downstream, while the other half deflects upstream, as shown on Figure No. 4- 34). The maximum upstream displacement is located on the left side of the dam, between the left abutment contact and the center of the dam. If only one joint were to open due to this upstream inertia, then the maximum width of the opening would be limited to approximately 0.26 inches. This is not wide enough to overcome the amplitude of the crack asperities due to the 1.5 inch maximum size aggregate (MSA) in the concrete. Therefore, based on the displacement results, it is highly unlikely that a free cantilever will develop in the raised portion of the dam during the extreme seismic loading event.

The results from the analysis show that all compressive stresses in the dam are less than the allowable strength of the concrete for EXLC-1. Localized areas of horizontal arch tensile stress develop near the top of the original dam at times 11.48 and 11.49 seconds, as shown on Figure No. 4- 42 and Figure No. 4- 45, respectively. The figures show that the peak tensile stresses are isolated to one face of the dam, and the corresponding point on the opposite face is in compression. This information indicates that the arch continuity will be maintained during the earthquake since at least one face of the dam is in compression. Therefore, the stress results indicate that the arch continuity in the original dam will be maintained during the seismic load.

The cantilever stress results from the analysis show that all significant tensile stress develops on the upstream face near the base of the dam at 11.48 and 11.49 seconds. This indicates that the dam/foundation interface may undergo some cracking during the seismic loading condition. Previous studies for the static loads showed that when the base of the dam is allowed to crack the load is redistributed to the arch in the dam. As shown in the static load results, the redistribution does not significantly increase the load on the arches, because the structure is support for the reservoir is due to the arch action in the dam. Therefore, cracking at the base during the seismic load is not expected to significantly increase the compressive load on the arches, and the dam is considered to have adequate safety against overstressing during the extreme load combination, EXLC-1.

4.3.3.2 Stability Results

The normal and shear stress results along the dam/foundation contact were used to evaluate the sliding stability by computing the SFOS for planes defined along the dam/foundation contact. The results from these stability computations for each sliding plane are summarized in Table 4-11 and are shown on Figure No. 4- 57. The most sever stability condition for the left abutment occurs are time 11.53 seconds, and at time 14.67 seconds for the right abutment.

**Table 4-11
Extreme Load Combination 1,
Sliding Factor of Safety**

Description	Sliding Plane	Area	Time	Factor of Safety
		(ft²)	(seconds)	
Left Abutment	L1	12	11.53	6.1
Left Abutment	L2	28		2.0
Left Abutment	L3	49		1.5
Left Abutment	L4	63		1.5
Right Abutment	R1	24	14.67	3.9
Right Abutment	R2	23		6.4
Right Abutment	R3	44		1.2
Minimum Allowable Factor of Safety				1.1

Notes: ft^2 square feet
kips 1000 pounds

The results show that Trout Lake Dam has adequate safety against sliding for EXLC-1.

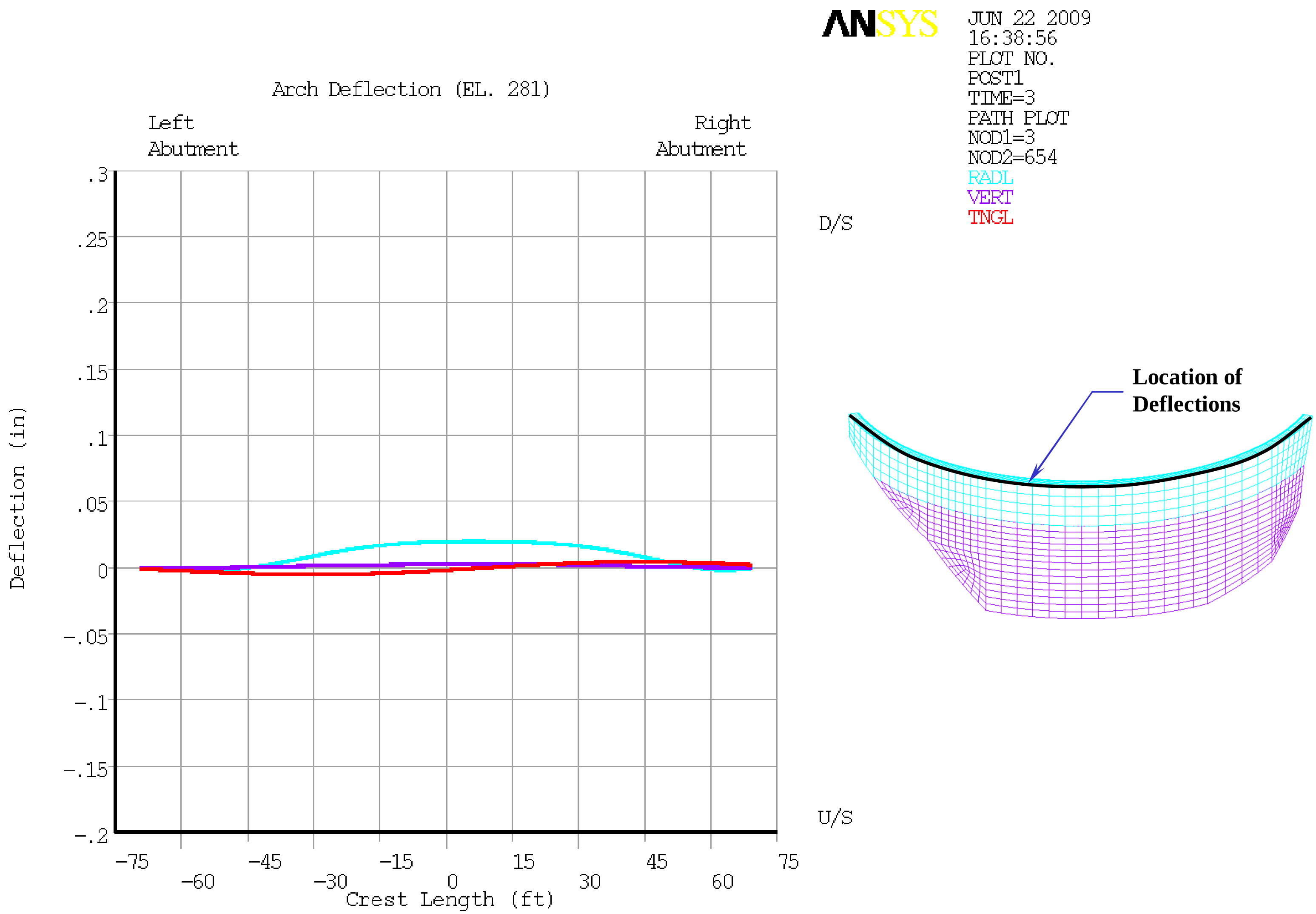

Trout Lake Dam

Usual Load 1

Dam Crest Deflection

Figure No. 4- 1

URS

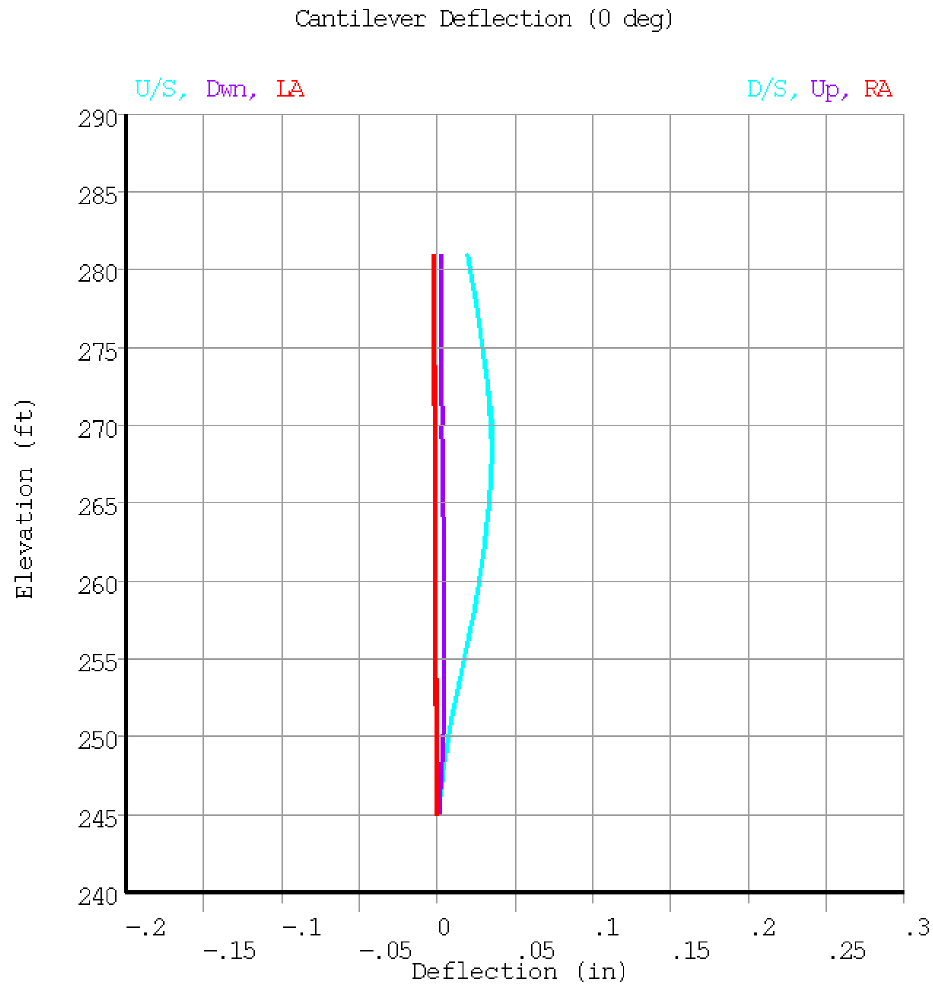

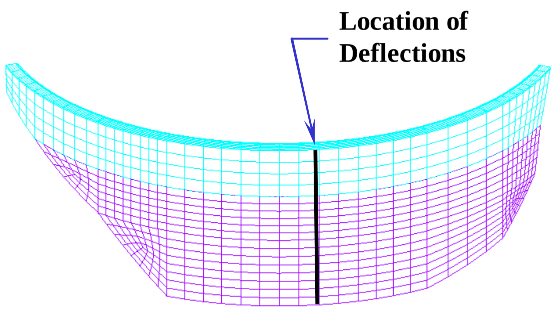

Trout Lake Dam
Usual Load 1
Crown Cantilever Deflection

Figure No. 4- 2

URS

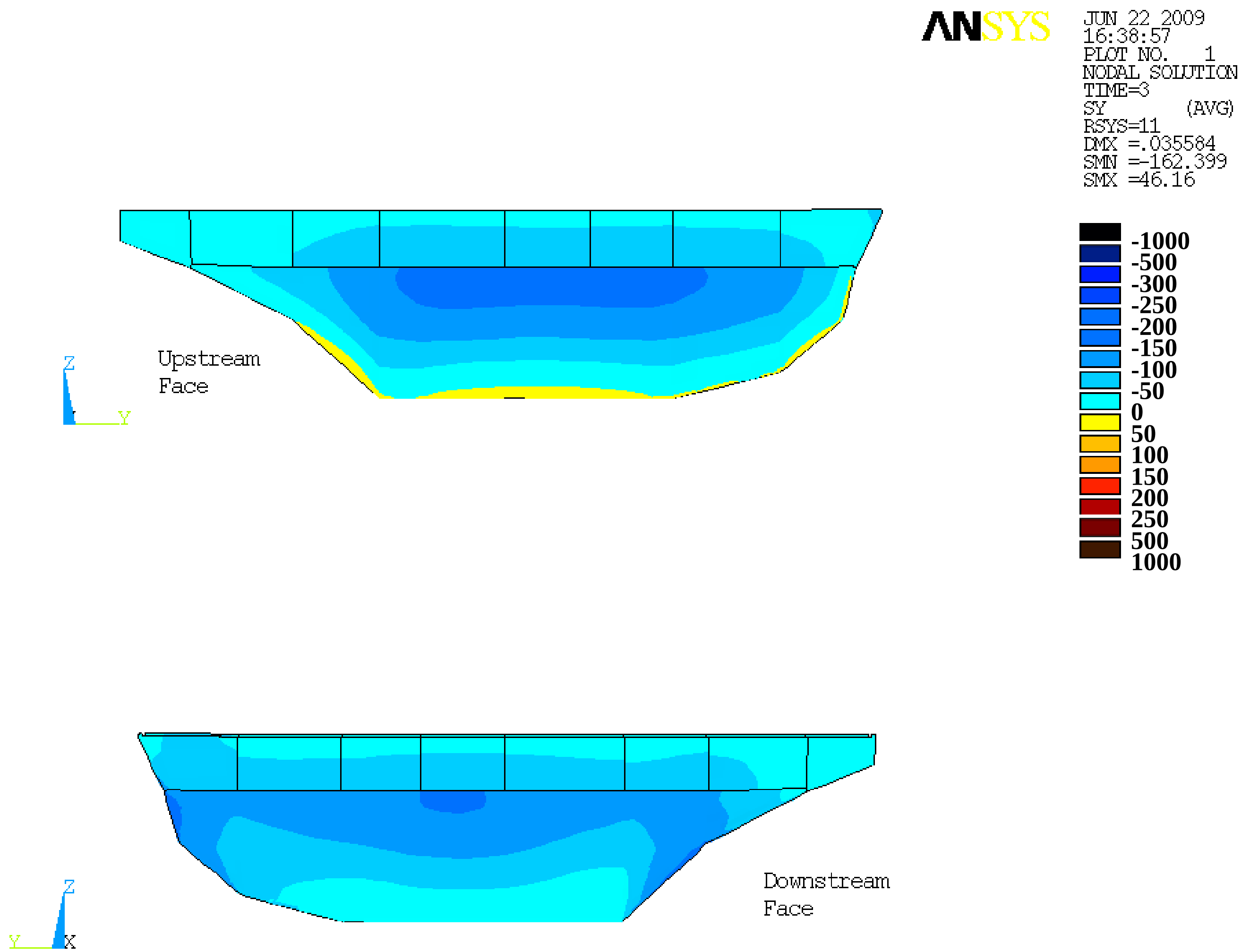

Trout Lake Dam
Usual Load 1
Arch Stress

Figure No. 4- 3

URS

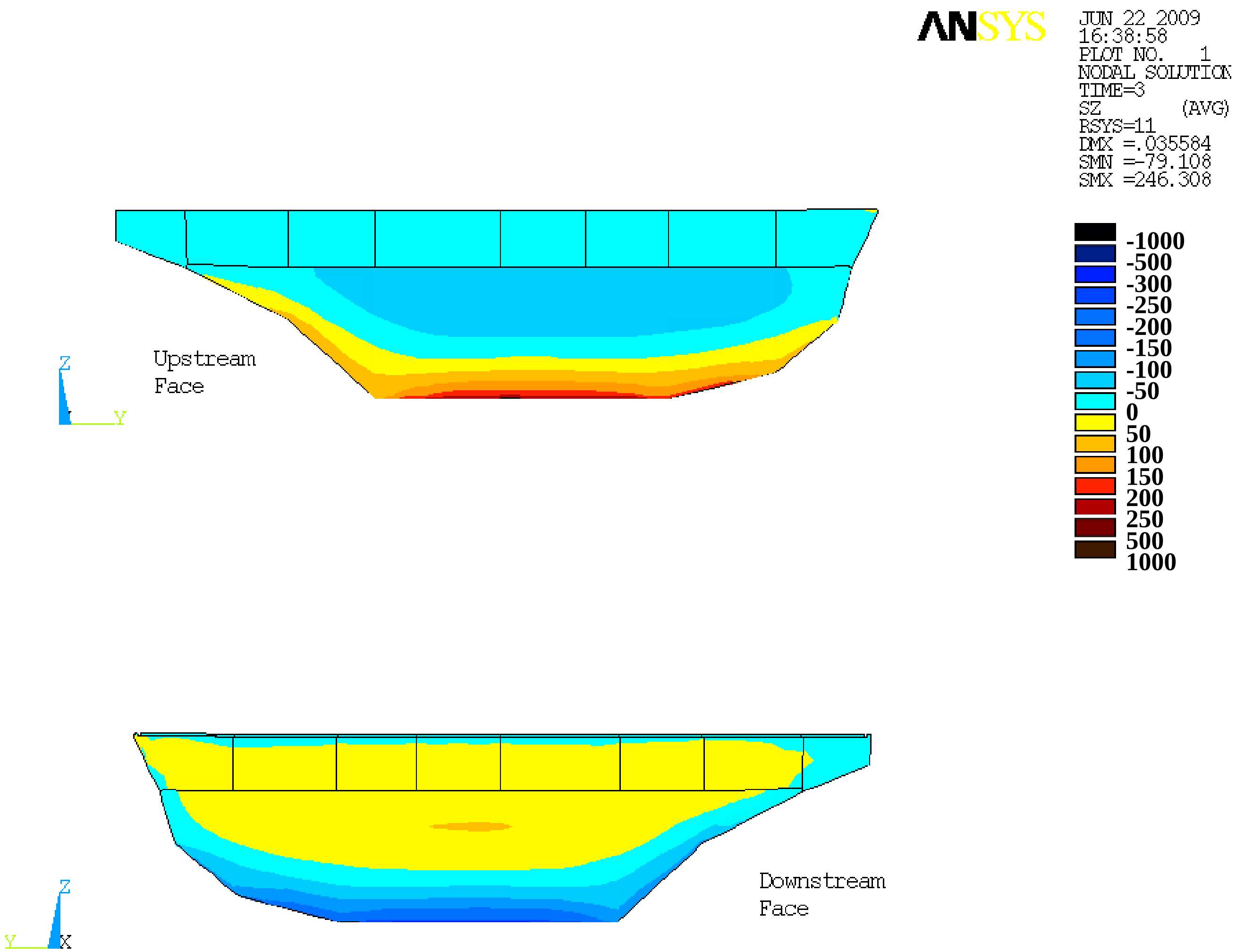

URS

Trout Lake Dam
Usual Load 1
Cantilever Stress

Figure No. 4- 4

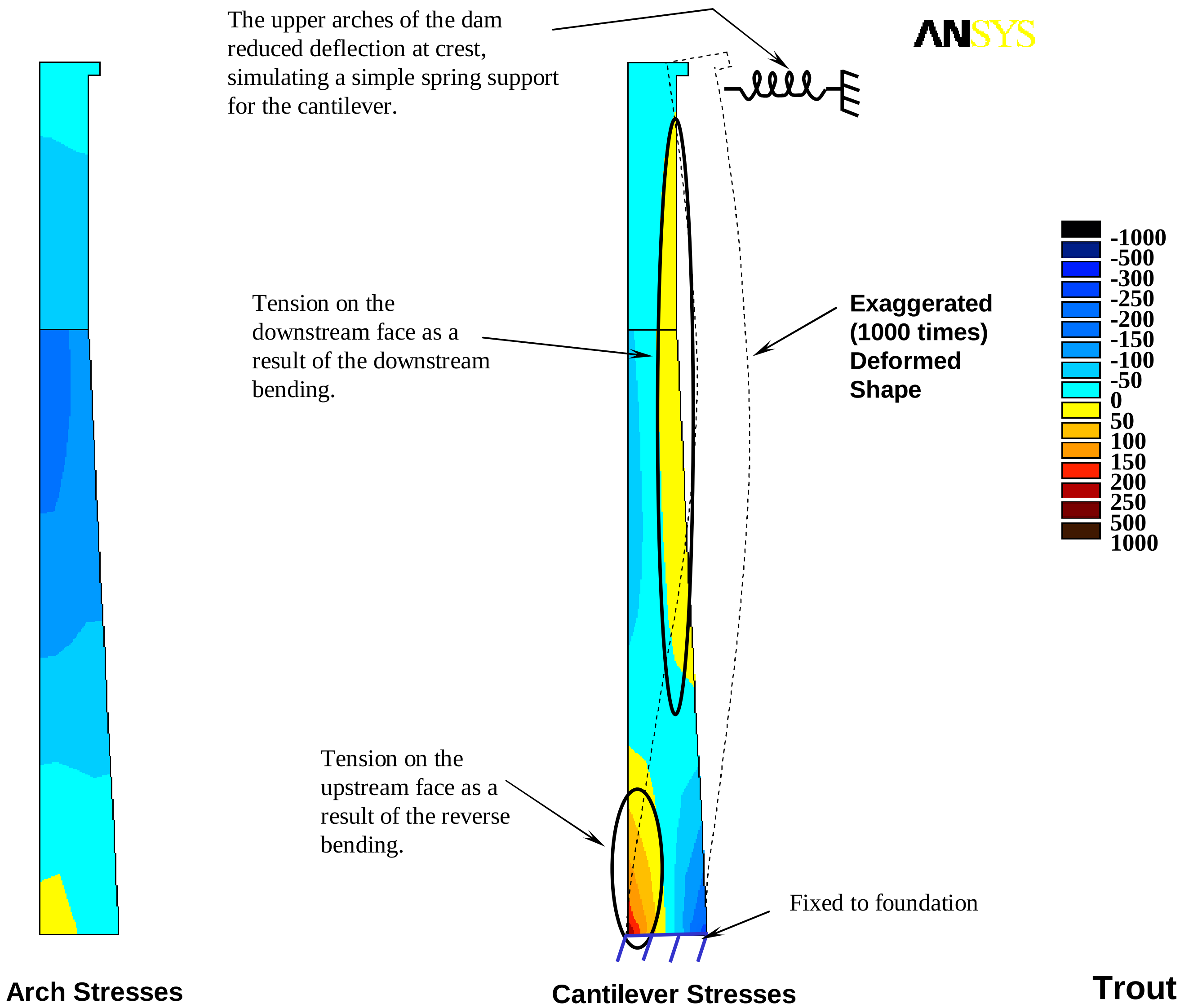

Trout Lake Dam
Usual Load 1
Crown Cantilever Section

URS

Figure No. 4- 5

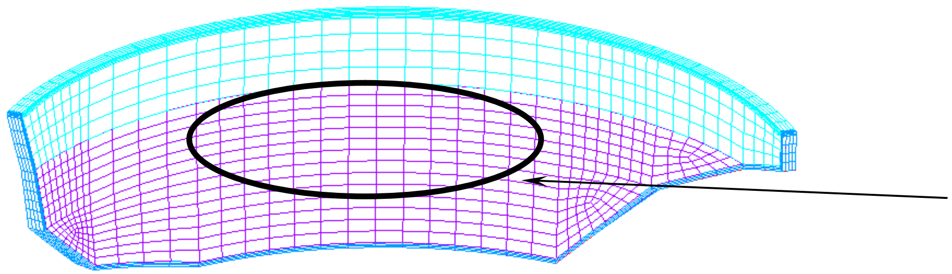

The location of the softened elements on the downstream face. The thickness of the dam is made up of four elements. The most downstream elements in this area has been softened.

Downstream View

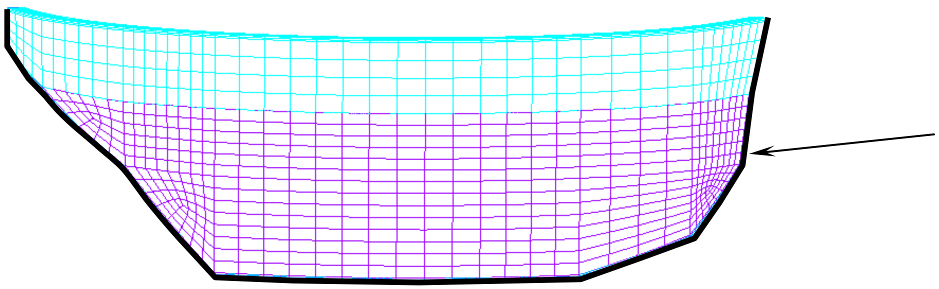

The location of the softened transition elements. The thickness of the dam/foundation is made up of four transition elements. The two most upstream elements have been softened.

Upstream View

Trout Lake Dam
Usual Load 1a
Location of Softened Elements

URS

Figure No. 4- 6

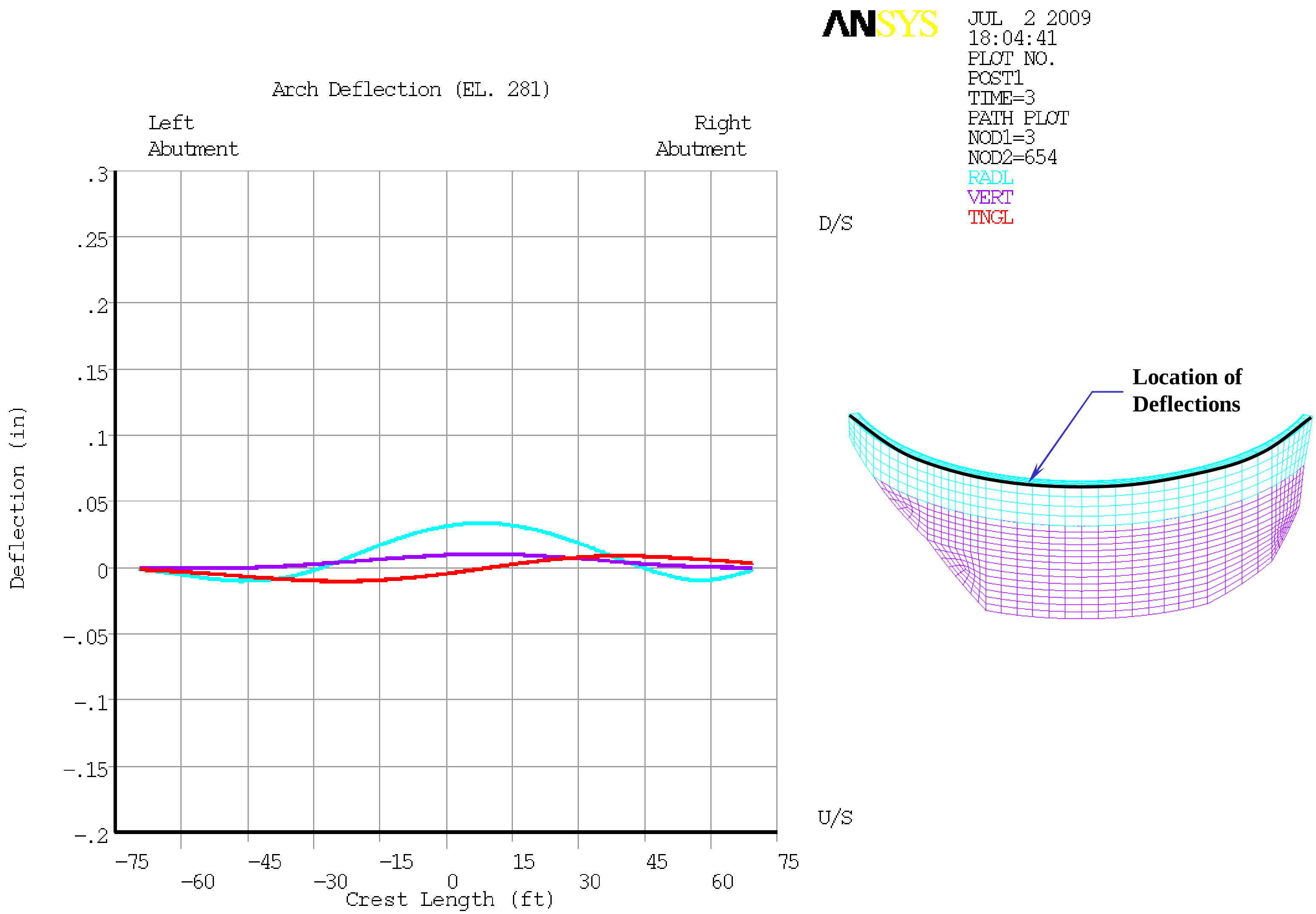

Trout Lake Dam
Usual Load 1a
Dam Crest Deflection

Figure No. 4- 7

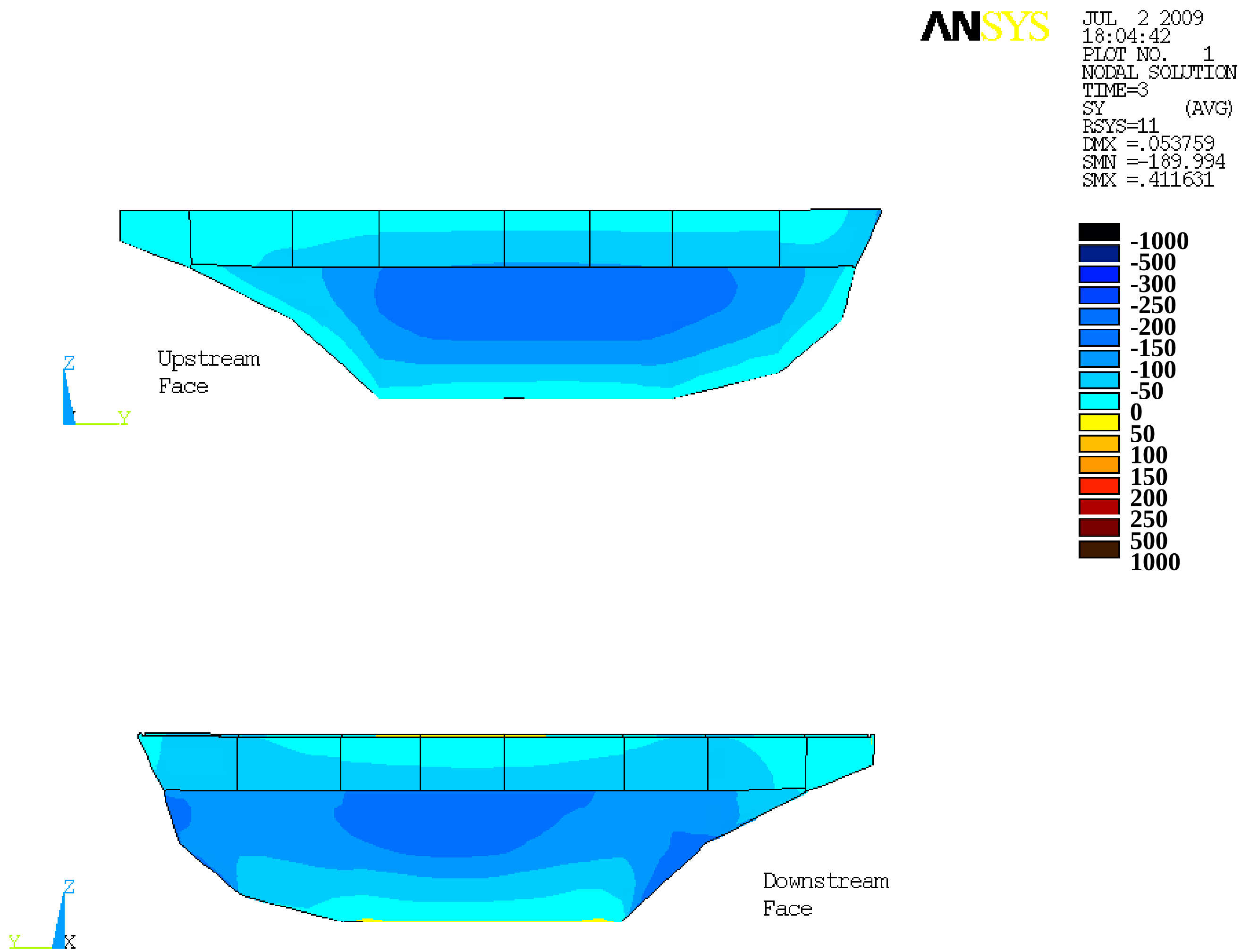

Trout Lake Dam
Usual Load 1a
Arch Stress

URS

Figure No. 4- 8

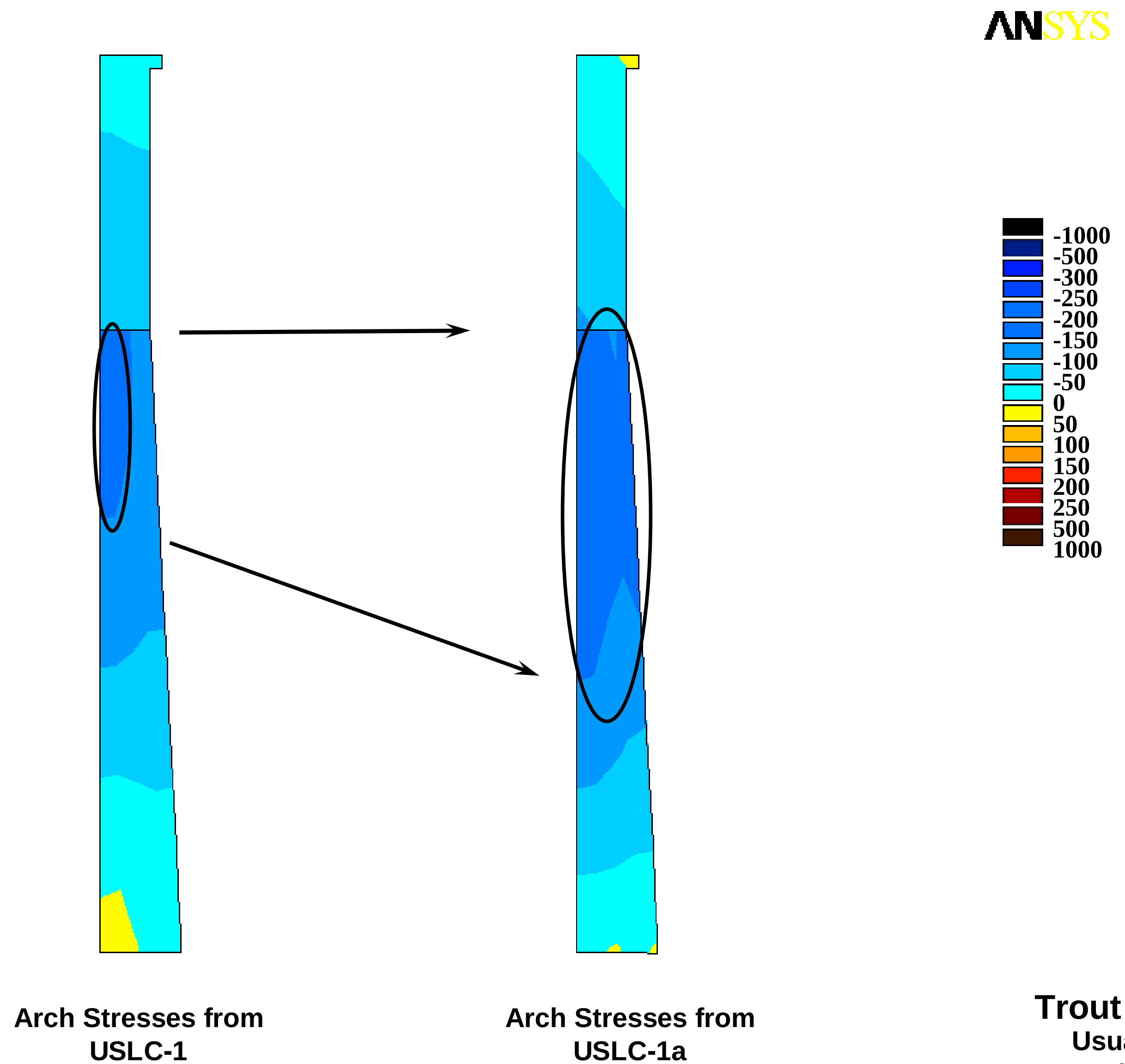

Trout Lake Dam
Usual Load 1a
Arch Stresses
Crown Cantilever Section
Figure No. 4- 9

URS

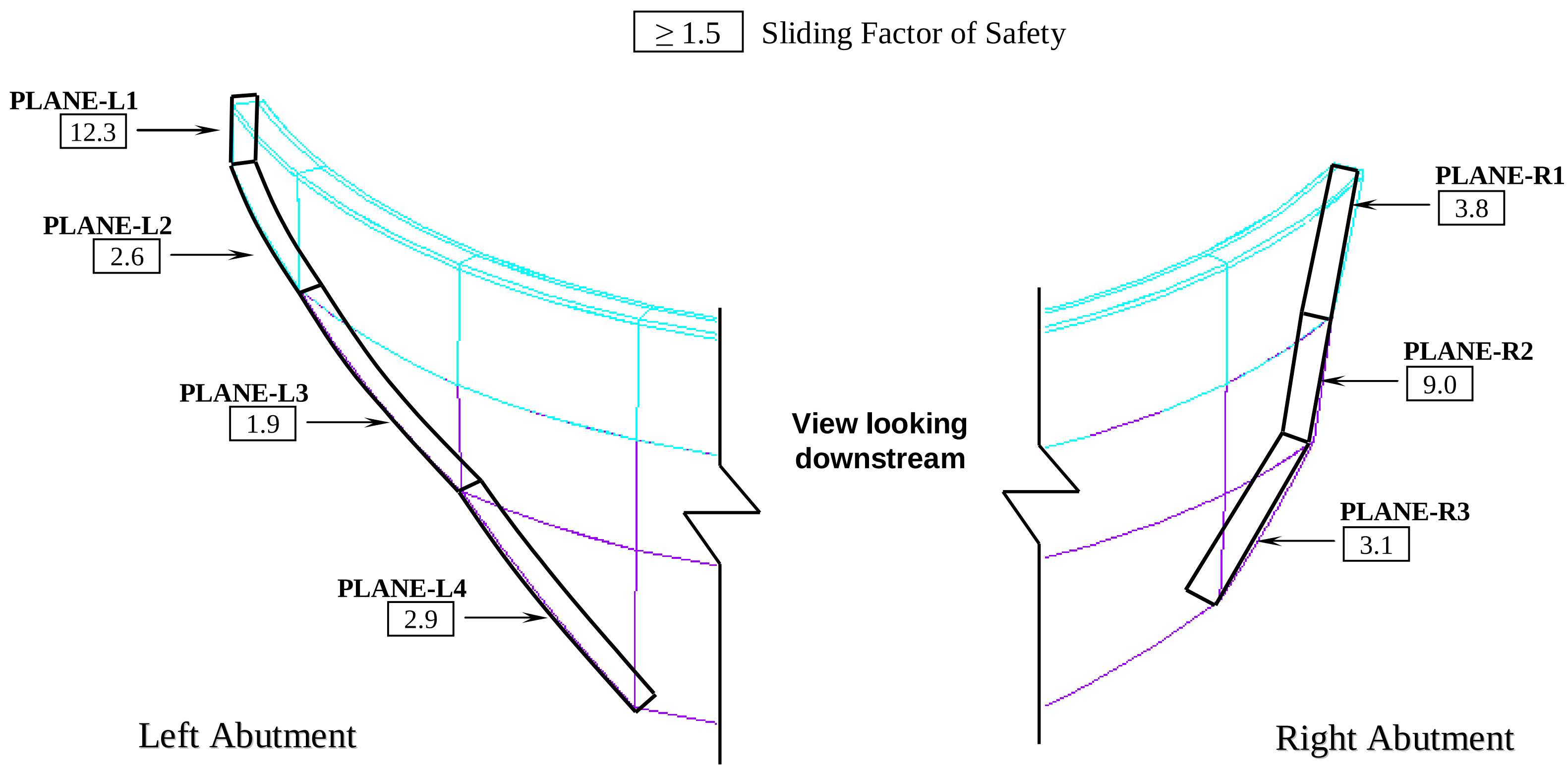

Trout Lake Dam
Usual Load 1a
Sliding Planes
Sliding Factors of Safety
Figure No. 4- 10

URS

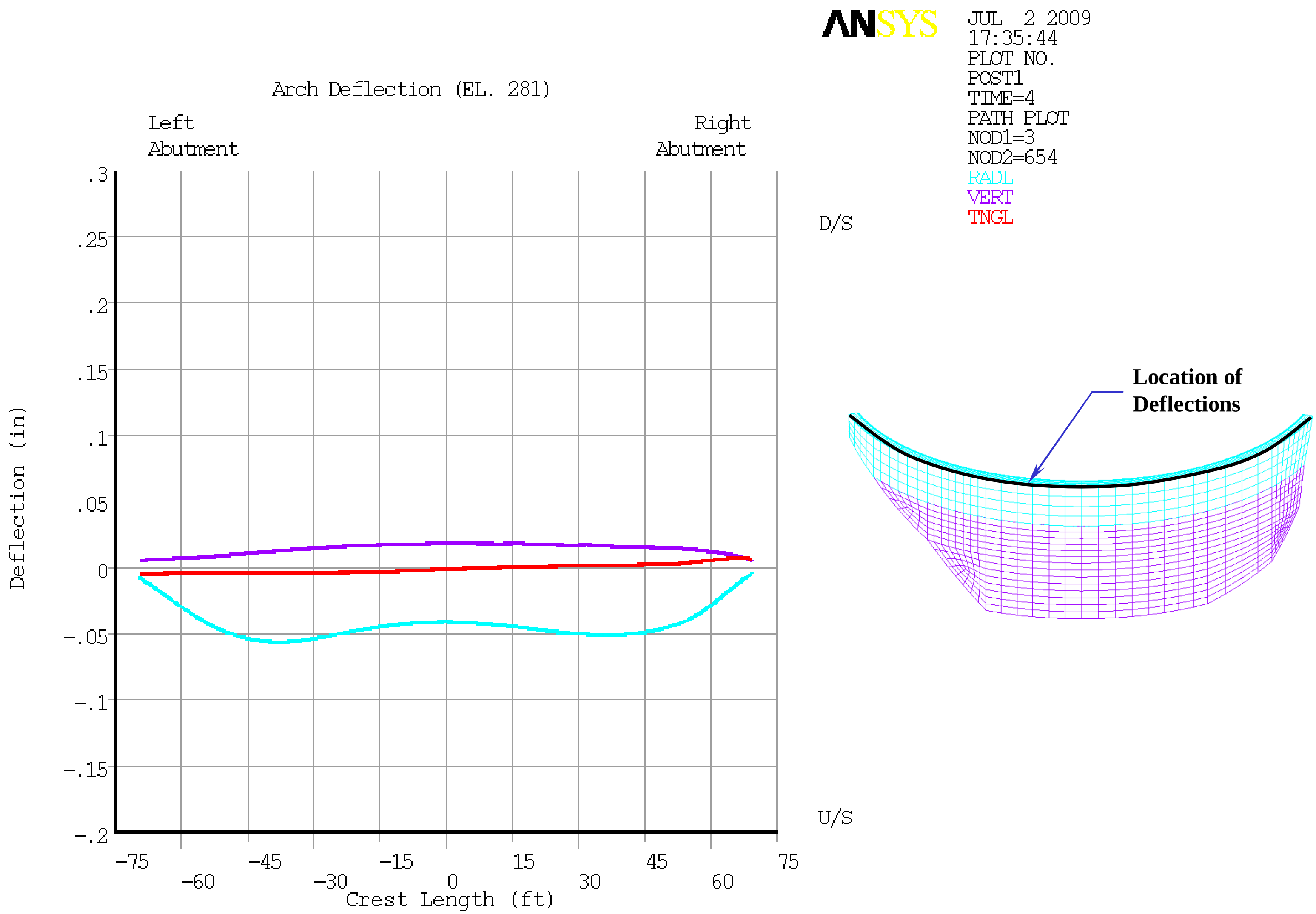

Trout Lake Dam
Usual Load 2
Dam Crest Deflection

Figure No. 4- 11

URS

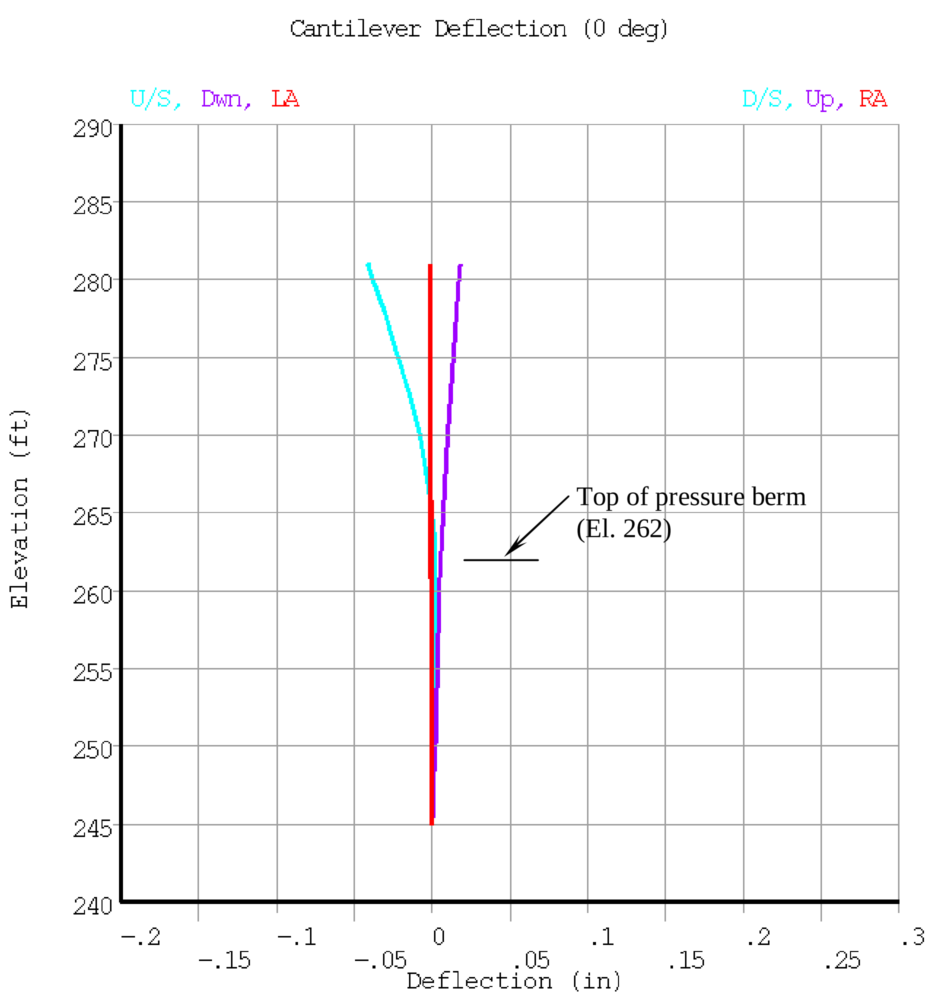

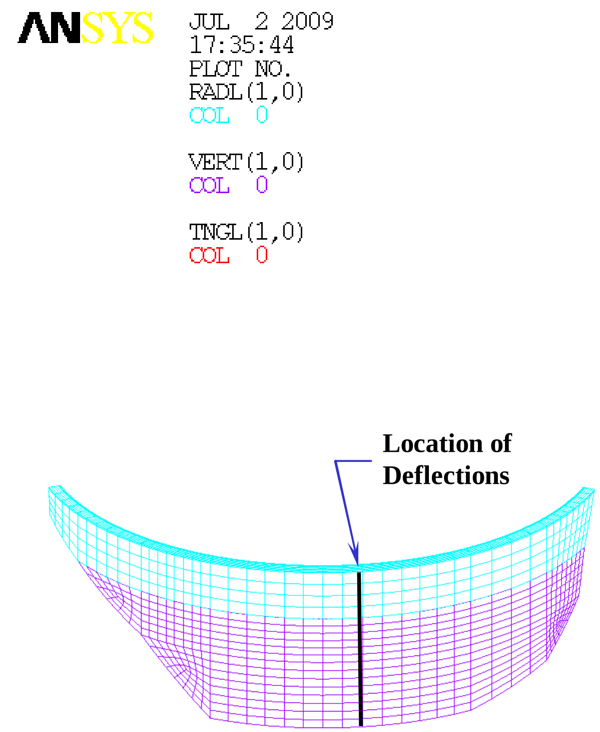

Trout Lake Dam
Usual Load 2
Crown Cantilever Deflection

URS

Figure No. 4- 12

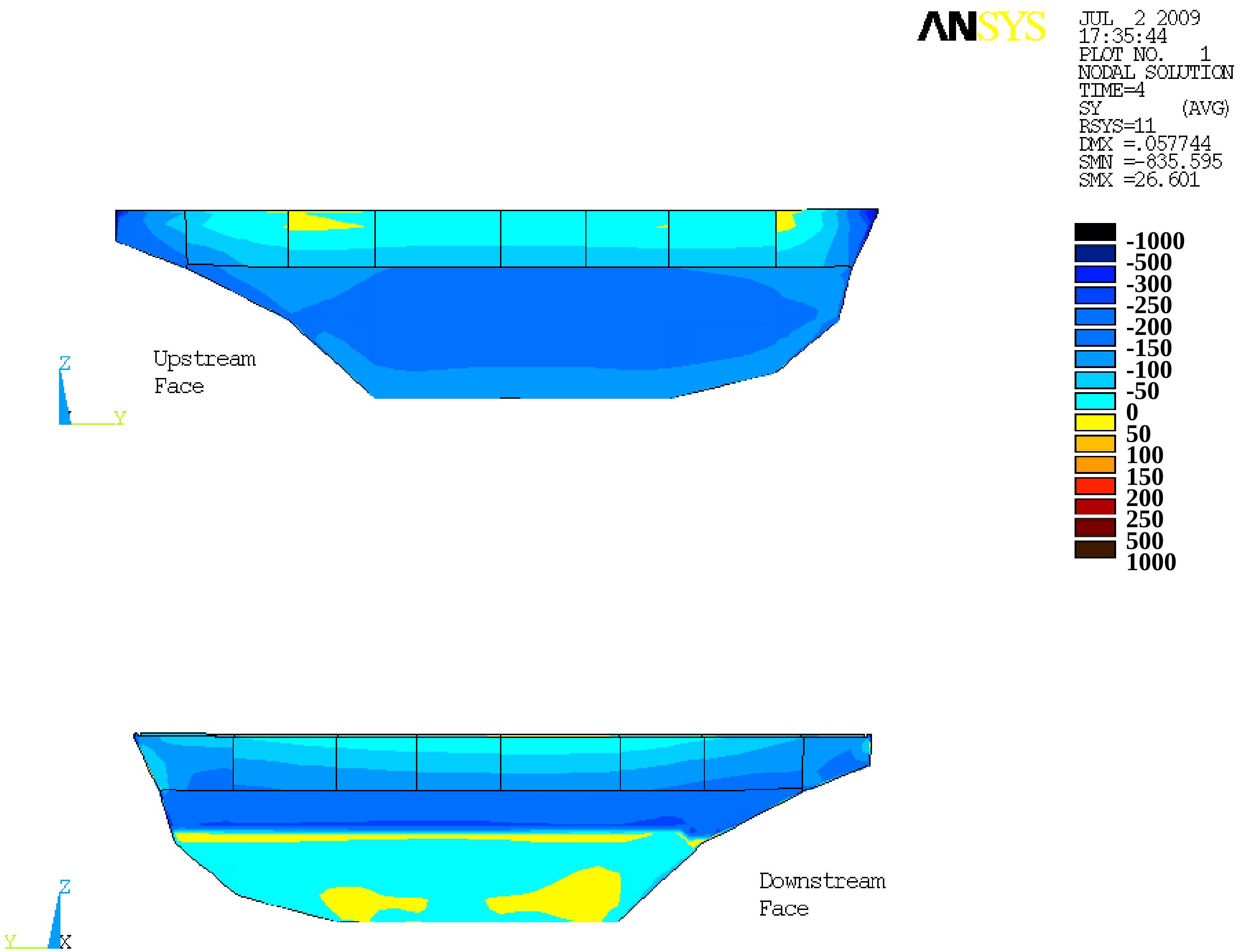

Trout Lake Dam
Usual Load 2
Arch Stress

Figure No. 4- 13

URS

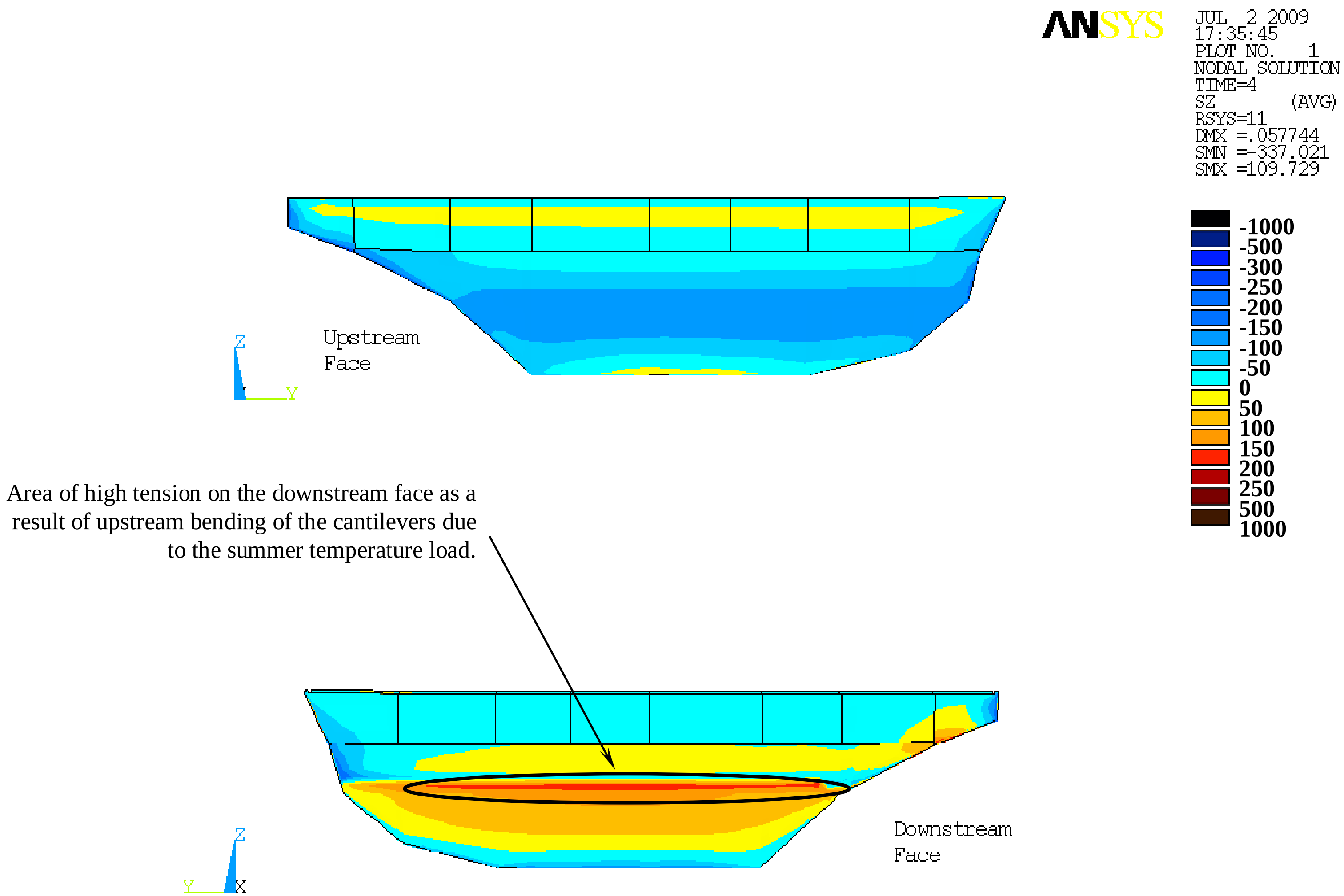

Trout Lake Dam
Usual Load 2
Cantilever Stress

Figure No. 4- 14

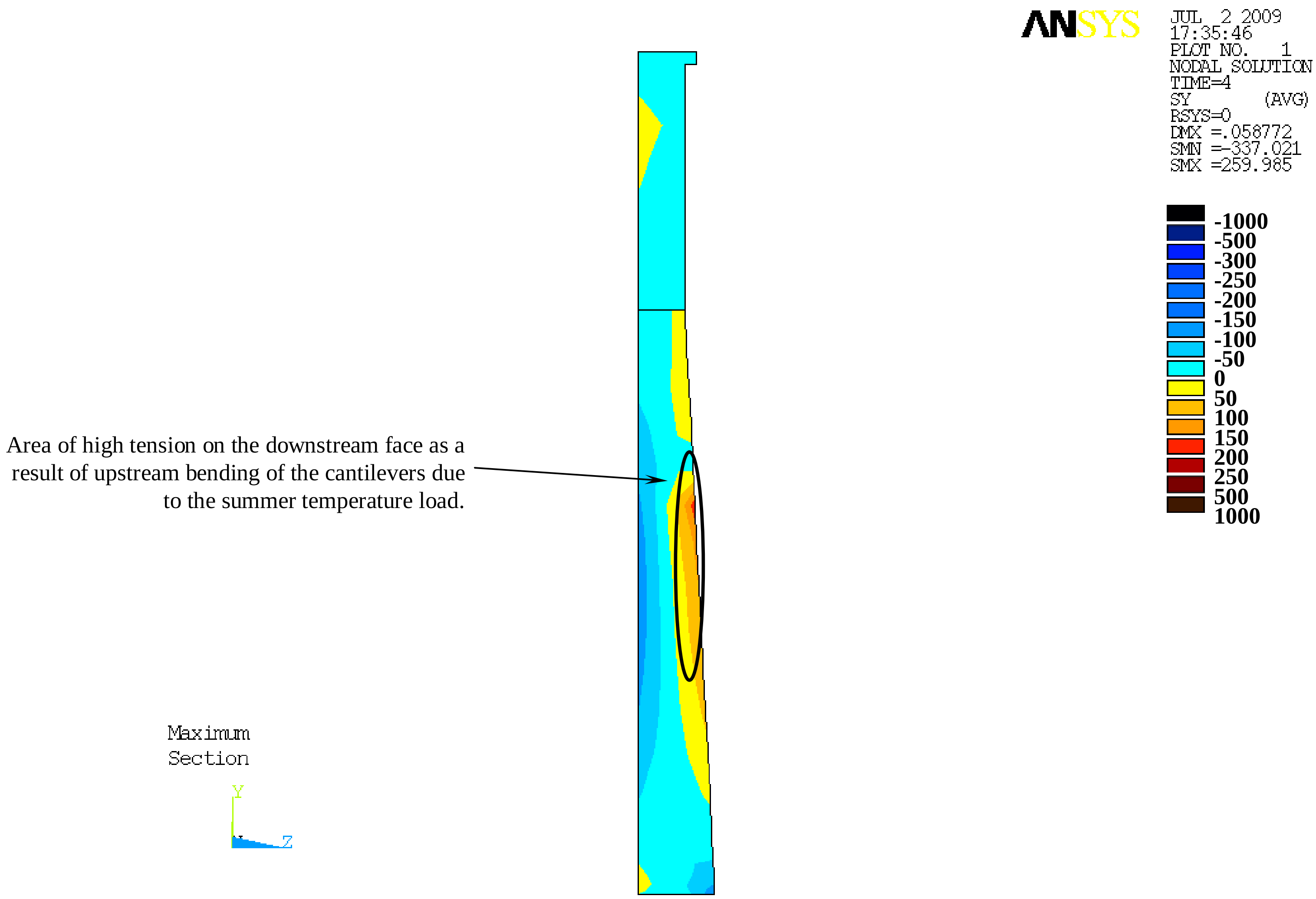

Trout Lake Dam
Usual Load 2
Crown Cantilever Section

URS

Figure No. 4- 15

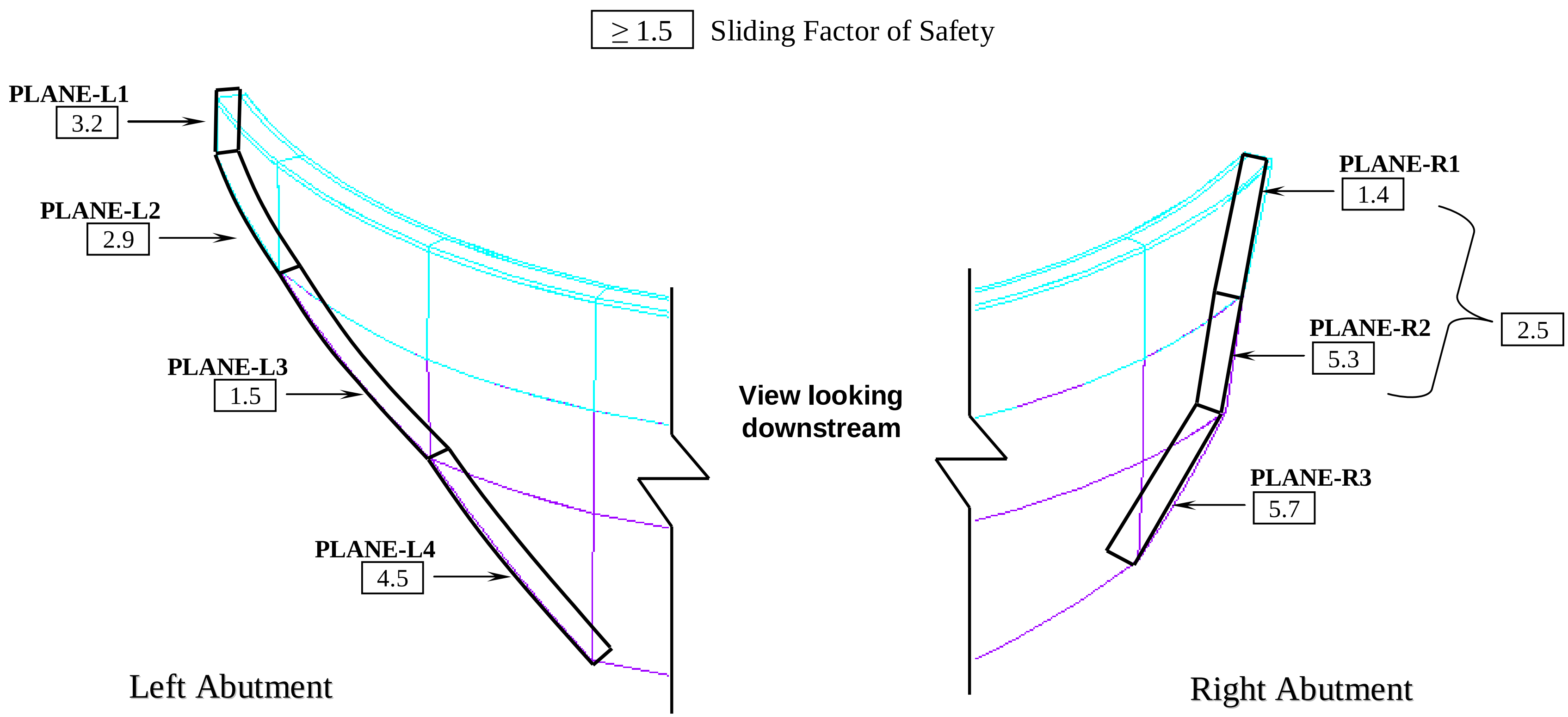

URS

Trout Lake Dam
Usual Load 2
Sliding Planes
Sliding Factors of Safety
Figure No. 4- 16

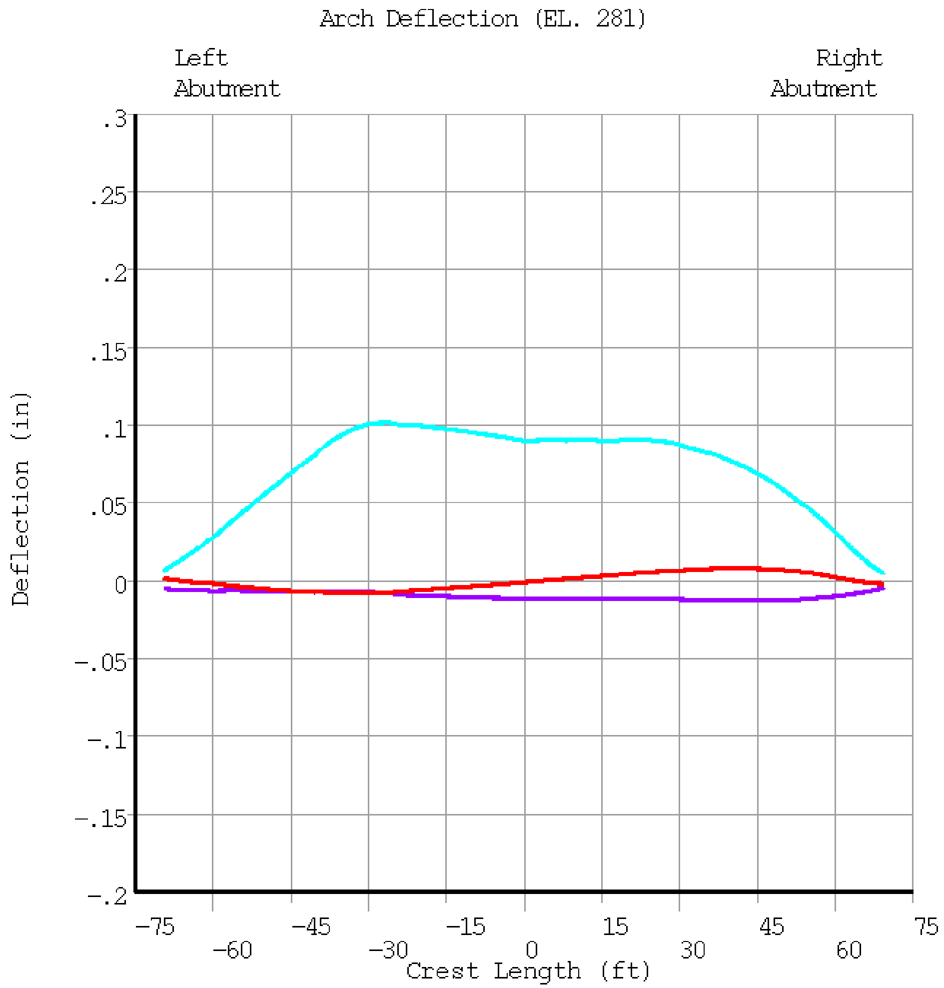

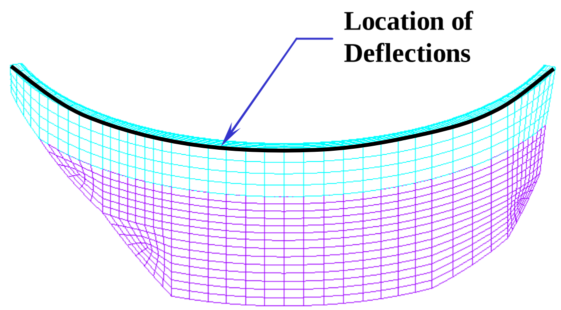

Trout Lake Dam
Usual Load 3
Dam Crest Deflection

Figure No. 4- 17

URS

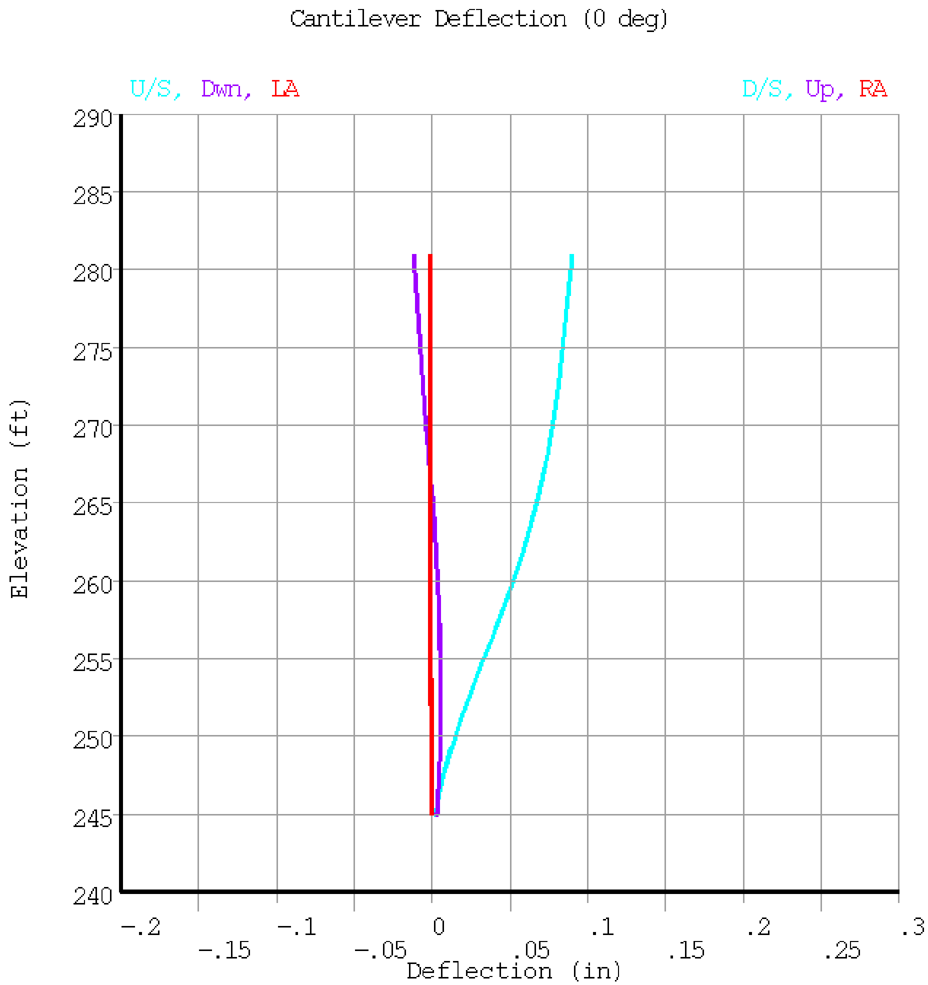

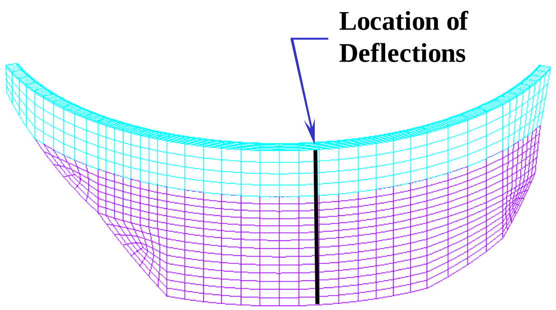

URS

Trout Lake Dam
Usual Load 3
Crown Cantilever Deflection

Figure No. 4- 18

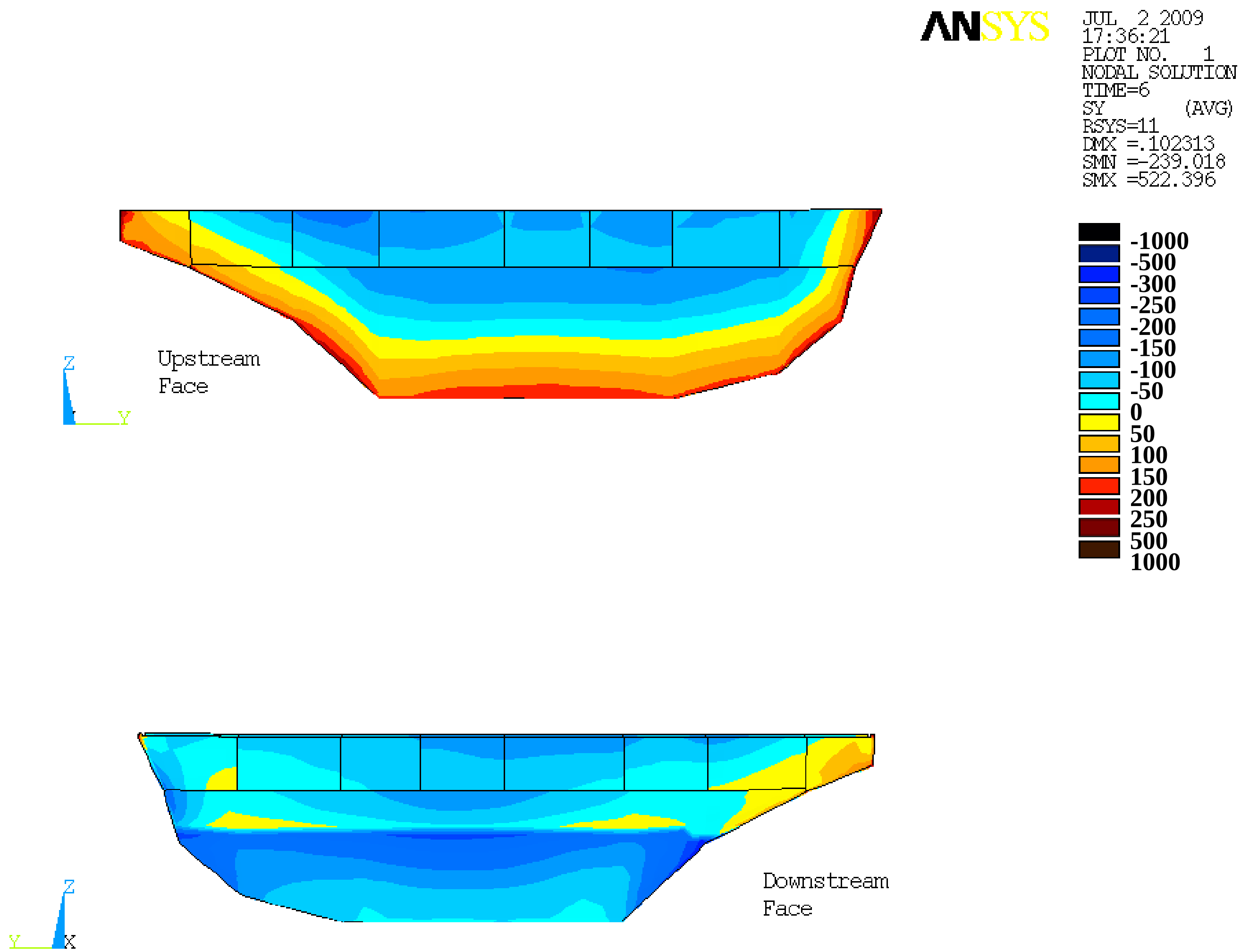

Trout Lake Dam
Usual Load 3
Arch Stress

Figure No. 4- 19

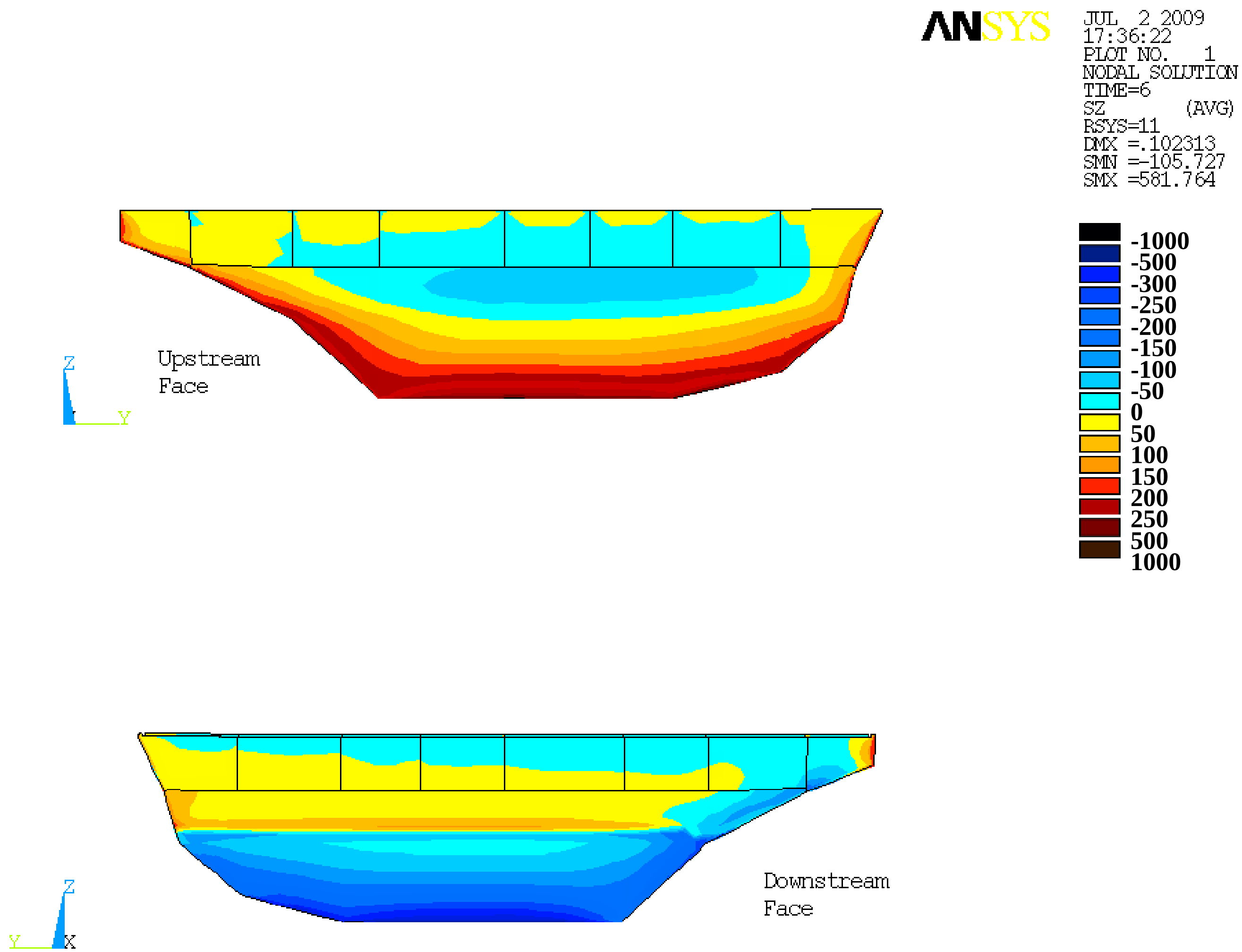

Trout Lake Dam
Usual Load 3
Cantilever Stress

URS

Figure No. 4- 20

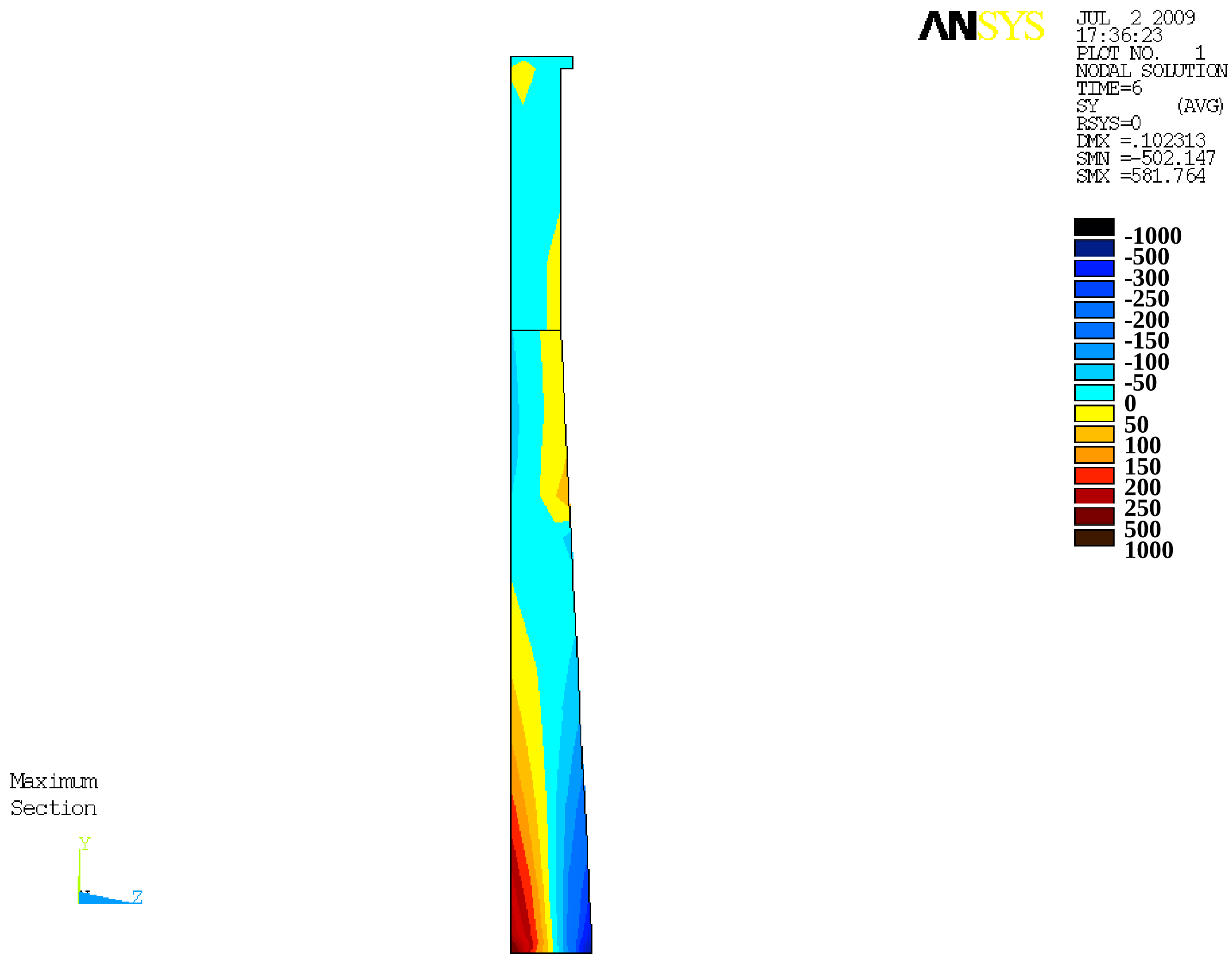

Trout Lake Dam
Usual Load 3
Crown Cantilever Section

URS

Figure No. 4- 21

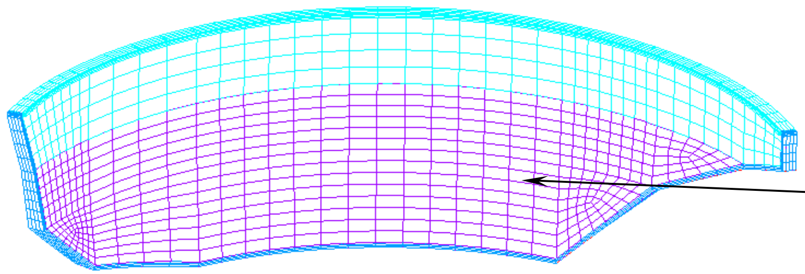

Downstream View

All the elements on the downstream face of the dam were softened. The thickness of the dam is made up of four elements. The most downstream elements have been softened.

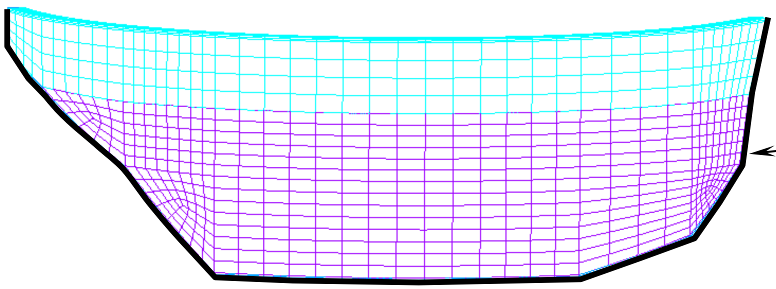

Upstream View

The location of the softened transition elements. The thickness of the dam/foundation is made up of four transition elements. The two most upstream elements have been softened.

Trout Lake Dam
Usual Load 3a
Location of Softened Elements

URS

Figure No. 4- 22

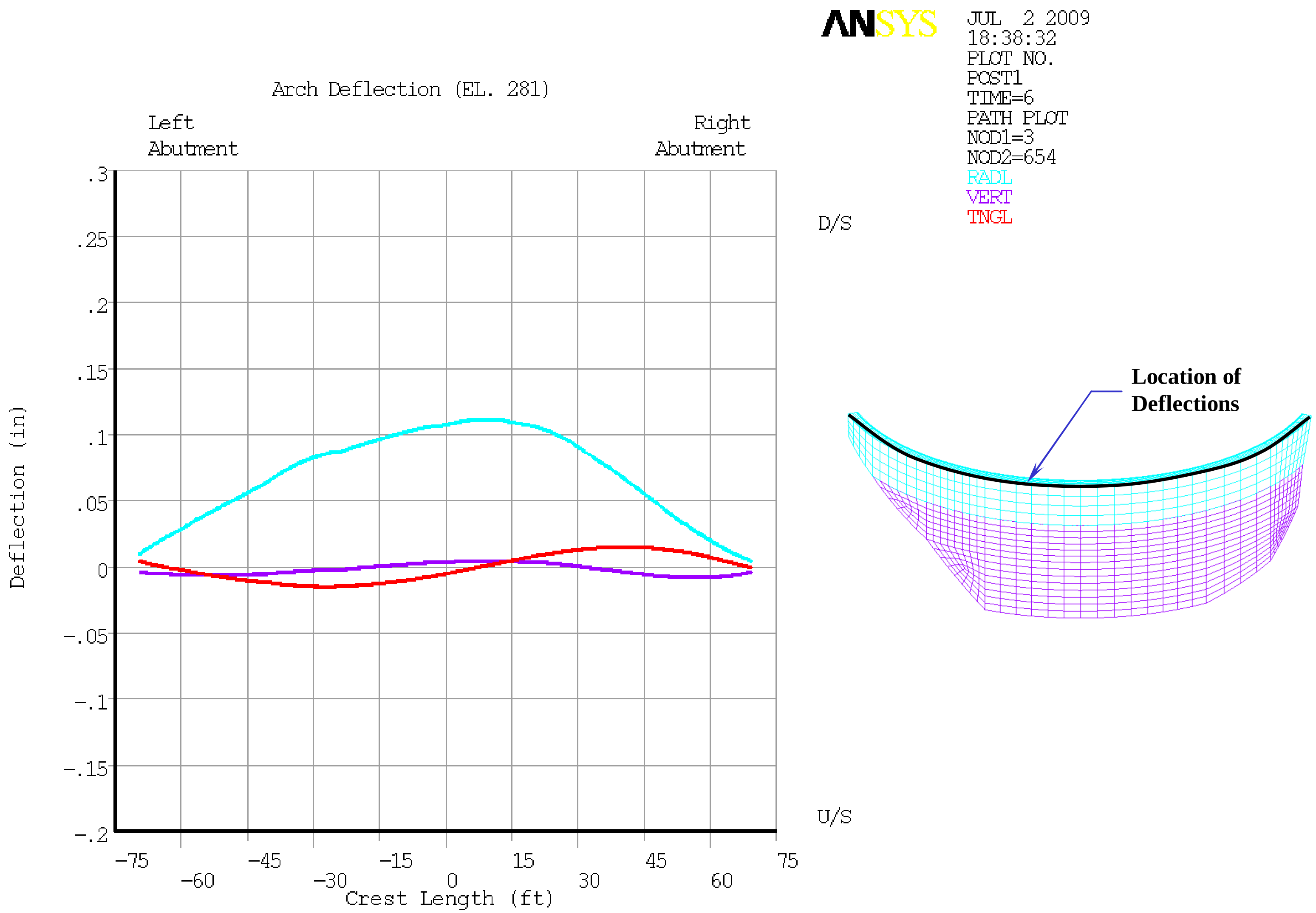

Trout Lake Dam
Usual Load 3a
Dam Crest Deflection

Figure No. 4- 23

URS

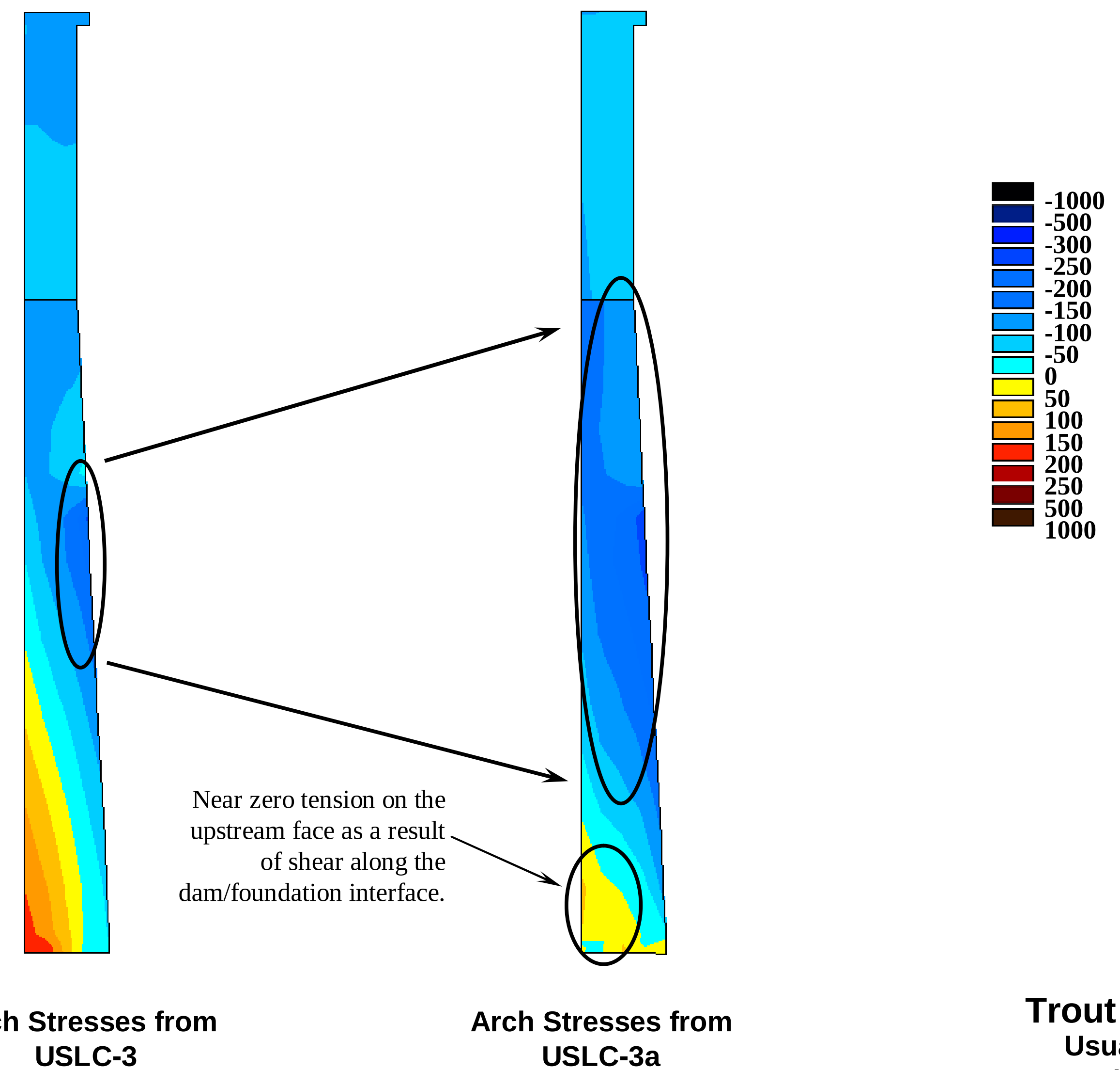

Trout Lake Dam
Usual Load 3a
Arch Stresses
Crown Cantilever Section
Figure No. 4- 24

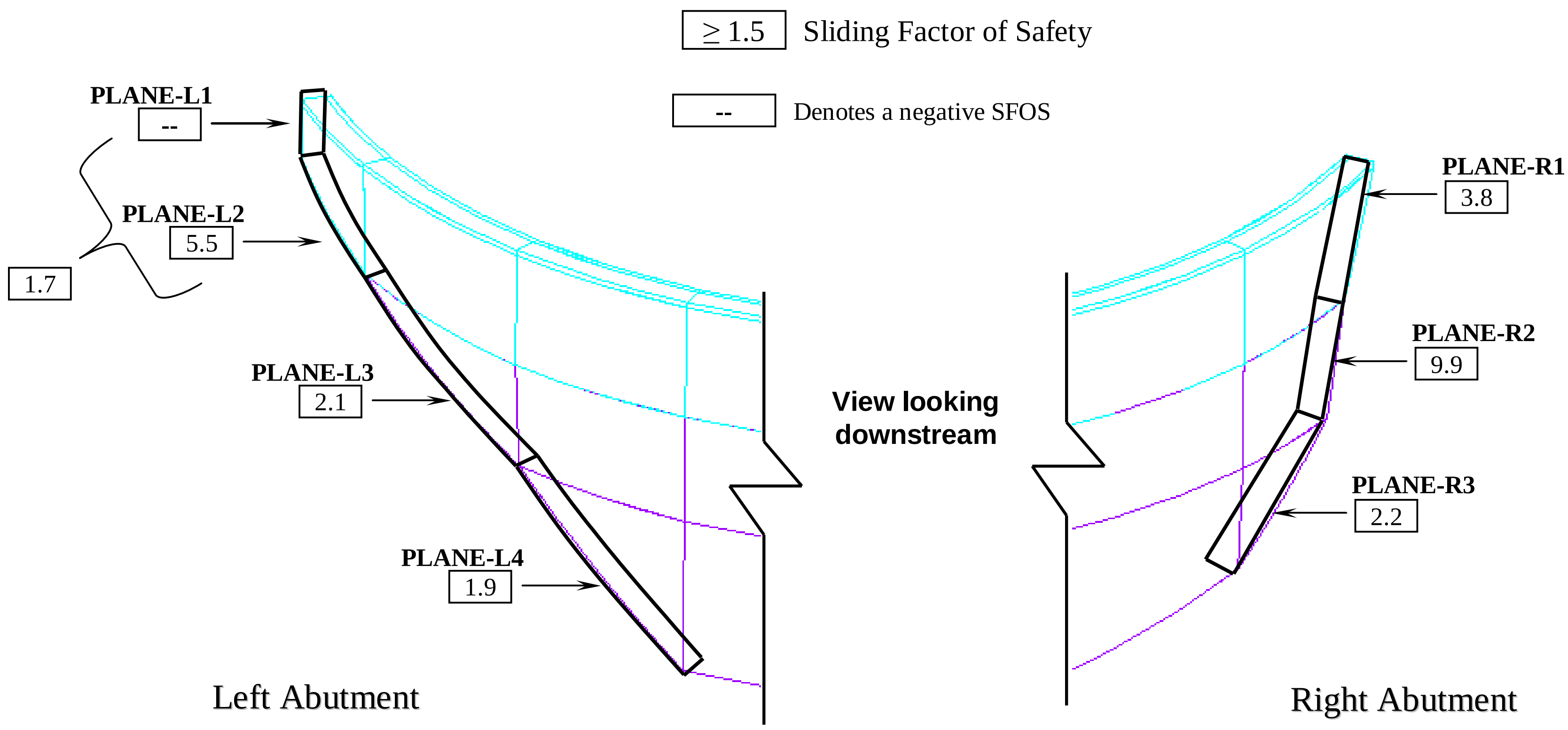

URS

Trout Lake Dam
Usual Load 3a
Sliding Planes
Sliding Factors of Safety
Figure No. 4- 25

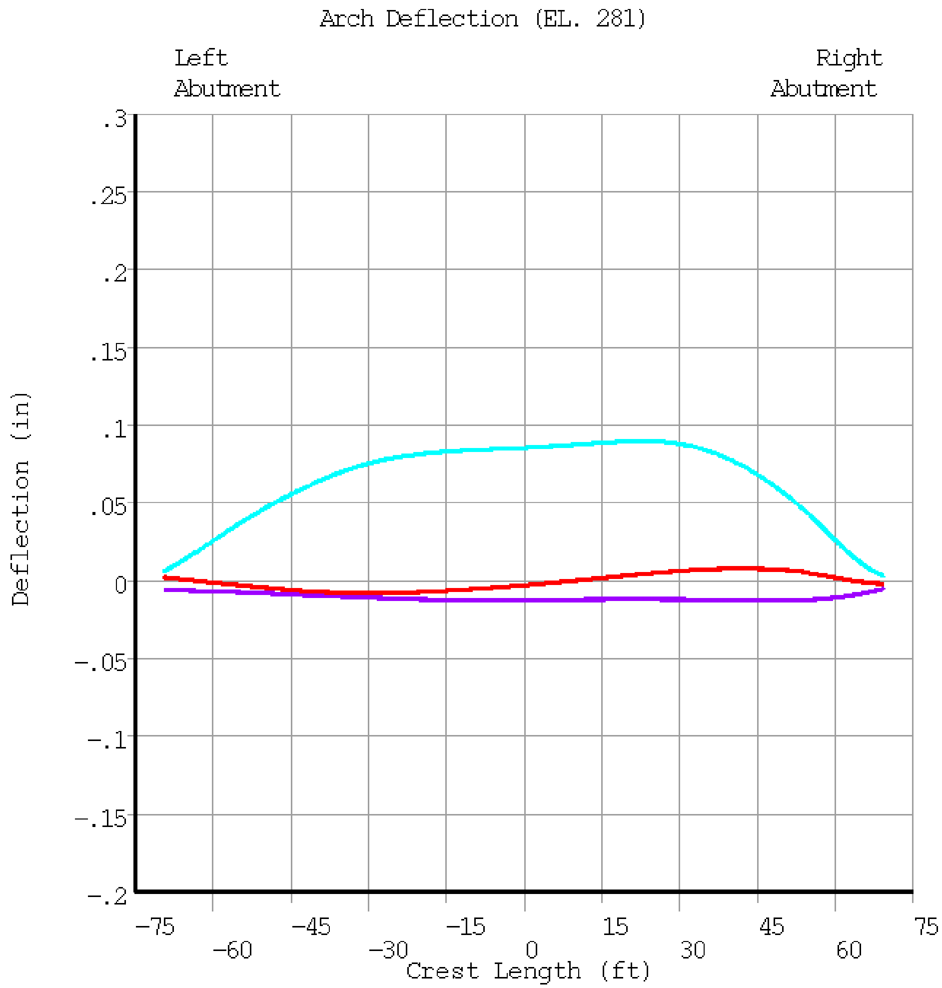

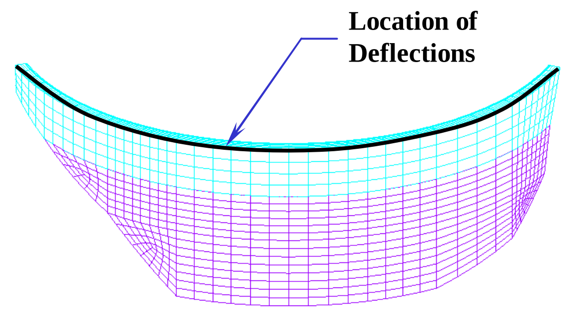

Trout Lake Dam
Unusual Load 1
Dam Crest Deflection

Figure No. 4- 26

URS

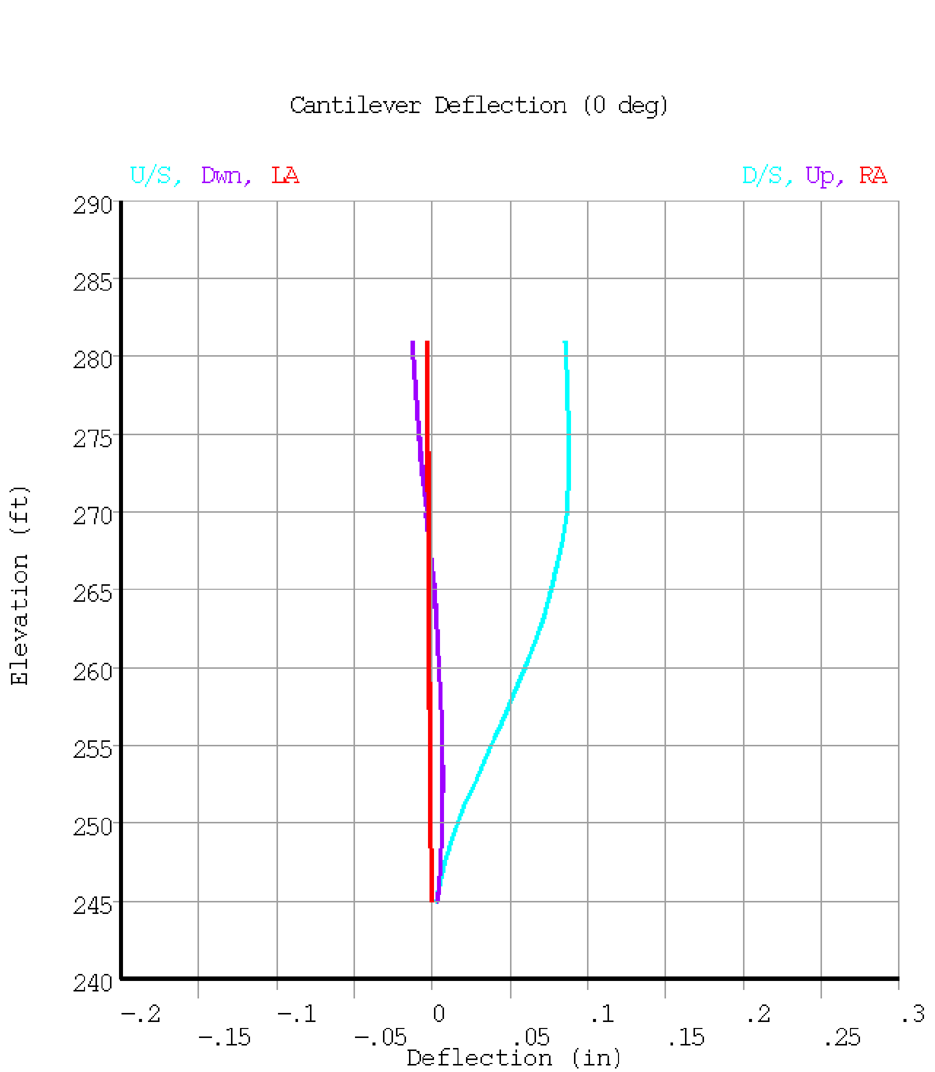

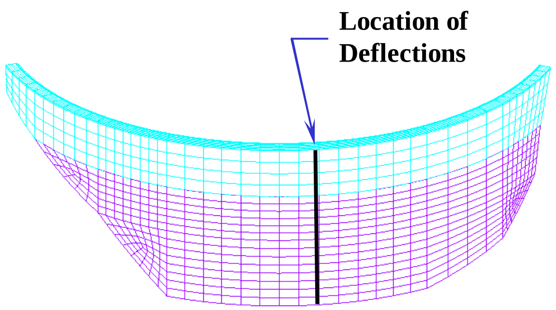

Trout Lake Dam
Unusual Load 1
Crown Cantilever Deflection

Figure No. 4- 27

URS

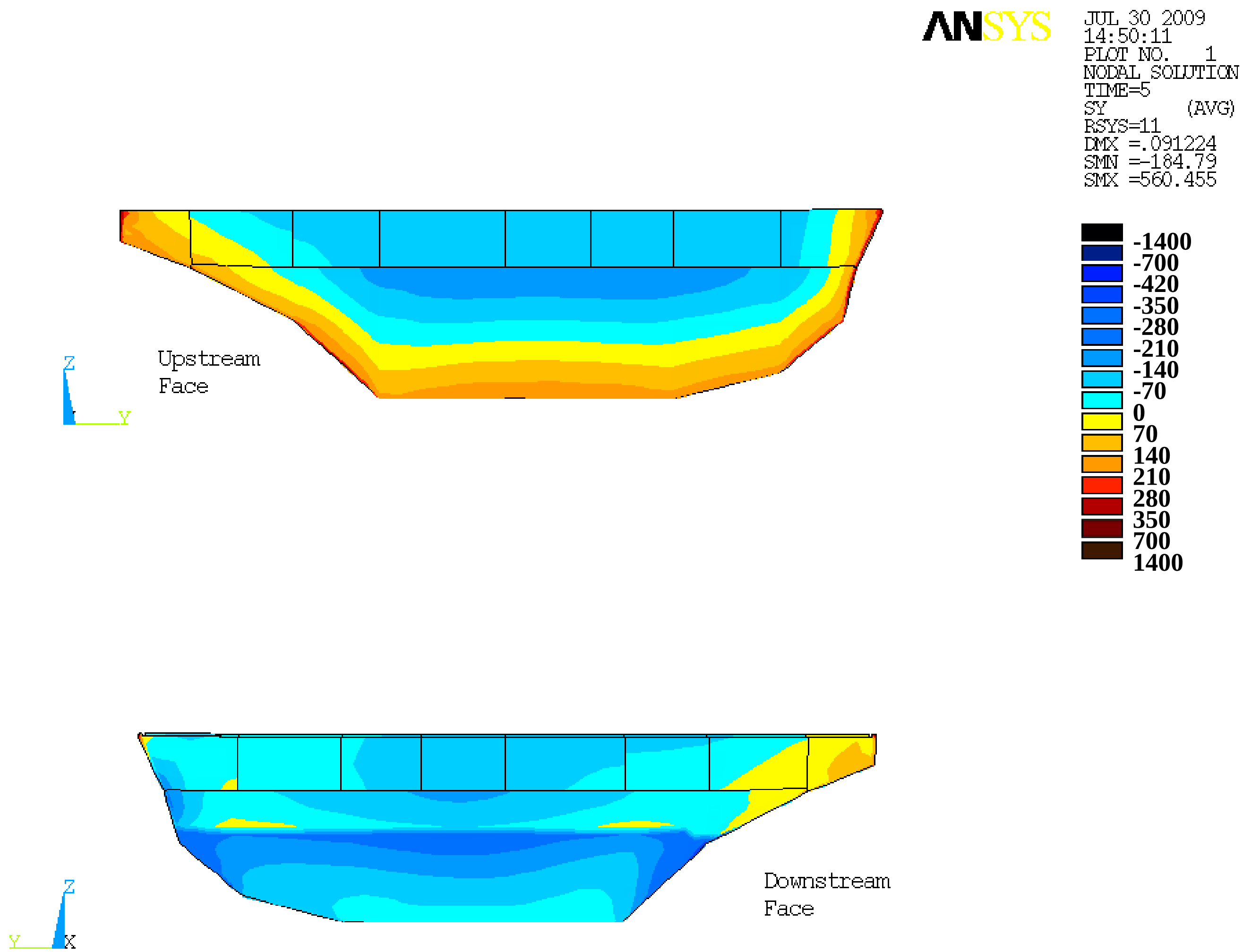

Trout Lake Dam
Unusual Load 1
Arch Stress

URS

Figure No. 4- 28

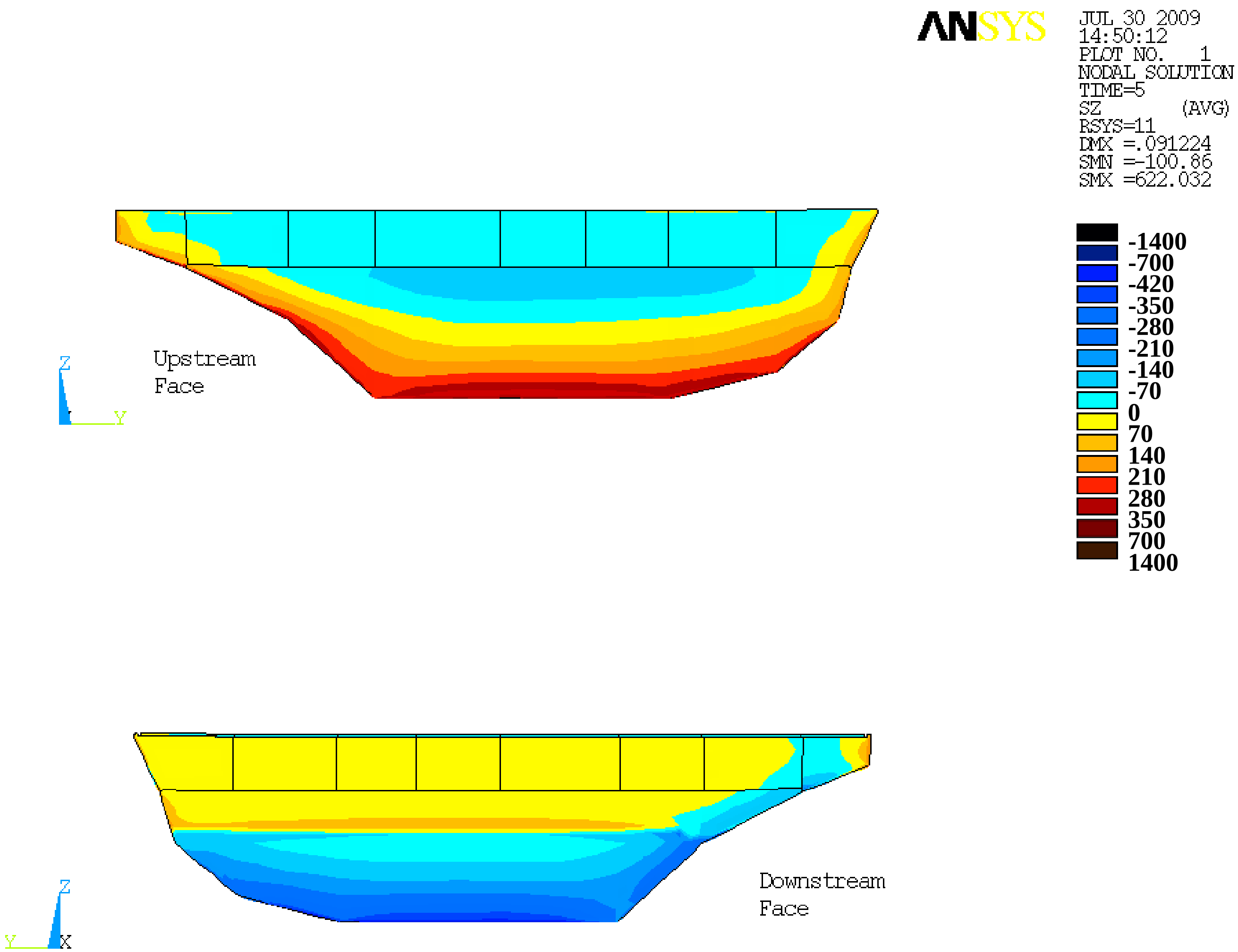

Trout Lake Dam
Unusual Load 1
Cantilever Stress

URS

Figure No. 4- 29

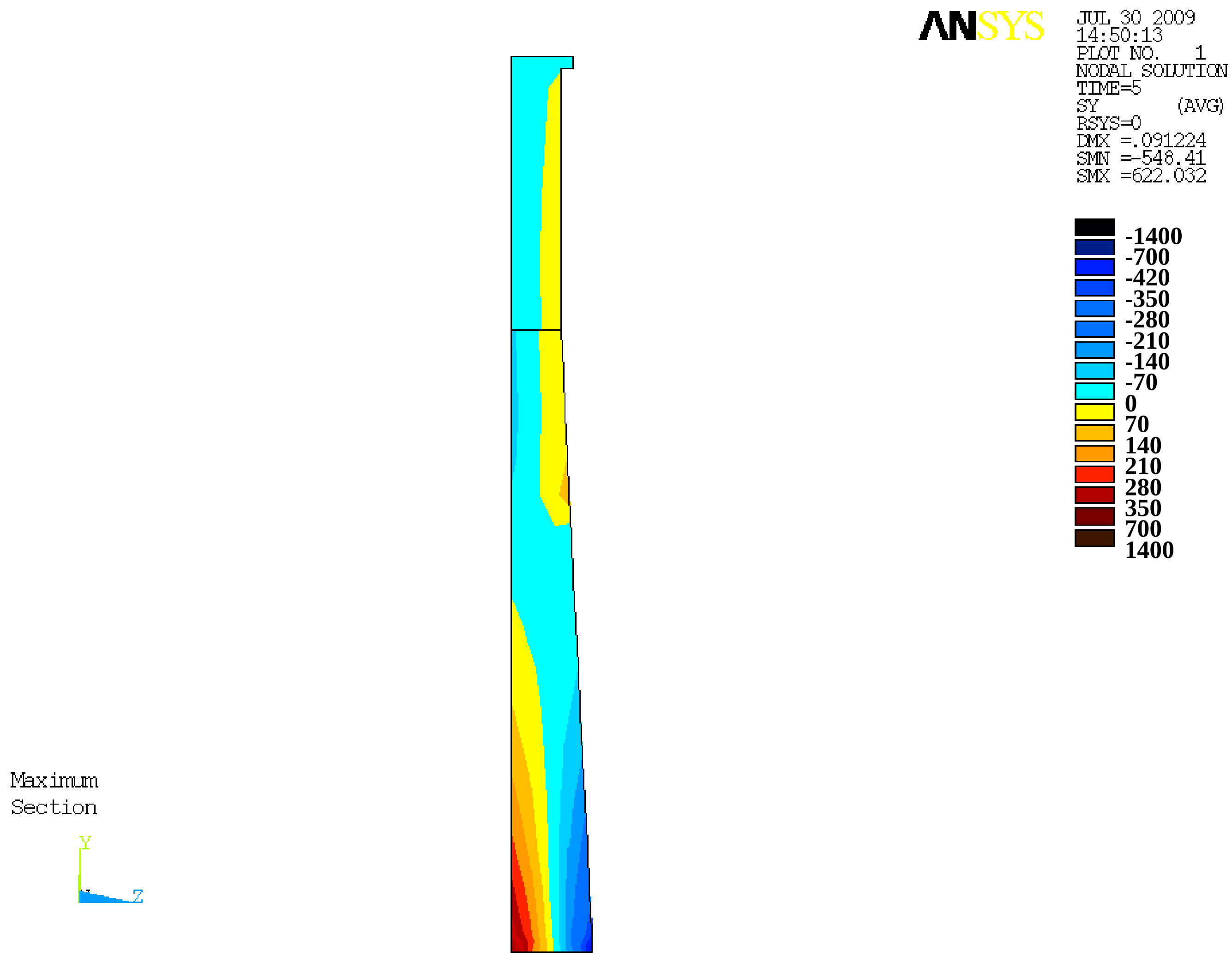

Trout Lake Dam

Unusual Load 1

Crown Cantilever Section

Figure No. 4- 30

URS

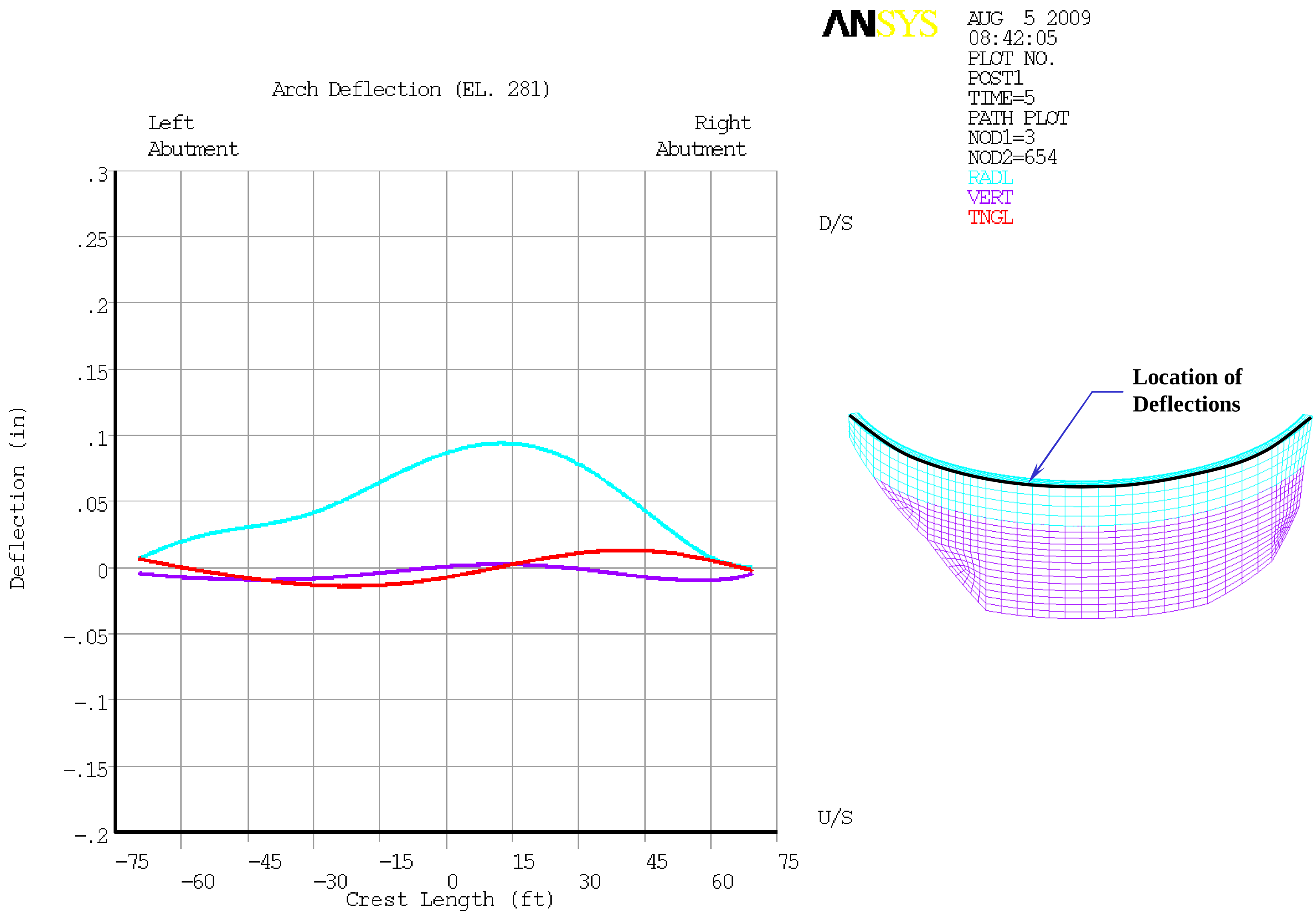

URS

Trout Lake Dam
Unusual Load 1a
Dam Crest Deflection

Figure No. 4- 31

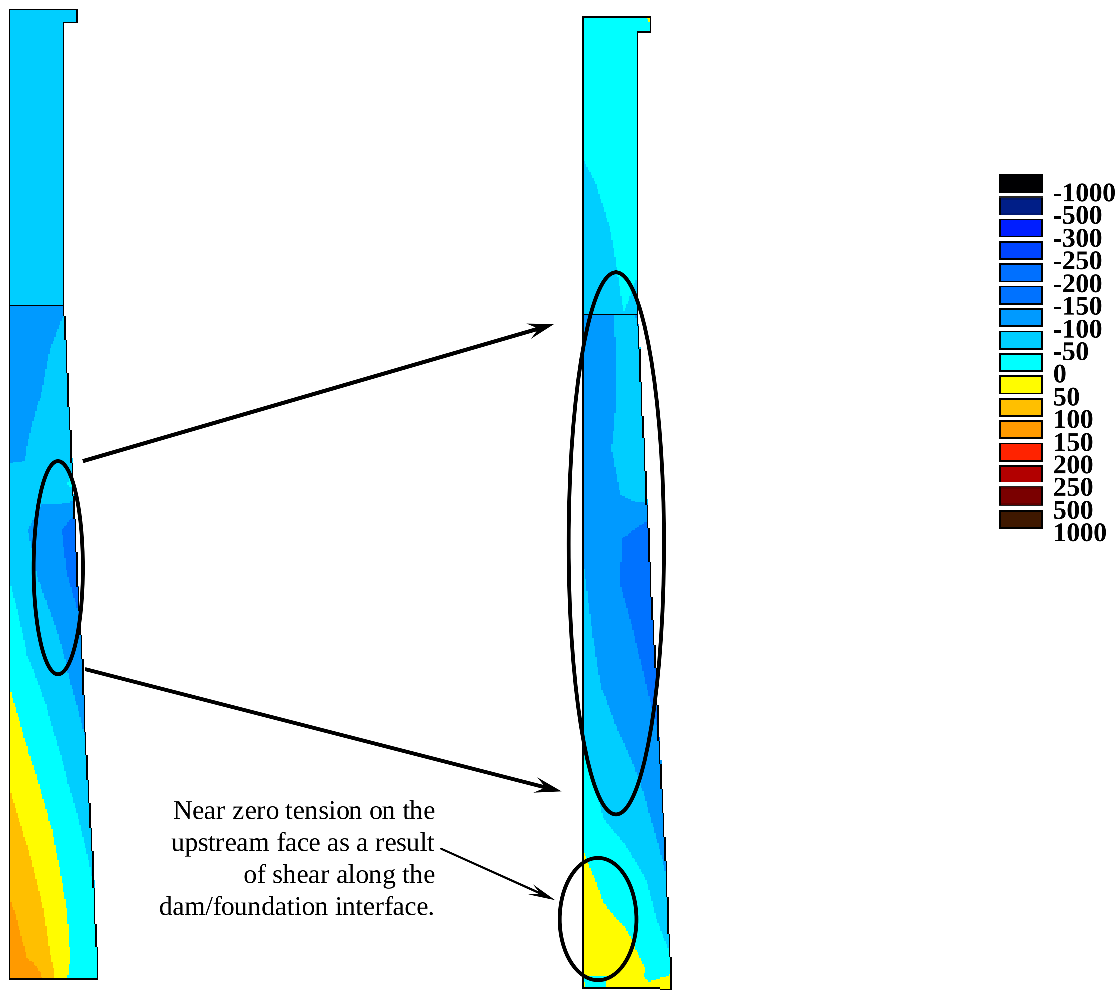

Arch Stresses from
UNLC-1

Arch Stresses from
UNLC-1a

Trout Lake Dam
Unusual Load 1a
Arch Stresses
Crown Cantilever Section
Figure No. 4- 32

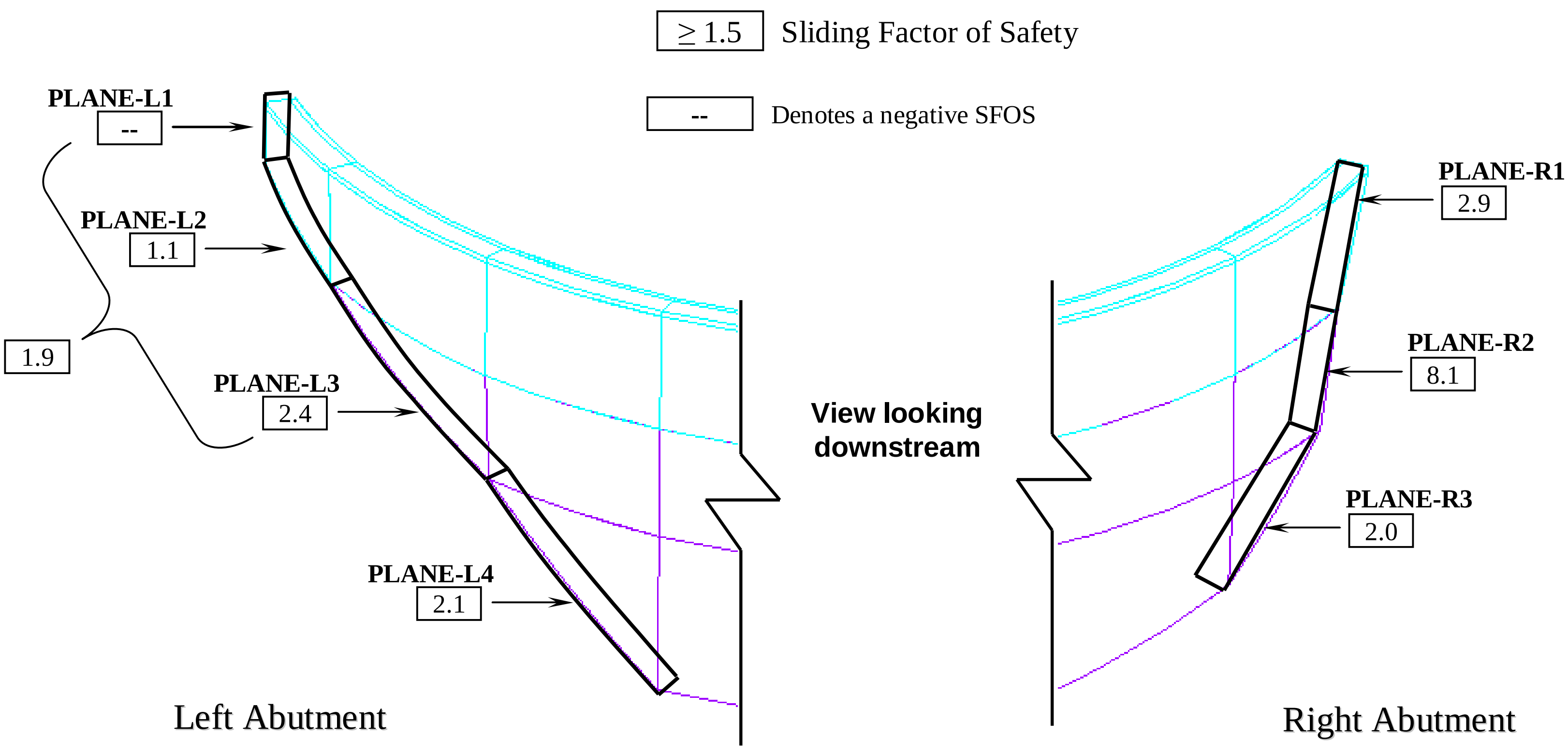

Trout Lake Dam
Unusual Load 1a
Sliding Planes
Sliding Factors of Safety
Figure No. 4- 33

URS

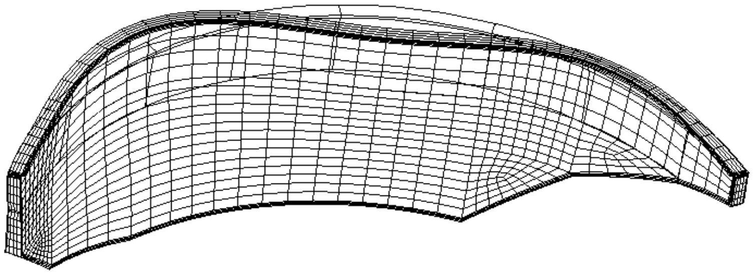

Mode No. 1

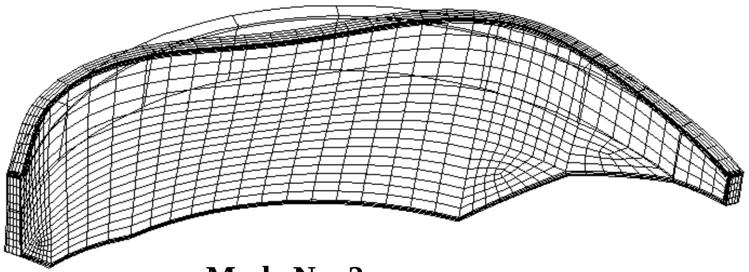

Mode No. 2

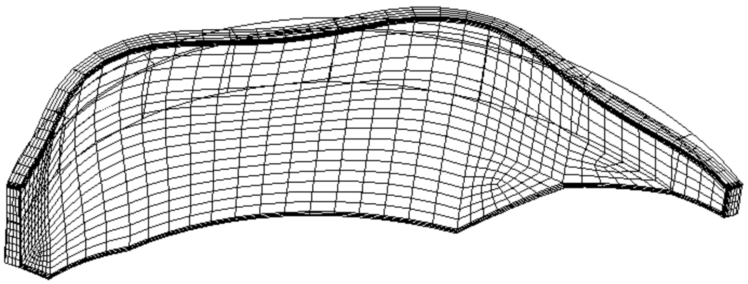

Mode No. 3

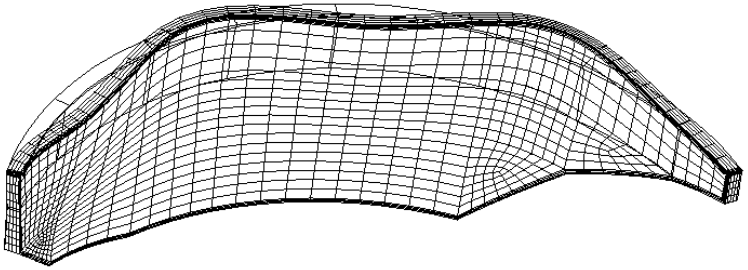

Mode No. 4

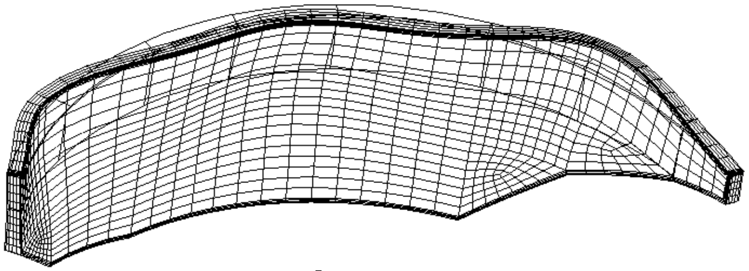

Mode No. 5

URS

Trout Lake Dam

Extreme Load 1

Mode Shapes 1-5

Figure No. 4- 34

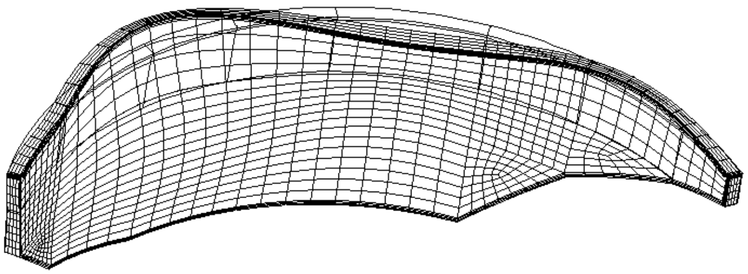

Mode No. 6

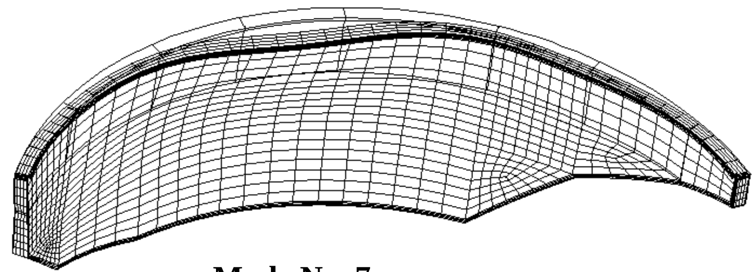

Mode No. 7

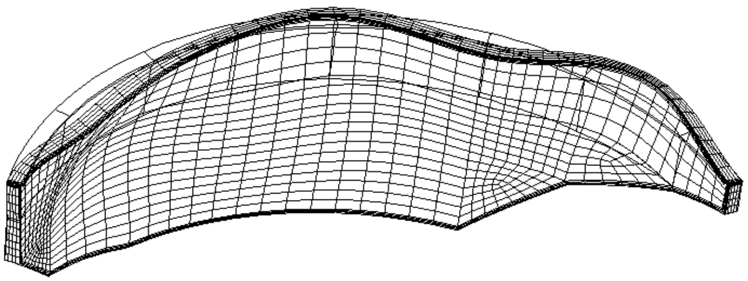

Mode No. 8

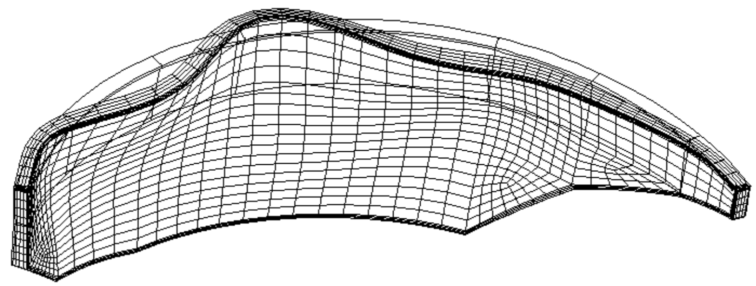

Mode No. 9

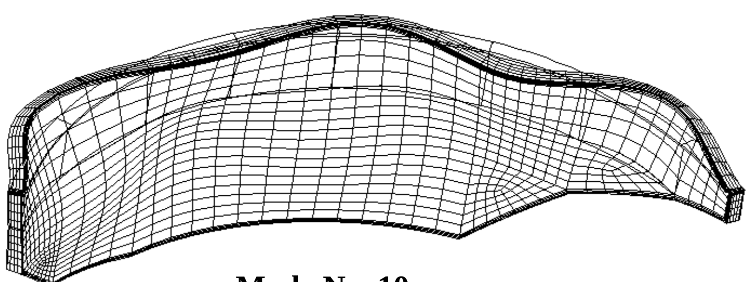

Mode No. 10

URS

Trout Lake Dam
Extreme Load 1
Mode Shapes 6-10

Figure No. 4- 35

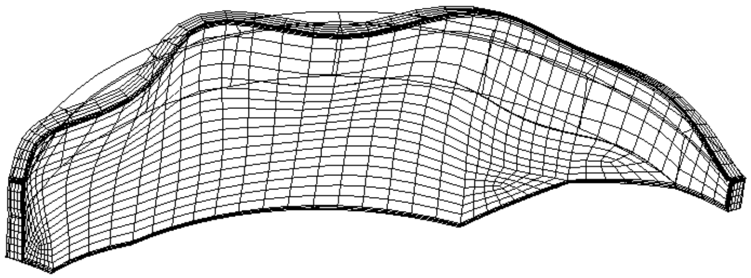

Mode No. 11

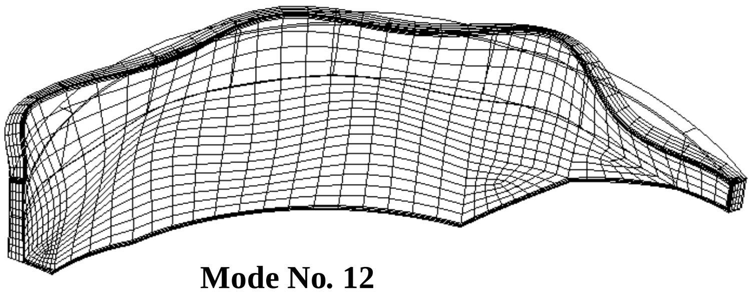

Mode No. 12

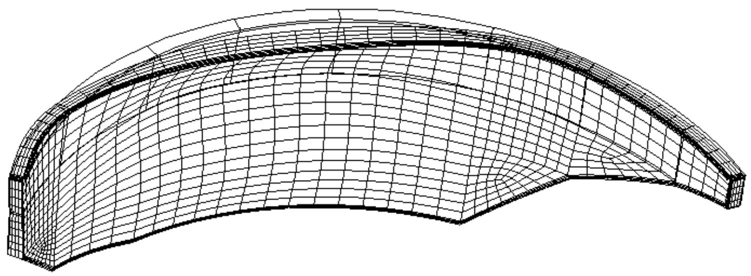

Mode No. 13

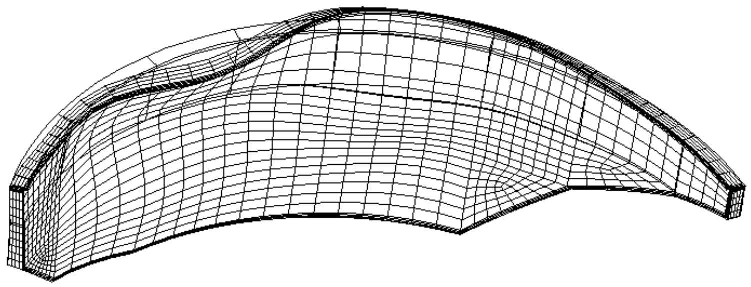

Mode No. 14

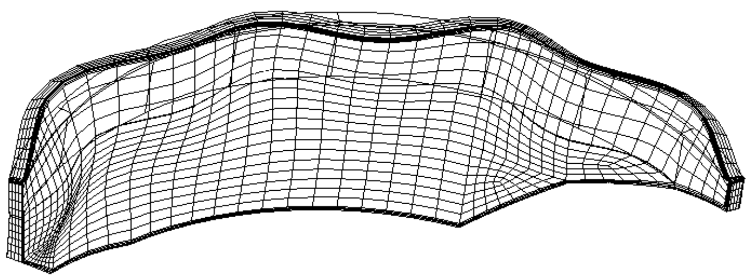

Mode No. 15

URS

Trout Lake Dam
Extreme Load 1
Mode Shapes 11-15

Figure No. 4- 36

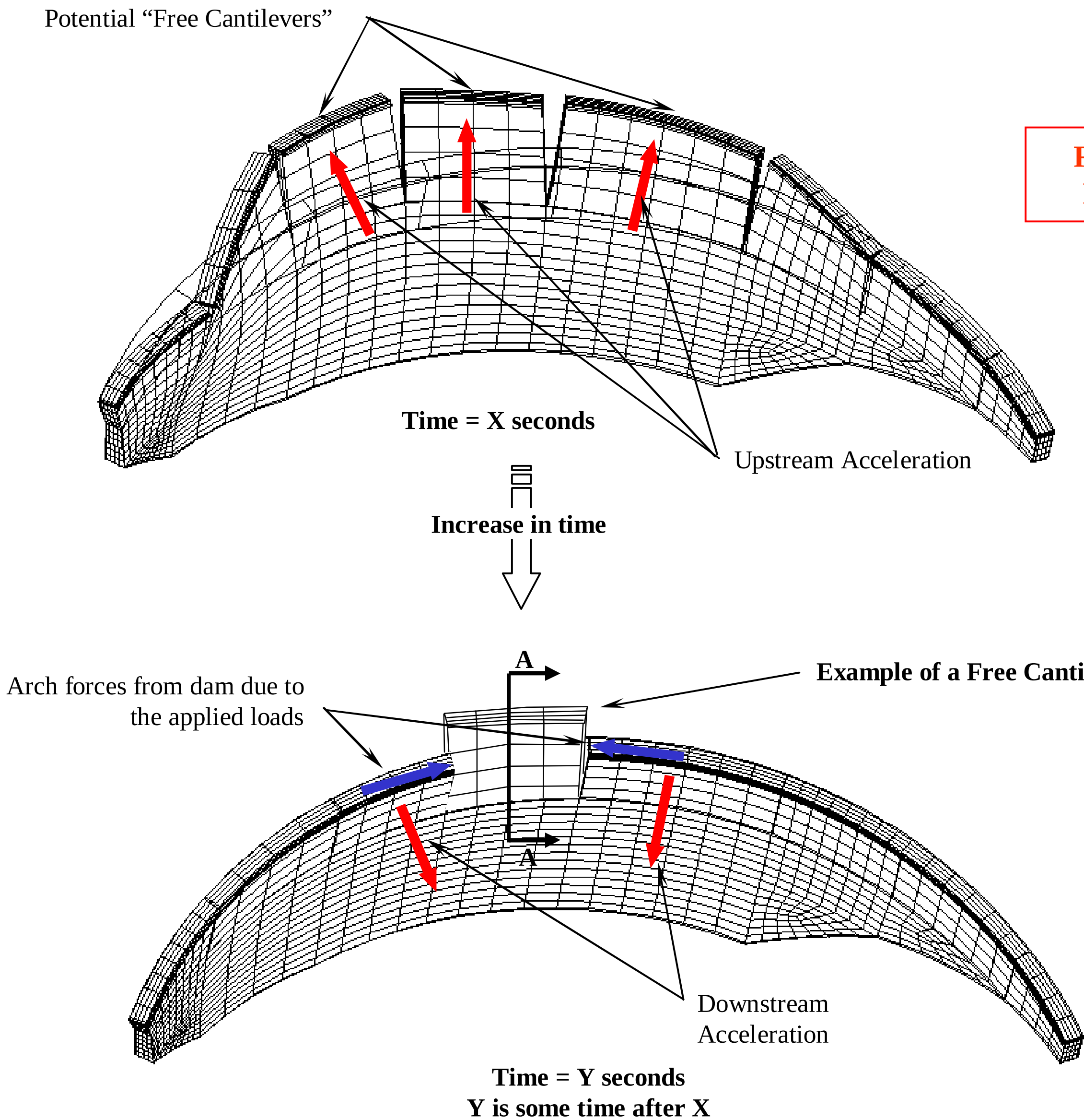

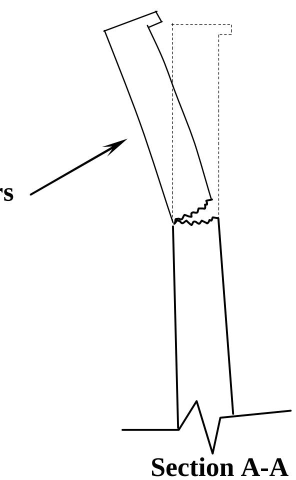

FOR ILLUSTRATION ONLY, NOT BASED ON ANALYSIS

Trout Lake Dam
Example of a "Free Cantilever"

Figure No. 4- 37

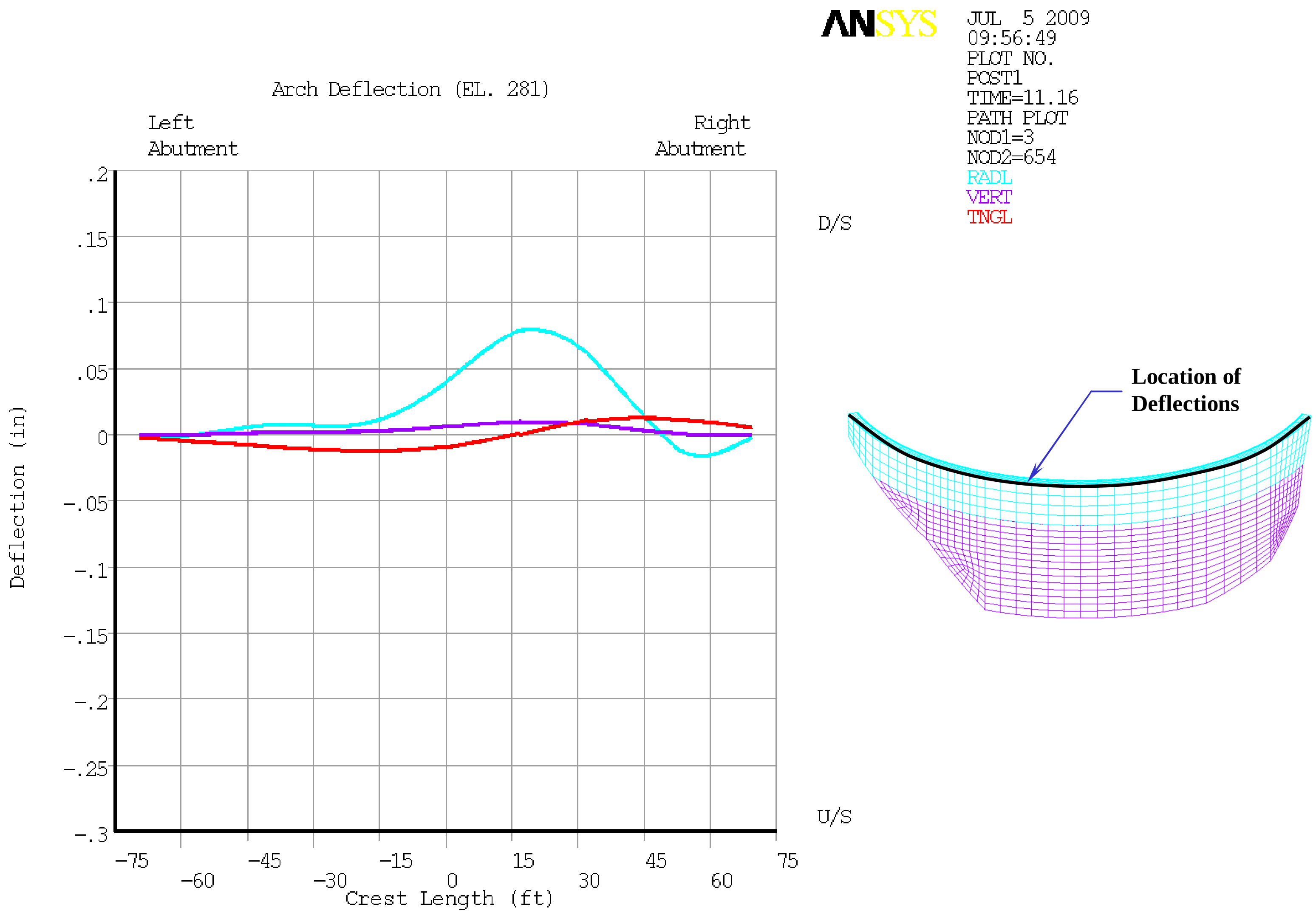

Trout Lake Dam

Extreme Load 1

Dam Crest Deflection

11.16 Seconds

Figure No. 4- 38

URS

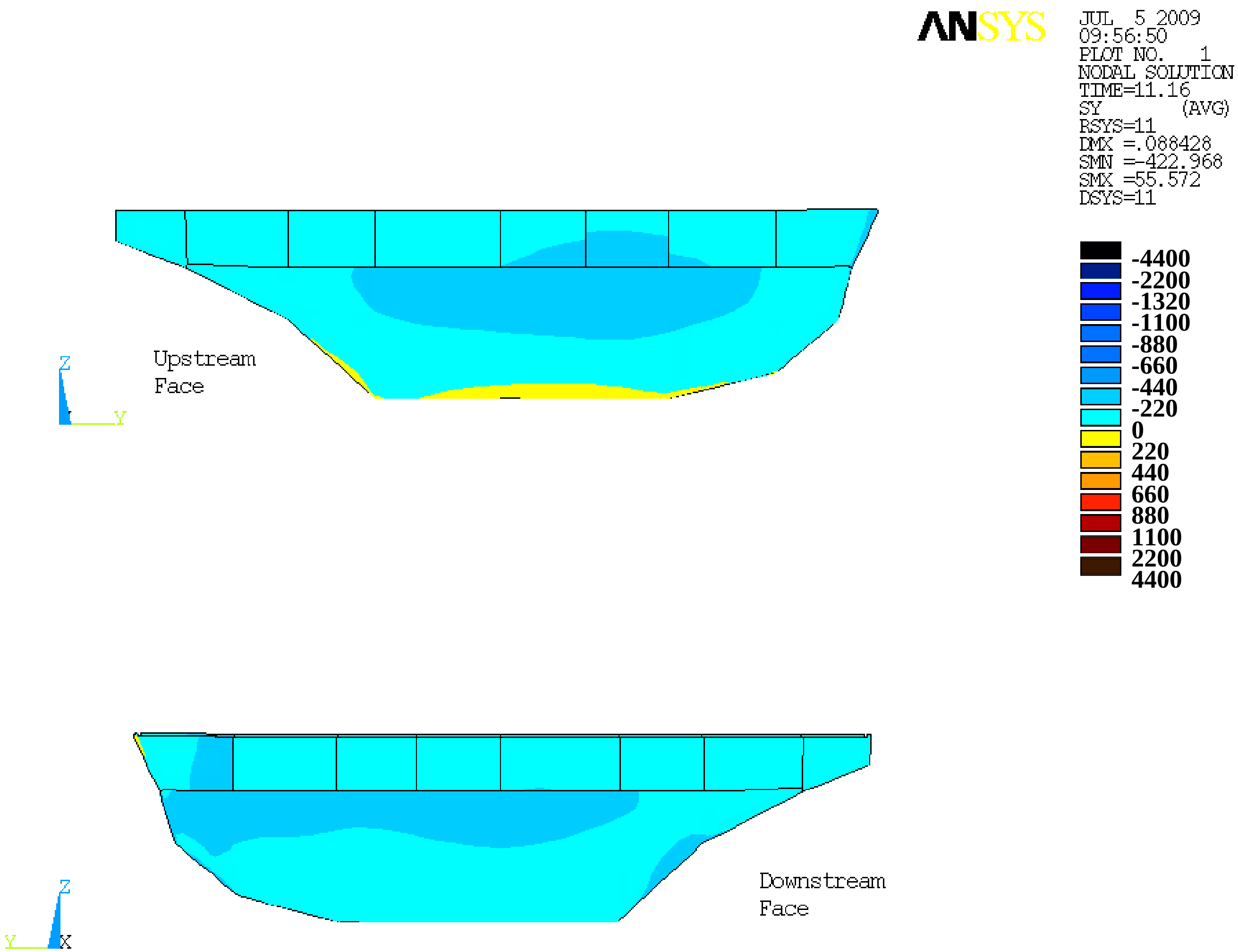

URS

Trout Lake Dam
Extreme Load 1
Arch Stress
11.16 Seconds
Figure No. 4- 39

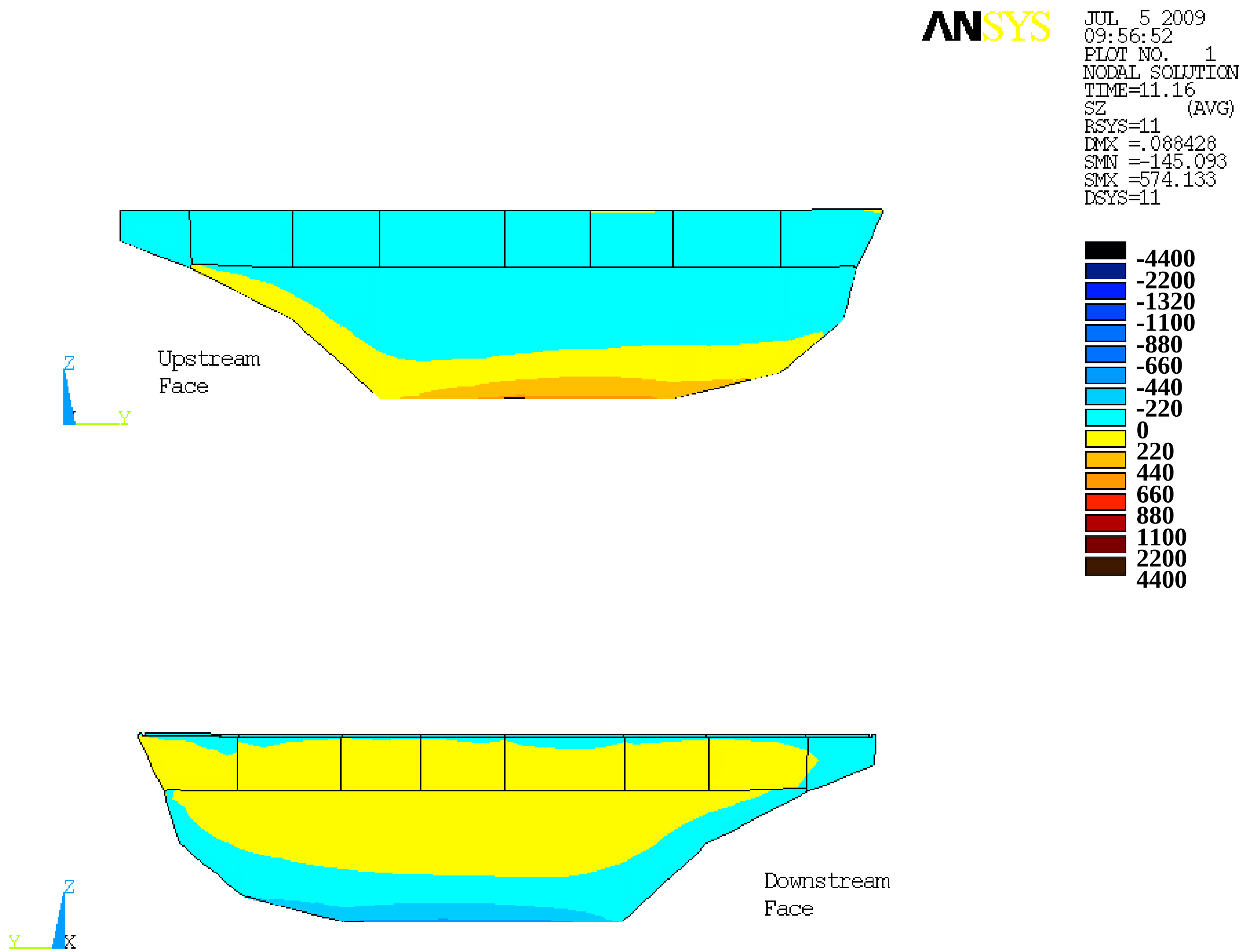

URS

Trout Lake Dam
Extreme Load 1
Cantilever Stress
11.16 Seconds
Figure No. 4- 40

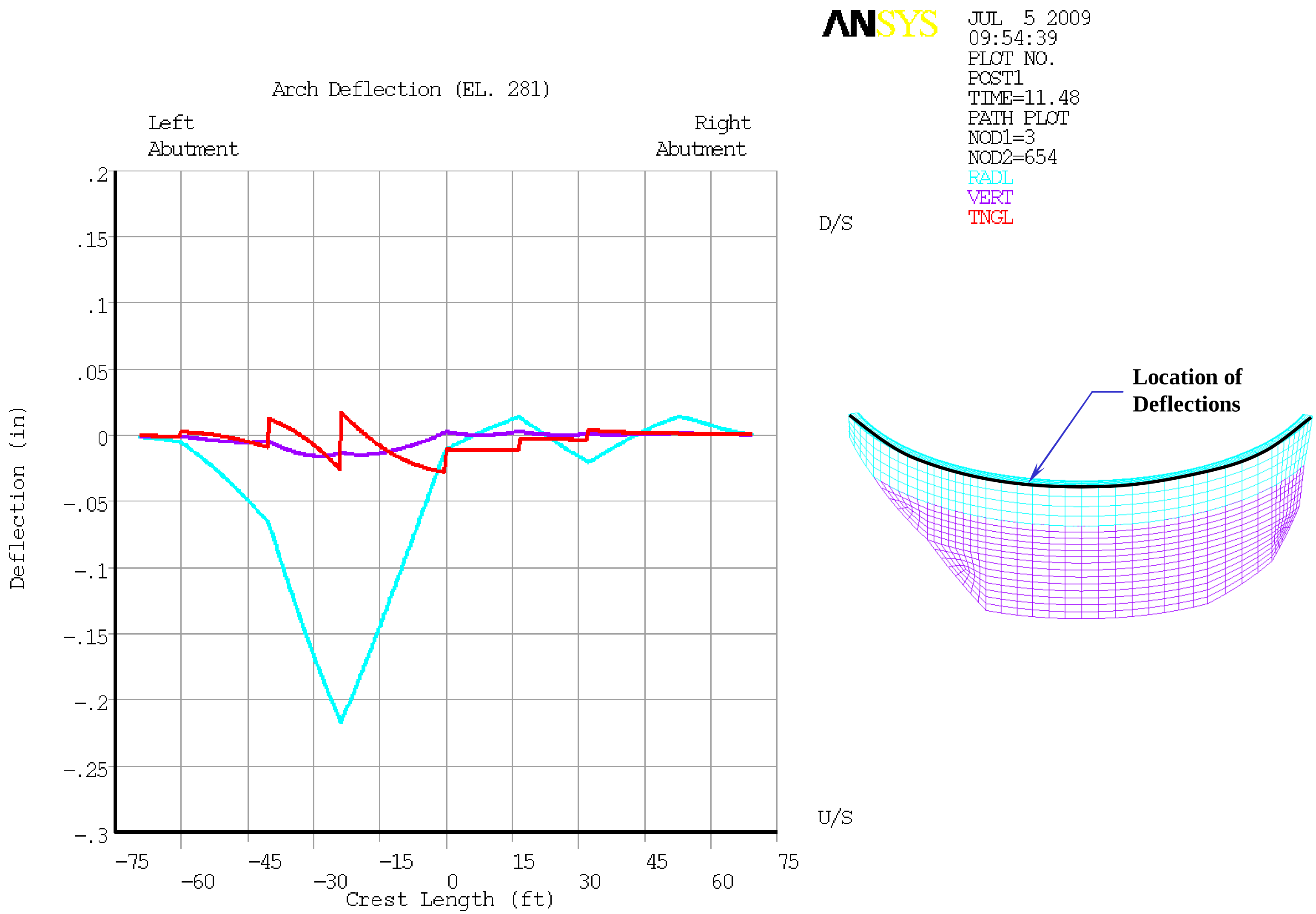

Trout Lake Dam

Extreme Load 1

Dam Crest Deflection

11.48 Seconds

Figure No. 4- 41

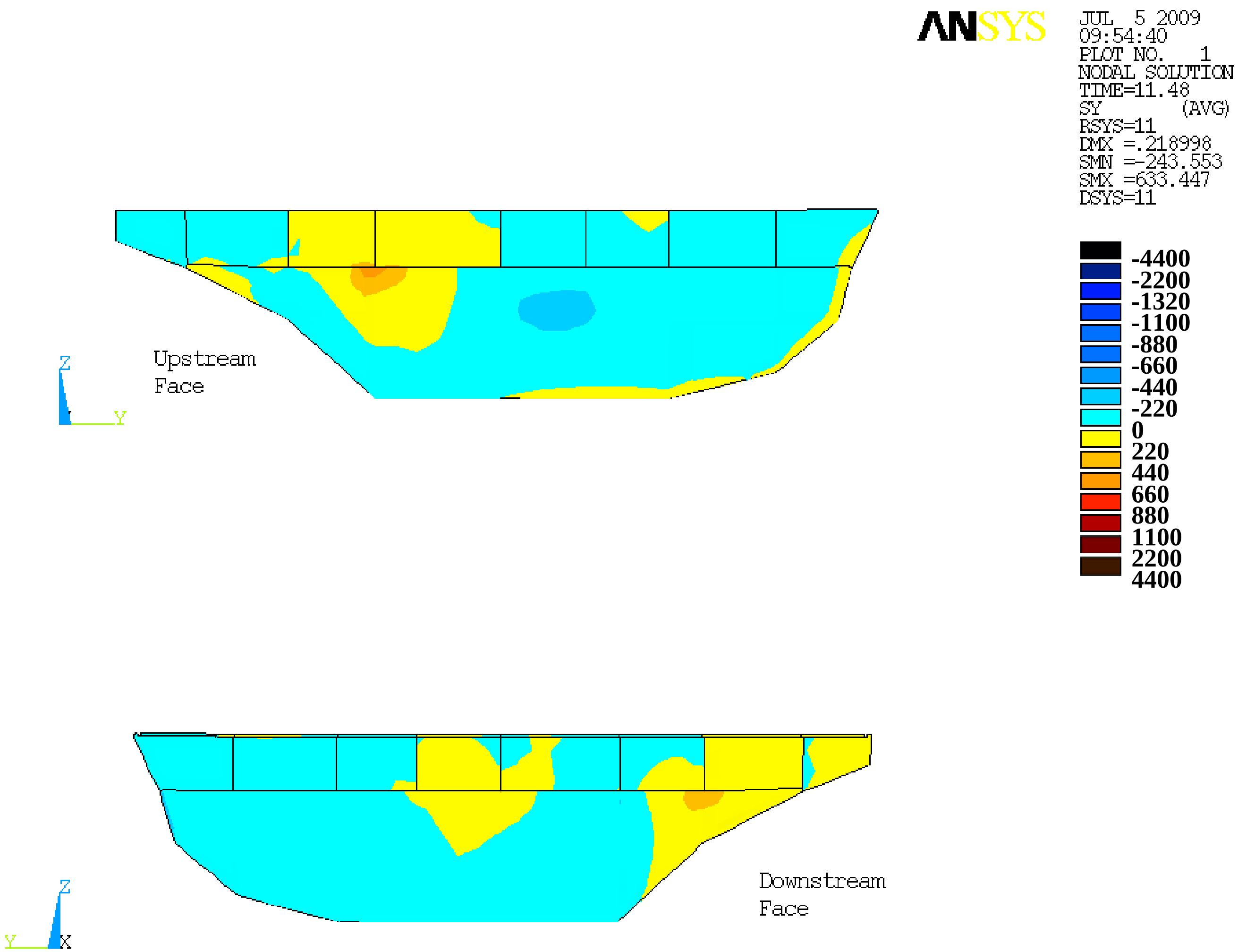

URS

Trout Lake Dam

Extreme Load 1

Arch Stress

11.48 Seconds

Figure No. 4- 42

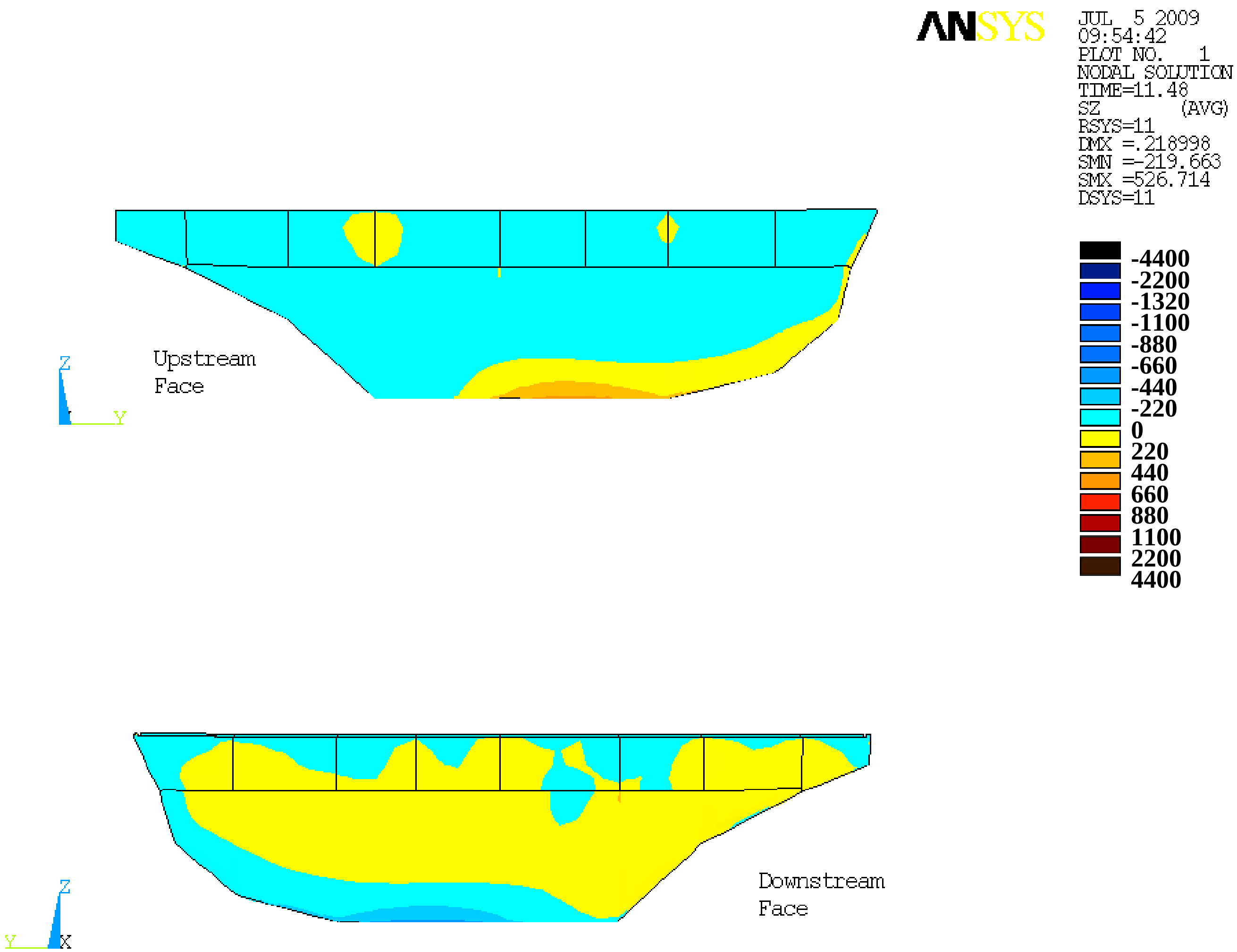

Trout Lake Dam
Extreme Load 1
Cantilever Stress
11.48 Seconds
Figure No. 4- 43

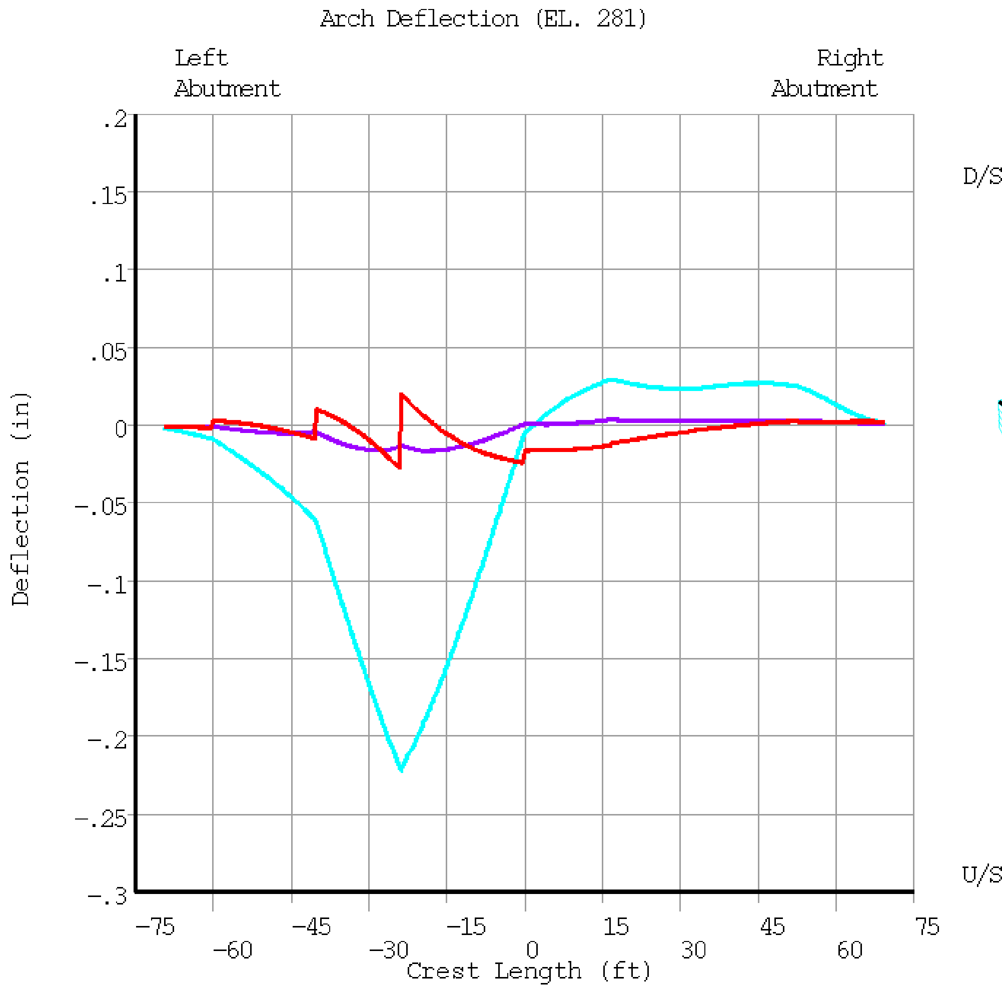

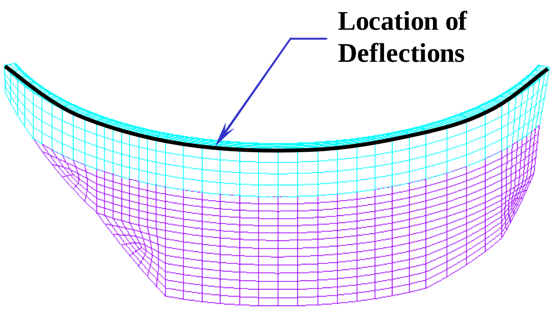

Trout Lake Dam
Extreme Load 1
Dam Crest Deflection
11.49 Seconds
Figure No. 4- 44

URS

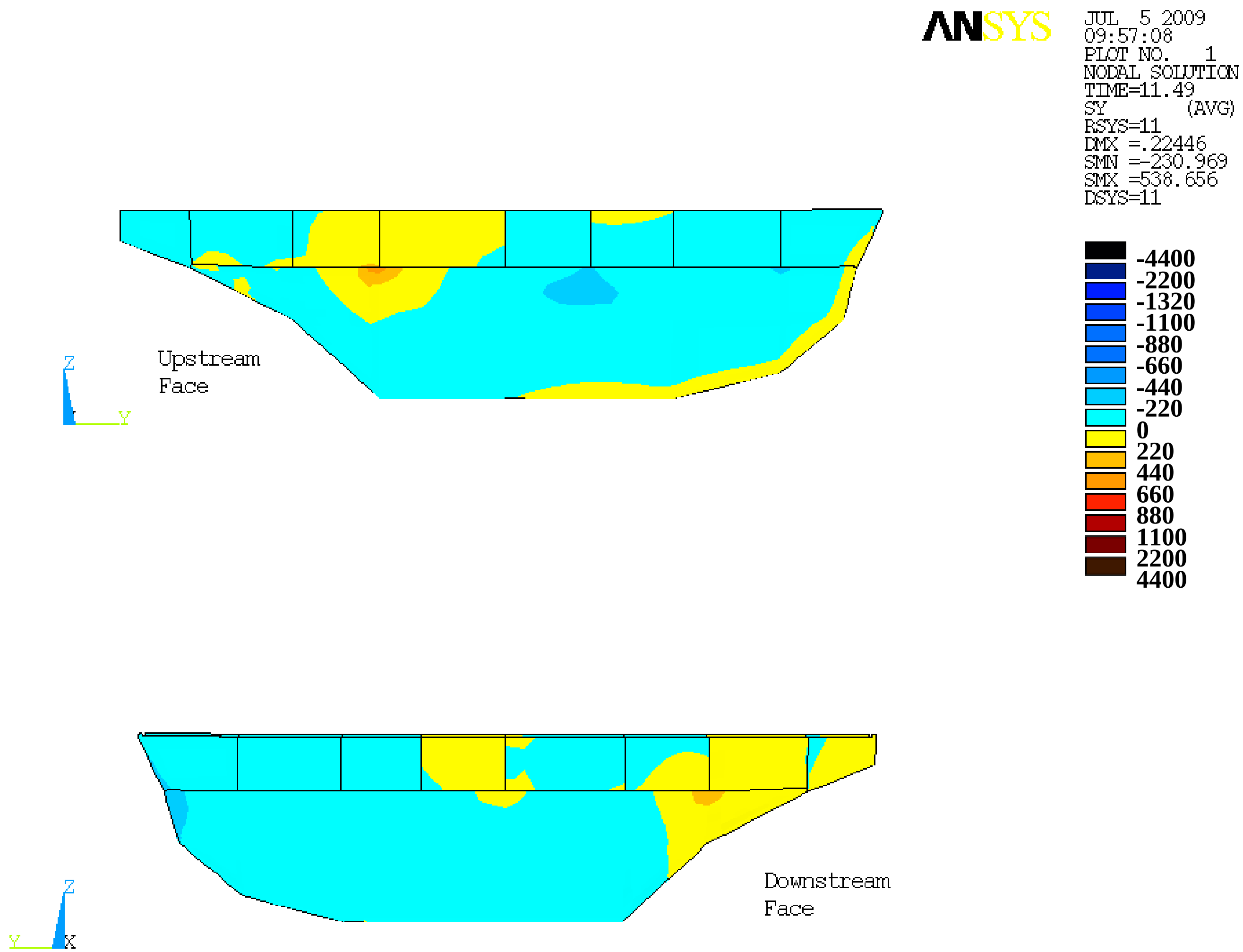

Trout Lake Dam

Extreme Load 1

Arch Stress

11.49 Seconds

Figure No. 4- 45

URS

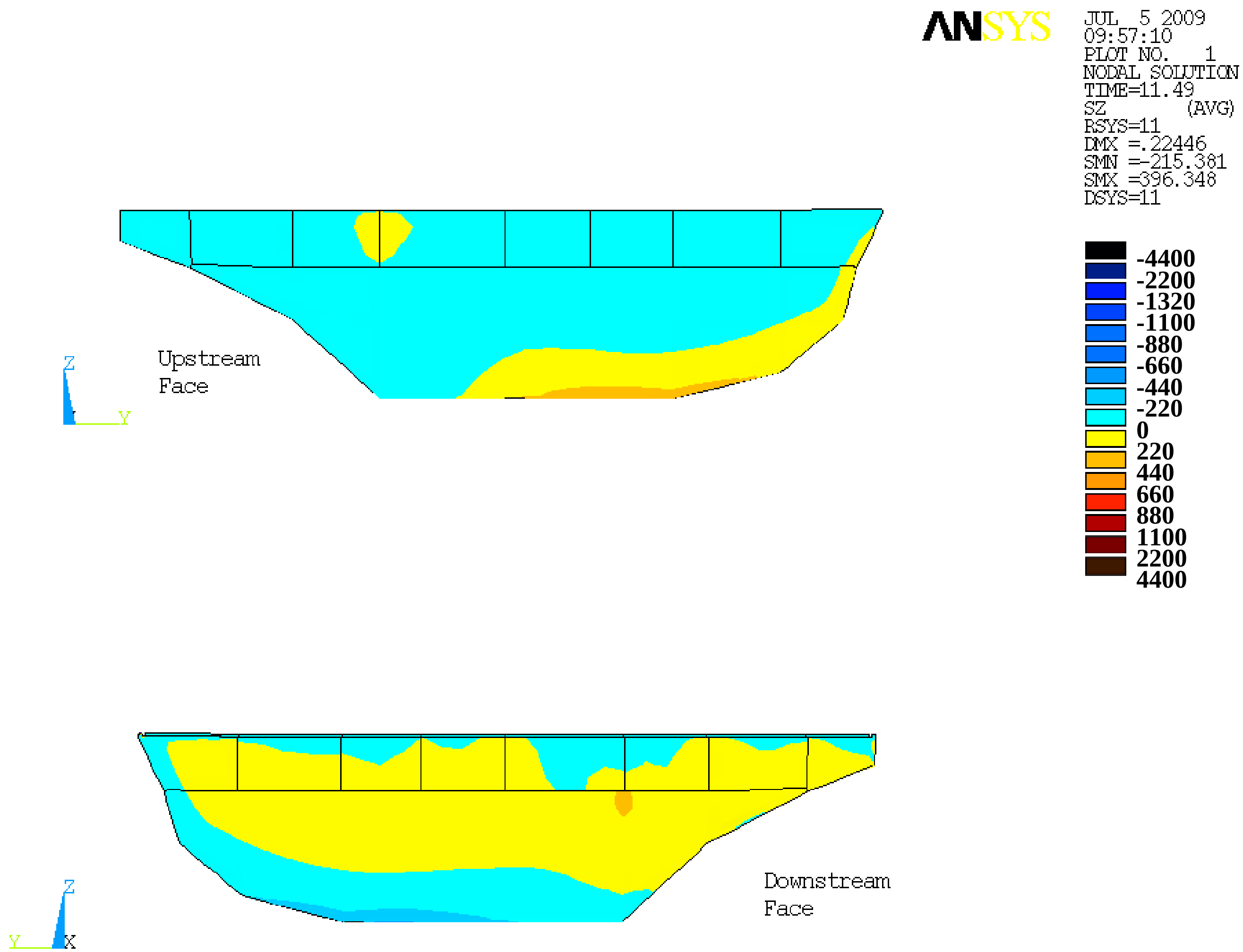

Trout Lake Dam

Extreme Load 1

Cantilever Stress

11.49 Seconds

Figure No. 4- 46

URS

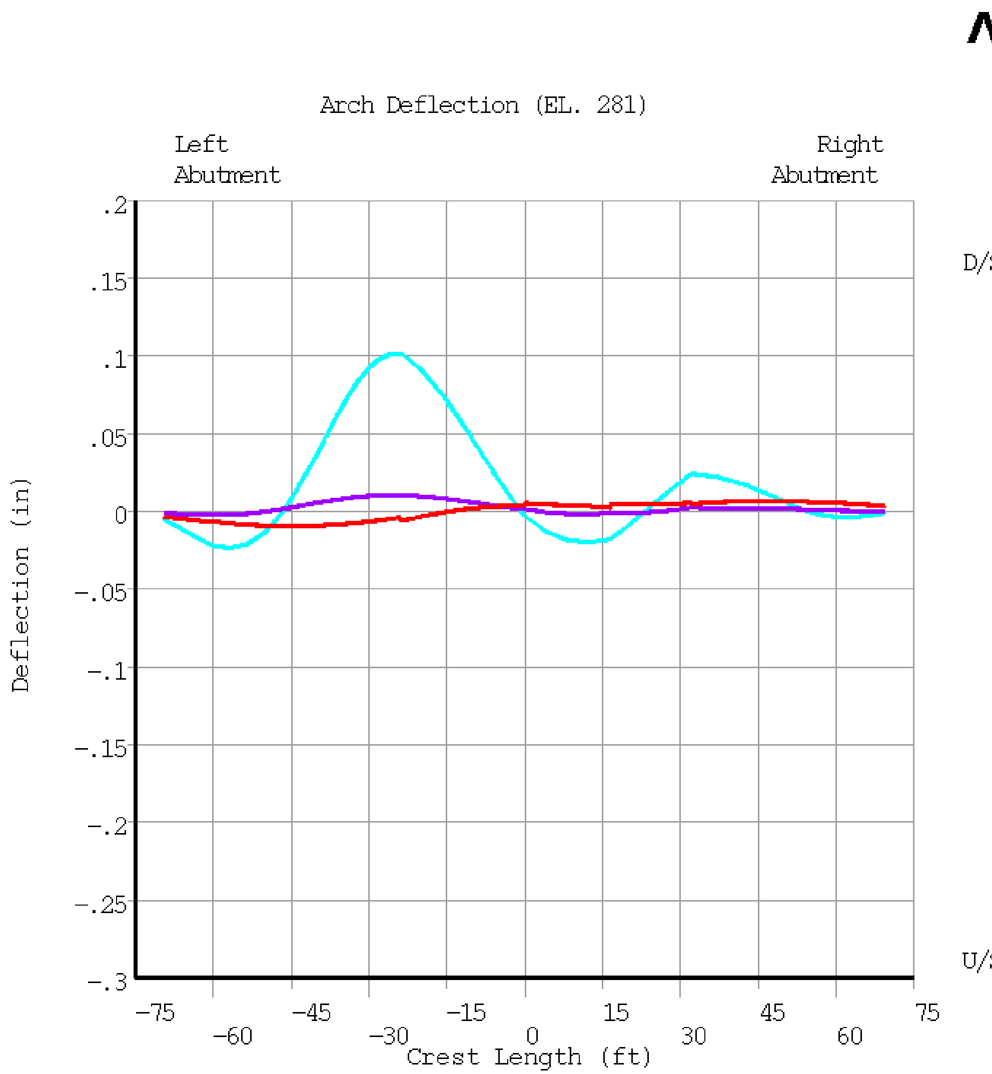

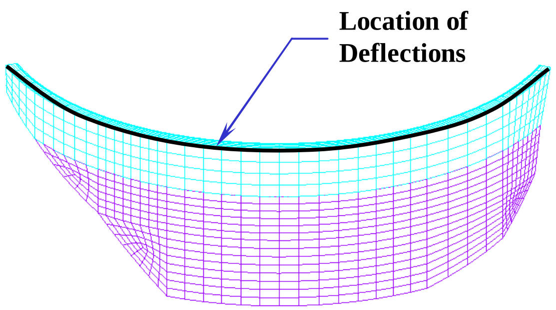

Trout Lake Dam
Extreme Load 1
Dam Crest Deflection
11.53 Seconds
Figure No. 4- 47

URS

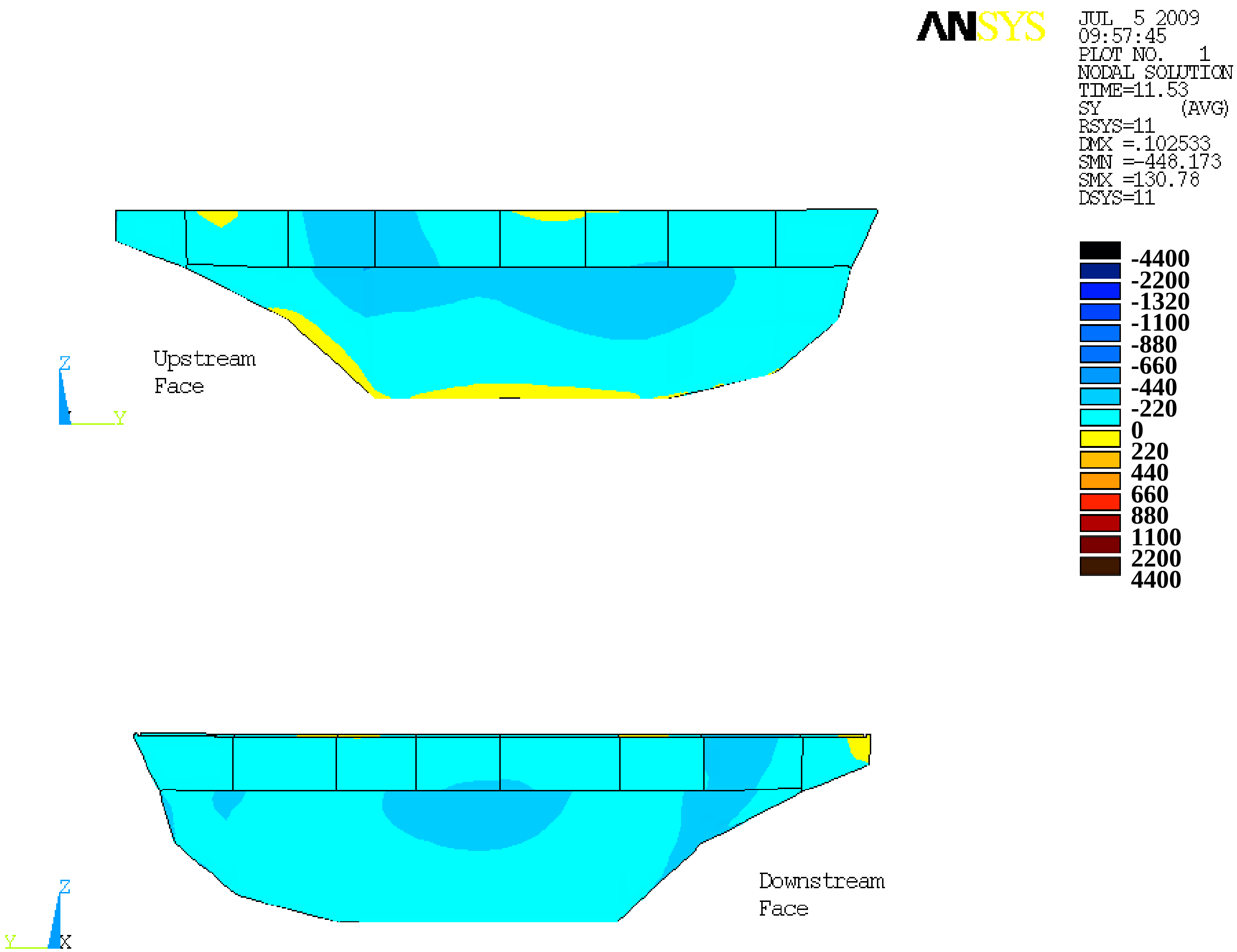

Trout Lake Dam

Extreme Load 1

Arch Stress

11.53 Seconds

Figure No. 4- 48

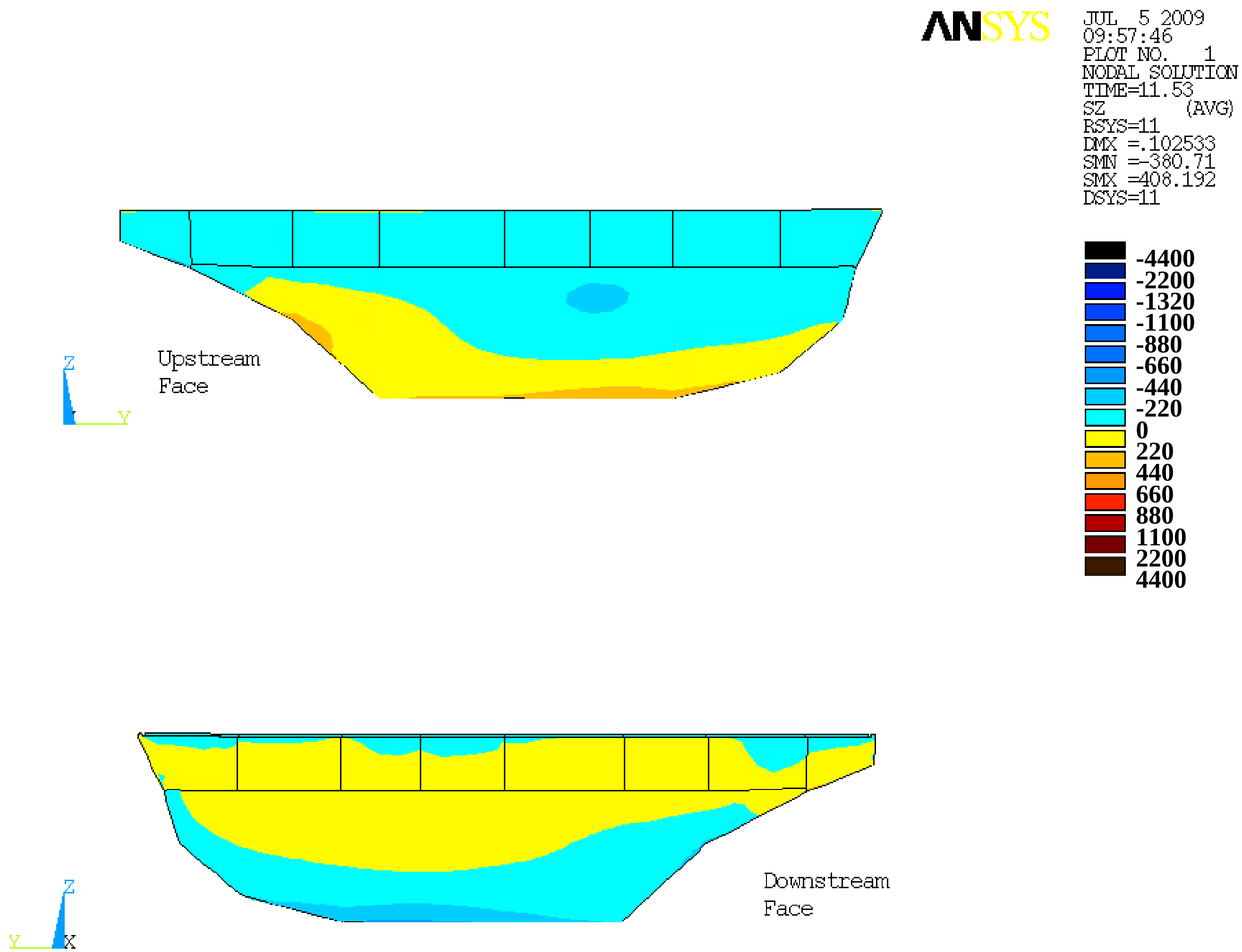

Trout Lake Dam
Extreme Load 1
Cantilever Stress
11.53 Seconds
Figure No. 4- 49

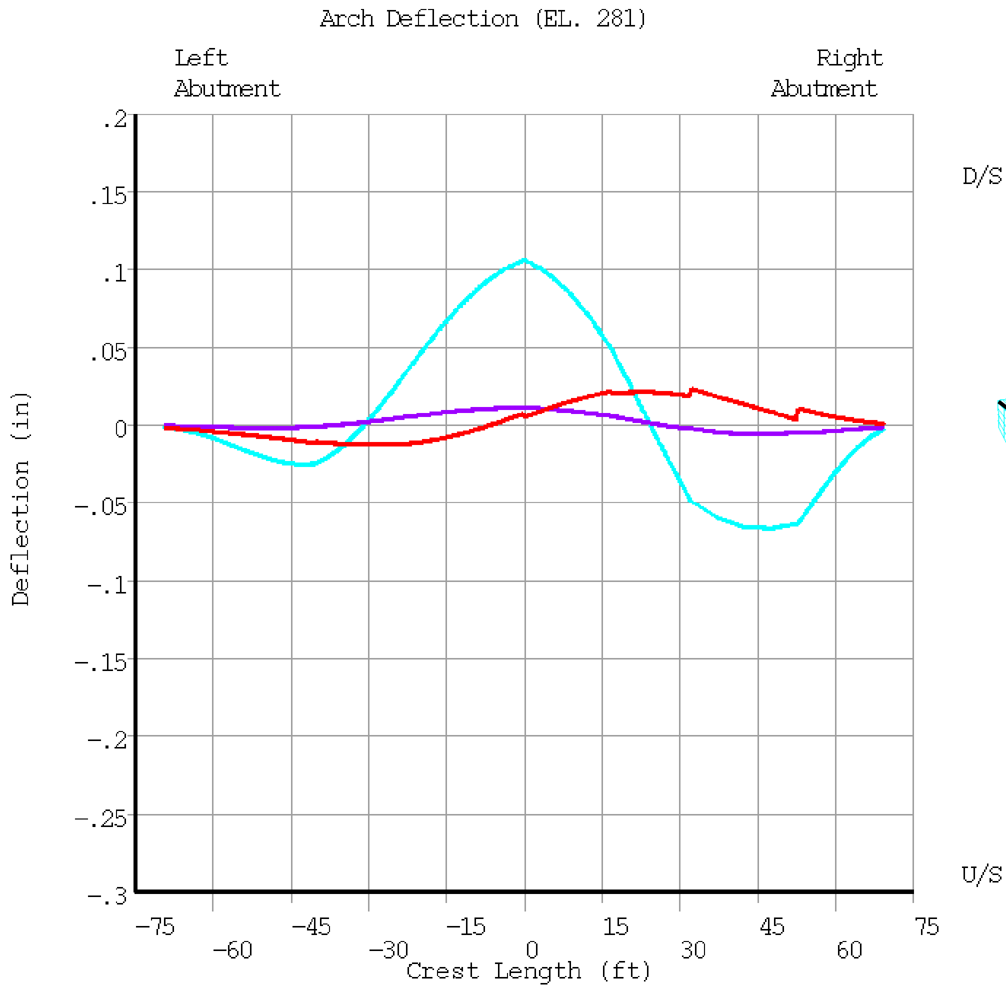

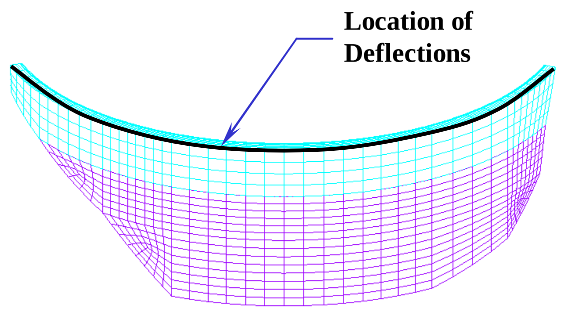

URS

Trout Lake Dam
Extreme Load 1
Dam Crest Deflection
14.62 Seconds
Figure No. 4- 50

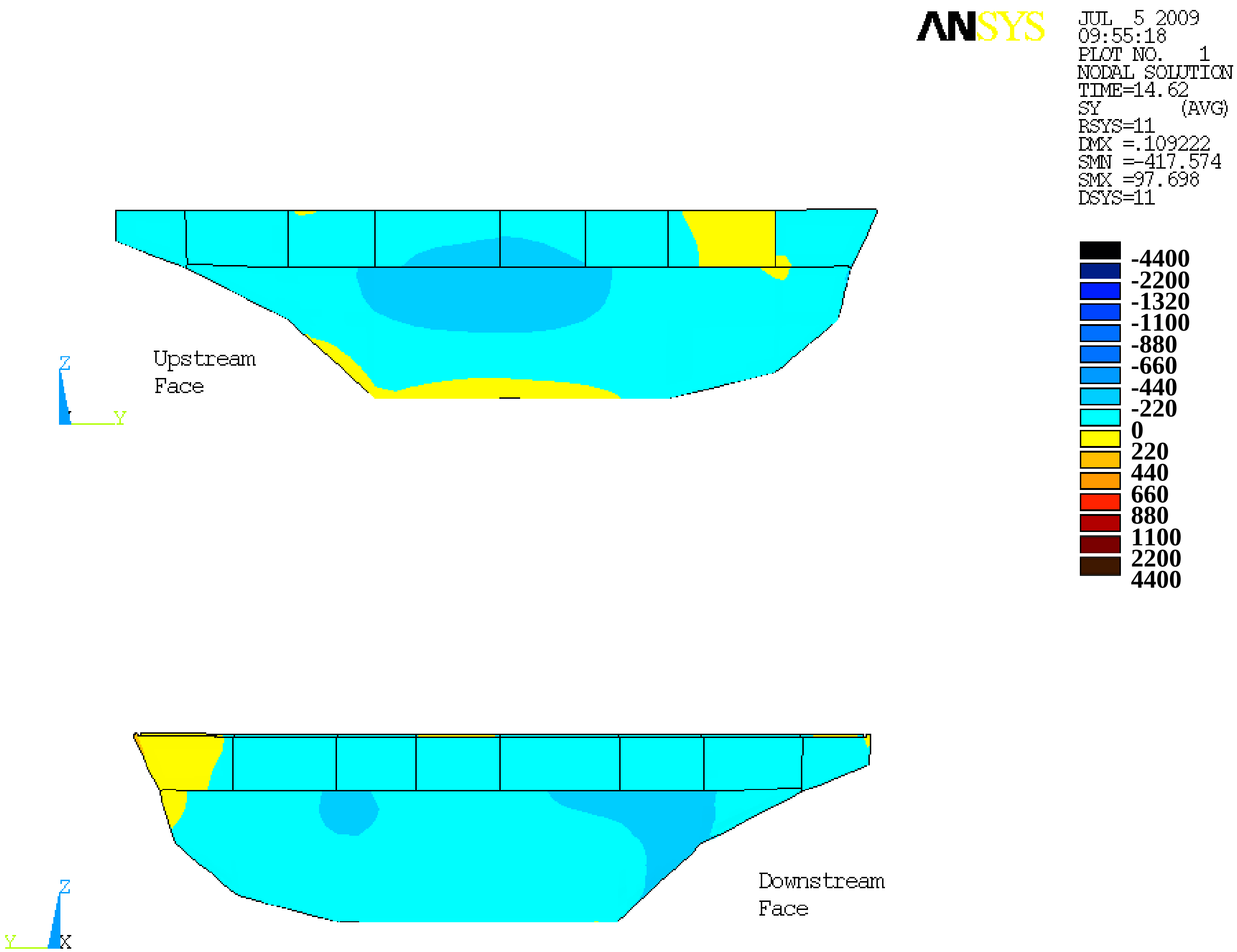

Trout Lake Dam
Extreme Load 1
Arch Stress
14.62 Seconds
Figure No. 4- 51

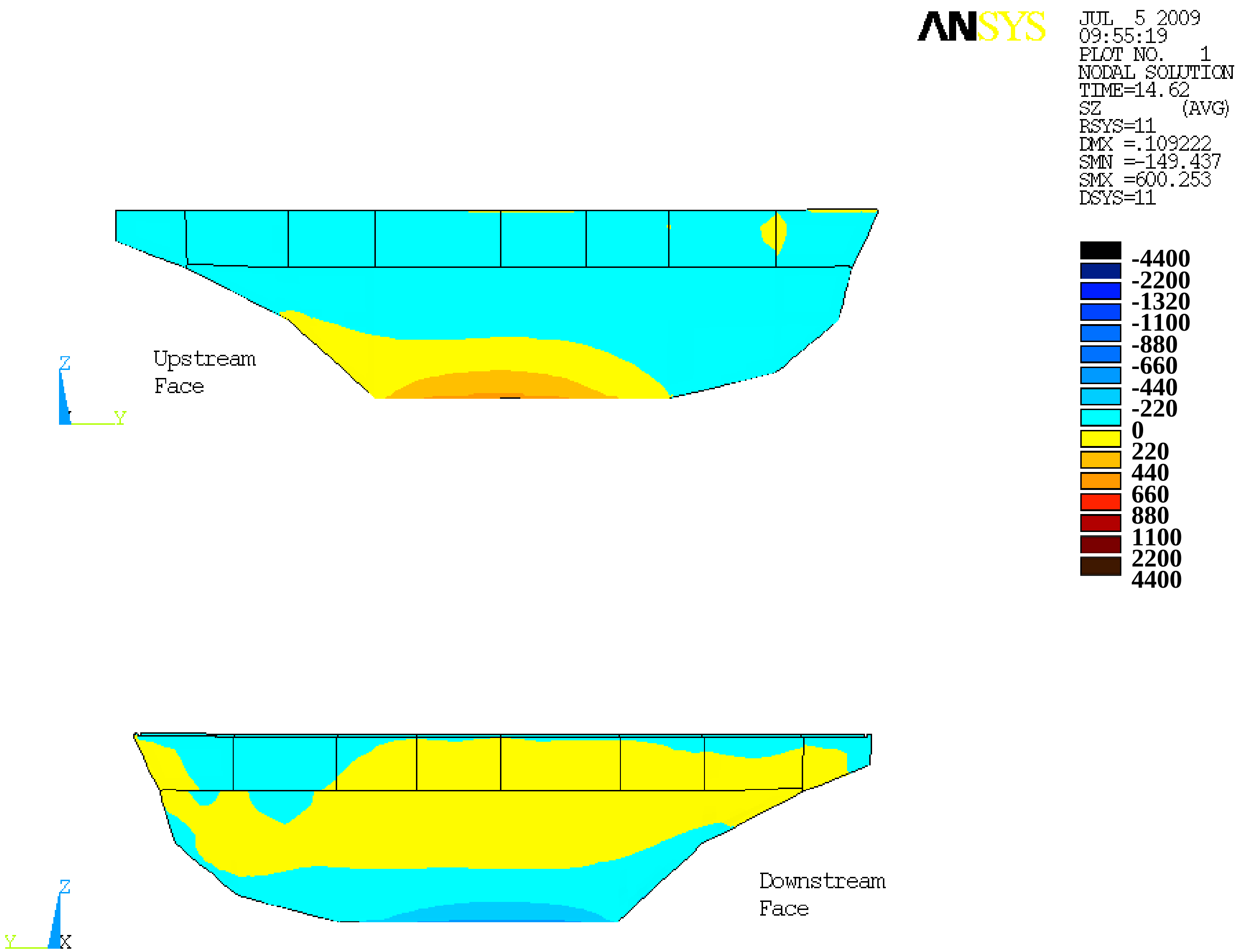

Trout Lake Dam
Extreme Load 1
Cantilever Stress
14.62 Seconds
Figure No. 4- 52

URS

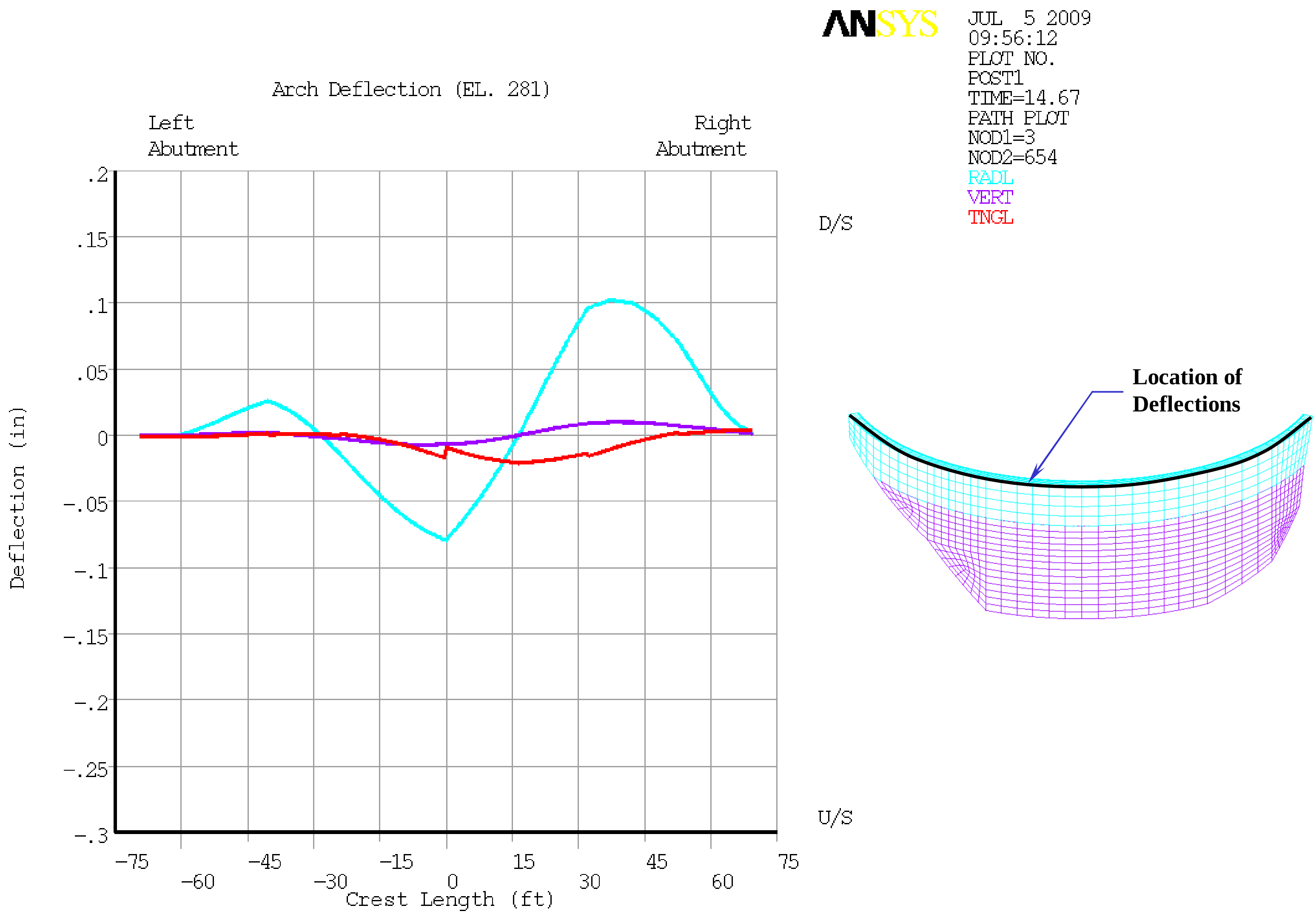

Trout Lake Dam

Extreme Load 1

Dam Crest Deflection

14.67 Seconds

Figure No. 4- 53

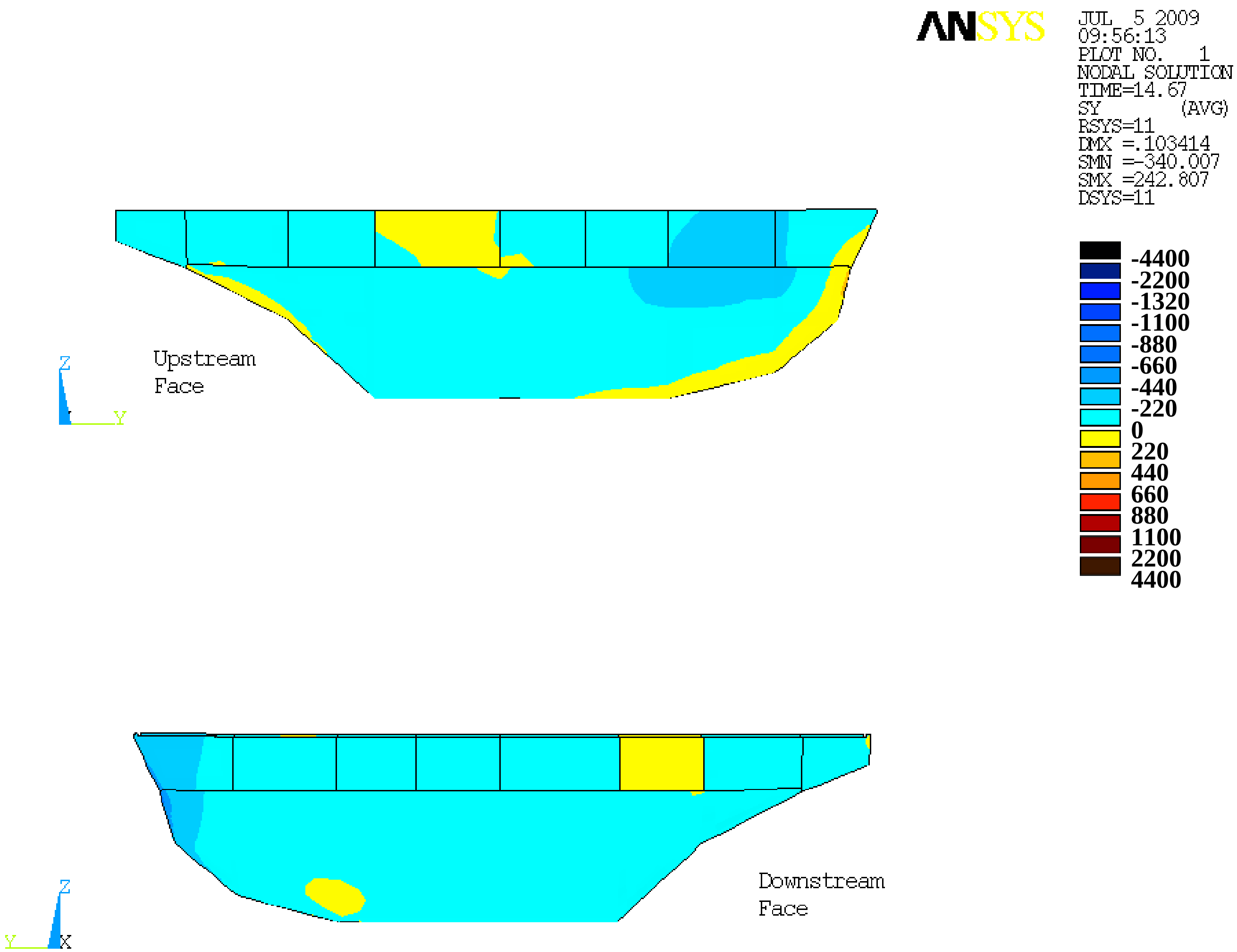

Trout Lake Dam

Extreme Load 1

Arch Stress

14.67 Seconds

Figure No. 4- 54

URS

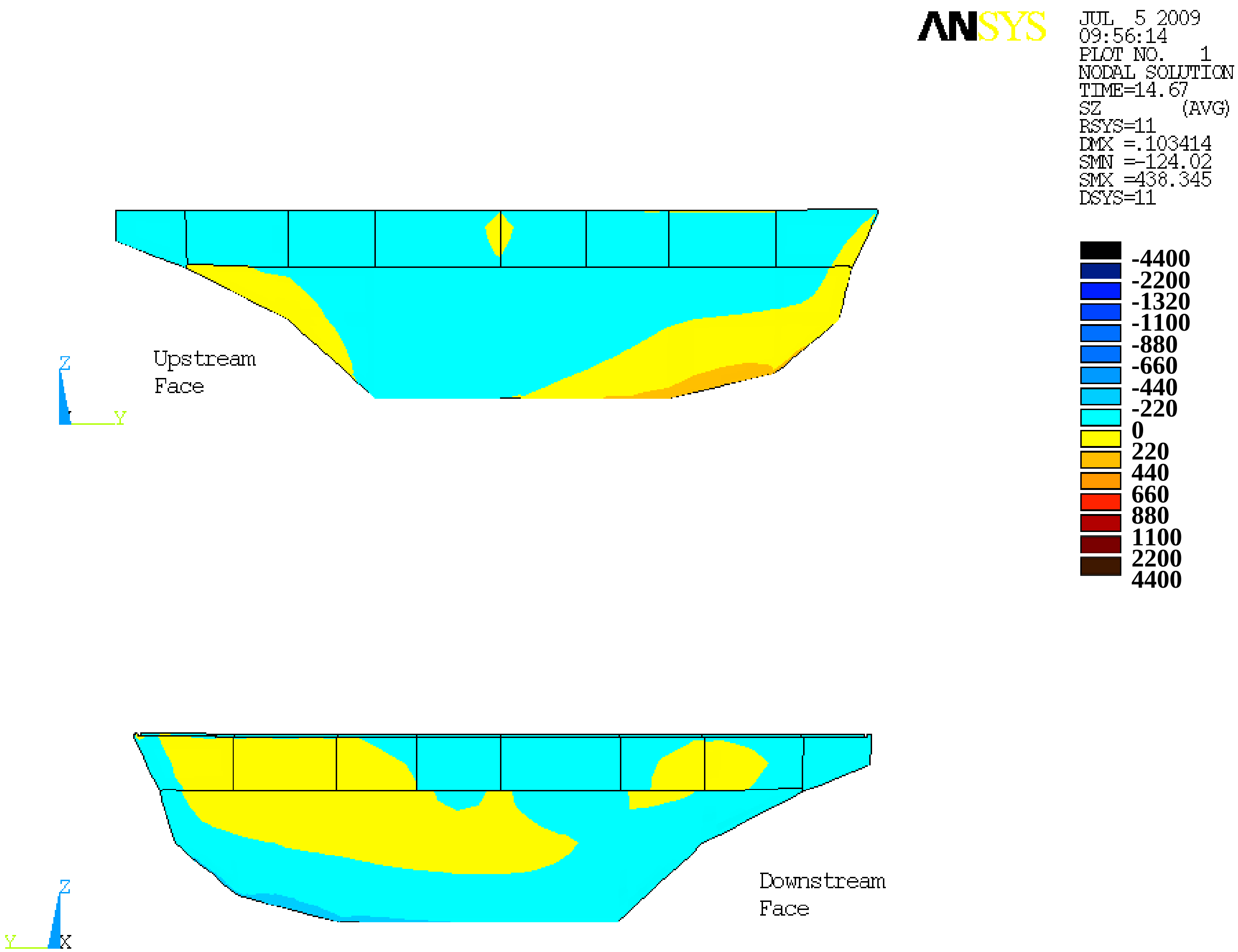

Trout Lake Dam
Extreme Load 1
Cantilever Stress
14.67 Seconds
Figure No. 4- 55

URS

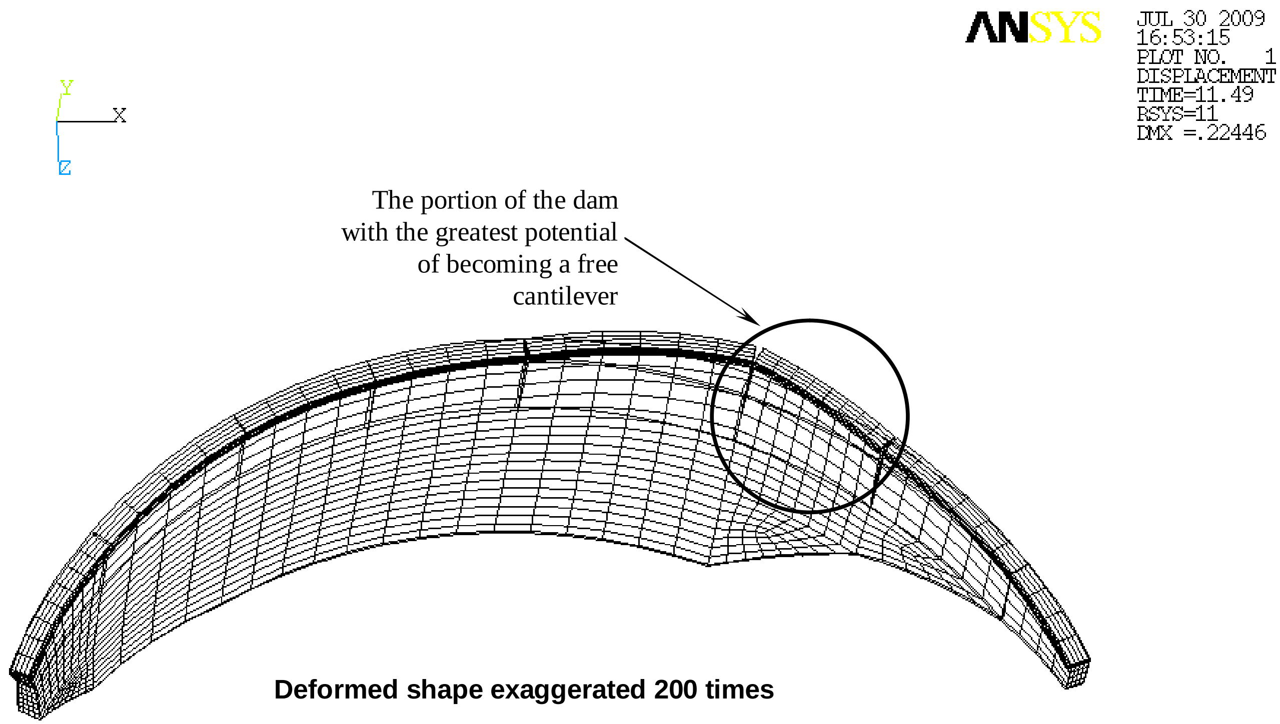

URS

Trout Lake Dam
Extreme Load 1
Deformed Shape of Dam
11.49 Seconds
Figure No. 4- 56

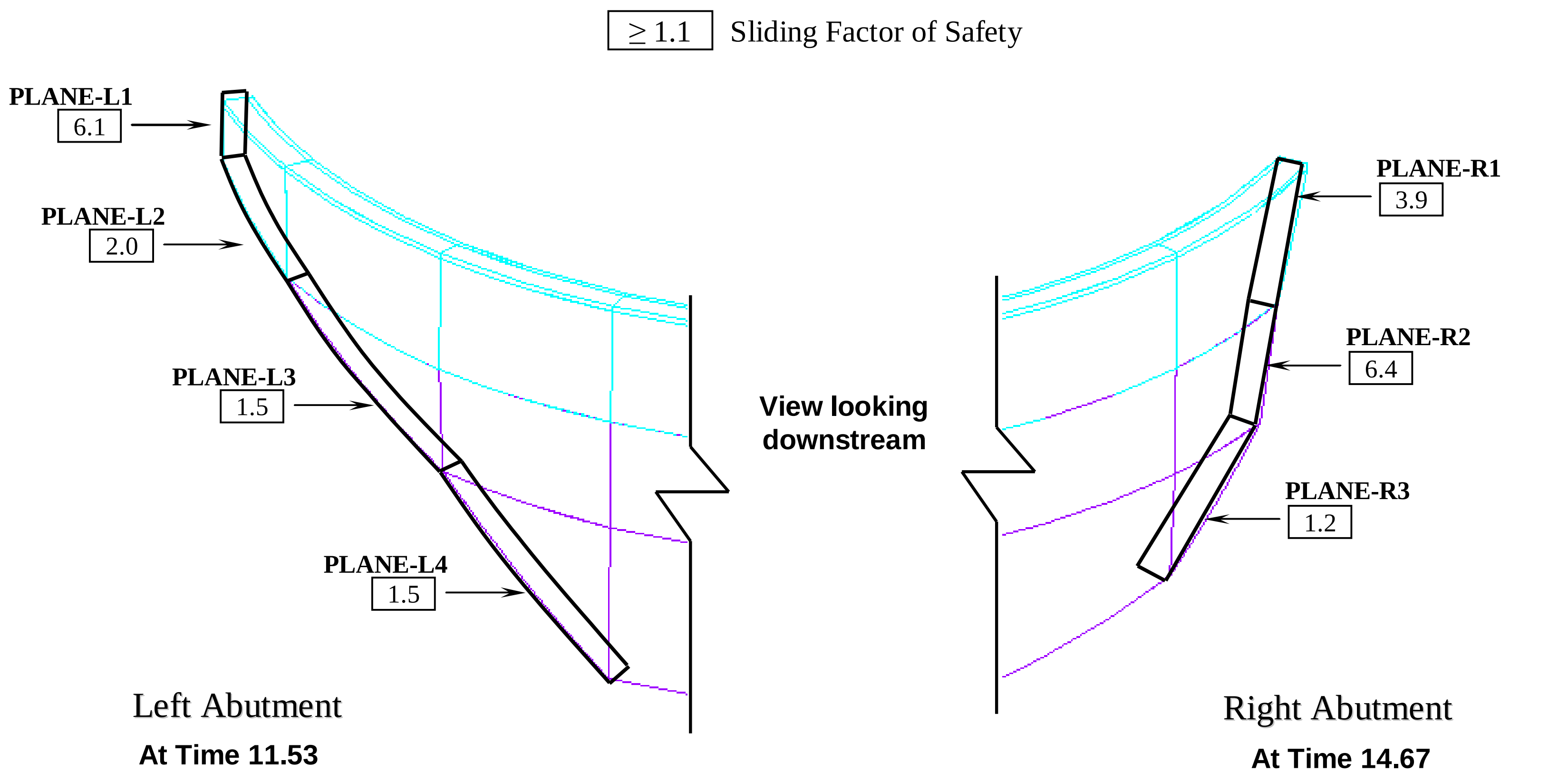

URS

Trout Lake Dam
Extreme Load 1
Sliding Planes
Sliding Factors of Safety
Figure No. 4- 57

5.1 ABUTMENT STABILITY

To evaluate the abutment stability of the dam the, first step is identify if there are any potential rock blocks that could become kinematically released from the right or left abutments by the pressure of the dam. This evaluation was performed by plotting the joint sets listed in Section 2.2.1, Joint Sets, on a stereo net. The stereo net representing the left and right abutments are shown on Figure No. 5- 1 and Figure No. 5- 2, respectively.

The results from the stereo net is that there are no rock blocks at could kinematically release from the right or left abutments. Therefore the abutments of Trout Lake Dam are considered to have adequate stability for the loading conditions presented in this report.

5.2 ERODIBILITY ANALYSIS

Historical observations at other dam sites have noted rock scour during significant discharging events, such as floods. Rock scour at concrete dams, such as Trout Lake Dam, which rely on the rock abutments for the stability of the structure, can present a significant hazard to dam safety. Current Federal Energy Regulatory Commission's (FERC) guidelines require an assessment of rock scour when the dam under consideration is expected to overtop during high flow conditions *[4]*.

5.2.1 Erodibility Index

The Erodibility Index Method developed by Annandale (1995) is based on an erosion threshold *[17]*. The threshold, known as the *Erodibility Index,* relates the relative ability of rock and other earth materials to resist scour to the relative magnitude of the erosive capacity of the water, as shown in Illustration No. 1. The magnitude of the erosive capacity is expressed in terms of its rate of energy dissipation, also known as *Stream Power*. If the stream power is greater than the Erodibility Index, then rock scour will likely develop. If the stream power is less than the Erodibility Index, then rock scour will not likely occur.

An evaluation of the geologic characteristics of the foundation rock was performed to estimate the Erodibility Index (see Section 2.2). The Erodibility Index for the rock was estimated to be approximately 6220. The corresponding stream power will then be approximately 700 kW/m^2, as shown in illustration 1.

For these studies the erodibility of the rock was performed for the probable maximum flood (PMF) event. The maximum reservoir surface due to the PMF event is estimated to be at El. 282 feet.

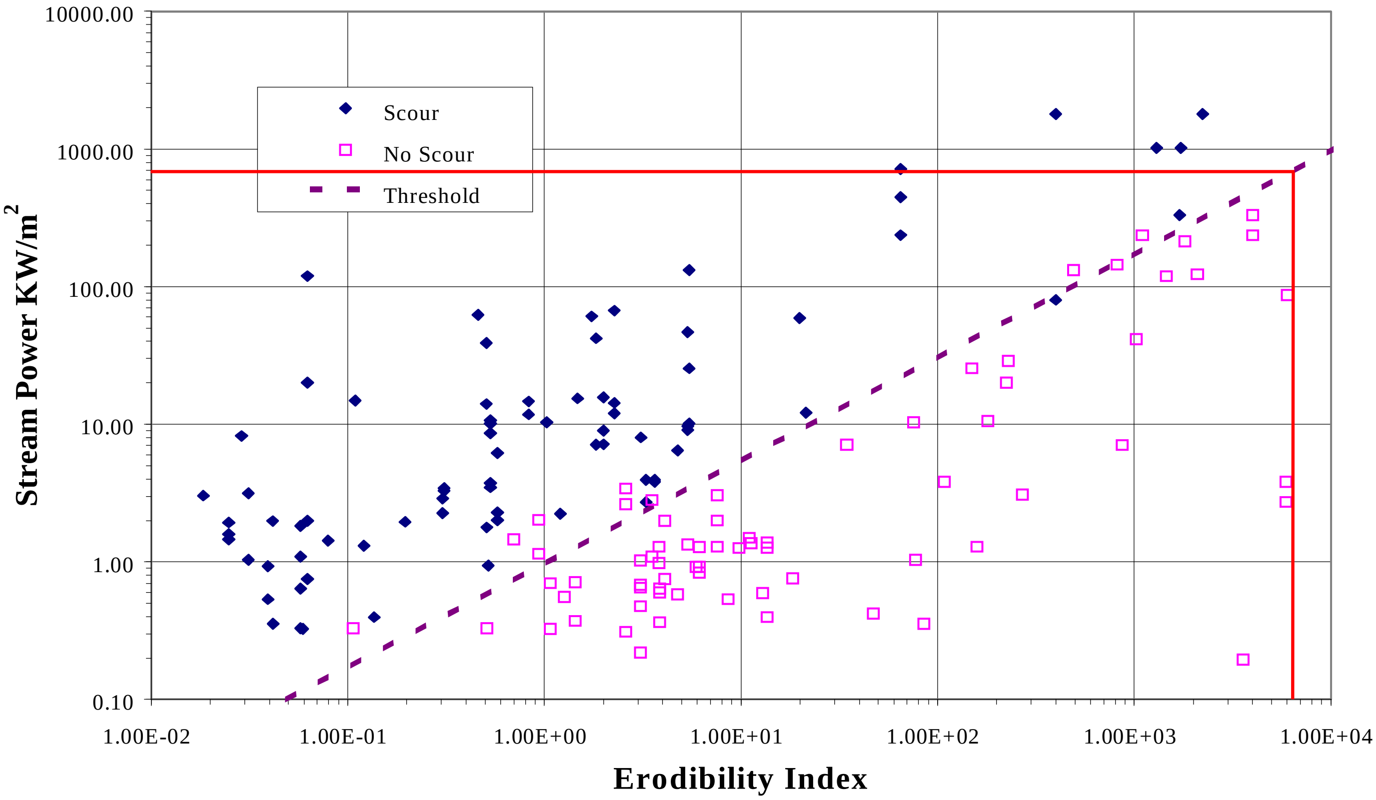

Illustration 1

5.2.2 Stream Power

The computation of stream power is inversely related to the area of the jet when it impacts the rock (see Equation 7). The area of the jet can be computed using the overtopping profile, which is shown on Figure No. 5- 3. The profile was computed using the following hydraulic parameter assumptions:

- The discharge coefficient for the crest of the dam was conservatively assumed to be 3.0.
- The friction factor was conservatively assumed to be 0.01.
- The dispersion of the jet below tailwater is at approximately 11 degrees, which is a slope of 1:5.

The stream power is computed using Equation 7, as shown in Section 3.1.3, Rock Scour (Erosion).

The results from this study show that the computed stream power of 140 kW/m^2 is significantly less than the rock erodibility index (700 kW/m^2), which indicates there is not a likelihood for development of rock scour on the surface of the foundation.

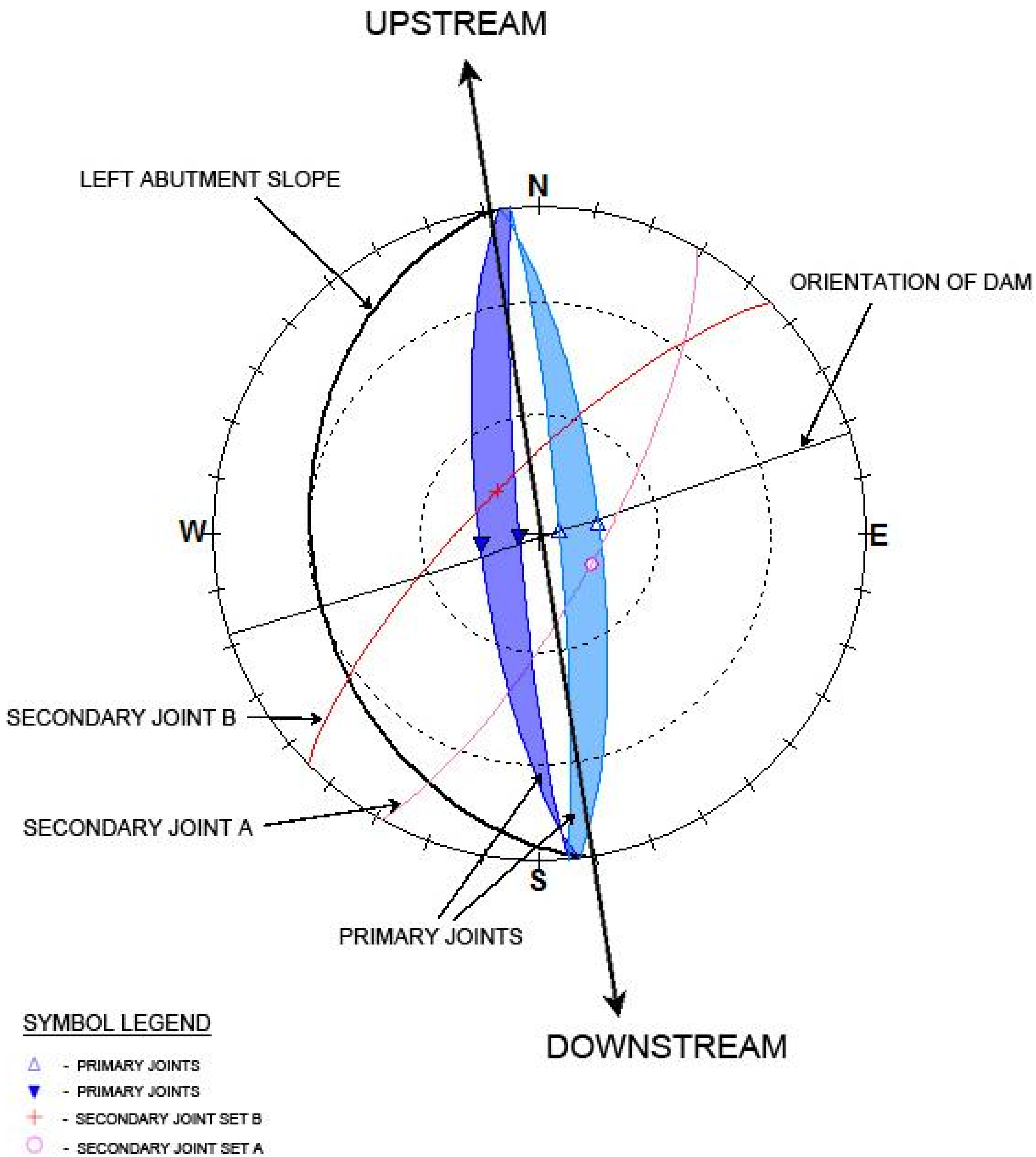

URS

Trout Lake Dam
Abutment Stability
Left Abutment
Stereo Net
Figure No. 5- 1

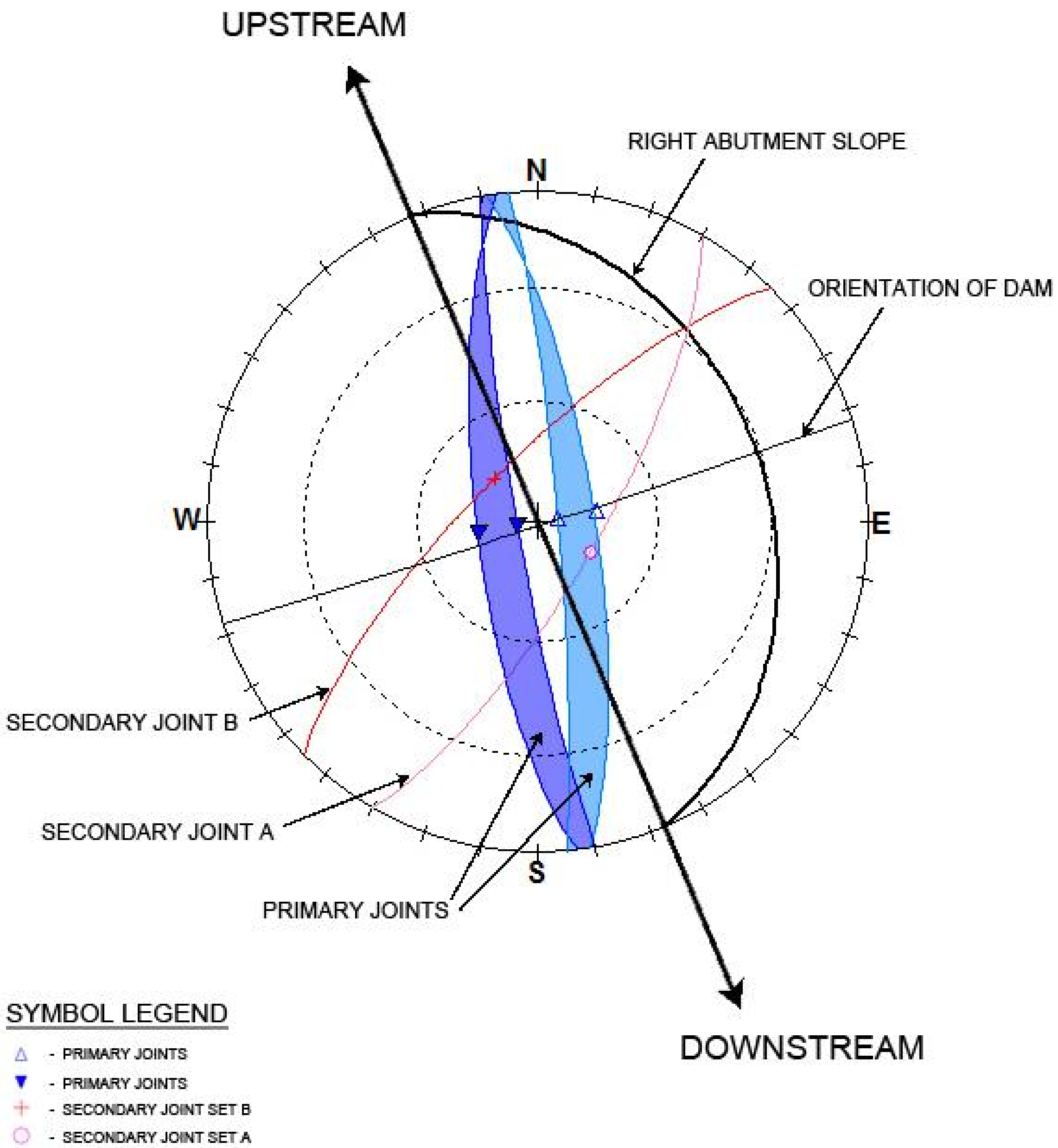

Trout Lake Dam
Abutment Stability
Right Abutment
Stereo Net
Figure No. 5- 2

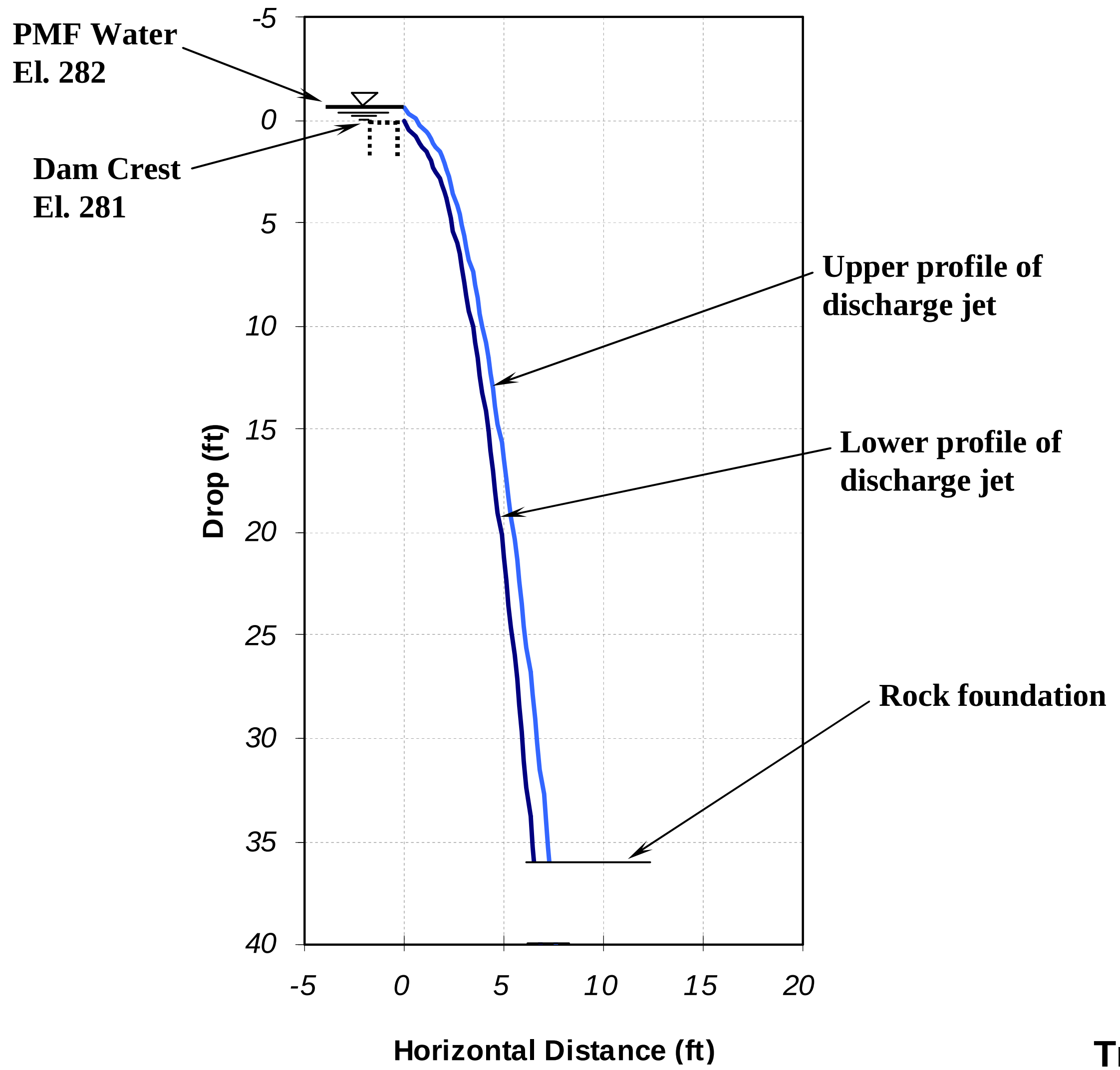

Trout Lake Dam
Erodibility Analysis
Jet Profile

Figure No. 5- 3

URS

URS Corporation (URS) was retained by the Town of Friday Harbor to perform a comprehensive structural stability analysis of Trout Lake Dam for the usual (normal), unusual (flood), and extreme (seismic) loading conditions and evaluate the safety and stability of the dam.

6.1 STRUCTURAL ANALYSIS

The structural analysis was performed using the finite element method of analysis. The concrete and foundation material parameters were estimated based on design data for the dam, and other published engineering sources. The estimated properties of concrete and foundation rock simulate the material behavior in the finite element analysis.

A three-dimensional finite element model was developed to study the behavior of the dam. The model also included a significant portion of the foundation rock around the dam. Different element types were used to simulate selected structural behaviors. Solid elements were used to simulate the concrete and foundation rock mass. Transition elements were used to simulate cracks and potential separation at the dam/foundation interface. Mass elements were used to simulate the dam/reservoir interaction during the seismic loading event.

The purpose of the analysis was to evaluate the structural capacity of the dam for several different loading conditions. Static analyses were performed to evaluate the usual (normal) loading conditions and the unusual (PMF) loading conditions. A dynamic analysis was performed to evaluate the extreme (seismic) loading conditions.

The details of the analysis, such as structural behavior and modeling modifications, are discussed in detail in the preceding sections of this report.

6.1.1 Evaluation Criteria

The structural safety of Trout Lake Dam was evaluated against the following known type of failure modes for these types of structures.

- *Concrete Overstressing*. The ability of the concrete in the structure to support the assumed loads without cracking or crushing.
- *Stability*. The safety of the dam against sliding at the dam/foundation interface.
- *Rock Block Stability*. The safety of the left and right abutments to support the assumed loads without movement of potentially isolated rock block, which are formed by the intersection of joints and topographic surfaces.
- *Erosion*. There is a potential for rock scour, or erosion, during a flooding event caused by the reservoir overtop the dam. The analysis evaluated the strength of the surrounding rock to resist the hydraulic energy (stream power) due to flood overtopping.

6.1.2 Usual Load, USLC-1 (Spring/Fall Condition)

The results from the structural analyses for the usual spring/fall loading condition indicate that the dam has adequate safety against overstressing. The results from initial analysis showed cantilever tensile stress at the upstream heel and downstream face of the dam. This may indicate that some horizontal cracking on the downstream face of the dam may develop, and that there may be minor separation at the dam/foundation interface. Modifications were performed to the finite element model to simulate these potential changes in structural behavior, and the results showed that the dam still has adequate safety against the usual load 1, USLC-1. Based on these studies, the dam is considered to have adequate safety against overstressing for the assumed usual spring/fall load.

The sliding stability of the Trout Lake Dam was evaluated using the results from the modified finite element model. The computed results showed that Trout Lake Dam has adequate safety against sliding for the spring/fall loading condition.

6.1.3 Usual Load, USLC-2 (Summer Condition)

The results from the structural analyses for the usual summer loading condition indicate that the dam has adequate safety against overstressing. The results show that the stresses are all less than the allowable strength of the concrete except for the cantilever tensile stresses on the downstream face of the dam near mid-height. The tensions in the cantilevers are again not a concern regarding the stability of the dam, because of the restoring hydrostatic pressure from the reservoir. Based on these studies, the dam is considered to have adequate safety against overstressing for the assumed usual summer load.

The sliding stability of the Trout Lake Dam was evaluated using the results from the finite element model. The computed results show that the dam has adequate against sliding for the usual summer loading condition.

6.1.4 Usual Load, USLC-3 (Winter Condition)

The results from the structural analysis for the usual winter loading condition show that large areas of the tensile stresses develop due to concrete contraction from the colder winter temperature loads. Additional studies were performed to simulate cracks in the concrete within the area of significant tension. The results show that the load is redistributed to the arches in the dam, and the arches have sufficient capacity to support the assumed load. Based on these results, the dam has adequate safety against overstressing for the assumed usual winter load.

The results from the analysis identified isolated areas near the base of the dam where the computed SFOS was less than the minimum allowable limit. However, due to the interaction of adjacent areas, the overall safety of the dam was considered to be adequate against sliding for the usual winter loading condition.

6.1.5 Unusual Load, UNLC-1 (PMF Condition)

The results from the structural analysis for the unusual loading condition, including winter temperatures and the probable maximum flood (PMF), are similar to those for load USLC-3. Similarly, the results indicate that some cracking of the concrete may develop. The structural model was modified to simulate the cracked state, and the results show that the dam has adequate safety against overstressing for the assumed unusual loading condition

The results from the stability analysis indicate that the overall factor of safety for the dam will be greater than the minimum required values; therefore, the dam is considered to have adequate safety against sliding for the unusual PMF loading condition.

6.1.6 Extreme Load, EXLC-1 (Seismic condition)

The seismic analysis of the dam was performed using a non-linear full transient method of analysis. The dam/reservoir interaction was simulated using the generalized Westergaard's Theory for added mass.

The analysis evaluated the stress results at the selected times when the maximum stresses develop in the dam. The results from the extreme loading condition indicated that all stresses in the dam were less than the allowable seismic strength of the concrete. Based on these studies, the dam is considered to have adequate safety against overstressing for the maximum design earthquake (MDE) event.

The evaluation of the results indicates that the arch in the dam will maintain continuity during the seismic load, therefore, the dam will not develop any free cantilevers during the earthquake load. Therefore, the structure will have adequate integrity to support the seismic load, and the post earthquake static load that may develop.

The results from the stability analysis indicate that the overall factor of safety for the dam will be greater than the minimum required values; therefore, the dam is considered to have adequate safety against sliding for the extreme seismic loading condition.

6.2 ABUTMENT STABILITY

The primary and secondary joint sets were plotted on a stereo net. The results from the stereo net was that there are no rock blocks at could kinematically release from the right or left abutments. Therefore the abutments of Trout Lake Dam are considered to have adequate stability for the loading conditions presented in this report.

6.3 ERODIBILITY ANALYSIS

The erodibility analysis utilized both the Erodibility Index Method to evaluate the potential for rock scour at the dam.

The results from the Erodibility Index Method of analysis indicated that the stream power of the overtopping jet is less than the Erodibility Index of the abutment rock. Therefore Trout Lake Dam is considered to have adequate safety against rock scour for the PMF overtopping condition.

[1] Willis T. Batcheller, Inc. Consulting Enineers, *"Specifications for a Masonry Dam, Town of Friday Harbor, Washington"*, October 1928

[2] 1958 Specifications

[3] U.S. Department of the Interior, Bureau of Reclamation, "*Properties of Mass Concrete in Bureau of Reclamation Dams"*, Denver, 1961.

[4] FERC Guidelines. Federal Energy Regulatory Commission, Office of Hydropower Licensing, *"Engineering Guidelines for the Evaluation of Hydropower Projects"*, Washington, D.C., October 1999, Chapter 11-Arch Dams.

[5] American Concrete Institute, *"Building Code Requirements for Reinforced Concrete (ACI 318-08)"*, 2008.

[6] U.S. Department of the Interior, Bureau of Reclamation, Engineering Monograph No. 19, "*Design Criteria for Concrete Arch and Gravity Dams"*, Denver: GPO, 1977.

[7] Washington State Department of Ecology, *"Periodic Dam Safety Inspection Report"*, Olympia, 1993.

[8] KCM, Incorporated, *"Trout Lake Dam Improvement Feasibility Study"*, Seattle, 1997.

[9] U.S. Department of the Interior, Bureau of Reclamation, *"Rock Mechanics Properties of Typical Foundation Rocks Types"*, REC-ERC-74-10, Denver, GPO, 1974.

[10] Hueze, F.E., *"Scale Effects in the Determination of Rock Mass Strength and Deformability"*, Rock Mechanics, Volume 12, 1980.

[11] Hoek, Evert, *"Rock Engineering"*, (notes prepared by Dr. Hoek for use in his civil and mining engineering courses), http://www.rocscience.com/hoek/PracticalRockEngineering.asp, 2000

[12] U.S. Department of the Interior, Bureau of Reclamation, Engineering Monograph No. 34, *"Control of Cracking in Mass Concrete Structures"*, Denver, GPO, 1981.

[13] Water Resource Program, Dam Safety Office, *"Hydrology Update"*, (calculations performed by Bruce Barker for the March 1993 Periodic Inspection report and reviewed by Doug Johnson on February 18, 2009)

[14] Westergaard, H.W., Paper, American Society of Civil Engineers, *"Water Pressures on Dams During Earthquakes"*, 1932.

[15] U.S. Committee on Large Dams, "*Updated Guidelines for Selected Parameters of Dam Projects*", 1998 50 pages plus 2 appendices.

[16] Email from Jerald LaVassar, Subject: Seismic ground motions at Trout Lake Dam Friday Harbor Washington, April 20, 2009

[17] Annandale, George, D.Eng., P.E, *"Scour of Rock Downstream of Dams: An Overview of Current Technology,"* ASDSO Annual Dam Safety Conference, September 2004

Appendix A

Foundation Strength Computations

EXHIBIT 4.7-2

CALCULATION COVER SHEET

Client: Town of Friday Harbor

Project Name: Trout Lake Dam

Project/Calculation Number: 22240846

Title: Foundation Materials Strengths/Parameters

Total Number of Pages (including cover sheet): 5 and appendix A

Total Number of Computer Runs:

Prepared By: Damien Gonsman **Date:** 3/10/09

Checked By: Chad Gillan **Date:** 3/11/09

Description and Purpose
The purpose of this calculation package is to develop estimates of rock foundation material strengths/parameters.

Design Basis/References/Assumptions

1. Hoek, E. & J. W. Bray, Rock Slope Engineering, Institution of Mining and Metallurgy, London, 1996
2. Hoek, E. & J. W. Bray, Underground Excavations in Rock, Institution of Mining and Metallurgy, London, 1982.
3. U.S. Depatment of the Interior, Bureau of Reclamation, Rock Mechanic Properties of Typical Foundation Rock Types, REC-ERC-74-10, Denver, 1974.
4. Goodman, Richard E., Introduction to Rock Mechanics, John Wiley & Sons, 1980.
5. U.S. Bureau of Reclamation, Physical Properties of some Typical Foundation Rocks, Concrete Laboratory Report No. SP-39, August 1953.
6. Hueze, F.E., "Scale Effects in the Determination of Rock Mass Strength and Deformability", Rock Mechanics, Volume 12, 1980.
7. Bieniawski, Z.T., Engineering Rock Mass Classifications, 1989.
8. Barton, N.R. and Choubey, V., "The Shear Strength of rock Joints in theory and practice", Rock Mech. 10 (1-2), 1977.
9. Bieniawski, Z.T., "The Point load Test in Geotechnical Practice", Engineering Geology (9) 1-11, 1974.
10. Bieniawski, Z.T., "The Point load Test in Geotechnical Practice", Engineering Geology (9) 1-11, 1974.
11. Terrametrics Instruction Manual for Terrametrics Point Load Tester Model No. T-500, copyright 1984.

Remarks/Conclusions/Results See attached pages and Appendix A

Calculation Approved By:

Project Manager/Date

Revision No.: Revision Description: Approved By:

Project Manager/Date

SUMMARY OF MATERIALS

REVIEW DOCUMENTS

1. Geologic Map of the Washington Portion of the Roche Harbor 1:100,000 Quadrangle, by Robert L. Logan, dated 2003.

2. Geologic Map of Washington State, prepared by Eric Schuster, dated 2005.

3. Periodic Dam Safety Inspection Report for Trout Lake Dam, prepared by the Department of Ecology, Water Resources Program, Dam Safety Section, dated March 1993.

Based on our review of the documents listed above the following conclusions and assumptions have been made regarding the foundation bedrock material at Trout Lake Dam:

- Samples of rock were collected at the Trout Lake Dam Site and are characterized as strong, slightly weathered, slightly altered, extrusive igneous rocks with a fine grained, dark blue-gray groundmass with 3 mm pyroxene phenocrysts and minor amounts of quarts, olivine and biotite. The rock has vesicles that are just barley visible without magnification. The rock is classified as a metavolcanic rock with chemical composition between andesite and basalt.

- URS reviewed of the *Geologic Map of the Washington Portion of the Roche Harbor (Review Doc. No. 1)*. Based on our review, the Trout Lake Dam Site is mapped as marine metasedimentary rocks consisting of metamorphosed sandstone, argillite, mudstone and conglomerate. The map indicates that metavolcanic rocks are located west of the dam site and consist of basalt, breccia, tuff and chert.

- URS also reviewed the Periodic Dam Safety Inspection Report for Trout Lake Dam dated March 1993 (*Review Doc. No. 3*). This report indicated that the dam site is located on volcaniclastic sandstone and metabasalt or greenstone of the Constitution Formation. Joints and fractures are reported to be closed with no significant infilling material. Primary discontinuity spacing is reported to be between 20 and 40 feet with a secondary set of discontinuities spaced at 29 feet.

FOUNDATION PARAMETERS

Compressive Strength (Fr):

URS performed Point Load Testing using a Terrametrics Point Load Tester Model No. T-500 on 10 samples of rock collected from the Trout Lake Dam site to aid in estimating the Uniaxial Unconfined Compressive Strength of the rock. Samples of rock material were prepared by trimming rocks to the appropriate dimensions for testing with the Terrametrics Point Load Tester. Sample dimension ranged from 39 to 65 mm tall by 35 to 62 wide. Point Load Testing was performed in general accordance with the procedures shown on the Terrametrics Instruction Manual.

The data collected from the point load testing and calculation are shown on Appendix A, Table 1. Failure of Sample No. 8 was not consistent was acceptable failure modes as described in the Terrametrics Instruction Manual and therefore was excluded.

Uniaxial Compressive Strength (UCS) was calculated following the procedures listed in the Terrametrics Instruction Manual and in general accordance with ASTM D 5731-08, Standard Test Method for Determination for the Point Load Strength Index of Rock and Application to Rock Strength Classifications. The following general equation was used to estimate UCS:

$\sigma = K * I_s$ where σ = Uniaxial Compressive Strength (UCS)
K = Index to Strength Conversion Factor
I_s = Point Load Strength Index

Index to Strength Conversion Factor (K) was taken from *The Point load Test in Geotechnical Practice, Engineering Geology (9) 1-11*, by Bieniawski, 1974 (Reference No. 9)

A summary of Point load test results is shown on the following table and indicate compressive strengths for rock material at the Trout Lake Dam Site range from 16,755 pounds per square inch (psi) (Sample No. 6) to 7,793 psi (Sample No. 4) using the Terrametrics procedures for correlating Point Load Testing to UCS. UCS ranges from 13,551 psi (Samples No. 6) to 6,417 psi (Sample No. 4) using ASTM procedures for correlating Point Load Tests to UCS.

Average UCS of 11,298 psi and 8,918 psi were calculated using the Terrametrics and ASTM procedures; respectively. The average UCS of the rock material using both test procedures is 10,108 psi. URS estimates that 10,100 psi is a conservative uniaxial compressive strength of the rock material at the Trout Lake Dam Site.

Summary of Estimated Unconfined Compressive Strength (UCS)

Sample No.	Estimated UCS (psi) Terrametrics Method	Estimated UCS (psi) ASTM Method
1	9557	6824
2	12290	9009
3	11208	9683
4	7793	6417
5	11763	10265
6	16755	8553
7	15337	13551
8	0	0
9	8456	7590
10	8528	8372
Average	11298	8918

Fr = (11298+8918)/2

Fr = 10,108 psi

Use Fr = 10,100 psi

Intact Modulus of Deformation (Ef):

Based on the results of point load testing, UCS estimates and rock descriptions, the rock at Trout Lake Dam Site is similar to Group B Basalt that was tested and reported in the *Engineering and Research Center, Bureau of Reclamation, Rock Mechanic Properties of Typical Foundation Rock Types,* dated July 1974 (page 23) (Reference No. 3). The rock at Trout Lake Dam is slightly altered, slightly weathered and vesicles are approximately 0.1 mm diameter. The chemical composition of the rock is intermediate between basalt and andesite and has similar compressive strengths as fresh, vesicular basalt. The reported laboratory Intact Modulus (Ef) ranges from $4.8\text{x}10^6$ psi to $6.3\text{x}10^6$ psi.

Ef = $4.8\text{x}10^6$ psi to $6.3\text{x}10^6$ psi pounds per square inch (psi) Reference 3, page 23

Use the average of values $4.8 \text{ x}10^6$, $5.4 \text{ x}10^6$, $5.9 \text{ x}10^6$, $6.3 \text{ x}10^6$

$Ef_{avg} = 5.6 \text{ x}10^6$ psi

InSitu Modulus of Deformation (Efi):

URS reviewed the article *Scale Effects in the Determination of Rock Mass Strength and Deformability, Rock Mechanics, Volume 12,* by F.E. Hueze, dated *1980 (Reference No. 6).* Based on our review the in-situ modulus (E_i) of deformation can range from 20 to 60 percent of the intact laboratory modulus (E). The metavolcanic rock at the site is slightly weathered, slightly altered with small vesicles (0.1mm dia) and discontinuities spaced 20 to 40 feet apart, with no significant aperture or infilling material. Our observations indicate that in-situ modulus may be close to the upper limits of values reported by Hueze, 1980. We estimate in-situ modulus: $E_i = (0.5)(E)$.

Efi = Ef(0.5)

Ef = 5.6×10^6 psi

Efi = $(5.6 \times 10^6)(0.5)$

Efi = 2.8×10^6 psi

Poisson's Ration (Ec):

Laboratory values for Poisson's ratio (E_c) are reported in Reference No. 3. E_c values ranged from 0.11 to 0.16. URS estimates that the average of reported values is representative of the rock at the Trout Lake Dam Site.

Ec = 0.11 to 0.16 <u>Reference 3</u>, page 23

Use the average of values 0.11, 0.13, 0.15, 0.16

$Ec_{avg} = 0.14$

APPENDIX A

TROUT LAKE DAM POINT LOAD TEST RESULTS AND ESTIMATED UNCONFINED COMPRESSIVE STRENGTH (UCS)

Sample No.	Distance between Compressive Points, D (mm)	Maximum Width of Sample, L (mm)	Cross Sectional Area*, A (mm^2)	Cross Sectional Area*, A (in^2)	Equivalent Core Diameter, D_e^2 (mm^2)	Equivalent Core Diameter, D_e^2 (in^2)	Sample Diameter, D^2 (inches)	Piston Area, A_p (in^2)	Load at Failure, L_f (psi from Gauge)
	(measured)	*(measured)*	*(D*L)*	*(D*L)*	*(4*A)/PI*	*(4*A)/PI*	*(D^2)*	*(from Terrametrics)*	*(measured)*
1	50.00	55.00	2750.00	4.26	3501.41	5.43	3.88	5.00	325.00
2	42.00	45.00	1890.00	2.93	2406.42	3.73	2.73	5.00	315.00
3	44.00	40.00	1760.00	2.73	2240.90	3.47	3.00	5.00	310.00
4	65.00	62.00	4030.00	6.25	5131.16	7.95	6.55	5.00	400.00
5	50.00	45.00	2250.00	3.49	2864.79	4.44	3.88	5.00	400.00
6	39.00	60.00	2340.00	3.63	2979.38	4.62	2.36	5.00	380.00
7	45.00	40.00	1800.00	2.79	2291.83	3.55	3.14	5.00	440.00
~~8~~	~~40.00~~	~~35.00~~	~~1400.00~~	~~2.17~~	~~1782.54~~	~~2.76~~	~~2.48~~	~~5.00~~	~~0.00~~
9	40.00	35.00	1400.00	2.17	1782.54	2.76	2.48	5.00	200.00
10	50.00	40.00	2000.00	3.10	2546.48	3.95	3.88	5.00	290.00

Sample No.	Force at failure, F_f (lbs)	Force at failure, F_f (N)	Index to Strength Conversion Factor **(K)**	I_{s50} Correction Factor **(F)**	Uncorrected I_s (ASTM) (MPa)	Uncorrected I_s (Terrametrics) (psi)	Corrected I_{s50} (ASTM) (MPa)	**Estimated UCS (Terrametrics) (psi)**	**Estimated UCS (ASTM) (MPa)**	**Estimated UCS (ASTM) (psi)**
	(A_p*L_f)	(A_p*L_f)	*(from Reference No. 9)*	*$(D_e^2/50)^2$ (inches)*	(F_f/D_e^2)	(F_f/D^2)	(I_s*F)	(I_s*K)	(I_s*K)	(I_s*K)
1	1625.00	7228.36	22.79	0.37	2.06	419.35	0.76	9557.46	47.05	6824.01
2	1575.00	7005.95	21.34	0.31	2.91	576.04	0.91	12290.51	62.12	9009.41
3	1550.00	6894.74	21.70	0.30	3.08	516.53	0.93	11208.66	66.77	9683.58
4	2000.00	8896.44	25.52	0.44	1.73	305.40	0.76	7793.28	44.24	6417.00
5	2000.00	8896.44	22.79	0.34	3.11	516.13	1.04	11763.03	70.78	10265.18
6	1900.00	8451.62	20.79	0.34	2.84	805.92	0.97	16755.81	58.98	8553.99
7	2200.00	9786.09	21.88	0.30	4.27	700.91	1.30	15337.29	93.44	13551.61
~~8~~	~~0.00~~	~~0.00~~	~~20.97~~	~~0.27~~	~~0.00~~	~~0.00~~	~~0.00~~	~~0.00~~	~~0.00~~	~~0.00~~
9	1000.00	4448.22	20.97	0.27	2.50	403.23	0.68	8456.73	52.34	7590.74
10	1450.00	6449.92	22.79	0.32	2.53	374.19	0.81	8528.19	57.73	8372.53
Average	1700.00	7561.98	22.29	0.33	2.78	513.08	0.91	**11298.99**	61.49	**8918.67**

Combined average estimated UCS (psi)	**10108.83**

* Note: Cross Sectional Area (A) for Point Load Test is represented by a plane made by the distance between compressive points (D) and the maximum width of the sample (L)

Appendix B

Site-Specific Seismic Hazard Evaluation

F I N A L   R E P O R T

SITE-SPECIFIC SEISMIC HAZARD EVALUATION AND DEVELOPMENT OF SEISMIC EVALUATION EARTHQUAKE GROUND MOTIONS FOR TROUT LAKE DAM, SAN JUAN, WASHINGTON

Prepared for the
Town of Friday Harbor

8 January 2010

Prepared by

URS

Ivan Wong, Judith Zachariasen, Mark Dober, Laura Hansen, and Susan Olig
URS Corporation
Seismic Hazards Group
1333 Broadway, Suite 800
Oakland, California 94612

Job No. 22240846

TABLE OF CONTENTS

Tables

TABLE OF CONTENTS

Figures

At the request of the Town of Friday Harbor, Washington, a site-specific seismic hazard analysis has been performed and Seismic Evaluation Earthquake (SEE) ground motions have been developed as part of the Trout Lake Dam Stability Analysis (Figure 1). The seismic hazard evaluation incorporates recent information on seismic sources in the Puget Sound region and recently developed ground motion attenuation relationships for crustal earthquakes in tectonically active regions. The objective of this analysis is to estimate the levels of ground motions that could be exceeded at specified annual frequencies (or return periods) at the damsite by performing a probabilistic seismic hazard analysis (PSHA).

Trout Lake Dam is a thin concrete arch dam originally constructed in 1928, and raised in 1958. It has a structural height of 36 ft, crest length of 141 ft and radius of 60 ft. The thickness of the dam reportedly is 3.25 ft at the base, and 2 ft at the crest. The downstream toe of the dam was backfilled in 1958 to buttress the older dam and control seepage. The backfill height is 17 ft. Trout Lake Dam has recently been reclassified as a HIGH hazard class 1C structure by the Washington Department of Ecology, Dam Safety Office (DSO). As a result of the revised hazard classification, the dam is required to have a structural analysis performed, as mandated by the State.

In this PSHA, we used readily available geologic, geodetic and seismologic data to evaluate and characterize potential seismic sources, the likelihood of earthquakes of various magnitudes occurring on those sources, and the likelihood of the earthquakes producing ground motions over a specified level. The site is located in the seismically active Puget Sound region of northwest Washington, within the forearc region of the Cascadia subduction zone (CSZ) (Figures 2 and 3). The site will be subjected to strong ground shaking generated by future large events on numerous active faults within the region and the CSZ. Despite years of geologic, geophysical, and seismologic research, there are still significant uncertainties in the characterization of seismic sources in northwest Washington. Thus, the use of a PSHA is ideal for incorporating uncertainties into estimation of the hazard at the Trout Lake damsite.

The PSHA methodology used in this study allows for the explicit inclusion of the range of possible interpretations in components of the seismic hazard model, including seismic source characterization and ground motion estimation. Uncertainties in models and parameters are incorporated into the PSHA through the use of logic trees (Figure 4). Two important state-of-the-science aspects of this PSHA are: (1) the use of the recently published Pacific Earthquake Engineering Research (PEER) Center's Next Generation of Attenuation (NGA) relationships; and (2) incorporation of recently acquired geodetic data within the region. The following describes the methodology used, the seismic source characterization, the ground motion attenuation relationships used, the PSHA results for the site, and the development of SEE ground motion parameters.

1.1 SCOPE OF WORK

The following describes the scope of work of this study.

Task 1 – Seismic Source Characterization

We identified and characterized the seismic source parameters for all local and regional faults in the Puget Sound region that may be significant to the site in terms of ground shaking hazard. These fault parameters include geometry and rupture dimensions, maximum earthquake, nature and amount of slip for the maximum earthquake, and rate and nature of earthquake recurrence. The CSZ, both the megathrust and the Wadati-Benioff zone sources, and background crustal seismicity also were characterized for the hazard analysis.

Task 2 – Input for Ground Motion Predictive Models

Historical seismicity was evaluated in the vicinity of the site based on a historical catalog compiled for the site region. Historical ground shaking at the site from past events was evaluated. Recurrence rates of the historical seismicity for defined seismotectonic provinces were calculated for input into the PSHA.

Task 3– Selection of Attenuation Models

State-of-the-science attenuation relationships were selected for the three types of seismic sources considered in the PSHA: CSZ megathrust and intraslab, and crustal faults. The recently released PEER NGA relationships for crustal earthquakes and recent models for subduction zones were reviewed and selected for use in the PSHA.

Task 4 – Probabilistic Seismic Hazard Analysis

Based on our seismic source model for the region and attenuation relationships, site-specific ground motions for a specified probability of exceedance or return period, in this case 3,000 years, were calculated. The hazard was calculated for a hard rock site condition. A horizontal uniform hazard spectrum (UHS) at 5% damping was calculated. The hazard was deaggregated at 0.2 and 1.0 sec to characterize the controlling earthquakes.

Task 5 – Development of Time Histories

Based on the results of the PSHA, a single set of time histories was developed by spectral matching.

Task 6 – Final Report

The approach and results of all tasks were described and summarized in the draft report. The report was peer reviewed and the resulting review comments were addressed in the final report.

1.2 ACKNOWLEDGMENTS

This evaluation of Trout Lake Dam was performed by the following personnel of the Seismic Hazards Group of URS Corporation:

Seismic Source Characterization	Judith Zachariasen, Susan Olig, and Ivan Wong
PSHA	Mark Dober and Ivan Wong
SEE Ground Motion Development	Ivan Wong and Laura Hansen
Report Preparation	Ivan Wong, Judith Zachariasen, and Mark Dober

Our thanks to Guy Lund, URS Project Manager and Chad Gillan, Task Manager. Our appreciation to Melinda Lee and Fabia Terra for their assistance in the preparation of this report and to Keith Knudsen for his review of the report.

The following is a description of the PSHA methodology used in this study. The inputs to the PSHA are described in Section 3. The PSHA approach used in this study is based on the model developed principally by Cornell (1968). The occurrence of earthquakes on a fault is assumed to be a Poisson process. The Poisson model is widely used and is a reasonable assumption in regions where data are sufficient to provide only an estimate of average recurrence rate (Cornell, 1968). When there are sufficient data to permit a real-time estimate of the occurrence of earthquakes, the probability of exceeding a given value can be modeled as an equivalent Poisson process in which a variable average recurrence rate is assumed. The occurrence of ground motions at the site in excess of a specified level is also a Poisson process if (1) the occurrence of earthquakes is a Poisson process, and (2) the probability that any one event will result in ground motions at the site in excess of a specified level is independent of the occurrence of other events. The probability that a ground motion parameter "Z" exceeds a specified value "z" in a time period "t" is given by:

$$p(Z > z) = 1 - e^{-\nu(z) \bullet t} \tag{1}$$

where $\nu(z)$ is the annual mean number (or rate) of events in which Z exceeds z. It should be noted that the assumption of a Poisson process for the number of events is not critical. This is because the mean number of events in time t, $\nu(z) \bullet t$, can be shown to be a close upper bound on the probability $p(Z > z)$ for small probabilities (less than 0.10) that generally are of interest for engineering applications. The annual mean number of events is obtained by summing the contributions from all sources, that is:

$$\nu(z) = \sum_{n} \nu_n(z) \tag{2}$$

where $\nu_n(z)$ is the annual mean number (or rate) of events on source n for which Z exceeds z at the site. The parameter $\nu_n(z)$ is given by the expression:

$$\nu_n(z) = \sum_{i}\sum_{j} ß_n(m_i) \bullet p(R=r_j|m_i) \bullet p(Z>z|m_i,r_j) \tag{3}$$

where:

$ß_n(m_i)$ = annual mean rate of recurrence of earthquakes of magnitude increment m_i on source n;

$p(R=r_j|m_i)$ = probability that given the occurrence of an earthquake of magnitude m_i on source n, r_j is the closest distance increment from the rupture surface to the site;

$p(Z > z|m_i,r_j)$ = probability that given an earthquake of magnitude m_i at a distance of r_j, the ground motion exceeds the specified level z.

The calculations were made using the computer program HAZ38 developed by Norm Abrahamson. The program has been validated in the Pacific Earthquake Engineering Research (PEER) Center's "Validation of PSHA Computer Programs" Project (Wong *et al.*, 2004) and qualified for use by the U.S. Department of Energy.

2.1 SEISMIC SOURCE CHARACTERIZATION

Two types of earthquake sources are characterized in this seismic hazard analysis: (1) fault sources and (2) areal source zones. Fault sources are modeled as three-dimensional fault surfaces, and details of their behavior are incorporated into the source characterization. An areal source zone (actually volumetric in dimensions) is where earthquakes are assumed to occur randomly or the historical seismicity can be assumed to be stationary in space and hence smoothed using a Gaussian filter. Both approaches were used in this PSHA.

The geometric source parameters for faults include fault location, segmentation model, dip, and thickness of the seismogenic zone. The recurrence parameters include recurrence model, recurrence rate (slip rate or average recurrence interval for the maximum event), slope of the recurrence curve (*b*-value), and maximum magnitude. Clearly, the geometry and recurrence are not totally independent. For example, if a fault is modeled with several small segments instead of large segments, the maximum magnitude is lower, and a given slip rate requires many more small earthquakes to accommodate a cumulative seismic moment.

Uncertainties in the source parameters are included in the hazard model using logic trees (e.g., Figure 4). In the logic tree approach, discrete values of the source input parameters are included along with our estimate of the likelihood that the discrete value represents the actual value. In this PSHA, generally all input parameters are represented by three values; the values represent a distribution about our best estimate.

2.1.1 Source Geometry

In the PSHA, earthquakes may occur randomly along the length of a given fault or segment. The distance from an earthquake to the site is dependent on the source geometry, the size and shape of the rupture on the fault plane, and the likelihood of the earthquake occurring at different points along the fault length. The distance to the fault is defined to be consistent with the specific attenuation relationship used to calculate the ground motions. The distance, therefore, is dependent on both the dip and depth of the fault plane, and a separate distance function is calculated for each geometry and each attenuation relationship. The size and shape of the rupture on the fault plane are dependent on the magnitude of the earthquake, with larger events rupturing longer and wider portions of the fault plane. For a given magnitude, the associated rupture surface is uniformly distributed along the fault length and width. Ruptures are constrained to occur entirely on the defined fault plane. We modeled the rupture dimensions following the magnitude-rupture area and magnitude-rupture width relationships of Wells and Coppersmith (1994).

2.1.2 Fault Recurrence

The recurrence relationships for the faults are modeled using the characteristic earthquake, maximum moment and exponentially truncated Gutenberg-Richter recurrence models. These models are weighted to represent our judgment on their applicability to the sources. For areal source zones, only the truncated exponential recurrence relationship is considered appropriate.

We use a model in which the faults rupture with a "characteristic" magnitude on specific segments; this model is described by Aki (1983) and Schwartz and Coppersmith (1984). For the characteristic model, we use the numerical model of Youngs and Coppersmith (1985). In the characteristic model, the number of events exceeding a given magnitude is the sum of the characteristic events and the non-characteristic events. The characteristic events are distributed uniformly over ± 0.25 magnitude units around the characteristic magnitude and the remainder of the moment rate is distributed exponentially with a maximum magnitude one unit lower than the characteristic magnitude (Youngs and Coppersmith, 1985).

The maximum moment model can be regarded as an extreme version of the characteristic model. We adopted the maximum moment model proposed by Wesnousky (1986), in which there is no exponential portion of the recurrence curve, i.e., no events can occur between the minimum magnitude of **M** 5.0 and the distribution (normal) about the maximum magnitude.

We have used the general approach of Molnar (1979) and Anderson (1979) to arrive at the recurrence for the truncated exponential model. The number of events exceeding a given magnitude, *N(m)*, for the truncated exponential relationship is

$$N(m) = \alpha(m^o)\frac{10^{-b(m-m^o)} - 10^{-b(m^u-m^o)}}{1 - 10^{-b(m^u-m^o)}} \tag{4}$$

where $\alpha(m^o)$ is the annual frequency of occurrence of earthquakes greater than the minimum magnitude, m^o; b is the Gutenberg-Richter parameter defining the slope of the recurrence curve; and m^u is the upper-bound magnitude event that can occur on the source. An m^o of moment magnitude (**M**) 5 was used for the hazard calculations because smaller events are not considered likely to produce ground motions with sufficient energy to damage well-designed structures.

It should be noted that when reference is made to "maximum" magnitude in this report, we are referring to the "maximum characteristic" magnitude. The magnitudes estimated for the seismic sources summarized in Table 1 are maximum characteristic magnitudes, that is, they represent the peak in the distributions for the various recurrence models.

The recurrence rates for the fault sources are defined by either the slip rate or the average return time for the maximum or characteristic event and the recurrence *b*-value. The slip rate is used to calculate the moment rate on the fault using the following equation defining the seismic moment:

$$M_o = \mu \, A \, D \tag{5}$$

where M_o is the seismic moment, μ is the shear modulus, A is the area of the rupture plane, and D is the slip on the plane. Dividing both sides of the equation by time results in the moment rate as a function of slip rate:

$$\dot{M}_o = \mu \, A \, S \tag{6}$$

where $\dot{M}_o$ is the moment rate and S is the slip rate. M_o has been related to **M** by Hanks and Kanamori (1979):

$$\mathbf{M} = 2/3 \log M_o - 10.7 \tag{7}$$

Using this relationship and the relative frequency of different magnitude events from the recurrence model, the slip rate can be used to estimate the absolute frequency of different magnitude events.

The average return time for the characteristic or maximum magnitude event defines the high magnitude (low likelihood) end of the recurrence curve. Combining this with the relative frequency of different magnitude events from the recurrence model establishes the recurrence curve.

2.2 GROUND MOTION CHARACTERIZATION

To characterize the ground motions at the site in the PSHA, we use several state-of-the-art empirical attenuation relationships for response spectral acceleration. The relationships used in this study were selected on the basis of the appropriateness of the site conditions and tectonic environment for which they were developed.

We included the uncertainty in ground motion attenuation in the PSHA by using the log-normal distribution about the median values as defined by the standard error associated with each attenuation relationship. Three standard deviations about the median value are included in the analysis.

The Puget Lowland region in which the site is located overlies a complex crustal boundary between the Eocene basement rocks of the Coast Range to the west and the pre-Tertiary rocks of the Cascade province to the east (Pratt *et al.*, 1997). Seismic reflection data has illuminated the concealed structure of the Puget Lowlands and suggests that this region is undergoing shortening. This shortening is visible in basin formation, folding, and reverse faulting along essentially east-west-trending structures. Johnson *et al.* (1994) suggest that the Puget Lowland may actually be located within a restraining left-bend between two north-trending dextral-slip faults. The basement rocks beneath the Puget Lowland consist of the Crescent Formation. There are basins in the Puget Lowland region that are defined by large negative gravity anomalies, such as the Seattle and Tacoma basins (Blakely *et al.*, 1999; Pratt *et al.*, 1997). Within the Seattle basin, the Crescent Formation is overlain by upper Eocene marine sediments, deep marine turbidites, non-marine Miocene sediments, and Quaternary deposits (Pratt *et al.*, 1997). Much of the surficial expression of the Puget Lowland reflects the effects of Pleistocene glaciation in the region, and surficial deposits largely consist of thick packets of glacial sediments (Pratt *et al.*, 1997).

Beneath the Puget Lowlands and most of the coastal Pacific Northwest is the CSZ, created by the northeastward subduction of the oceanic Juan de Fuca plate beneath the continental North American plate (Figures 5 and 6). The CSZ accommodates approximately 75 to 80 percent of the 36 to 50 mm/yr relative motions between the two plates. The CSZ extends about 1,100 km northward from the Mendocino fault off the coast of northern California to the Nootka fault west of central Vancouver Island in British Columbia (Figure 5). It extends inland from the coast approximately 250 to 300 km. McCrory *et al*. (2006) modeled the depth to the top of the subducted Juan de Fuca plate (Figures 5 and 6). Based on their model, the dip of the subducted Juan de Fuca plate increases from about 5 degrees along the western edge of the subduction zone, to about 12 degrees at a depth of 20 km, to about 24 degrees below a depth of 40 to 50 km. The subducted slab is bent beneath the Olympic Mountains and Puget Lowland. The bend results in somewhat shallower dips above a depth of 50 km (Figures 5 and 6).

The historical earthquake record of the Pacific Northwest began in 1820 with the first documented earthquake reported at Mt. Rainier (Coombs *et al.*, 1977). Prominent within this record are the three deep **M** 6.8 Wadati-Benioff earthquakes beneath Puget Sound – the 1949 Olympia, 1965 Seattle-Tacoma, and 2001 Nisqually earthquakes (see below) – and several recent moderate-sized damaging events of **M** 5 to 6 (Figure 2). As in most of the western U.S., the historical record extends back less than 200 years, which is a relatively short period compared to the recurrence intervals of most active crustal faults.

In the 1949 earthquake, the southern Puget Sound was struck by a **M** 6.8 earthquake just before noon on 13 April. The event had its origin at a depth of 54 km beneath an area between Olympia and Tacoma (Baker and Langston, 1987). The earthquake caused eight deaths and numerous injuries, and $150 billion (1984 dollars) in damage (Noson *et al.*, 1988). Like the 1949 and 1965 events, the impact of the 53-km-deep 2001 **M** 6.8 Nisqually earthquake was somewhat minimized because of its great depth.

Other significant earthquakes in the Puget Sound region include the 12 November 1939 **M** 5.75 event, which was felt at a maximum intensity of Modified Mercalli (MM) VII, and the 14 February 1946 **M** 6.3 event (MM VII), both of which occurred in the southern Puget Sound

(Figure 2). The latter earthquake caused damage in Seattle, Tacoma, and Olympia (Noson *et al.*, 1988).

The closest earthquake of **M** 5.0 and greater to the site occurred on 24 January 1920, **M** 5.5 about 10 km northeast of the damsite. Three other **M** ≥ 5.0 occurred within 50 km of the damsite, in 1864, 1909, and 1976.

The following section describes the characterization of the seismic sources considered in the PSHA, and the empirical ground motion attenuation relationships selected and used.

4.1 SEISMIC SOURCES

In this study, we considered known seismic sources that could potentially generate strong ground shaking at the site. Seismic source characterization is concerned with three fundamental elements: (1) the identification of significant sources of earthquakes; (2) the maximum size of these earthquakes; and (3) the rate at which they occur. The seismic source model includes: potential earthquakes associated with the CSZ (Section 3.1.1); potential crustal earthquakes generated by active faults within about 100 km of the dam (Section 4.1.2), and areal source zones, which account for background crustal seismicity that cannot be attributed to identified structures explicitly included in the seismic source model (Section 4.1.3). The CSZ Wadati-Benioff zone also was treated as an areal source zone. The seismic source model presented here for the crustal sources was developed as part of a large regional seismic hazard study performed for BC Hydro.

4.1.1 Cascadia Subduction Zone

Two seismic sources are identified in the CSZ, the megathrust and Wadati-Benioff zone (Figure 6). Megathrust earthquakes are generated at the interface between the subducting and overriding plates. There are no historical North American accounts of megathrust earthquakes on the CZS (the exception possibly being the 1992 **M** 7.0 Cape Mendocino, California earthquake; Oppenheimer *et al.*, 1992), but geologic evidence indicate that they occurred at average intervals of about 500 to 600 years in the Holocene (Atwater and Hemphill-Haley, 1997; Goldfinger *et al.*, 2009). Geologic evidence and historical tsunami accounts in Japan indicate that the last CSZ megathrust event occurred in January 1700 AD (Satake *et al.*, 1996). Wadati-Benioff zone, or intraslab earthquakes, occur within the subducting plate (Figure 6) due in part to down-dip tensional forces. Numerous historical Wadati-Benioff zone earthquakes have occurred within the CSZ and have been concentrated in the region of the plate bend beneath the Puget Lowland (Figure 5). Historical **M** 6.5+ intraslab events include the 1949 Olympia, 1965 Seattle-Tacoma, and 2001 Nisqually earthquakes.

For this study we generally adopt the seismic source models for the CSZ megathrust and Wadati-Benioff zone that are described by the U.S. Geological Survey (USGS) in their documentation for the 2008 update of the U.S. National Seismic Hazard Maps (Petersen *et al.*, 2008). These models are described in the following report subsections.

4.1.1.1 Megathrust

The following describes the source characteristics of the megathrust.

Updip and Downdip Extent

The following describes the characterization of the geometry of the CSZ megathrust rupture, its updip, downdip, and lateral extent. In the USGS megathrust model, the updip extent of the seismogenic portion of the CSZ plate interface is identified as the deformation front (weight of 1.0) (Figure 7). Four potential downdip locations are identified with their weights:

- Base of elastic zone or top of transition zone (0.1 weight)
- Midpoint of transition zone (0.2 weight)
- Base of transition zone (0.2 weight)
- Longitude of 123.8 degrees with a bend to the northwest at the plate bend as an approximation of a 20-km-depth-to-subducted-plate contour (0.5 weight)

The locations of the updip and downdip extents are shown on Figure 7.

Updip and downdip extents in the USGS model are based on the work of Flück *et al*. (1997). Flück *et al*. (1997) postulate that the updip extent of the seismogenic portion of the rupture zone would extend up to the deformation front located near the base of the continental slope. Clay minerals that allow aseismic slip are unstable and dehydrate above temperatures of 100°C to 150°C, and these temperatures are exceeded at the deformation front. Flück *et al*. (1997) identify a locked zone on the basis of thermal constraints and GPS measurements that extends from the deformation front, east and downdip about 60 km to a transition zone. The transition zone extends east and downdip about an additional 60 km (Figure 7). Within the transition zone, they postulate that slab temperatures (about 350°C to 450°C) are too great for brittle rupture to initiate; however, coseismic rupture may extend into the transition zone if initiated farther updip in the locked zone.

A relatively low weight (0.1) is given to the seismogenic rupture being confined solely to the locked zone. The remaining weight (0.9) is divided among the three models, which rupture into the transition zone. The highest weight (0.5) in the USGS model is given to the model in which the rupture surface extends from the deformation front, east to latitude of 123.8 degrees. Petersen *et al.* (2008) indicate that this model is based on a 20-km-depth contour to the subducted plate estimated by Hyndman and Wang (1995). We updated the 123.8 degree line using the depth contour of 25 km from the updated slab geometry of McCrory *et al*. (2006) (Figure 5). While the 25 km depth contour is based on updated slab geometry, it corresponds closely with the 123.8 degree line near the latitude of the dams (Figure 7). That depth is postulated by Parsons *et al.* (2005) to be the seismogenic depth limit of CSZ megathrusts.

Maximum Magnitude

Two rupture scenarios are modeled by Petersen *et al.* (2008) with different maximum magnitudes for each scenario. These two rupture scenarios are:

- CSZ ruptures in a single event (0.67 weight)
- CSZ ruptures in multiple events (0.33 weight)

In support of the single-event scenario, the USGS 2008 hazard maps cite work by Satake *et al*. (1996) on an historic tsunami in Japan with a causative earthquake that is thought to be a **M** 9 event from rupture of the entire CSZ length. For the single event scenario, the entire 1100 km fault length would rupture over a width of about 60 km (top of transition zone) to 120 km (base of transition zone) with corresponding fault rupture length-to-width-ratios of 18 (top of transition zone) to 9 (base of transition zone). While these ratios may be relatively high, the ratios and actual dimensions, particularly for the base-of-the-transition-zone model, are comparable to the dimensions of the 2004 **M** 9.2 Sumatra-Andaman subduction zone megathrust earthquake. The fault rupture associated with the 2004 Sumatra-Andaman earthquake was reported to have a length of about 1200 to 1500 km and width of approximately 150 km (Chlieh *et al*., 2007; Henstock *et al*., 2006). These fault dimensions correspond to length-to-width ratios of 8 to 10. M_{max} used in the USGS model for the single-event scenario are **M** 8.8 (0.2 weight), **M** 9.0 (0.6 weight) and **M** 9.2 (0.2 weight).

In support of the multiple-event scenario, the USGS 2008 hazard maps cite work by Nelson *et al.* (2006) who report CSZ-rupture-related tsunami deposits along the southern Oregon coast that do not correspond with known CSZ-rupture evidence in Washington. For the multiple-event scenario, the USGS model consists of eight equally weighted M_{max} between **M** 8.0 to 8.7 (i.e., **M** 8.0, 8.1, 8.2, 8.3, 8.4, 8.5, 8.6, and 8.7).

Earthquake Recurrence and Moment Rate

The primary constraint in the USGS model is that megathrust events occur on average once every 500 years beneath sites on the coast over the CSZ. The cited bases for this constraint are paleoseismic studies of coastal subsidence and tsunami deposits (e.g., Atwater and Hemphill-Haley, 1997). Additional data sources used to estimate recurrence intervals include coastal subsidence and tsunami deposit studies along the southern Oregon coast (i.e., Kelsey *et al*., 2002; Witter *et al*., 2003; Kelsey *et al*., 2005) and offshore turbidite dating studies along the entire CSZ (Goldfinger *et al*., 2009). The average of the recurrence intervals is approximately 540 years. For the single-event scenario in the USGS model, the characteristic recurrence interval is assumed to be 500 years. We use the slightly longer average recurrence interval of 540 years.

To cover the range of reported average recurrence intervals around the overall average of 540 years in a roughly symmetrical manner, we also consider average recurrence intervals of 500 and 600 years. The weights for the 500-, 540-, and 600-year average recurrence intervals are 0.2, 0.6, and 0.2, respectively. We use the same maximum magnitude for the single-event scenario as the USGS (i.e., **M** 8.8 to 0.2 weight; **M** 9.0 to 0.6 weight; and **M** 9.2 to 0.2 weight) and a characteristic maximum magnitude distribution model.

For the multiple-event scenario, the USGS model calculates *a* and *b* values for eight magnitude bins between **M** 8.0 to 8.7 (i.e., **M** 8.0, 8.1, 8.2, 8.3, 8.4, 8.5, 8.6, and 8.7). For a given magnitude bin, the average yields one rupture at any one location on the CSZ in 500 years. The magnitude-rupture length relation for subduction zone earthquakes by Geomatrix Consultants (1995) is used in calculating the *a* and *b* values. The rupture zones for each magnitude scenario are floated along the length of the CSZ at 5 km increments. The *a* and *b* values and corresponding recurrence interval for each magnitude bin calculated by the USGS for the multiple event scenario are provided in Table K-1 in Petersen *et al.* (2008). The recurrence intervals corresponding to the *a* and *b* values for the various magnitude bins range between 78 and 245 years and are apparently much smaller than the estimated average paleoseismic recurrence intervals. Petersen *et al.* (2008) explain that the small recurrence intervals for the multiple event scenario are because the events are treated independently in the PSHA whereas they would likely be clustered in time to explain the similar timing of coastal subsidence events along the CSZ. Each magnitude bin is equally weighted. That is, each magnitude in this scenario has a weight of 0.041, which is one-eighth of the multiple-scenario weighting of 0.33 (1/8 x 0.33 = 0.041).

The seismic moment rate between the single- and multiple-event scenarios may be used as another measure in evaluating the model appropriateness and relative weighting, provided the actual seismic moment rate on the CSZ can be reasonably estimated. The CSZ moment rate has been estimated from recent GPS-based studies and also can be estimated using historical/paleoseismic studies. McCaffrey *et al.* (2007) estimate the moment rate of the subduction zone based on GPS measurements and crustal modeling. They estimate a total moment rate of approximately 1.5 x 10^{20} Nm/yr on the CSZ interface and a reduced moment rate of approximately 1.3 x 10^{20} Nm/yr when subtracting the estimated moment rate associated with "slow" quakes observed since 1997 on the CSZ. For the January 1700 AD CSZ megathrust event, Satake *et al*. (2003) use historical Japanese tsunami data, paleoseismic subsidence and tsunami deposit data along the coast of Washington and Oregon, and three-dimensional elastic dislocation models of the CSZ to calculate a best estimate range of moments between 4.4 to 9.2 x 10^{22} Nm (corresponding **M** are 9.0 and 9.2, respectively) and complete rupture of the entire 1100 km long CSZ. Using an average recurrence interval of 540 years for complete rupture of the CSZ, the moment rates from Satake *et al*. (2003) range between 8.1 x 10^{19} to 1.7 x 10^{20} Nm/yr. The moment rates based on historical and paleoseismic studies bracket and are in relative agreement to the GPS-based moment rate of 1.3 x 10^{20} Nm/yr.

The moment rate for the single-event scenario **M** 8.8 is 3.7 x 10^{19} Nm/yr or about 1/3 of the GPS-based moment rate and about one half of the lower bound of the paleoseismic best-estimate range; the moment rates for the **M** 9.0 and 9.2 are 7.4 x 10^{19} and 1.5 x 10^{20} Nm/yr and are near or within the best-estimate range. The cumulative moment rate for the multiple-event scenario (the sum of the moment rates for each magnitude bin) is 3.3 x 10^{19} Nm/yr, or about ¼ of the GPS-based moment rate and less than half of the lower bound of the paleoseismic best-estimate range. The moment rate for individual magnitude bins in the multiple-event scenario range from 1.6 x 10^{19} (**M** 8.0 bin) to 5.8 x 10^{19} Nm/yr (**M** 8.7 bin) or about 1/10 to ½ of the GPS-based moment rate. In the USGS model, the single-event-scenario moment rate is higher and more closely matches the GPS and historical/paleoseismic moment rates than does the multiple-event scenario. The higher weight (0.67) given to the single-event scenario than the multiple-event scenario (0.33) is consistent with relative differences in the moment rates.

For the multiple event scenario, we only used magnitude bins for which the scenario rate is at least ½ of the lower bound of the paleoseismic best-estimate. Using this criterion, the multiple event magnitude bins of **M** 8.5, **M** 8.6, and **M** 8.7 are used. These three magnitude bins are equally weighted. That is, each magnitude in this scenario has a weight of 0.11, which is one-third of the multiple-scenario weighting of 0.33 (1/3 x 0.33 = 0.11).

4.1.1.2 Wadati-Benioff Zone

In the USGS model, Wadati-Benioff zone earthquakes are modeled by spatially smoothed gridded historical seismicity and areal source zones below a depth of 35 km with a *b* value of 0.4

for the area below the Puget Lowland. The USGS selected a M_{max} of **M** 7.2, slightly greater than generally-quoted M_S 7.1 for the 1949 Olympia earthquake although a more recent analysis indicates that the 1949 was **M** 6.8 in size (Ichinose *et al.*, 2006). It should be noted that all the historical large intraslab earthquakes have been confined to the southern Puget Sound and none have occurred near the site (Figure 2). It has been argued that an east-northeast-striking linear trend called the Nisqually trend represents a tear in the Juan de Fuca plate along its southern margin and that it is the source of the 1949, 1965, and 2001 events (McCrory *et al.*, 2003). Hence the intraslab potential beneath Puget Sound may not be uniform as assumed in the use of an area source (0.5 weight).

We use the updated plate geometry of McCrory *et al*. (2006) (Figure 5). Based on the plate geometry and the observed depth of historical seismicity, the source zone extends to a depth of approximately 100 km.

4.1.2 Crustal Fault Sources

Based on our review of published and unpublished data, we consider the active and potentially active seismogenic faults shown on Figure 3 to be seismic sources significant to the site in terms of strong ground shaking. Each seismic source is characterized using the latest geologic, seismological, and paleoseismic data and the currently accepted models of fault behavior. We include faults that we judge to be at least potentially active and that would potentially contribute to the probabilistic hazard because of their maximum earthquakes and/or proximity to the site.

The faults characterized as sources in the study region are dominantly reverse oblique-slip faults. Faults are generally modeled as single, independent, planar sources, although we modeled some fault sources as a zone with multiple parallel planes within defined zone boundaries. We calculate preferred maximum earthquake magnitudes using empirical relationship of Wells and Coppersmith (1994) and Hanks and Bakun (2002; 2008) between **M** and parameters of rupture dimension, including rupture width and rupture area. Rupture area is calculated from rupture length and width; rupture length estimates are straight line end-to-end distances taken from mapped fault lengths and widths are the down-dip extent of the planar fault.

In assigning probabilities of activity for each fault source, we considered both the likelihood that the structure exists and is capable of independently generating earthquakes (i.e., is seismogenic), and the likelihood that it is still active within the modern stress field. We incorporated many factors in assessing these likelihoods, such as: orientation in the modern stress field, fault geometry (length, continuity, depth extent, and dip), relation to other faults, age of youngest movement, geomorphic expression, amount of cumulative offset, rates of activity, similarity to known active faults, and any evidence for a non-tectonic origin. Faults with definitive evidence for repeated Quaternary activity were generally assigned probabilities of being active and seismogenic of 1.0. Exceptions include faults that may be secondary and dependent on other faults, faults or fault features that may have a non-seismogenic origin, and faults that may be too short ($\leq$ 10 km) to independently generate significant earthquakes. The probability of activity for faults that do not show definitive evidence for repeated Quaternary activity was individually judged based on the available data and the criteria explained above.

Table 1 lists the fault parameters in our seismic source model. The model consists largely of the source parameters developed from published fault studies, along with data compiled in the USGS Quaternary fault and fold database and the 2008 National Seismic Hazard Maps (Petersen *et al.*, 2008). We have added a number of other active or potentially active faults that are not included in the USGS database, including potentially active faults in southwestern British Columbia.

In these analyses, we model all faults as single, independent, planar sources extending the full extent of the seismogenic crust. Thus, fault dips are averages estimated over the seismogenic crust. The seismogenic crust in the forearc region of the CSZ ranges from 20 to 30 km thick, based on contemporary seismicity, modeling of heat flow, and seismic tomography analyses, although local variations are accounted for in the model.

A lack of reliable paleoseismic data means that the recurrence rates for many of the faults within the northern Washington and southern British Columbia region are either poorly understood or unknown. Fault activity for most faults is therefore expressed as an average annual slip rate (in mm/yr) rather than as a recurrence interval. The uncertainty in the slip rates and the other input parameters is accommodated in the probabilistic hazard through the use of logic trees (Figure 4).

Uncertainties in determining recurrence models can significantly impact the hazard analysis. We considered the maximum magnitude, truncated exponential, and characteristic recurrence models. Observations of historical seismicity and paleoseismic investigations along faults in the western U.S. (e.g., San Andreas fault) suggest that characteristic behavior is more likely for individual faults (Schwartz and Coppersmith, 1984). Therefore, for most fault sources, we favored the characteristic model (weight of 0.6), while the maximum-magnitude model was weighted 0.3 and the truncated exponential was weighted 0.1. The source model includes some fault zones, in which faulting is not defined on a particular plane but is nevertheless concentrated within a relatively narrow region. For fault zones, we used a different weighting scheme to reflect the likelihood that faulting distributed through a finite volume is more likely to have exponential characteristics. We still favored the characteristic model (weight of 0.5), but reduced the weight for the maximum moment model (weight of 0.2) and increased the weight on the exponential model to 0.3.

The following describes the most important faults to the site: the Devils Mountain fault, the Leech River fault, the Southern Whidbey Island fault (SWIF), and the little-studied but potentially active faults within the San Juan Islands and Georgia Strait. Parameters for the other fault sources included in the model appear in Table 1.

Devils Mountain fault

The Devils Mountain fault is located in the northern Puget Lowland, and its western end is 17 km from Trout Lake Dam. The east-west-striking Devils Mountain fault extends about 125 km from just east of Vancouver Island, where it strikes into the Leech River and San Juan faults (Figure 3), to the foothills of the Cascades, where it meets the south-east-striking Darrington fault. The fault zone has been active since at least the mid-Eocene and has sustained both transtensional and transpressional movement (Dragovich and DeOme, 2006). Johnson *et al.* (2001a) report that the fault has no geomorphic expression across northern Whidbey Island, but it does appear as a clear lineament in the Cascade foothills. Offshore seismic reflection data suggest the fault has a moderate to steep (about 45 to 75°) north dip, becoming steeper eastward (Johnson *et al.*, 2001a, b).

Johnson *et al.* (2001a, b) infer from offset and fault patterns that the Devils Mountain fault is currently a left-lateral oblique transpressional structure, with the strike-slip component dominant. They interpret the moderate to steep dip that increases eastward and numerous northwest-trending *en echelon* secondary faults and folds as consistent with sinistral oblique motion. Hayward *et al.* (2006) also interpret offshore seismic data to infer that the Devils Mountain fault has been predominantly a left-lateral transpressional structure during the Quaternary although it may have initiated in the Eocene as a reverse-dextral structure.

Dragovich and DeOme (2006) and Dragovich and Stanton (2007) consider, based on geologic mapping on Whidbey Island and the mainland, that the Darrington-Devils Mountain fault is dominantly reverse, with a moderate left-lateral component, and occupies a broad zone comprising multiple faults, with most post-glacial displacement concentrated on a single main strand. They consider the Devils Mountain fault to be a primary structure that flattens with depth into a décollement at about 16 km depth; the Oak Harbor, Utsalady Point and Strawberry Point faults are hanging wall structures that also terminate at the décollement. Although Johnson *et al.* (2001a) do not discuss the geometry of the fault onshore and their offshore data indicate a north dip to the fault, they also argue that the Utsalady Point and Strawberry Point faults are probably subsidiary en echelon structures to a master Devils Mountain fault.

Zollweg and Johnson (1989) analyzed seismicity of the Darrington seismic zone and determined that it delineated a moderately (≥ 40°) south-dipping probably reverse fault in the vicinity of the Devils Mountain fault. Dragovich and DeOme (2006) and Dragovich *et al.* (2003) argue that this and other seismicity is coincident with a moderately south-dipping Devils Mountain fault ramping into the décollement. The USGS Quaternary fault and fold database describes the fault as sinistral, with a reverse component. The 2008 NSHM, however, characterizes the Devils Mountain fault as a 60-degree-north-dipping reverse fault (Petersen *et al.*, 2008).

Hayward *et al.* (2006) propose the existence of a NNE-trending cross or transfer structure at about 122.95° and argue that amount and distribution of both Tertiary and Quaternary offset has varied across this feature. Johnson *et al.* (2001a) indicate that a tear fault in Skagit Bay east of Whidbey Island may represent a segment boundary, and there may be another in the eastern Strait of Juan de Fuca south of southeastern San Juan Island, at approximately 122.95°. If these discontinuities do represent segment boundaries, the segment lengths would be, from west to east: west (25 km), central (30 km), and east (70 km).

There is little displacement or rate information available for the Devils Mountain fault. Johnson *et al.* (2001a) analyzed outcrops exposed at the east edge of Whidbey Island and well-log data to infer about 12 ± 8 m of vertical displacement on the 80 ka Whidbey Island formation, or a rate of about 0.05 to 0.3 mm/yr; these results are consistent with their Quaternary vertical displacement rates obtained from offshore data. Brocher *et al.* (2001) report that structural relief across the fault increases westward. Dragovich and DeOme (2006) and Dragovich and Stanton (2007) report evidence of Holocene displacement on the fault on the mainland, including apparently uplifted Holocene terrace deposits, offset (reverse and strike-slip) of latest Pleistocene lake sediments in Lake Cavanaugh, and apparently faulted 15 ka glacial deposits exposed in a trench. They do not report rate information. Hayward *et al.* (2006) indicate that Quaternary offset on the primary fault of the Devils Mountain fault zone is greater west of about 122.95°W, whereas to the east offset is more broadly distributed.

We favor the interpretation that the Devils Mountain fault is a north-dipping reverse oblique fault. Evidence in favor of a shallow south-dipping décollement remains speculative, and observations of the fault nearest San Juan Island indicate a steep north dip. The ratio of reverse to strike-slip is uncertain, so we consider both reverse-oblique and strike-slip models, weighted 0.3 and 0.7, respectively (Table 1). We include both unsegmented and segmented rupture models, with segment boundaries derived from those proposed by Johnson *et al.* (2001a) and Hayward *et al.* (2006). We have used empirical relationships between fault length and magnitude and between fault area and magnitude from Wells and Coppersmith (1994) and Hanks and Bakun (2002; 2008) to develop a distribution of maximum magnitudes for the fault. The calculated values range from **M** 7.0 to 7.6 for the unsegmented model and **M** 6.8 to 7.3 for the segmented model.

As noted above, the slip rate on this fault is unknown. The 2008 NSHM uses a 0.15 mm/yr vertical displacement rate based on Johnson *et al.* (2001a) as the slip rate (Petersen *et al.*, 2008). We, however, consider this rate inappropriate since it does not include any component of strike-slip on a fault that has been characterized as oblique-slip and perhaps dominantly strike-slip. We have developed a slip rate distribution calculated from the observed vertical displacement rates cited above combined with fault dip and the ratio of horizontal to vertical displacement observed in trenches across the Utsalady Point fault (Table 1); the Utsalady Point fault is subparallel to the Devils Mountain fault and may be part of that system (see discussion above).

Southern Whidbey Island Fault (SWIF)

The SWIF traverses Whidbey Island in the northern Puget Lowland, and its western end is 20 km from Trout Lake Dam (Figure 3). The SWIF extends southeast at least 100 km from Puget Sound between Vancouver and Whidbey Islands, across southern Whidbey Island onto the mainland between Seattle and Everett, where it marks the southern boundary of the Tertiary Everett Basin (Brocher *et al.*, 2001, 2005; Johnson *et al.*, 1996; Ramachandran *et al.*, 2005). Johnson *et al.* (1996) interpret the fault as a segment of the Coast Range boundary fault, a fundamental structural boundary separating the pre-Tertiary rocks of the Cascades block to the north from the Eocene marine rocks of the Crescent terrane to the south, which began as a roughly north-south-striking dextral fault and has been rotated into a NW-SE-striking transpressional fault. Its western extent is uncertain, but Ramachandran *et al.* (2005) propose that it extends to just offshore of Victoria, Vancouver Island and merges with the Devils Mountain fault. Its extension farther southeast on the mainland is also uncertain, but Sherrod *et al.* (2008) propose, based on analysis of aeromagnetic, LiDAR, seismic reflection and field mapping data, that it continues to the southeast along the northern edge of the Seattle Basin to at least Woodinville and may ultimately merge with the Seattle fault zone east of Seattle for a total length of about 150 km.

Linear northwest-trending magnetic anomalies near Everett, WA extend at least 16 km and are on strike with the SWIF in Whidbey Island (Blakely *et al.*, 2004). Several of the anomalies are coincident with largely north-side-up scarps identified in LiDAR and on the ground that crosscut the predominant grain of glacial fluting, suggesting the anomalies may be caused by faulting (Sherrod *et al.*, 2008).

The fault zone comprises two main north-side up faults west of Whidbey Island and becomes progressively wider and more complex southeastwards (Johnson *et al.*, 1996; Sherrod *et al.*, 2008). On South Whidbey Island and in Possession Sound east of the island, it includes three strands across a 7-km-wide zone. On the mainland, the fault zone comprises numerous anastomozing, predominantly north-side up strands distributed across a zone as much as 20 km wide (Sherrod *et al.*, 2008). According to Sherrod *et al.* (2008), there are at least three active traces corresponding to three aeromagnetic lineaments in this area.

The sense of slip on the SWIF also is uncertain. The fault shows evidence of oblique slip with predominantly north-side up displacement, although it bounds the south side of the deep Everett Basin. It also bounds the north sides of the Port Townsend and Seattle basins, northwest and south of the Everett basin, respectively, suggesting variable along-strike kinematics. Johnson *et al.* (1996) analyzed seismic reflection, outcrop and borehole data and proposed that the SWIF is a steeply north-dipping transpressional fault with north-side-up reverse movement. They had no data supporting the direction of recent lateral slip, but inferred dextral shear based on their interpretation of the fault as a formerly dextral strike-slip fault rotated into transpression.

Brocher *et al.* (2001), using tomographic data, assert that there is little structural relief at the northwestern end of the fault, with the greatest relief at the Port Ludlow Uplift, where the fault displays northeast-side-down relief. Brocher *et al.* (2005) propose that the SWIF is a fold and thrust belt formed in response to NE-SW compression in the forearc and that the surface faults are northeast-dipping reverse backthrusts that sole into a southwest-dipping blind master thrust fault at shallow (3 to 4 km) depth. Sherrod *et al.* (2008) propose a model in which the SWIF responds to a stress field in which north-south convergence in southern and central Puget Sound gives way to NE-SW-directed shortening in the north (Wells *et al.*, 1998; McCaffrey *et al.*, 2007). The fault in this model has predominantly north-side-up reverse motion to the northwest and becomes primarily dextral-oblique to the southeast where the stress and the fault are oriented differently. They explain observations to the southeast, near Woodinville, of north-side-up surface offsets, superimposed on long term post-Eocene south-side-up motion, with a model of the fault as a dextral oblique fault in which the observed faults are northeast-dipping back thrusts in the hanging wall of a larger south-dipping reverse oblique fault.

The SWIF has clear evidence of Quaternary activity. Johnson *et al.* (1996) show offshore seismic reflection profiles documenting folding and faulting of late Quaternary strata, and borehole data on Whidbey Island show abrupt thickness variations in Quaternary strata across the fault. Gower *et al.* (1985) mapped Quaternary faults on Whidbey Island. Johnson *et al.* (1996) document numerous Quaternary liquefaction features in the vicinity of the SWIF. Kelsey *et al.* (2004) document folding across a blind reverse fault 2800 to 3200 years ago. The folding and faulting appear in seismic reflection profiles east of Whidbey Island. Onshore, coastal marshes on either side of the fault record different relative sea-level histories, indicating that the north side of the fault was uplifted 1 to 2 m relative to the south side.

Bourgeois and Johnson (2001) observed evidence of abrupt subsidence, a tsunami, and at least three liquefaction episodes at Snohomish delta near the SWIF since AD 800. Sherrod *et al.* (2008) trenched several of the scarps identified in LiDAR data that overlie aeromagnetic lineaments on the mainland. The scarps have north-side-up separation and are 1 to 5 m high. The trenches revealed evidence of multiple faulting and folding events since deglaciation at about 16.4 ka. Combining their observations with the paleoseismic data from Whidbey Island, Sherrod *et al.* (2008) argue for at least four SWIF surface-deforming events since 16.4 ka; they also propose that there may be as many as eight documented Holocene events if deformation from Snohomish delta and a possible early Holocene event exposed in their trenches constitute independent events.

Johnson *et al.* (1996; 2004b) report a minimum slip rate, really a vertical separation rate, of 0.6 mm/yr on the SWIF based on observations of 150 m of structural relief on an onshore anticline overlying a positive flower structure identified in offshore reflection profiles; the material in the core of the anticline is 250-ka Double Bluff drift. There is no reported rate for any lateral displacement.

Although the mapping is incomplete offshore, the multiple strands comprising the SWIF appear to converge westward, where the fault is nearest the site; the greatest complexity occurs farther away. In light of this, and the lack of knowledge of the rupture characteristics of the SIWF, we have simplified the fault zone in this model into a single structure, coincident with the northernmost mapped strand of the fault; this is somewhat conservative. Given the uncertainties in the characterization of the SWIF, we consider two rupture models, weighted equally (Table 1). One characterizes the fault as a steeply north-dipping strike-slip fault similar to the Devils Mountain fault strike-slip model (see above). The other characterizes the fault as a shallowly south-dipping reverse fault analogous to the Seattle fault zone (Table 1). We also include two models of the western extent, either to central Puget Sound just west of Whidbey Island or across the sound to Vancouver Island (Table 1). Maximum magnitudes calculated from empirical relationships (Wells and Coppersmith, 1994; Hanks and Bakun, 2002; 2008) range from **M** 6.9 to 7.4 for the reverse model and **M** 7.3 to 7.6 for the strike-slip model.

For the strike-slip model, we develop a slip rate distribution for the SWIF using the vertical displacement rates of Johnson *et al.* (1996; 2004b) and Utsalady Point fault displacement data in the manner described for the Devils Mountain fault (see above and Table 1). For the reverse slip model, we use the Johnson *et al.* (1996) vertical rates to calculate slip rates based on fault dip. Given the large uncertainties in the data, we have simplified the model to apply a single slip rate distribution to apply to all dip models rather than make each slip rate dip-dependent (Table 1).

Leech River Fault

The Leech River fault is located in southernmost Vancouver Island and reaches to within 22 km of the dam site (Figure 3). The Leech River fault (LRF) strikes east-west across southern Vancouver Island. It marks the boundary between the Metchosin Igneous Complex, considered a part of the Eocene Crescent terrane that underlies the Olympic Peninsula, on the south and the Mesozoic Leech River Schist, which may be part of the Pacific Rim Complex forearc assemblage, on the north (Macleod *et al.*, 1977; Groome, 2000). The LRF continues offshore west of Vancouver Island but its extent is not well constrained. Macleod *et al.* (1977) and Snavely and Wells (1991) map it as extending about 40 km west of the coast, where it is truncated by the northwest extension of the Calawah or Crescent fault. Some studies (e.g.

Roddick *et al.*, 1979), however, extend it only a few kilometers offshore, to the intersection with the Tofino fault, which runs parallel to Vancouver Island just off the west coast.

The LRF has been interpreted as a sub-vertical left-lateral fault based on field kinematic indicators (Fairchild, 1979; Fairchild and Cowan, 1982) and as a north-dipping thrust fault based on results from Lithoprobe (Clowes *et al.*, 1987). Groome (2000) describes the Bear Creek shear zone, coincident with the LRF, as predominantly sinistral with north-side-up motion based on stretching lineations, shear fabrics, and shear bands in mylonites. His preferred interpretation is that the Bear Creek shear zone is the surface expression of a sinistral-oblique LRF that dips steeply at the surface and becomes listric with depth. Macleod *et al.* (1977), citing Clapp (1917), report that the LRF dips 36° to 70° N. Calvert *et al.* (2006) show the fault dipping about 50° to 80° and being cut off at about 20 km by the subhorizontal E-layer. Clowes *et al.* (1987) report a 35° to 45° north dip and state that the fault extends to about 10 km depth.

No definitive evidence exists to indicate that the Leech River fault has or has not been active in the Quaternary. Macleod *et al.* (1977) considers the fault probably to have been inactive since the early Tertiary because, on the west coast of Vancouver Island, Upper Oligocene sedimentary rocks overlie strongly sheared Leech River Schist and Metchosin Igneous Complex rocks but are undeformed. Preliminary investigation of LiDAR data reveals no surface expression of the fault across Quaternary terraces where the fault emerges from the valley on the east coast of Vancouver Island (G. Rodgers, GSC, pers. comm., 2008). Reconnaissance field investigations of lineaments identified in the LiDAR did not yield evidence of faulting, and the lineaments could be explained as glacial or fluvial features.

Its location on strike and immediately adjacent to the Quaternary-active Devils Mountain fault and possibly the SWIF, however, raise the possibility that the LRF may still be active. Johnson *et al.* (2001), citing mapping by Muller (1983), propose that the Devils Mountain fault may continue onto and merge with the LRF. Mosher *et al.* (2003) describe the WSIF and LRF as being essentially the same structure and propose that this structure has been active in the Quaternary, although they do not specifically assert activity on the LRF proper. Alternatively, they suggest the Devils Mountain fault deformation may transfer onto northwest-striking structures in Haro Strait. They also identified a late Pleistocene-Holocene landslide off the east coast of Vancouver Island and suggested it could have been induced by ground shaking generated by the LRF. Johnson *et al.* (1996; 2001) interpret the Quaternary-active SWIF to form part of the boundary of the northward migrating forearc with continental North America, which juxtaposes Eocene rocks to the south against pre-Tertiary basement to the northeast. This boundary continues into Vancouver Island as the LRF. The continued activity of this structure in the Eastern Strait of Juan de Fuca suggests the possibility that it may be active on Vancouver Island as well. Finally, unpublished studies of seismic reflection data offshore of the west coast of Vancouver Island indicate the possibility that the Leech River fault affects the sea floor topography, suggesting recent deformation (Schmidt, 2003). The correlation of the fault with the sea floor deformation remains uncertain, so still no definitive evidence of Quaternary activity has been identified. Vaughn Barrie of the Geological Survey of Canada has also, in ongoing unpublished work, identified in offshore seismic reflection and multibeam data faulting associated with the Devils Mountain fault extending right up to the Vancouver Island coast, on strike with the LRF, increasing the likelihood that the faulting extends into the LRF proper (V. Barrie, pers. comm., 2009).

Given the lack of specific evidence suggesting Quaternary displacement, the unfaulted Oligocene rocks on the West Coast, the possible sea floor offset, and the clear evidence of Quaternary faulting on structures that are structurally similar and possibly continuations of the LRF, we consider two interpretations: 1) that the fault ceased activity in the Tertiary and 2) that it is an active structure that transfers deformation from faults in the eastern Strait of Juan de Fuca (e.g., Devils Mountain fault and SWIF) westward into southern Vancouver Island. We model the fault with a probability of activity of 0.7. Because the model in which the fault is active is based on its continuity with active oblique-slip faulting extending to Vancouver Island, we model the fault only as a moderately to steeply north-dipping reverse oblique fault similar to the Devils Mountain fault; interpretations of the fault as a low-angle thrust fault are considered within the inactive model. Therefore, as we did for the Devils Mountain fault, we model the fault as both reverse-oblique and strike-slip.

As noted above, the westward extent of the Leech River fault is uncertain. We allow it to extend about 40 km offshore, as mapped by Macleod (1977) and Snavely and Wells (1991), but also include rupture lengths that limit rupture to the onshore fault or a portion of it. The maximum magnitudes calculated from these rupture lengths and empirical relationships range from **M** 7.0 to 7.6.

No information about slip rate on the Leech River fault is reported in the literature. Because the model in which the fault is active is based on an interpretation of continuity with active faults in the eastern Strait of Juan de Fuca and northern Puget Sound (e.g., Devil's Mountain fault), we apply the slip rate distribution developed for the Devils Mountain fault to LRF.

Faults in the San Juan Islands

No definitive evidence of late Quaternary activity on any mapped fault in or around Vancouver Island has been documented in published literature, in spite of the region's location in the forearc of an active subduction zone. This absence of identified late Quaternary faulting is more likely due to limited active fault investigation in the area to date as well as the difficulty in identifying geomorphic expression of recent faulting in terrain that is steep, forested and that was heavily modified by glaciation until about 11,000 years ago. Ongoing recent investigations focusing on offshore data, including seismic reflection and multibeam bathymetry data, however, have begun to reveal evidence suggestive of active faulting. In light of these data, therefore, we are including a number of potentially active fault sources in and around Vancouver Island. Although some of the data suggest clear evidence of post-glacial faulting according to the investigators, we do not assign a probability of activity of 1.0 to any fault source, since most of these results have not yet appeared in published literature. We briefly describe some of the sources included in the model below.

Skipjack Fault

The Skipjack fault strikes EW across South Pender Island and the northern arm of Haro Strait. Vaughn Barrie has identified this fault on the basis of multibeam bathymetric data and subsurface stratigraphic offsets in seismic reflection data (V. Barrie, Geological Survey of Canada, pers. comm., 2009). He contends that the fault affects Holocene deposits. We include the Skipjack fault as a fault source with a probability of activity of 0.8, based on the unpublished results of Vaughn Barrie. It is located at the north end of the San Juan Islands, near the transition from the tectonic setting of the Puget Lowland (PL zone, see below) to that of Vancouver Island and Georgia Strait (VI zone, see below). In light of the lack of any information about its sense of slip or rupture characteristics, our model is based on analogy to other, better known faults in the area. Given its location and strike, we model it both as a steeply dipping strike-slip fault, analogous to but simplified from the Devils Mountain fault to the south, and as a shallowly dipping reverse fault, analogous to the Boulder Creek fault to the east, with slightly higher weight on the strike-slip model (Table 1). We apply simplified slip rate distributions from these analogues. For the strike-slip model, we scale the slip rate to the shorter length of the Skipjack fault relative to the Devils Mountain fault; for the reverse fault model, we use the slip rate of the Boulder Creek fault but with a wider distribution to reflect the greater uncertainty.

San Juan Island Fault Zone

Again using bathymetric and seismic reflection data, Vaughn Barrie has identified numerous locations in the straits west and southwest of San Juan Island that he says show evidence of Holocene faulting. He has developed a preliminary fault map in and around the San Juan Islands; the faults pass through the deformation sites but also extend beyond those regions. We have used his map to define the San Juan Island fault zone, a northwest-striking zone that encompasses several of the fault strands in his map. The data points constraining recent activity in the zone are largely concentrated at the northwest end of the zone, but the zone extends the length of his mapped faults. Based on his observations of what he considers strong evidence for Holocene faulting, tempered by the lack of such data along the full extent of the mapped faults and the unpublished nature of the results, we have assigned a probability of activity to the fault zone of 0.7. In addition, we include two possible geometries and rupture scenarios for the fault zone, a wide and a narrow model. The narrow model is limited to the region offshore west and southwest of San Juan Island, where the faults Barrie has mapped include or extend to identified sites of Holocene deformation. In the wide model, the zone extends north into San Juan Island and includes all the northwest-striking faults that Barrie has mapped, even those that do not contain sites with documented Holocene deformation. The dam site is located within the wide zone but not the narrow zone. We have weighted the narrow model 0.8 and the wide model 0.2.

There is no direct geologic evidence defining the style and rate of faulting in this fault zone. Because the zone strikes northwest, is only a couple of kilometers north of the Devils Mountain fault, and the observations recorded by Vaughn Barrie suggest vertical faults in the shallow subsurface, we apply the Devils Mountain fault as an analogue, modeling the zone as oblique- and strike-slip, with a slip rate distribution simplified from that fault's slip rate.

4.1.3 Crustal Background Sources

The hazard from background (floating or random) earthquakes that are not associated with known or mapped faults is incorporated into the hazard analysis. Earthquake recurrence estimates in the site region and maximum magnitudes are required to assess this hazard.

4.1.3.1 Crustal Source Zones

We have divided the study area into crustal source zones for the purposes of analyzing the hazard from background earthquakes. The seismic source zone boundaries were delineated based on characteristics of seismicity, geophysical data such as stress, heat flow, gravity, and magnetics, and geological and geodetic data. We defined the boundaries of zones to separate areas of contrasting properties such that within an individual source zone, the expected future earthquake behavior is relatively uniform. Thus, source zone boundaries define changes in rate, seismogenic depth, maximum magnitude, etc. We have defined three seismic source zones for this study; their characterization is summarized in Table 2.

The PL zone occupies the Puget Lowland region, extending from the San Juan Islands in the north to Tacoma in the south and from the Olympic Mountains in the west to the Cascades volcanic arc in the east (Figure 3). Trout Lake Dam is located in this zone. Seismologic and geodetic data indicate that the Washington-Oregon fore-arc sliver is undergoing north-south-directed shortening and crustal thickening caused by clockwise rotation and northward translation of the Oregon coast block at rates that decrease northward to near zero at or near the international boundary (e.g., Wells *et al.*, 1998; Miller *et al.*, 2001; Lewis *et al.*, 2003). The PL zone, located in the northeast corner of this forearc sliver, is characterized by north-south-directed shortening and crustal thickening that is accommodated by strike-slip, thrust, and oblique-slip displacements on a series of west- and west-northwest-trending faults in the Puget Lowland. The crust in the PL is thick, with crustal seismicity to 25 to 30 km in the western part of the zone, shallowing eastward toward the hotter volcanic arc; we model the seismogenic depth from 20 to 30 km (Table 2). Numerous Quaternary faults have been identified within the PL zone and tend to strike west-northwest to east-northeast and have reverse or reverse-oblique slip (Section 4.1.4); we apply this orientation and style of faulting as the preferred style for modeling background earthquakes. The PL zone has been the focus of considerable active fault research and mapping is probably fairly complete in this zone compared to the others; the northernmost portion, in the San Juan Islands, is the exception. The long-term shortening rate in the Puget Lowland area determined from geodetic data is comparable to the cumulative shortening rate on mapped faults obtained from paleoseismic investigations (Sherrod *et al.*, 2008). We conclude from this that most significant Quaternary faults in the PL have been identified and are accommodating the regional long-term strain. Given this, and the relatively high rates of historical seismicity, we model the rates of background earthquake occurrence from historical seismicity. We model a range of maximum magnitudes from **M** 6.7 to 7.3, with most weight between **M** 6.7 and 7.0, reflecting the relatively complete identification of crustal faults; the **M** 7.3, with 0.1 weight, reflects the possibility that a moderately large, unidentified, probably blind thrust might exist, especially in the northern part of the zone.

The VI zone includes most of Vancouver Island and the Georgia Strait and covers the fore-arc region between the subducted Explorer and Juan de Fuca plates to the west and the volcanic arc to the east. The VI zone is differentiated from the PL zone to the south based on changes in GPS residual strain and style of active faulting, as well as data completeness. It is characterized by northeast-directed shortening probably accommodated by a combination of reverse faulting and northwest-directed dextral shear (Mazzotti *et al.*, 2008; McCaffrey *et al.*, 2007). The VI zone is a region of historical earthquake activity, including a **M** ~6.9 event in 1918 and a **M** 7.3 event in 1946. Both of these events are due to strike-slip faulting. The crust under Vancouver Island is thick and cool (Lewis *et al.*, 1997); the seismogenic depth is not well constrained by seismicity, but Hyndman *et al.* (2009) show an elastic thickness of 20 to 25 km. We consider weighted seismogenic depths of 15 (0.2), 20 (0.4), and 25 (0.4) km. For background seismicity, we use range of maximum magnitudes from **M** 6.7 to 7.5 (Table 2). The range reflects the possibility that the 1946 event occurred either on the Beaufort Range fault (Figure 3) or in the background on an as yet unmapped fault. We apply a rate of occurrence of background earthquakes in the VI zone obtained from both historical seismicity and geodetic data (Section 4.1.3.2), weighted equally.

The OLY zone occupies the forearc west of PL and south of VI and encompasses the Olympic Peninsula. It is similar to the PL zone in comprising a part of the northward-migrating forearc sliver, but is distinguished from the PL on the basis of slightly higher geodetic shortening rates and significantly lower seismicity rates. The OLY zone is differentiated from the VI zone to the north based on changes in GPS residual strain and style of active faulting. Geodetic data suggest the shortening direction in OLY is north-south (e.g. Miller *et al.*, 2001; Mazzotti *et al.*, 2003), whereas geologic data are indicative of a north-south to northeast-southwest direction (Lewis *et al.*, 2003). Mapped Quaternary structures in the northern part of the zone include west-northwest-striking left-lateral-reverse oblique slip (Nelson *et al.*, 2007; McCrory *et al.*, 2005), whereas, along the eastern edge of the peninsula, several north-northeast-striking faults, although more ambiguous, suggest right-lateral-reverse oblique slip. Crust in the OLY zone is thick and cold; seismicity, though sparse, occurs to 25 to 30 km; We model the seismogenic depth from 20-30 km, with most weight on the high end (Table 2). Fault mapping is probably incomplete in the OLY zone; active faults have only been identified in coastal regions and offshore, not in the rugged and heavily vegetated interior mountains. We consider it likely, therefore, that there are additional fault sources that could produce large earthquakes in the OLY background zone. We include a range of maximum magnitudes from **M** 6.7 to 7.5 to account for such an event. Historical seismicity is sparse in the OLY and is at odds with relatively high geodetic shortening rates (Mazzotti *et al.*, 2003; Hyndman *et al.*; 2003). The reasons for the discrepancy are not clear, but in light of it and the probably incomplete identification of fault sources, we use both seismicity and geodetic data, weighted equally, to model the rate of occurrence of background earthquakes.

4.1.3.2 Geodetic Data

GPS-based models of crustal deformation provide an alternate and indirect estimate of potential earthquake recurrence for areal sources in the region. These data can be used to estimate strain rates, and hence earthquake recurrence rates, across a zone and are used as one basis for rate estimates for the OLY and VI crustal source zones. These zones have probably been incompletely mapped, and geodetic data provide a constraint on the amount of crustal strain that could be released in earthquakes on unidentified fault sources. In both zones, geodetic rates are higher than historical seismicity rates. The reasons for this are unclear. A portion of geodetic strain may be released aseismically and thus geodetic rates overestimate the rate of occurrence of earthquakes. Conversely, the short record of historical seismicity may not reflect long-term averages nor account for unidentified faults that are locked between large earthquakes and do not have associated historical seismicity. Ward (1998a, b) compared seismicity-based, geodetic and geologic rates globally and found that geodetic strain rates always exceeded seismicity rates. He concluded that, although aseismic deformation may account for some of the discrepancy, historical seismicity catalogues, especially in slowly deforming regions, underestimate long-term earthquake rates. In light of these uncertainties, and the opposite effects the two datasets may have on estimating earthquake occurrence rates (i.e. geodetic rates may overestimate earthquake rates because they do not account for aseismic slip, and seismicity rates may underestimate earthquake rates because the catalogues are incomplete), we include both seismicity-based and geodetically-based rates for VI and OLY. There does not appear to be a significant discrepancy between seismicity, geodetic, and geologic rates in the PL (e.g., Sherrod *et al.*, 2008; Hyndman *et al.*, 2003), so we do not include a geodetic model for that zone.

Numerous GPS studies in recent years have constrained the rate of crustal deformation in the Olympic Peninsula region, with long-term rates ranging from about 4 to 7 mm/yr (e.g. Miller *et al.*, 2001; Mazzotti *et al.*, 2003; 2008; McCaffrey *et al.*, 2007). To model geodetic rates for the OLY, we use the rates from Mazzotti *et al.* (2003), which differentiates the inner and outer fore-arc, with the outer fore-arc corresponding approximately to the OLY zone. They obtained estimates of about 3.4 mm/yr of observed differential motion and 6.5 mm/yr of residual crustal shortening in a north-south direction in the outer fore-arc between the Columbia River to Vancouver Island. We model the background by a zone of distributed slip with strain rates based on these geodetic rates minus the cumulative north-south component of geologically constrained slip rates on mapped faults, which is about 0.4 mm/yr (Table 2). We converted strain rates into seismic moment rates to characterize earthquake occurrence rates.

For the VI zone, we use geodetic estimates from the deformation models of Mazzotti *et al.* (2002; 2008). These models, based on residual GPS velocities obtained from subtracting a model of interseismic strain accumulation on a completely coupled subduction zone from the observed velocities, suggest that up to 3 mm/yr of slip may be accommodated on faults within the Vancouver Island fore-arc region. In the geodetic background rate model, we use a range of rates from 1 to 5 mm/yr (Table 2). The high end of this range reflects maximum uncertainty in the geodetic data and the possibility that Vancouver Island remains in a stress shadow from the 1918 and/or 1949 earthquakes. From these rates, we subtract the contribution to total strain from the modeled faults (about 0.9 mm/yr), and calculate earthquake occurrence rates.

4.2 GROUND MOTION ATTENUATION

To characterize the attenuation of ground motions in the PSHA, we have used recently developed empirical attenuation relationships appropriate for tectonically active regions such as the western U.S. These new attenuation relationships were developed as part of the NGA Project sponsored by the PEER Center Lifelines Program and have been published in the *Earthquake Spectra*. The NGA models have a substantially better scientific basis than previous relationships (e.g., Abrahamson and Silva, 1997) because they are developed through the efforts of five selected attenuation relationship developer teams working in a highly interactive process with other researchers who have: (a) developed an expanded and improved database of strong ground motion recordings and supporting information on the causative earthquakes, the source-to-site travel path characteristics, and the site and structure conditions at ground motion recording stations; (b) conducted research to provide improved understanding of the effects of various parameters and effects on ground motions that are used to constrain attenuation models; and (c) developed improved statistical methods to develop attenuation relationships including uncertainty quantification. The relationships have benefited greatly from a large amount of new strong motion data from large earthquakes (**M** > 7) at close-in distances (< 25 km). Data include records from the 1999 **M** 7.6 Chi Chi, Taiwan, 1999 **M** 7.4 Kocaeli, Turkey, and 2002 **M** 7.9 Denali, Alaska earthquakes. Review of the NGA relationships indicate that, in general, ground motions particularly at short-periods (e.g., peak acceleration) are significantly reduced particularly for very large magnitudes (**M** 7.5) compared to earlier relationships.

The relationships by Chiou and Youngs (2008), Campbell and Bozorgnia (2008), Abrahamson and Silva (2008), and Boore and Atkinson (2008) were used in the PSHA. The relationships were reviewed and weighted equally in the PSHA. The hazard was calculated for a "rock outcrop" site condition. No *in situ* velocity investigations have been performed at the damsite but the foundation is known to consist of volcaniclastic sandstone and metabasalt or greenstone of the Constitution Formation. In lieu of site-specific velocity data at the damsite, a V_s30 (shear-wave velocity in the top 30 m) of 1,000 m/sec was used in the PSHA.

Other input parameters include $Z_{2.5}$, the depth to the Vs of 2.5 km/sec (a proxy for basin effects), which is only used in one model, Campbell and Bozorgnia (2008). We have used the default value of 2.0 km as recommended by the authors in lieu of site-specific data. Other parameters such as depth to the top of rupture (zero for all surficial faults unless specified otherwise), dip angle, rupture width, and aspect ratio of each fault are specified or calculated within the PSHA code.

For the CSZ megathrust, the Youngs *et al.* (1997), Zhao *et al.* (2006), and Atkinson and Macias (2009) attenuation relationships were used with equal weights. Strong motion recordings of the recent 2001 **M** 6.8 Nisqually, Washington, earthquake suggest that the Youngs *et al.* (1997) relationship may slightly overpredict ground motions for the intraslab events (Wong *et al.*, 2004). The Zhao *et al.* (2006) model is based on Japanese strong motion data.

For the CSZ intraslab (Wadati-Benioff zone), the Atkinson and Boore (2003), Zhao *et al.* (2006), and Garcia *et al.* (2005) models were used with equal weights. The latter is based on Mexican strong motion data.

The following presents the results of the PSHA and a comparison with the USGS National Hazard Maps.

5.1 RESULTS

The results of the PSHA of the Trout Lake damsite are presented in terms of ground motion as a function of annual exceedance probability. This probability is the reciprocal of the average return period. Figures 8 and 9 show the total mean, median (50th percentile), 5th, 15th, 85th, and 95th percentile hazard curves for peak horizontal ground acceleration (PGA) and 0.2 sec and 1.0 sec spectral acceleration (SA). These fractiles indicate the range of epistemic uncertainty about the mean hazard. For example, at a return period of 3,000 years, there is a difference of about a factor of two between the 5th and 95th horizontal PGA hazard (Figure 8). The sources of uncertainty that contribute most to the probabilistic hazard are generally the attenuation relationships and the recurrence rates and models of the controlling seismic sources.

The contributions of the various seismic sources to the mean PGA hazard are shown on Figure 10. This hazard is controlled by the intraslab zone beneath the Puget Sound where the site is located. The San Juan Island fault zone becomes a significant contributor to the PGA hazard at return periods greater than 1,000 years (Figure 10). At 1.0 sec SA, the CSZ megathrust controls the hazard at the damsite (Figure 11).

By deaggregating the hazard by magnitude and distance bins, Figures 12 and 13 illustrate the contributions by events at the return period of 3,000 years. At PGA, the high-frequency hazard is coming from three sources: intraslab earthquakes of **M** 6.5 to 7.2 at distances of 50 to 90 km, crustal events from the San Juan Island fault zone, **M** 5.0 to 7.0 at distances less than 30 km, and the CSZ megathrust. At 1.0 sec horizontal SA, the CSZ is the obvious contributor with **M** > 8.5 from 90 to 130 km away (Figure 13).

Based on the magnitude and distance bins (Figures 12 and 13), the controlling earthquakes as defined by the modal magnitude M* and modal distance D* can be calculated. Table 3 lists the M*, D*, and ε* for 3,000-year return period for PGA and 1.0 sec horizontal SA. Epsilon is the difference between the logarithm of the ground motion amplitude and the modal logarithm of ground motion (for that M and R) measured in units of the standard deviation (σ) of the logarithm of the ground motion.

A horizontal UHS is shown on Figure 14 for a return period of 3,000 years. A UHS displays the spectral accelerations at all periods (or frequencies) at the same probability of exceedance (or return period).

5.2 COMPARISON WITH NATIONAL HAZARD MAPS

In the 2008 version of the USGS National Hazard Maps, which are the basis for the U.S. building code (International Building Code), Petersen *et al.* (2008) estimated probabilistic ground motions for the U.S. for the annual exceedance probability of 2% 5%, and 10% in 50 years (2,475, 975, and 475-year return periods). The 2,475-year return period USGS PGA for the damsite for a firm rock site condition (NEHRP B/C; V_S30 760 m/sec) is 0.48 g. Our hard rock value is 0.45 g. The site-specific 1.0 sec SA value is 0.32 g compared to the USGS value of

0.38 g. The values are surprisingly close given the differences in seismic source characterization. The slightly lower values from this study can be due to the higher V_S of the damsite foundation (760 m/sec versus 1,000 m/sec).

5.3 SEE GROUND MOTIONS

Given the high hazard class 1C classification of Trout Lake Dam, we are recommending the SEE ground motions for structural analysis of the dam be probabilistically based and have a return period of 3,000 years. The SEE horizontal ground motions are represented by the 3,000-year return period horizontal UHS (Figure 14; Table 4). As stated earlier, at PGA the probabilistic hazard is controlled by intraslab earthquakes. This is true at short periods such as 0.1 sec, the natural period of the dam. The vertical UHS is also shown on Figure 14. There is no attenuation model for vertical ground motions from intraslab earthquakes and so we have assumed that using a crustal earthquake model, in this case Campbell and Bozorgnia (2003), is appropriate to calculate V/H ratios.

One set of time histories (2 horizontal- and 1 vertical-component) were developed for the 3,000-year return period SEE spectrum. Because the response spectrum of a time history has peaks and valleys that deviate from the design response spectrum (target spectrum), it is necessary to modify the motion to improve its response spectrum compatibility. The procedure proposed by Lilhanand and Tseng (1988), as modified by Norm Abrahamson (written communication, 1999), has been used to develop the acceleration time histories through spectral matching to the target spectrum. This time-domain procedure has been shown to be superior to previous frequency-domain approaches because the adjustments to the time history are only done at the time at which the spectral response occurs resulting in only localized perturbations on both the time history and the spectra (Lilhanand and Tseng, 1988).

As discussed earlier, the contributions to the hazard at Trout Lake Dam are coming from multiple sources (Figure 12). Thus the UHS may be very broadband and not realistic in terms of a single scenario earthquake to derive time histories. To check this possibility, a deterministic intraslab scenario earthquake median spectrum for the modal **M** 7.1 at a modal distance of 62.5 km (Table 3) was calculated using the same attenuation models used in the PSHA (Figure 15) and scaled to the SEE spectrum at 0.2 sec (Figure 16). The scaled deterministic spectrum matches the SEE spectrum at all periods of engineering significance (< 0.2 sec) to the dam and so is used as the target spectrum for the spectral matching.

Seed time histories from one set of recordings from the 2001 Nisqually earthquake were selected for the spectral matching and are listed in Table 5 and shown in Figure 17. Time histories were selected based on the earthquake magnitude, distance, site geology, and response spectral shapes. The spectral matches and resulting acceleration, velocity, and displacement time histories are shown on Figures 18 to 23. Figures showing the spectral matches also show the response spectrum computed from the matched time history.

Abrahamson, N.A. and Silva, W.J., 1997, Empirical response spectral attenuation relations for shallow crustal earthquakes: Seismological Research Letters, v. 68, p. 94-127.

Abrahamson, N.A. and Silva, W.J., 2008, Summary of the Abrahamson and Silva NGA ground motion relations. Earthquake Spectra, v. 24, p. 67-97.

Aki, K., 1983, Seismological evidence in support of the existence of "Characteristic Earthquakes": Earthquake Notes, v. 54, p. 60-61.

Anderson, J.G., 1979, Estimating the seismicity from geological structure for seismic risk studies: Bulletin of the Seismological Society of America, v. 69, p. 135-158.

Atkinson, G.M., and Boore, D.M., 2003, Empirical ground-motion relations for subduction zone earthquakes and their applications to Cascadia and other regions: Bulletin of the Seismological Society of America, v. 93, p. 1703-1729.

Atkinson, G.M. and Macias, M., 2006, Predicted ground motions for great interface earthquakes in Cascadia subduction zone: Bulletin of the Seismological Society of America, revised electronic supplement: http:/www.seismotoolbox.ca/Predgm. html.

Atwater, B.F. and Hemphill-Haley, E., 1997, Recurrence intervals for great earthquakes of the past 3500 years at Northeastern Willapa Bay, Washington: U.S. Geological Survey Professional Paper 1576.

Baker, G.E. and Langston, C.A., 1987, Source parameters of the 1949 magnitude 7.1 south Puget Sound, Washington, earthquake as determined from long-period body waves and strong ground motions: Bulletin of the Seismological Society of America, v. 77, p. 1530-1557.

Barnett, E.A., 2007, Active faulting at the northeast margin of the Greater Puget Lowland: A paleoseismic and magnetic-anomaly study of the Kendall fault Scarp, Whatcom County, Northwest Washington: M.S. thesis, Humboldt State University, 77 p.

Barnett, E.A., Kelsey, H.M., Sherrod, B., Blakely, R.J., Hughes, J., Schermer, E.R., Haugerud, R.A., Weaver, C., Siedlecki, E.M., and Blakely, R.J., 2007, Active faulting at the northeast margin of the greater Puget Lowland; a trenching and wetland coring study of the Kendall Fault scarp, Whatcom County, northwest Washington: Geological Society of America Abstracts with Programs, v. 39, p. 61.

Barrie, J.V. and Hill, P.R., 2004, Holocene faulting on a tectonic margin: Georgia Basin, British Columbia, Canada: Geo-Mar Lett, v. 24, p. 86-96.

Blakely, R.J., Sherrod, B.L. , Wells, R.E.,. Weaver, C.S, McCormack, D.H., Troost, K.G., and Haugerud, R.A., 2004, The Cottage Lake aeromagnetic lineament: a possible onshore extension of the southern Whidbey Island fault, Washington: U.S. Geological Survey Open File Report 2004-120, 460 p.

Blakely, R.J., Wells, R.E., Weaver, C.S., and Johnson, S.Y., 1999, Tectonic setting and earthquake hazards of the Seattle fault, Washington: Implications from high-resolution aeromagnetic data: Seismological Research Letters, v. 70, p. 219.

Boore, D.M., and Atkinson, G.M., 2008, Ground motion predictive equations for the average horizontal component of PGA, PGV, and 5% damped PSA at spectral periods between 0.01s to 10.0s: Earthquake Spectra, v. 24, p. 99-138.

Bourgeois, J. and Johnson, S.Y, 2001, Geologic evidence of earthquakes at the Snohomish delta, Washington, in the past 1200 yr: Geological Society of America Bulletin., v. 113, p. 482–494.

Brocher, T.M., Blakely, R.J., and Wells, R.E., 2004a, Interpretation of the Seattle uplift, Washington, as a passive roof duplex: Bulletin of the Seismological Society of America, v. 94, p. 1379– 1401.

Brocher, T.M., Blakely, R.J., Wells, R.E., Sherrod, B.L., Ramachandran, K., 2005, The Transition Between N-S and NE-SW Directed Crustal Shortening in the Central and Northern Puget Lowland: New Thoughts on the Southern Whidbey Island Fault: Eos Transactions, American Geophysical Union, v. 86, Fall Meeting Supplement, Abstract S54A-06.

Brocher, T.M., Parsons, T., Blakely, R.J., Christensen, N.I., Fisher, M.A., Wells, R.E., and SHIPS Working Group, 2001, Upper crustal structure in Puget Lowland, Washington--Results from the 1998 seismic hazards investigation in Puget Sound: Journal of Geophysical Research, v. 106, p. 13,541-13,564.

Bucknam, R.C., Hemphill-Haley, E., and Leopold, E.B., 1992, Abrupt uplift within the past 1700 years at southern Puget Sound, Washington: Science, v. 258, p. 1611–1614.

Calvert, A.J., Ramachandran, K., Kao, H., Fisher, M.A., 2006, Local thickening of the Cascadia forearc crust and the origin of seismic reflectors in the uppermost mantle: Tectonophysics, v. 420, p. 175–188.

Campbell, K.W. and Bozorgnia, Y., 2008, NGA ground motion model for the geometric mean horizontal component of PGA, PGV, PGD, and 5% damped linear elastic response spectra for periods ranging from 0.01 to 10s: Earthquake Spectra, v. 24, p. 139-171.

Chiou, B.S.J. and Youngs, R.R., 2008, An NGA model for the average horizontal component of peak ground motion and response spectra: Earthquake Spectra, v. 24, p. 173-215.

Chlieh, M., Avouac, J., Hjorleifsdottir, V., and others, 2007, Coseismic slip and afterslip of the great Mw 9.15 Sumatra-Andaman earthquake of 2004: Bulletin of the Seismological Society of America, v. 97, p. S152-S173.

Clapp, C.H., 1917, Sooke and Duncan map area, Vancouver Island, British Columbia: Geological Survey of Canada Memoir 96.

Clowes, R.M., Brandon, M.T., Green, A.G., Yorath, C.J., Sutherland Brown, A., Kanasewich, E.R. and Spencer, C., 1987, Lithoprobe - southern Vancouver Island: Cenozoic subduction complex imaged by deep seismic reflections: Canadian Journal of Earth Sciences, v. 24, p.31-51.

Coombs, H.A., Milne, W.G., Nuttli, O.W., and Slemmons, D.B., 1977, Report of the review panel on the December 14, 1872 earthquake, in Washington Public Power Supply System Nuclear Projects Nos. 1 and 4, Preliminary site analysis report, Amendment 23, v. 2A, subappendix 2R-A, p. 2R-A-i to 31, includes Appendixes A-D.

Cornell, C.A., 1968, Engineering seismic risk analysis: Bulletin of the Seismological Society of America, v. 58, p. 1583-1606.

Dadisman, S.V., Childs, J.R., Johnson, S.Y., and Rhea, S.V., 2000, Data Report for Cruise G#-95-PS, June, 1995, in Mosher, D.C., Johnson, S.Y., Rathwell, G.J., Kung, R.B., and Rhea, S.B. (eds.), Neotectonics of the eastern Strait of Juan de Fuca; a digital geological and geophysical atlas: Geological Survey of Canada Open File Report 3931, (CD digital product), 1 sheet.

Dash, R.K., Spence, G.D., Riedel, M., Hyndman, R.D., and Brocher, T.M., 2007, Upper-crustal structure beneath the Strait of Georgia, Southwest British Columbia: Geophysics Journal International, v. 170, p. 800-812.

Dragovich, J. and DeOme, A.J., 2006, Skagit and Snohomish Counties, Washington, with a discussion of the evidence for Holocene activity on the Darrington–Devils Mountain fault zone: Washington Division of Geology and Earth Resources, Geologic Map GM-61.

Dragovich, J.D. and Stanton, B.W., 2007, The Darrington–Devils Mountain fault—A probably active reverse-oblique-slip fault zone in Skagit and Island Counties, Washington: Washington Division of Geology and Earth Resources, Open File Report 2007-2, 2 sheets (101 x 36 in. and 26 x 36 in.), scale 1:31,104.

Dragovich, J.D.; Stanton, B.W.; Lingley, W.S., Jr.; Griesel, G.A.; Polenz, M., 2003, Geologic map of the Mount Higgins 7.5-minute quadrangle, Skagit and Snohomish Counties, Washington: Washington Division of Geology and Earth Resources Open File Report 2003-12, 1 sheet, scale 1:24,000.

Dragovich, J.D., Zollweg, J.E., Qamar, A.I., and Norman, D.K., 1997, The Macaulay Creek thrust, the 1990 5.2-magnitude Deming earthquake, and Quaternary geologic anomalies in the Deming area, western Whatcom County, Washington--Cause and effects?" Washington Geology, v. 25, no. 2, p. 15-27.

Fairchild, L.H., 1979, The Leech River unit and Leech River fault, Southern Vancouver Island, British Columbia: M.S. Thesis, University of Washington, Seattle, WA., 170 p.

Fairchild, L.H. and Cowan, D.S., 1982, Structure, petrology and tectonic history of the Leech River Cornplex northwest of Victoria, Vancouver Island: Canadian Journal of Earth Sciences, v. 19, p. 181 7-1 835.

Flück, P., Hyndman, R.D., and Wang, K., 1997, Three-dimensional dislocation model for great earthquakes of the Cascadia subduction zone: Journal of Geophysical Research, v. 102, p. 20,539-20,550.

Garcia, D., Singh, S.K., Herraiz, M., Ordaz, M., and Pacheco, J.F., 2005, Inslab earthquakes of central Mexico: peak ground-motion parameters and response spectra: Bulletin of the Seismological Society of America, v. 95, p. 2272-2282.

Geomatrix Consultants, 1995, Seismic design mapping, state of Oregon: unpublished report prepared for the Oregon Department of Transportation, Project No. 2442.

Goldfinger, C., Nelson, C.H., Johnson, J.E., Morey, A.E., Gutierrez-Pastor, J., Karabanov, E., Eriksson, A.T., Gracia, E., Dunhill, g., Patton, J., Enkin, R., Dallimore, A., Vallier, T., and the Shipboard Scientific Parties, 2009, Turbidite event history: methods and implications for Holocene paleoseismicity of the Cascadia subduction zone (in press).

Gower, H.D., Yount, J.C., and Crosson, R.S., 1985, Seismotectonic map of the Puget Sound region, Washington: U.S. Geological Survey Miscellaneous Investigations Series Map I-1613, 15 p., scale 1:250,000.

Gregor, N.J., Silva, W.J., Wong, I.G., and Youngs, R.R., 2002, Ground-motion attenuation relationships for Cascadia subduction zone megathrust earthquakes based on a stochastic finite-fault model: Bulletin of the Seismological Society of America, v. 92, p. 1823-1932.

Groome, W., 2000, Magmatism and metamorphism in the Leech River Complex, Southern Vancouver Island, British Columbia, Canada, Implications for Eocene tectonics of the Pacific Northwest: M.Sc. Thesis, Simon Fraser University, 272 p.

Hanks, T.C. and Bakun, W.H., 2002, A bilinear source-scaling model for M-log A observations of continental earthquakes: Bulletin of the Seismological Society of America, v. 92, p. 1841-1846.

Hanks, T.C. and Bakun, W.H., 2008, M-log A observations for recent large earthquakes: Bulletin of the Seismological Society of America, v. 98, p. 490–494.

Hanks, T.C. and Kanamori, H. 1979, A moment magnitude scale: Journal of Geophysical Research, v. 84, p. 2348-2350.

Haugerud, R.A., Sherrod, B.L., Wells, R.E., and Hyatt, T., 2005, Holocene displacement on the Boulder Creek Fault near Bellingham, WA and implications for kinematics of deformation of the Cascadia Forearc: Geological Society of America Abstracts with Programs, v. 37, p. 476.

Hayward, N., Nedimović, M.R., Cleary, M., and Calvert, A.J., 2006, Structural variation along the Devil's Mountain fault zone, northwestern Washington: Canadian Journal of Earth Sciences, v. 43, p. 433–446.

Henstock, T.J., McNeill, L.C., and Tappin, D.R., 2006, Seafloor morphology of the Sumatran subduction zone: surface rupture during megathrust earthquakes?: Geology, v. 34, p. 485-488.

Hyndman, R.D., Currie, C.A., Mazzotti, S. and Frederiksen, A., 2009**,** Temperature control of continental lithosphere elastic thickness, *Te* vs *Vs*: Earth and Planetary Science Letters, v. 277, p. 539-548.

Hyndman, R.D., Mazzotti, S., Weichert, D.H., and Rogers, G.C., 2003, Frequency of large crustal earthquakes in Puget Sound - S. Georgia Strait predicted from geodetic and geological deformation rates: Journal of Geophysical Research, v. 108, no. B1, 2033, p. 12-1 - 12-12.

Hyndman, R.D. and Wang, K., 1995, The rupture zone of Cascadia great earthquakes from current deformation and the thermal regime: Journal of Geophysical Research, v. 100, p. 22, 133-22, 154.

Ichinose, G.A., Thio, H.K., and Somerville, P.G., 2006, Moment tensor and rupture model for the 1949 Olympia, Washington, earthquake and scaling relations for Cascadia and global intraslab earthquakes: Bulletin of the Seismological Society of America, v. 96, no. 3, p. 1029-1037.

Johnson, J.M., Satake, K., Holdahl, S.R., and Sauber, J., 1996, the 1964 Prince William Sound earthquake: Joint inversion of tsunami and geodetic data: Journal of Geophysical Research, v. 101, p. 523-532.

Johnson, S.Y., compiler, 2001a, Fault number 571, Strawberry Point fault: in Quaternary fault and fold database of the United States: U.S. Geological Survey website, http://earthquakes.usgs.gov/regional/qfaults.

Johnson, S.Y., Blakely, R.J., and Brocher, T.M., compilers, 2001b, Fault number 574, Devils Mountain fault, in Quaternary fault and fold database of the United States: U.S. Geological Survey website, http://earthquakes.usgs.gov/regional/qfaults.

Johnson, S.Y., Blakely, R.J., and Brocher, T.M., compilers, 2003a, Fault number 573, Utsalady Point fault, in Quaternary fault and fold database of the United States: U.S. Geological Survey website, http://earthquakes.usgs.gov/regional/qfaults.

Johnson, S.Y., Blakely, R.J., Brocher, T.M., Sherrod, B.L., Lidke, D.J., and Kelsey, H.M., compilers, 2004b, Fault number 572, Southern Whidbey Island fault zone, in Quaternary fault and fold database of the United States: U.S. Geological Survey website, http://earthquakes.usgs.gov/regional/qfaults.

Johnson, S.Y., Dadisman, S.V., Mosher, D.C., Blakely, R.J., and Childs, J.R., 2001, Active tectonics of the Devils Mountain fault and related structures, northern Puget Lowland and eastern Strait of Juan de Fuca region, Pacific Northwest: U.S. Geological Survey Professional Paper 1643, 46 p., 2 pls.

Johnson, S.Y., Mosher, D.C., Dadisman, S.V., Childs, J.R., and Rhea, S., 2000, Tertiary and Quaternary structures of the eastern Strait of Juan de Fuca--Interpreted map, in Mosher, D.C., Johnson, S.Y., Rathwell, G.J., Kung, R.B., and Rhea, S.B. (eds.), Neotectonics of the eastern Strait of Juan de Fuca; a digital geological and geophysical atlas: Geological Survey of Canada Open File Report 3931 (CD digital product), 1 sheet.

Johnson, S.Y., Nelson, A.R., Personius, S.F., Wells, R.E., Kelsey, H.M., Sherrod, B.L., Okumura, K., Koehler, R., Witter, R., Bradley, L., and Harding, D.J., 2003b, Maps and data from a trench investigation of the Utsalady Point fault, Whidbey Island, Washington: U.S. Geological Survey Miscellaneous Field Studies Map MF-2420.

Johnson, S.Y., Nelson, A.R., Personius, S.F., Wells, R.E., Kelsey, H.M., Sherrod, B.L., Okumura, K., Koehler, R., Witter, R., Bradley, L., and Harding, D.J., 2004a, Evidence for Late Holocene earthquakes on the Utsalady Point fault, northern Puget Lowland, Washington: Bulletin of the Seismological Society of America, v. 94, p. 2299 - 2316.

Johnson, S.Y., Potter, C.J., and Armentrout, J.M., 1994, Origin and evolution of the Seattle basin and Seattle fault: Geology, v. 22, p. 71-74.

Kelsey, H.M., Nelson, A.R., Hemphill-Haley, E., and Witter, R.C., 2005, Tsunami history of an Oregon coastal lake reveals a 4600 yr record of great earthquakes on the Cascadia subduction zone: Geological Society of America Bulletin, v.117, p. 1009-1032.

Kelsey, H.M., Sherrod, B.L., Johnson, S.Y., and Dadisman, S.V., 2004, Land-level changes from a late Holocene earthquake in the northern Puget Lowland, Washington: Geology, v. 32, p. 469 – 472.

Kelsey H.M., Sherrod B.L., Nelson A.R., Brocher T.M., 2008, Earthquakes generated from bedding plane-parallel reverse faults above an active wedge thrust, Seattle fault zone: Geological Society of America Bulletin, in press.

Kelsey, H.M., Witter, R.C., and Hemphill-Haley, E., 2002, Plate-boundary earthquakes and tsunamis of the past 5500 yr, Sixes River estuary, southern Oregon: Geological Society of America Bulletin, v. 114, p. 298-314.

Lewis, T.J., Lowe, C., and Hamilton, T.S., 1997, Continental signature of a ridge-trench-triple junction: Northern Vancouver Island: Journal of Geophysical Research, v. 102, p. 7767-7781.

Lewis, J.C., Unruh, J.R., and Twiss, R.J., 2003, Seismogenic strain at the Cascadia convergent margin: Geology, v. 31, pp. 183-186.

Lidke, D.J., compiler, 2004, Fault number 551, Unnamed faults in the Strait of Juan de Fuca and Puget Sound, in Quaternary fault and fold database of the United States: U.S. Geological Survey website, http://earthquakes.usgs.gov/regional/qfaults, accessed 06/03/2009 02:59 PM.

Lilhanand, K. and Tseng, W.S., 1988, Development and application of realistic earthquake time histories compatible with multiple-damping design spectra: Proceeding of the 9th World Conference on Earthquake Engineering, Tokyo-Kyoto, Japan, August.

Macleod, N.S., Tiffin, D.L., Snavely, P.D., Jr., and Currie, R.G., 1977, Geologic interpretation of magnetic and gravity anomalies in the Strait of Juan de Fuca, U.S.—Canada: Canadian Journal of Earth Science, v. 14, no. 2, p. 223-238.

Mazzotti, S., Dragert, H., Henton, J., Schmidt, M., Hyndman, R.D., James, T., Lu, Y., and Craymer, M., 2003a, Current tectonics of northern Cascadia from a decade of GPS measurements: Journal of Geophysical Research, v. 108, p. 2554.

Mazzotti, S., Dragert, H., Hyndman, R.D., Miller, M.M., Henton, J.A., 2002, GPS deformation in a region of high crustal seismicity: N. Cascadia forearc: Earth and Planetary Science Letters, v.198, p. 41-48.

Mazzotti S., Jones, C., Thomson R.E., 2008, Relative and absolute sea level rise in western Canada and northwestern United States from a combined tide gauge-GPS analysis: Journal of Geophysical Research, v. 113, p. C11019.

McCaffrey, R., Qamar, A.I., King, R.W., Wells, R., Khazaradze, G., Williams, C.A., Stevens, C.W., Vollick, J.J., and Zwick, P.C., 2007, Fault locking, block rotation and crustal deformation in the Pacific Northwest: Geophysical Journal International, doi: 10.1111/j. 1365-246X.2007.033371.x.

McCrory, P.A., Blair, J.L., Oppenheimer, D.H., and Walter, S.R., 2006, Depth to the Juan de Fuca slab beneath the Cascadia subduction margin – a 3-D model for sorting earthquakes: U.S. Geological Survey Data Series 91, version 1.2, available: http://pubs.usgs.gov/ds/91.

McCrory, P.A., Pollitz, F.F., and Blair, J.L., 2003, Evidence for a tear in the Juan de Fuca plate in the vicinity of the 2001 Nisqually earthquake (abs.): EOS Transaction, American Geology Union, v. 84, p. F1109.

McCrory, P.A., Wolf, S.C., Intelmann, S., Danforth, W.W., Weldon, R.J., II, and Blair, J.L., 2005, Quaternary tectonism in a collision zone, northwest Washington: Seismological Research Letters, v. 76, p. 264.

Miller, M.M., Johnson, D. J., Rubin, C. M., Dragert, H., Wang, K., Qamar, A., and Goldfinger, C., 2001, GPS-determination of along-strike variation in Cascadia margin kinematics: Implications for relative plate motion, subduction zone coupling, and permanent deformation: Tectonics, v. 20, p. 161-176.

Molnar, P., 1979, Earthquake recurrence intervals and plate tectonics: Bulletin of the Seismological Society of America, v. 69, p. 115-133.

Mosher, D.C., Johnson, S.Y. and Nedimovic, M.R. and Hayward, N., 2003, Fault recognition and active tectonics in the eastern Juan de Fuca Strait, Cascadia forearc region: Geological Association of Canada Annual Meeting, Abstract Volume, SS3-2.

Mulder, T.L. and Rogers, G.C., 2002, Seismicity in the vicinity of the Leech River Fault, in Seismological Society of America 2002, Annual Meeting 17-19 April 2002, Victoria Conference Centre, Victoria, British Columbia. Muller, J.E., 1983, Geology, Victoria: Geological Survey of Canada Map 1553A, scale 1:100,000.

Nelson, A.R., Johnson, S.Y., Kelsey, H.M., Wells, R.E., Sherrod, B.L., Pezzopane, S.K., Bradley, L., and Koehler, III, R.D., 2003, Late Holocene earthquakes on the Toe Jam Hill fault, Seattle fault zone, Bainbridge Island, Washington: Geological Society of America Bulletin, v. 115, p. 1388–1403.

Nelson, A.R., Lowe, M., Personius, S., Bradley, L., Forman, S.L., Klauk, R., and Garr, J., 2006, Holocene earthquake history of the northern Weber Segment of the Wasatch fault zone, Utah: Utah Geological Survey Miscellaneous Publication 05-8, 45 p.

Nelson, A.R., Personius, S.F., Buck, J., Bradley, L.-A., Wells, R.E., and Schermer, E.R., 2007, Field and laboratory data from an earthquake history study of scarps of the Lake Creek–Boundary Creek fault between the Elwha River and Siebert Creek, Clallam County, Washington: U.S. Geological Survey Scientific Investigations Map 2961, 2 sheets.

Noson, L.L., Qamar, A.I., and Thorsen, G.W., 1988, Washington State earthquake hazards, Washington Division of Geology and Earth Resources Information Circular 85, 77 p.

Oppenheimer, D.H., Wong, I.G., and Klein, F.W. 1992, Seismicity of the Hayward fault, *in* G. Borchardt, S. Hirschfeld, J. Lienkaemper, P. McClellan, P. Williams, and I. Wong (eds.), Proceedings of the Second Conference on Earthquake Hazards in the Eastern San Francisco Bay Area: California Division of Mines and Geology Special Publication 113, p. 91-100.

Parsons, T., Blakely, R.J., Brocher, T.M., and others, 2005, Crustal structure of the Cascadia fore arc of Washington: U.S. Geological Survey Professional Paper 1661-D, 40 p.

Petersen, M.D., Frankel, A.D., Harmsen, S.C., Mueller, C.S., Haller, K.M., Wheeler, R.L., Wesson, R.L., Zeng, Y., Boyd, O.S., Perkins, D.M., Luco, N., Field, E.H., Wills, C.J., and Rukstales, K.S., 2008, Documentation for the 2008 update of the United States National Seismic Hazard Maps: U.S. Geological Survey Open-File Report 2008-1128, 61 p.

Pratt, T.L., Johnson, S.Y., Potter, C.J., Stephenson, W.J., and Finn, C., 1997, Seismic-reflection images beneath Puget Sound, western Washington state - The Puget Lowland thrust system hypothesis: Journal of Geophysical Research, v. 102, p. 27,469-27,490.

Ramachandran, K., Dosso, S.E., Spence, G.D., Hyndman, R.D., and Brocher, T.M., 2005, Forearc structure beneath southwestern British Columbia: A three-dimensional tomographic velocity model: Journal of Geophysical Research, v. 110, B02303.

Roberts, T.H., 1991, Gravity investigation of crustal structure in the eastern Olympic Peninsula-Puget Lowland area, Washington: Bellingham, Western Washington University, unpublished M.S. thesis, 65 p.

Roddick, J.A., Muller, J.E., and Okulitch, A.V., 1979, Fraser River, B.C.-Washington: Geological Survey of Canada, Map 1386A, Geological Atlas, Sheet 92, scale 1:1,000,000.

Rogers, A. M., Walsh, T. J., Kockelman, W. J., and Priest, G. R., 1996, Earthquake hazards in the Pacific Northwest—An overview in Rogers, A. M., Walsh, T. J., Kockelman, W. J., and Priest, G. R. (eds.), Assessing Earthquake Hazards and Reducing Risk in the Pacific Northwest: U. S. Geological Survey Professional Paper 1560, v. 1, p. 1-54.

Satake, K. Shimazaki, K., Tsuji, Y., and Ueda, K., 1996, Time and size of a giant earthquake in Cascadia inferred from Japanese tsunami records of January 1700: Nature, v. 379, p. 246-249.

Satake, K., Wang, K., and Atwater, B.F., 2003, Fault slip and seismic moment of the 1700 Cascadia earthquake inferred from Japanese tsunami descriptions: Journal of Geophysical Research, v. 108, p. 2535.

Schmidt, U.B., 2003, Summary of search for expression of Leech River fault west of Vancouver Island: unpublished report prepared for Geological Survey of Canada.

Schwartz, D.P. and Coppersmith, K.J., 1984, Fault behavior and characteristic earthquakes--examples from the Wasatch and San Andreas fault zones: Journal of Geophysical Research, v. 89, p. 5681-5698.

Sherrod, B.L., Blakely, R.J. Weaver, C.S. Kelsey, H.M. Barnett, E. Liberty, L. Meagher, K.L. and Pape, K., 2008, Finding concealed active faults: Extending the southern Whidbey Island fault across the Puget Lowland, Washington: Journal of Geophysical Research, v. 113, p. B05313.

Sherrod, B.L., Brocher, T.M., Weaver, C. S., Bucknam, R.C., Blakely R.J., Kelsey, H.M., Nelson, A.R. and Haugerud, R., 2004, Holocene fault scarps near Tacoma, Washington, USA: Geology, v. 32, p. 9-12.

Siedlecki, E.M. and Schermer, E.R., 2007, Paleoseismology of the Boulder Creek fault, Kendall, WA: Geological Society of America Abstracts with Programs, v. 39, p. 26.

Snavely, P.D. and Wells, R.E., 1996, Cenozoic evolution of the continental margin of Oregon and Washington, in Rogers, A.M., Walsh, T.J., Kockelman, W.J., and Priest, G.R. (eds.), Assessing earthquake hazards and reducing risk in the Pacific Northwest: U.S. Geological Survey Professional Paper 1560, v. 1, p. 161-182.

ten Brink, U.S., Song, J., and Bucknam, R.C., 2006, Rupture models for the A.D. 900–930 Seattle fault earthquake from uplifted shorelines: Geology, v. 34, p. 585–588.

Wagner, H.C. and Tomson, J.H., 1987, Offshore geology of the Strait of Juan de Fuca; State of Washington and British Columbia, Canada: Washington Division of Geology and Earth Resources Open-File Report 87-1, 16 p.

Walsh, T.J. and Logan, R.L., 2007, Field data for a trench on the Canyon River fault, southeast Olympic Mountains, Washington: Washington Division of Geology and Earth Resources Open-file Report, OFR 2007-1, 1 sheet (60 x 36 in.).

Ward, S.N., 1998a, On the consistency of earthquake moment rates, geological fault data, and space geodetic strain: the United States: Geophysical Journal International, v. 134, p. 172-186.

Ward, S.N., 1998b, On the consistency of earthquake moment release and space geodetic strain rates: Europe: Geophysical Journal International, v. 135, p. 1011-1018.

Wells, D.L. and Coppersmith, K.J., 1994, New empirical relationships among magnitude, rupture length, rupture width, rupture area, and surface displacement: Bulletin of the Seismological Society of America, v. 84, p. 974-1002.

Wells, R.E., Weaver, C.S., and Blakely, R.J., 1998, Forearc migration in Cascadia and its neotectonic significance: Geology, v. 26, p. 759-762.

Wesnousky, S.G., 1986, Earthquakes, Quaternary faults, and seismic hazard in California: Journal Geophysical Research, v. 91, p. 12,587-12,631.

Wilson, J.R., Bartholomew, M.J., and Carson, R.J., 1979, Late Quaternary faults and their relationship to tectonism in the Olympic Peninsula, Washington: Geology, v. 7, p. 235-239.

Witter, R.C., Givler, R.W., and Carson, R.J., 2008, Two post-glacial earthquakes on the Saddle Mountain West fault, southeastern Olympic Peninsula, Washington, Bulletin of the Seismological Society of America, Vol. 98, No. 6, pp. 2894–2917, December 2008, doi: 10.1785/0120080127.

Witter, R.C., K.I. Kelson, A.D. Barron, and S.T. Sundermann, 2003, Map of Active Fault Traces, geomorphic features and Quaternary surficial deposits along the central Calaveras fault, Santa Clara County, California: U.S. Geological Survey, National Earthquake Hazards Reduction Program Final Technical Report, Award No. 01HQGR0212, 32 p.

Wong, I.G., Thomas, P.A., and Abrahamson, N., 2004, The PEER-Lifelines validation of software used in probabilistic seismic hazard analysis, *in* 2004 Geotechnical Engineering for Transportation Projects, Proceedings, M. Yegian and E. Kavazanjian (eds.), American Society of Civil Engineers, Geotechnical Special Publication No. 126, v. 1, p. 807-815.

Youngs, R.R., Chiou, S.-J, Silva, W.J., and Humphrey, J.R., 1997, Strong ground motion attenuation relationships for subduction zone earthquakes: Seismological Research Letters, v. 68, p. 58-73.

Youngs, R.R. and Coppersmith, K.J., 1985, Implications of fault slip rates and earthquake recurrence models to probabilistic seismic hazard estimates: Bulletin of the Seismological Society of America, v. 75, p. 939-964.

Zhao, J.X., Zhang, J., Asano, A., Ohno, Y., Oouchi, T., Takahashi, T., Ogawa, H., Irikuar, K., Thio, H.K., Somerville, P.G., Fukushima, Y., and Fukushima, Y., 2006, Attenuation relations of strong ground motion in Japan using site classification based on predominant period: Bulletin of the Seismological Society of America, v. 96, p. 898-913.

Zollweg, J.E. and Johnson, P.A., 1989, The Darrington seismic zone in northwestern Washington: Bulletin of the Seismological Society of America, v. 79, p. 1833-1845.

Table 1
Crustal Faults Included in the PSHA

Fault Name[2]	Probability of Activity	Rupture Model	Style of Faulting	Fault Dip (degrees)	Maximum Seismogenic Depth (km)	Maximum Rupture Length (km)[3]	Maximum Magnitude (M)[4]	Recurrence Models	Slip Rate (mm/yr)[5]	Comments
Beaufort Range fault	0.5	Unsegmented (1.0)	SS (1.0)	90 (1.0)	15 (0.2) 20 (0.4) 25 (0.4)	75 (1.0)	7.3	Characteristic (0.6) Maximum Magnitude (0.3) Exponential (0.1)	0.05 (0.3) 0.25 (0.4) 0.5 (0.3)	No unambiguous evidence of late Quaternary activity exists. The 1946 M 7.2 earthquake occurred in close proximity to fault and with fault-parallel nodal plane suggesting Beaufort Range fault could be source. Slip rate is unknown. Modeled rate reflects moderate geomorphic expression with large uncertainty.
Boulder Creek fault (not included in USGS Quaternary fault database; included in 2008 NSHM.)	1.0	Unsegmented (1.0)	Rev (1.0)	25 S (0.3) 40 S (0.35) 60 S (0.35)	20 (0.3) 25 (0.4) 30 (0.3)	Length fixed (0.5) 12 (0.5)	6.5	Characteristic (0.6) Maximum Magnitude (0.3) Exponential (0.1)	0.2 (0.2) 0.4 (0.6) 0.7 (0.2)	The Boulder Creek fault was an Eocene normal fault that may have been reactivated as a reverse fault, with Quaternary surface expression along the Kendall scarp (Haugerud et al., 2005; Barnett, 2007). Holocene events have been documented in trenches (Barnett, 2007; Barnett et al., 2007; Siedlecki and Schermer, 2007). Holocene Kendall fault scarps extend about 12 km (B. Sherrod, pers. comm. 2008). Mapped BCF trace is 17 km. Displacement per event is 0.8-1.9 m (Siedlecki and Schermer, 2007; Barnett, 2007; Barnett et al., 2007; B. Sherrod, pers. comm., 2008). Large slip suggests subsurface rupture length is longer than mapped fault length. We model Mmax using both magnitude-length and magnitude-displacement relationships. For Mmax from displacement, rupture must occur along mapped fault but may extend bilaterally beyond the mapped extent to length required by magnitude; magnitudes calculated from average displacements of 0.8, 1.2, 2.0 m. 1.9-2.5 m of vertical separation of soils just below Mazama ash (7700 yrs) in trenches suggests vertical displacement rate of 0.25-0.35 mm/yr, assuming little time between soil and Mazama (Barnett, 2007); 2008 NSHM uses 0.33 mm/yr. Preferred value of 0.4 from mean dip and vertical rate. Lower end includes lower vertical rate and steeper dip and some time lag between oldest event and Mazama eruption. Higher rate reflects higher vertical rate and shallower dip. Fault strike: N75E; N-S shortening: 0.3 mm/yr
						17 (0.5)	6.7	as above	as above	
						Length Unconstrained (0.5) *(magnitude calculated from average displacement; see comments)*	6.8 (0.2)	as above	as above	
							7.0 (0.6)	as above	as above	
							7.2 (0.2)	as above	as above	
Calawah fault (USGS #550 Class A; not included in 2008 NSHM.)	1.0	Unsegmented	RO (0.3)	45 N (0.5) 60 N (0.5)	20 (0.2) 25 (0.4) 30 (0.4)	83 (0.3)	7.4	Characteristic (0.6) Maximum Magnitude (0.3) Exponential (0.1)	0.05 (0.3) 0.2 (0.4) 1.0 (0.2) 2.0 (0.1)	Fault has been mapped as steep strike-slip, reverse, and normal. Recent mapping suggests left-lateral-reverse (McCrory et al., 2005). Mapped trace is 83 km. Rupture lengths include entire fault and half the fault rupturing. P. McCrory (pers. comm., 2008) reports post-glacial faulting. Dip unknown. Slip rate is unknown. Qfault assigns <0.2 based on lack of information. P. McCrory (pers. comm., 2008), based on unpublished mapping, considers slip rate can be no more than 1-2 mm/yr. Fault strike: ca. N60W; N-S shortening: ca. 0.1 mm/yr
						40 (0.7)	7.0	as above	as above	
			SS (0.7)	60 (0.3) 75 (0.4) 90 (0.3)	as above	83 (0.5)	7.4	as above	as above	
						40 (0.5)	7.0	as above	as above	
Devils Mountain fault (USGS #574 Class A; included in 2008 NSHM)	1.0	Unsegmented (0.7)	RO (0.3)	40 S (0.1) 45 N (0.45) 65 N (0.45)	20 (0.3) 25 (0.4) 30 (0.3)	40 (0.4)	7.0	Characteristic (0.6) Maximum Magnitude (0.3) Exponential (0.1)	0.08 (0.1) 0.2 (0.2) 0.35 (0.4) 0.5 (0.2) 0.75 (0.1)	Dragovich and DeOme (2006) and Dragovich and Stanton (2007) report evidence of Holocene activity onshore and latest Pleistocene offset in Lake Cavanuagh. Johnson et al. (2001) propose possible segment boundaries at discontinuities at about 122.95W and 122.55W; Hayward et al. (2006) note possible transfer structure at 122.95W. No evidence that these constitute rupture segments has been reported. Johnson et al. (2001) and Hayward et al. (2006) report fault is a left-lateral transpressional structure. NSHM 2008 model the fault as reverse. Fault length is 125 km. Segment lengths for segmented model based on proposed segment boundaries of Johnson et al. (2001). Johnson et al. (2001) see dips of 45-75N offshore, becoming steeper eastward. Dragovich and DeOme (2006) state outcrop patterns suggest ca. 40S. B. Sherrod (pers. comm. 2008) says definitely north dipping. 2008 NSHM use 60N. Slip rate unknown. Qfault assigns <0.2 mm/yr based on lack of information. Well-log and offshore data suggest vertical rate of 0.05-0.3 mm/yr, 0.16 mm/yr preferred (Johnson et al. 2001a). Model includes range of vertical rates of displacement from offshore and well-log data (Johnson et al., 2001) and H:V ratio from Utsalady fault observations (Johnson et al., 2004a; see Utsalady fault below) to develop slip rate distribution. Fault strike: N80W; N-S shortening: ca. 0.04 mm/yr
						60 (0.5)	7.2	as above	as above	
						125 (0.1)	7.6	as above	as above	
			SS (0.7)	60N (0.3) 70 N (0.4) 80 N (0.3)	as above	40 (0.3)	7.0	as above	as above	
						60 (0.4)	7.2			
						125 (0.3)	7.6			
		Segmented (0.3)								
		West	RO (0.3)	45 N (0.5) 65 N (0.5)	as above	25	6.8	as above	as above	
			SS (0.7)	60N (0.3) 70 N (0.4) 80 N (0.3)	as above	25	6.8	as above	as above	

Table 1
Crustal Faults Included in the PSHA

Fault Name[2]	Probability of Activity	Rupture Model	Style of Faulting	Fault Dip (degrees)	Maximum Seismogenic Depth (km)	Maximum Rupture Length (km)[3]	Maximum Magnitude (M)[4]	Recurrence Models	Slip Rate (mm/yr)[5]	Comments
		Central	RO (0.3)	45 N (0.5) 65 N (0.5)	as above	30	6.9	as above	as above	
			SS (0.7)	60N (0.3) 70 N (0.4) 80 N (0.3)	as above	30	6.9	as above	as above	
		East	RO (0.3)	40 S (0.1) 45 N (0.45) 65 N (0.45)	as above	70	7.3	as above	as above	
			SS (0.7)	60N (0.3) 70 N (0.4) 80 N (0.3)	as above	70	7.3	as above	as above	
Eastern Olympic Mountains Fault Zone (includes Saddle Mountains [SM] USGS #552 Class A; Hood Canal [HC] USGS # 575 Class B, Canyon River [CR], Frigid Creek [FC]) ; not included in 2008 NSHM.)	1.0	Fault Zone	RO (0.3)	60 E (0.4) 75 E (0.6)	20 (0.2) 25 (0.4) 30 (0.4)	90 (0.1)	7.4	Characteristic (0.5) Maximum Magnitude (0.2) Exponential (0.3)	0.2 (0.15) 0.5 (0.4) 1.0 (0.3) 4.0 (0.15)	Mapped faults are short (< 5km each) with large displacements, suggesting faults are longer than recognized at surface. Model treats region as 90-km long zone of transpression that includes the mapped faults and possible extensions. Constituent faults have oblique expression in trench exposures, but sense of lateral slip is ambiguous: SM East reported LL (Wilson et al (1979) and RL (Witter et al., 2008). Striations in CR suggest LL-reverse slip. HC interpreted as right-lateral and/or reverse. Holocene events documented on SMW, SME, and CR. SME, SMW, and CR have steeply east- to southeast-dipping faults in trenches. Seismic reflection profiles show faults along inferred HC with steep dips, both directions; Roberts (1991) models HC as east-dipping. Slip rates have been estimated for some constituent faults. Wilson et al. (1979) estimate of minimum 0.25 mm/yr vertical in Holocene on SMW. Walsh and Logan (2007) estimate of 3 mm/yr of slip on CR. Witter et al. (2008) observations on SME suggest slip rates from about 0.3 to 3 mm/yr, with 1-2 mm/yr preferred. Slip rate on HR is unknown. Fault strike: N25E.; N-S shortening: ca. 0.6 mm/yr
						60 (0.4)	7.2	as above	as above	
						30 (0.5)	6.9	as above	as above	
			SS (0.7)	60 E (0.2) 75 E (0.4) 90 (0.4)	as above	90 (0.3)	7.5			
						60 (0.4)	7.2	as above	as above	
						30 (0.3)	6.9	as above	as above	
Lake Creek-Boundary Creek (aka Little River) (not included in Qfault database; included in 2008 NSHM)	1.0	Unsegmented	RO (0.3)	60 N (0.4) 75 N (0.6)	20 (0.2) 25 (0.4) 30 (0.4)	22 (0.3)	6.7	Characteristic (0.6) Maximum Magnitude (0.3) Exponential (0.1)	0.1 (0.15) 0.5 (0.35) 1.0 (0.35) 2.5 (0.15)	Holocene events documented in trenches (Nelson et al., 2007) Trench stratigraphy shows north-side-up separation and indicates significant but unknown left-lateral component. Grooves in fault plane show 4:1 horizontal:vertical (Nelson et al. 2007). 2008 NSHM treats as reverse. Nelson et al. (2007) are certain of only 22 km. Length of mapped Quaternary trace is 30 km. Mapped bedrock trace is 64km. 2008 NSHM uses 30 km. Dip is near vertical to steeply N-dipping in trenches (Nelson et al., 2007). 2008 NSHM uses 60N. Slip rate is poorly constrained. 2 events have been documented between 600-2000 yrs, with a possible earlier event <5ka (Nelson et al. 2007). About 0.5-1.2 m net vertical displacement occurred in all events. Only about 2 m late Quaternary offset. In model, minimum rate is late Quaternary rate of about 0.1 mm/yr. Maximum rate of ca 2.4 mm/yr is latest Holocene rate with 1 m vertical in 2000 years and 4:1 H:V. 2008 NSHM uses 0.43 mm/yr, with no documentation Fault strike: ca N80W; N-S shortening: ca.-0.09 mm/yr
						30 (0.4)	6.9	as above	as above	
						64 (0.3)	7.2	as above	as above	
			SS (0.7)	60 N (0.2) 75 N (0.4) 90 (0.4)	as above	22 (0.3)	6.7	as above	as above	
						30 (0.4)	6.9	as above	as above	
						64 (0.3)	7.3	as above	as above	

Table 1
Crustal Faults Included in the PSHA

Fault Name[2]	Probability of Activity	Rupture Model	Style of Faulting	Fault Dip (degrees)	Maximum Seismogenic Depth (km)	Maximum Rupture Length (km)[3]	Maximum Magnitude (M)[4]	Recurrence Models	Slip Rate (mm/yr)[5]	Comments
Leech River fault (not included in Qfault database or 2008 NSHM)	0.7	Unsegmented	RO (0.3)	50 N (0.4) 65 N (0.4) 80 N (0.2)	20 (0.2) 25 (0.4) 30 (0.4)	110 (0.1)	7.5	Characteristic (0.6) Maximum Magnitude (0.3) Exponential (0.1)	0.08 (0.1) 0.2 (0.2) 0.35 (0.4) 0.5 (0.2) 0.75 (0.1)	Clowes et al. (1987) interpret LRF as thrust from Lithoprobe data. Bear Creek Shear Zone, coincident with LRF, is a steep left-lateral structure at surface (Groome, 2000). Fault is on strike with oblique-LL faults from Puget Sound. Mapped onshore fault length 75 km but fault extends offshore. Macleod et al. (1977) state it is truncated by Calawah/Crescent fault, suggesting maximum length of about 110 km. Shorter rupture lengths reflect lengths of segments with E-W and WNW-ESE strikes. No evidence of post Eocene displacement. Seismicity is mostly below and does not delineate fault (Mulder and Rogers, 2002). No fault scarps across Quaternary surfaces yet identified in LiDAR; lineaments interpreted as glacial and/or fkuvial features (G. Rogers, pers. comm., 2008). Fault is immediately adjacent to and on strike with late Quaternary faults in Puget Sound (e.g. Devils Mountain Fault). Lithoprobe shows shallow N dip; shear zones at surface have steeper dips. Calvert et al. (2006) show moderate north dip. Interpretation of LRF as having very low dip is considered in the inactive model. Plate interface is located at 25-30 km; the E-layer occurs at 18-25 km, in most areas at ca 20 km (Calvert et al., 2006). Clowes et al. (1987) suggest fault extends to about 10 km. Model reflects higher weight on the interpretation of the E layer as the control on the base of seismogenic crust. Active model assumes fault reaches surface. Slip rate is unknown. Modeled rate based on an interpretation of continuity with active faults in northern Puget Sound using slip rate distribution from the Devils Mountain fault (see Table 4.4-1b). Fault strike: ca E-W to N70W; N-S shortening: 0.01 mm/yr
						75 (0.4)	7.3	as above	as above	
						35 (0.5)	7.0	as above	as above	
			SS (0.7)	50 N (0.2) 65 N (0.4) 80 N (0.4)	20 (0.2) 25 (0.4) 30 (0.4)	110 (0.3)	7.6	as above	as above	
						75 (0.4)	7.4	as above	as above	
						35 (0.3)	7.0	as above	as above	
Outer Island fault	0.9	Unsegmented (1.0)	RO (0.5)	60 W (1.0)	15 (0.2) 20 (0.4) 25 (0.4)	50 (1.0)	7.1	Characteristic (0.6) Maximum Magnitude (0.3) Exponential (0.1)	0.1 (0.3) 0.5 (0.4) 1.0 (0.2) 2.0 (0.1)	Outer Island fault has geomorphic expression in offshore bathymetry and is revealed in seismic tomography (Dash et al., 2007). Dash et al. 92007) interpret fault as westd-ipping reverse fault. Fault is associated with and may include Porlier Pass fault of Barrie and Hill (2004) across which they see Holocene sediments truncated. Fault dips steeply and throw varies. Slip rate is unknown. Modeled rate reflects high uncertainty, evidence for Holocene displacement with possibly tens of meters of post-glacial movement (Barrie and Hill) and regional considerations.
			SS (0.5)	90 (1.0)	as above	50 (1.0)	7.1	as above	as above	
San Juan Island fault zone	0.7	Fault zone narrow (0.8)	RO (0.3)	60 N (0.5) 60 S (0.5)	20 (0.3) 25 (0.4) 30 (0.3)	55 (0.5)	7.2	Characteristic (0.5) Maximum Magnitude (0.2) Exponential (0.3)	0.03 (0.3) 0.15 (0.4) 0.3 (0.3)	Zone includes multiple faults mapped through western San Juan Island and offshore, and includes Trout Lake. Evidence of activity on faults is uncertain; they have strong geomorphic expression onshore but age is not well constrained because little study has been done. Offshore, V. Barrie has identified features interpreted as possible fault offsets in late Quaternary materials on some of the mapped fault traces. Given uncertainty in characterization of individual faults, we model the region as a fault zone. Probability of activity reflects offshore observations interpreted as Holocene fault displacements in unpublished work. Given location and orientation, we use Devils Mountain fault as analogue for style and rate. Slip rate is unknown. Modeled rate is simplified from Devils Mountain fault slip rate, scaled by relative fault length.
						27 (0.5)	6.8	as above	as above	
			SS (0.7)	60 N (0.3) 90 (0.4) 60 S (0.3)	as above	55 (1.0)	7.2	as above	as above	
		Fault zone wide (0.2)	RO (0.3)	60 N (0.5) 60 S (0.5)	20 (0.3) 25 (0.4) 30 (0.3)	55 (0.5)	7.2	Characteristic (0.5) Maximum Magnitude (0.2) Exponential (0.3)	0.03 (0.3) 0.15 (0.4) 0.3 (0.3)	Wide zone includes NW-striking faults on San Juan Island that are subparallel to faults offshore that have been identified as having Quaternary offset but do not have, and are not on strike with, identified offsets.
						27 (0.5)	6.8	as above	as above	
			SS (0.7)	60 N (0.3) 90 (0.4) 60 S (0.3)	as above	55 (1.0)	7.2	as above	as above	

Table 1
Crustal Faults Included in the PSHA

Fault Name[2]	Probability of Activity	Rupture Model	Style of Faulting	Fault Dip (degrees)	Maximum Seismogenic Depth (km)	Maximum Rupture Length (km)[3]	Maximum Magnitude (M)[4]	Recurrence Models	Slip Rate (mm/yr)[5]	Comments
Seattle Fault (USGS #570 Class A; included in 2008 NSHM)	1.0	Unsegmented (1.0)	Rev	30S (0.5) 45 S (0.5)	20 (0.3) 25 (0.4) 30 (0.3)	70 (0.5)	7.3	Characteristic (0.6) Maximum Magnitude (0.3) Exponential (0.1)	0.2 (0.1) 0.7 (0.2) 0.9 (0.4) 1.4 (0.2) 2.0 (0.1)	Fault zone comprises three traces at surface. NSHM 2008 treat each trace as independent. Brocher et al. (2004) and other models suggest one major structure with imbricate thrusts and backthrusts. Given distance from facilities, it is modeled here as a single fault. Ca. 900 A.D. event has been documented on the fault. Kelsey et al. (2008) argue that shallow bedding plane faults are also seismogenic and can be independent of basal thrust or rupture with it. Given distance from facilities, this scenario is not included in the model. Full length of zone is about 70 km. N-striking cross-fault about half way across dextrally offsets faults. Brocher et al. (2004; 2005) model master floor thrust with about 30° dip. Surficial faults are steeply north-dipping. Model includes blind and surface-rupturing scenarios, based on interpretation that tip of master ramp thrust is at about 4 km, with surficial backthrusts from 0-4 km. Nelson et al. (2003) report 0.2 mm/yr for post 16-ka slip rate. Late Holocene slip rate is about 2.0. ten Brink et al. (2006) estimate 1.1 shortening rate (1.4 mm/yr dip-slip on 38° fault) since 16 ka. USGS Qfault reports range of 0.7-1.0 mm/yr, with 0.9 mm/yr preferred. Modeled minimum rate represents the Nelson et al. (2003) post 16 ka rate. 0.9 mm/yr is preferred value from Qfault. 1.4 mm/yr is ten Brink et al. (2006) shortening rate on 38° fault. High end reflects Nelson et al. (2003) late Holocene rate. Fault strike: N85W; N-S shortening: ca. 0.8 mm/yr
						35 (0.5)	7.0	as above	as above	
Skipjack fault	0.9	Unsegmented (1.0)	Rev (0.4)	60 N (0.5) 60 S (0.5)	20 (0.4) 25 (0.4) 30 (0.2)	40 (1.0)	7.0	Characteristic (0.6) Maximum Magnitude (0.3) Exponential (0.1)	0.07 (0.3) 0.4 (0.4) 0.7 (0.3)	Only data on fault indicates Quaternary, possibly Holocene, displacement, with vertical fault in shallow subsurface. Source model based on analogy to better known nearby faults. Reverse model reflects analogy to Boulder Creek fault; strike-slip model reflects analogy to Devils Mountain fault. Slightly higher weight on SS because data indicate vertical fault. Slip rates also reflect these analogies; reverse uses Boulder Creek rate with greater uncertainty range covering an order of magnitude; strike-slip based on Devils Mountain fault scaled by fault length.
			SS (0.6)	90 (1.0)	as above	40 (1.0)	7.0	as above	0.03 (0.3) 0.15 (0.4) 0.3 (0.3)	
Southern Whidbey Island fault (SWIF) (USGS #572 Class A; included in 2008 NSHM)	1.0	Unsegmented (1.0)	Rev (0.5)	30 S (0.4) 45 S (0.4) 60 S (0.2)	20 (0.3) 25 (0.4) 30 (0.3)	30 (0.4)	6.9	Characteristic (0.6) Maximum Magnitude (0.3) Exponential (0.1)	0.7 (0.15) 0.9 (0.3) 1.2 (0.45) 1.5 0.2)	Mapping west of 123W is incomplete and traces are discontinuous. Linkage of discontinuous traces could extend SWIF to meet the Devils Mountain fault at about 123.3W. Model includes SWIF (western extent at 123W) and SWIF Extended (western extent at ca 123.3W;. SWIF comprises at least three strands, simplified here to one. Quaternary sense of slip unknown; Johnson et al. (2004a, b) describe zone as dextral-reverse based on Eocene history of dextral slip on Coast Range fault. Brocher et al (2005) and Sherrod et al. (2008) models include shallow (3-4 km) surface faults rooting into S-dipping thrust with minor strike-slip possible. Faults on northern Whidbey Island are sinistral-reverse. NSHM 2008 models SWIF as oblique. We include both shallowly dipping reverse model and steeply dipping oblique model. Reverse model rupture lengths include full, half, and 1/3 fault length with higher weight on half and third lengths, based on global dataset indicating 90+-km-long reverse ruptures are rare. Rupture lengths in strike-slip model are full and half fault ruptures, evenly weighted. Johnson et al. (1996) report faulting of late Quaternary strata. Kelsey et al. (2008) report Holocene faulting across SWIF on Whidbey Island. Sherrod et al. (2008) document multiple post-glacial events in trenches across lineaments on trend with SWIF on mainland. Individual faults dip moderately to steeply north near surface, which is included in oblique model. Reverse model dips to the south, based on Brocher et al (2005) and Sherrod et al (2008) models. Reverse model includes blind and surface-rupturing scenarios, based on interpretation that tip of master ramp thrust is at about 4 km, with surficial backthrusts from 0-4 km. Slip rate is unknown with certainty. Johnson et al. (2004b) report a minimum 0.6 mm/yr vertical displacement rate. 2008 NSHM uses 0.6 mm/yr vertical rate as the slip rate, divided equally across three strands. In reverse model, we use vertical displacement rate from Johnson et al. (2004b) and dip to develop reverse fault slip rate distribution
						45 (0.4)	7.1	as above	as above	
						90 (0.2)	7.4	as above	as above	
			SS (0.5)	60 N (0.5) 80 N (0.5)	as above	63 (0.5)	7.3	as above		
						126 (0.5)	7.6	as above	as above	

Fault Name[2]	Probability of Activity	Rupture Model	Style of Faulting	Fault Dip (degrees)	Maximum Seismogenic Depth (km)	Maximum Rupture Length (km)[3]	Maximum Magnitude (M)[4]	Recurrence Models	Slip Rate (mm/yr)[5]	Comments
										for zone. In strike-slip model, we use vertical rate of displacement from Johnson et al., (2004b) and the H:V ratio from Utsalady fault observations (Johnson et al., 2004a) to develop oblique slip rate distribution; see Utsalady fault below). Fault strike: N50W; N-S shortening: Reverse model: ca. 0.5 mm/yr; SS model: ca. 0.9 mm/yr; Average: ca. 0.7 mm/yr
Straits of Juan de Fuca Fault Zone (USGS #551 Class B; not included in 2008NSHM)	1.0	Fault Zone (1.0)	RO (0.5)	30 N (0.2) 60 N (0.3) 60 S (0.3) 30 S (0.2)	20 (0.3) 25 (0.4) 30 (0.3)	60 (0.5)	7.2	Characteristic (0.5) Maximum Magnitude (0.2) Exponential (0.3)	0.1 (0.3) 0.5 (0.4) 1.0 (0.3)	Suite of subparallel faults distributed across Strait with approx 5km spacing; strike on 270°-320° strike. Style is unknown. USGS Qfault (Lidke, 2004) assign normal, but this seems unlikely. Model assumes reverse oblique from regional considerations. Wagner and Tomsom (1987) and Johnson et al. (2000) report Quaternary and probably Holocene offset in offshore seismic data. Most faults moderate to steep, some lower angle (Lidke 2004). Slip rate distribution reflects lack of knowledge or clear late Quaternary expression; USGS Q fault assigns < 0.2 mm/yr (Lidke, 2004). McCaffrey et al. (2007) modeled rates of ca. 1.0 for boundary fault located within zone. Fault strike: ca. N70W; N-S shortening: ca 0.01 mm/yr
						30 (0.5)	6.9	as above	as above	
			SS (0.5)	60 N (0.3) 90 (0.4) 60 S (0.3)	as above	115 (0.4)	7.6	as above	as above	
						60 (0.4)	7.3	as above	as above	
						30 (0.2)	6.9	as above	as above	
Strawberry Point fault (USGS #571 Class A; included in 2008 NSHM)	1.0	Unsegmented (1.0)	RO (0.3)	45 N (0.5) 60 N (0.5)	20 (0.3) 25 (0.4) 30 (0.3)	26	6.8	Characteristic (0.6) Maximum Magnitude (0.3) Exponential (0.1)	0.2 (0.2) 0.5 (0.2) 0.8 (0.4) 1.1 (0.15) 2.0 (0.05)	Fault is left-lateral transpressional. Johnson et al. (2001) and Johnson (2001a) claim fault is predominantly strike-slip due to subvertical dip and change in sense of vertical displacement. Mapped length may be a minimum. Dadisman et al., (2000), Johnson et al. (2000), and Johnson et al. (2001a) suggest it may extend east of mapped extent to mainland. Johnson et al. (2001a), report minimum length of 22 km, but Johnson (2001a) reports minimum of 26 km and Qfault map shows 26 km. Fault offsets Late Quaternary (80-125 ka) Whidbey Island formation (Johnson et al., 2001a). Fault is subvertical at western end. At eastern end, fault splays into 4 45-degree north-dipping faults (Johnson et al., 2001). Change from south side up to north side up, suggests steep dip. NSHM 2008 uses 90. Johnson et al., (2001) report 0.25 mm/yr minimum vertical rate; 0.35 mm/yr minimum shortening, up to 2 mm/yr; unknown strike-slip on east side of Whidbey Island (WI) and 0.04-0.10mm/yr minimum vertical rate, with maximum of 2 mm/yr on west side WI. Qfault reports 0.25 mm/yr as preferred value);, and NSHM 2008 use 0.25 mm/yr , but this is a vertical rate (Johnson et al., 2001). Rates in model are based on vertical rates from this fault with 1.3-2.3 H:V ratio on Utsalady fault. Fault strike: N80W; N-S shortening: ca. 0.05 mm/yr
			SS (0.7)	60 (0.2) 75 (0.4) 90 (0.4)	as above	26	7.1	as above	as above	
Tacoma fault (USGS #581 Class A; not included in 2008 NSHM)	1.0	Unsegmented (1.0)	Rev	30 N (0.2) 45 N (0.4) 60 N (0.2) 70 N (0.2)	20 (0.3) 25 (0.4) 30 (0.3)	23 (0.3)	6.8	Characteristic (0.6) Maximum Magnitude (0.3) Exponential (0.1)	0.25 (0.2) 0.6 (0.7) 2.5 (0.1)	Tacoma fault bounds the south side of the Seattle uplift. Brocher et al. (2001), Johnson et al. (2004) and Sherrod et al. (2004) suggest Tacoma fault is a backthrust to the Seattle fault, which could rupture independently or in conjunction with the Seattle fault. Fault caused uplift of shorelines in an event between AD. 770 and 1160 (Bucknam et al., 1992; Sherrod et al., 2004). This is within the age range of the last Seattle fault earthquake (ca. AD 900). The Tacoma fault may have ruptured with the Seattle fault or independently within the same general time frame. Both ruptures contributed to several meters of 4m uplift of the Seattle Uplift. Given the distance from the sites, we model it only as an independent fault. 23 km of fault are mapped at the surface, along western end. Geophysical lineaments extend another 27+ km to the east, or about 50 km total, from Hood Canal to Tacoma (Sherrod et al., 2004; Brocher et al., 2001). Trench excavations show shallow dips (ca 20). Geophysical imaging indicates a steeper dip for the fault (ca 70) (Brocher et al., 2001; Johnson et al., 2004). Johnson et al. (2004) model a moderate dip for TF backthrust under Seattle Uplift pop-up. Brocher et al. (2004) suggest 35 N. Paleoseismic studies indicate uplift around Tacoma fault and one trench exposed folding and faulting that may be secondary (Sherrod et al., 2004). Model includes blind and surface-rupturing scenarios, analogous to Seattle fault. Nelson et al. (2003) report 0.2 mm/yr for post 16-ka slip rate. Late Holocene slip
						50 (0.7)	7.1	as above	as above	

Table 1
Crustal Faults Included in the PSHA

Fault Name[2]	Probability of Activity	Rupture Model	Style of Faulting	Fault Dip (degrees)	Maximum Seismogenic Depth (km)	Maximum Rupture Length (km)[3]	Maximum Magnitude (M)[4]	Recurrence Models	Slip Rate (mm/yr)[5]	Comments
										rate is about 2.0. ten Brink et al. (2006) estimate 1.1 shortening rate (1.4 mm/yr dip-slip on 38° fault) since 16 ka. USGS Qfault reports range of 0.7-1.0 mm/yr, with 0.9 mm/yr preferred. **Model:** Low end represents the Nelson et al. (2003) post 16 ka rate. 0.9 mm/yr is preferred value from Qfault. 1.4 mm/yr is ten Brink et al. (2006) shortening rate on 38° fault. High end reflects Nelson et al. (2003) late Holocene rate. Fault strike: E-W; N-S shortening: 0.5 mm/yr
Utsalady Point fault (USGS #573 Class A; included in 2008 NSHM)	1.0	Unsegmented	RO (0.3) SS (0.7)	45 N (0.5) 60 N (0.5)	20 (0.3) 25 (0.4) 30 (0.3)	28	6.9	Characteristic (0.6) Maximum Magnitude (0.3) Exponential (0.1)	0.15 (0.25) 0.3 (0.5) 0.4 (0.25)	Fault is transpressional, with sinistral component; Johnson et al. (2001) and Johnson (2001a) claim it is predominantly strike-slip due to subvertical dip. Johnson et al. (2004a) report LL/Rev in trench. 28 km mapped extent (Johnson et al., 2003b) and Qfault map; 30km reported by Johnson et al. (2003a) Qfault; suggestion of possible extension 25 km to the east based on aeromagnetic anomalies (Johnson et al., 2001). Holocene events documented in trench exposure (Johnson et al., 2003b; Johnson et al., 2004a). Fault is subvertical at western end. At eastern end, fault splays into 4-5 steeply north-dipping faults (Johnson et al., 2001). Change from south side up to north side up, suggests steep dip. NSHM 2008 uses 90. Two trenches show evidence for one, probably two Holocene earthquakes, one at 100-400 cal BP and possible other at 1100-2200 cal BP (Johnson et al., 2004a). Johnson et al. (2001a) report 0.10-0.15 mm/yr vertical on Quaternary strata (offshore and onshore). Most recent event (MRE) in trench had LL:vertical ratio of 1.3-2.3 (Johnson et al., 2004a). To model rates, we apply H:V ratio from trench to observed vertical displacement rates to estimate oblique-slip rates. Fault strike: N75W; N-S shortening: ca. 0.0 mm/yr
			SS (0.7)	60 (0.2) 75 (0.4) 90 (0.4)	as above	28	6.8	as above	as above	
West Coast fault	0.5	Unsegmented (1.0)	SS (1.0)	90 (1.0)	15 (0.2) 20 (0.4) 25 (0.4)	200 (0.2)	7.8	Characteristic (0.6) Maximum Magnitude (0.3) Exponential (0.1)	0.05 (0.3) 0.3 (0.4) 1.0 (0.3)	No slip rate data available. Model slip rate values similar to Beaufort Range fault with high end rate larger because fault is longer. Both faults are in close proximity to and could be sources of ca M 7.2 earthquakes.
						100 (0.4)	7.4	as above	as above	
						70 (0.4)	7.2	as above	as above	

1) Except as noted, known Quaternary faults within zones were included.
2) Fault numbers correspond to those in the USGS Quaternary Fault and Fold Database (URL: http://earthquake.usgs.gov/regional/qfaults/).
3) Length is measured as straight-line, end-to-end distance.
4) WC M-A: Wells and Coppersmith (1994) magnitude-area relationship for all faults; WC M-L: Wells and Coppersmith (1994) magnitude-rupture length relationship for all faults; Ells-B M-A: WGCEP (2003) Equation 4.5 magnitude-area relationship; HB: Hanks and Bakun (2002; 2008) magnitude-area relationship. An uncertainty of +/- 0.3 is included for each magnitude value.
5) For all fault sources in the OLY zone, the following b-value distribution was used to calculate earthquake recurrence: 0.8 (weighted 0.333), 0.9 (weighted 0.333), and 1.0 (weighted 0.333).

Additional Comments:
Sum of north-south shortening on modeled faults in Olympic Peninsula is ca. 0.4 mm/yr.

Faults in the USGS Quaternary fault data base not included in the model:
6) Unnamed fault along Barnes Creek (fault #557): Aligned facets in Tertiary bedrock led USGS to classify as Class B fault, but there is no other evidence of Quaternary activity.

Additional Comments:
Sum of north-south shortening on modeled faults is ca 2.4 mm/yr.

Faults in the USGS Quaternary fault data base not included in the model:
Macaulay Creek Thrust (MCT): Mapped bedrock NE-striking thrust fault. The USGS Quaternary fault database includes the fault as a B-class fault based on speculation of activity in Dragovich et al. (1997). Dragovich et al. (1997) propose this fault as the possible source of the M 5.2 Deming earthquake. Mapped extent is only 4 km, but Dragovich et al. (1997) suggest it may extend farther in the subsurface; they do not describe the location of the proposed extension. They also discuss the possibility that the MCT is kinematically linked to the ostensibly reactivated Eocene normal Boulder Creek and Smith Creek faults, but provide no evidence that this occurs. Given the uncertainty in correlation of the Deming earthquake with the MCT, the short mapped extent, and the lack of data regarding Quaternary fault characteristics, we do not include the MCT as a discrete fault source. The Deming earthquake is included within the background seismicity zone.

Table 2
Crustal Seismic Source Zone Parameters

Zone	Style of Faulting	Background Source Parameters Fault Strike (azimuth)	Fault Dip (degrees)	Zone Properties Maximum Magnitude (M)	Maximum Seismogenic Depth (km)	Rates and Recurrence Rates	Spatial Variation in Zone	Recurrence Models	Comment
Puget Lowland (PL)	RO (0.3) SS (0.7)	275 (0.3) 295 (0.4) 315 (0.3)	**RO:** 60 N (0.3) 60 S (0.4) 30 S (0.3) **SS:** 60 N (0.4) 90 N (0.6)	6.7 (0.4) 7.0 (0.5) 7.3 (0.1)	20 km (0.3) 25 km (0.4) 30 km (0.3)	From seismicity (1.0)	Uniform (0.5) Spatial smoothing (0.5)	Truncated Exponential (1.0)	Zone characterized by transpressional faulting on WNW-striking faults. Fault mapping is probably largely complete except in northernmost part of zone and possible blind faults offshore. Fault slip rates are comparable to geodetic shortening rates, so background is modeled with seismicity only. Cumulative N-S shortening rate on faults in PL is about 2.4 mm/yr.
Olympic Peninsula (OLY)	RO (0.3) SS (0.7)	275 (0.3) 295 (0.4) 315 (0.3)	40 N (0.2) 55 N (0.6) 70 N (0.2) **SS:** 60 N (0.2) 75 N (0.6) 90 N (0.2)	6.7 (0.3) 7.0 (0.4) 7.3 (0.2) 7.5 (0.1)	20 km (0.2) 25 km (0.4) 30 km (0.4)	From seismicity (0.5) From geodetics (0.5) *8 nanostrain/yr [4.6 mm/yr] (0.3)* *19 nanostrain/yr [3.1 mm/yr] (0.4)* *10 nanostrain/yr [1.6 mm/yr] (0.3)*	Uniform (0.5) Spatial smoothing (0.5)	Truncated Exponential (1.0)	Zone characterized by transpressional faulting on WNW-striking faults. Thick crust and probably incomplete fault mapping leads to Mmax reaching 7.5. Historical seismicity rate does not reflect interpreted geodetic shortening rates, so background is modeled both with seismicity and with geodetic rate. Cumulative N-S shortening rate on faults in OLY is ca. 0.4 mm/yr. Strain rates are in N-S direction; N-S length of zone is about 165 km.
Vancouver Island (VI)	Rev (0.5) SS (0.5)	NW (1.0)	60 NE (0.5) 60 SW (0.5) **SS:** 90 (1.0)	6.7 [0.2] 7.1 [0.4] 7.5 [0.4]	15 (0.2) 20 (0.4) 25 (0.4)	From seismicity (0.5) From geodetics (0.5) *[1.0 mm/yr-faults] (0.3)* *[2.5 mm/yr-faults] (0.4)* *[5.0 mm/yr-faults] (0.3)*	Uniform (0.5) Spatial smoothing (0.5)	Truncated Exponential (1.0)	Geodetic data suggest NNE shortening with dextral transpression on NW strikes. Quaternary fault mapping highly incomplete. Cumulative weighted average slip on modeled faults is ca. 0.9 mm/yr (range is 0.2-3.5 mm/yr). Strain rates are in NE direction. Geodetic background rate from 1-5 mm/yr minus fault slip rates.

Table 3

Controlling Earthquakes at 3,000-Year Return Period

	M*	**D* (km)**	**ε**
PGA	7.1	62.5	1.55
1.0 sec SA	9.1	112.5	1.75

Table 4

3,000-Year Return Period UHS

Period (sec)	Horizontal
0.01	0.477
0.03	0.477
0.10	1.089
0.15	1.138
0.20	1.070
0.30	0.876
0.40	0.734
0.50	0.622
0.75	0.440
1.00	0.347
1.50	0.236
2.00	0.174
3.00	0.107

Table 5

Summary of Seed Time Histories Used for Trout Lake Dam

Name of Station	Site Class	Event Name	Date	Magnitude (M)	Hypocentral Distance (km)	PGA (g)
Pierce County East Precinct	C (V_S30 =1445 ft/s)	Nisqually	2/28/2001	6.8	62	North: 0.213 East: 0.204 Vertical: 0.155

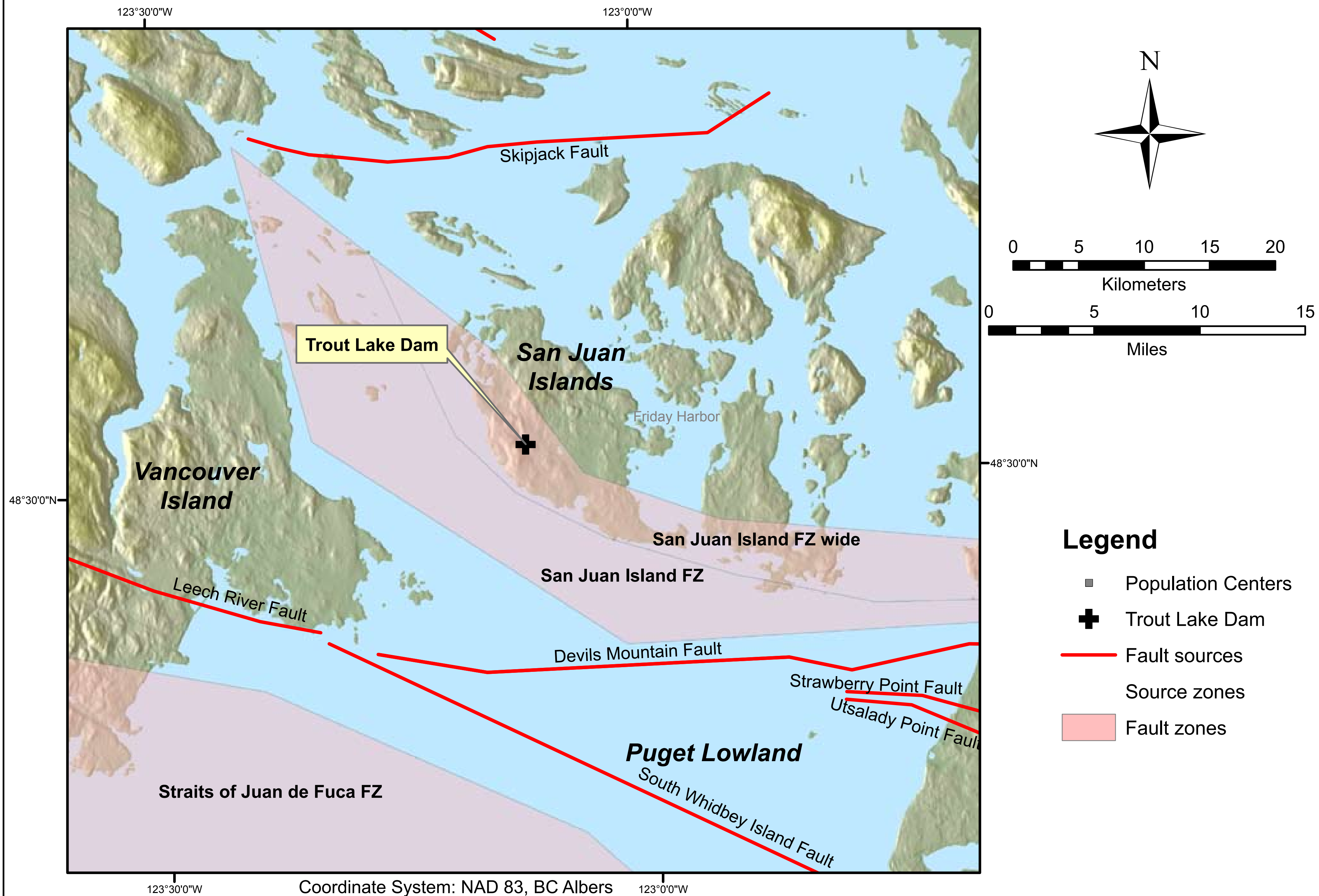

URS	Project No. 22240846	SITE VICINITY MAP	Figure 1
	Trout Lake Dam, Washington		

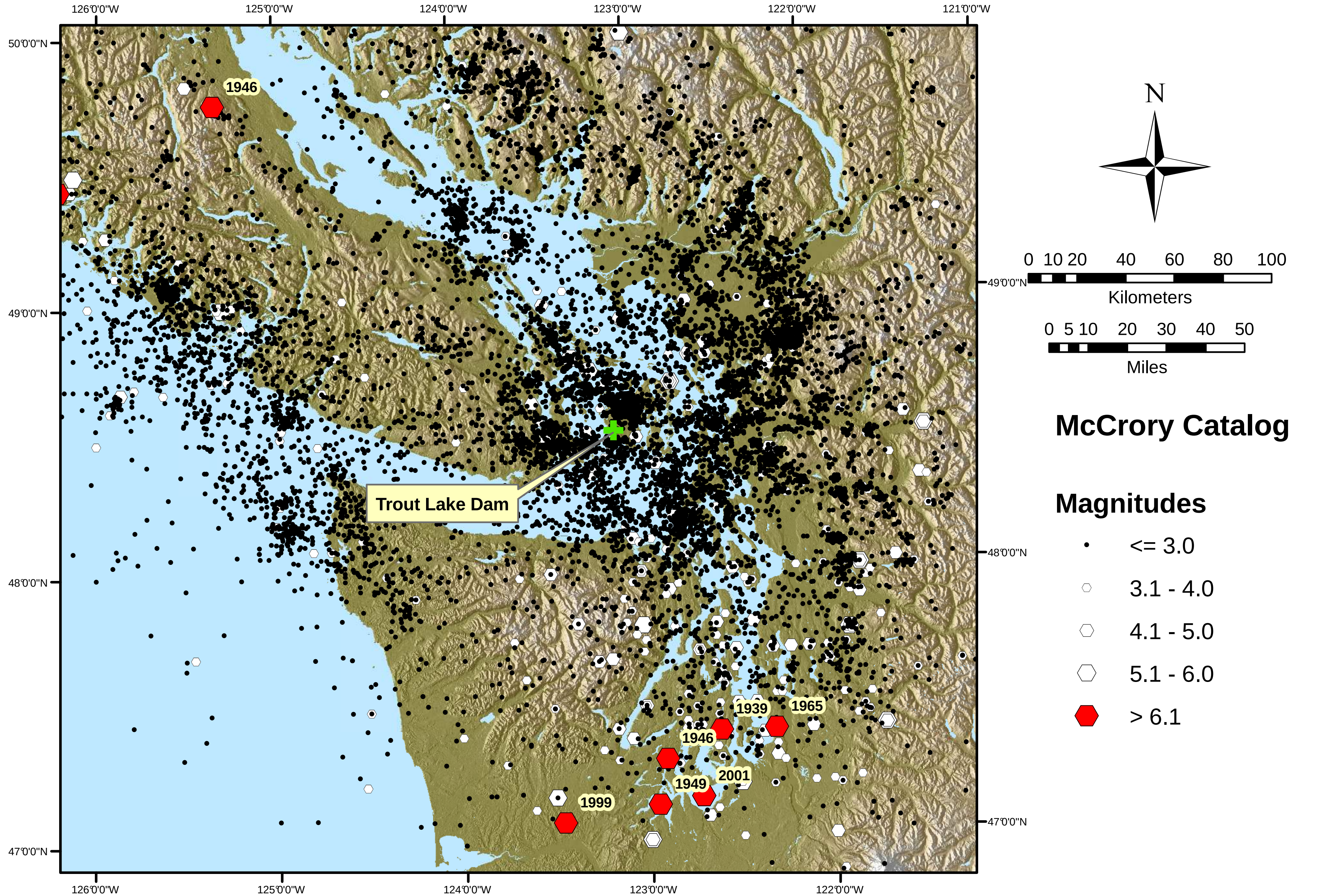

URS	Project No. 22240846	HISTORICAL SEISMICITY IN THE SITE REGION (1700-2007)	Figure 2
	Trout Lake Dam, Washington		

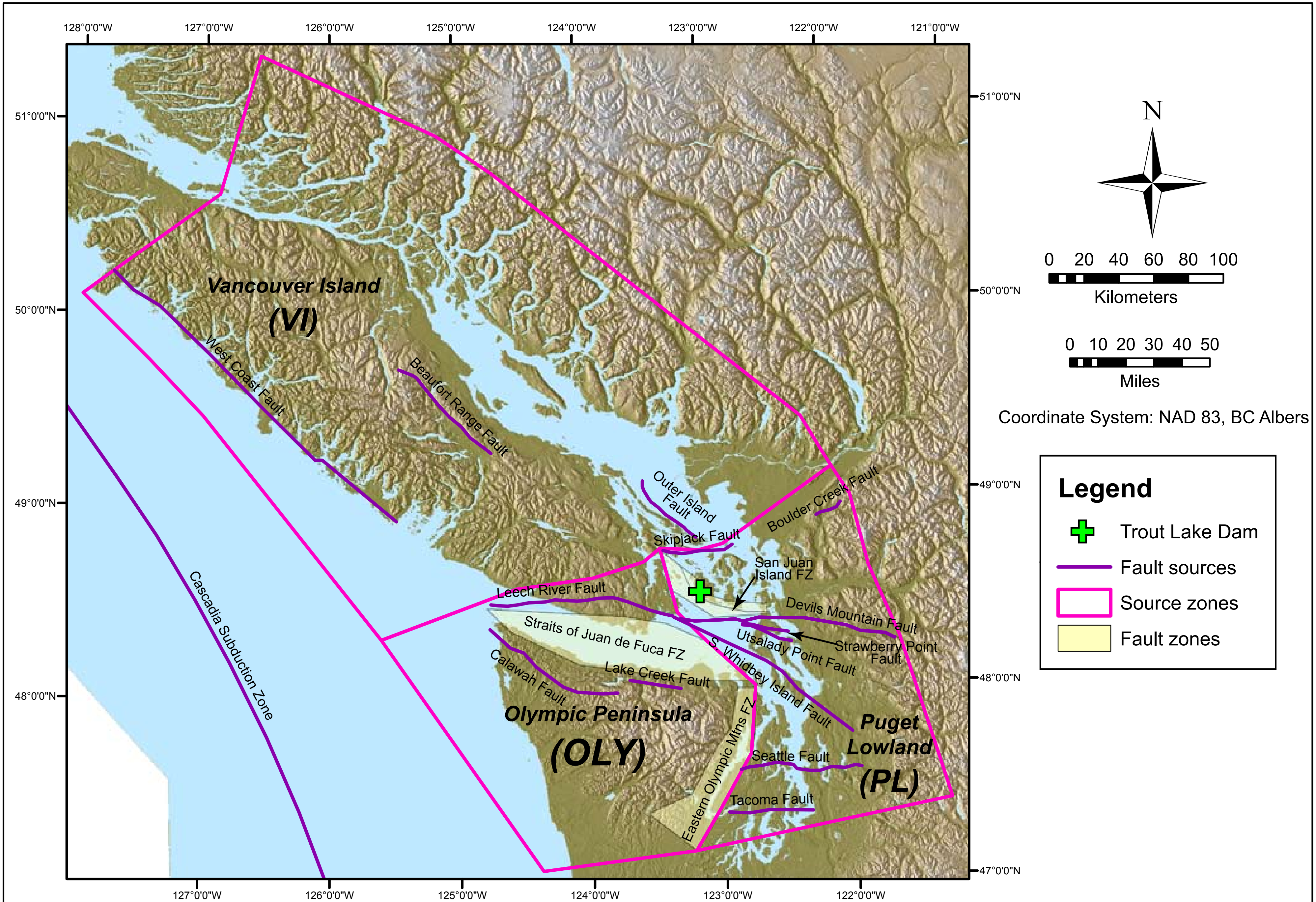

URS	Project No. 22240846 Trout Lake Dam, Washington	CRUSTAL SEISMIC SOURCES INCLUDED IN THE MODEL	Figure 3

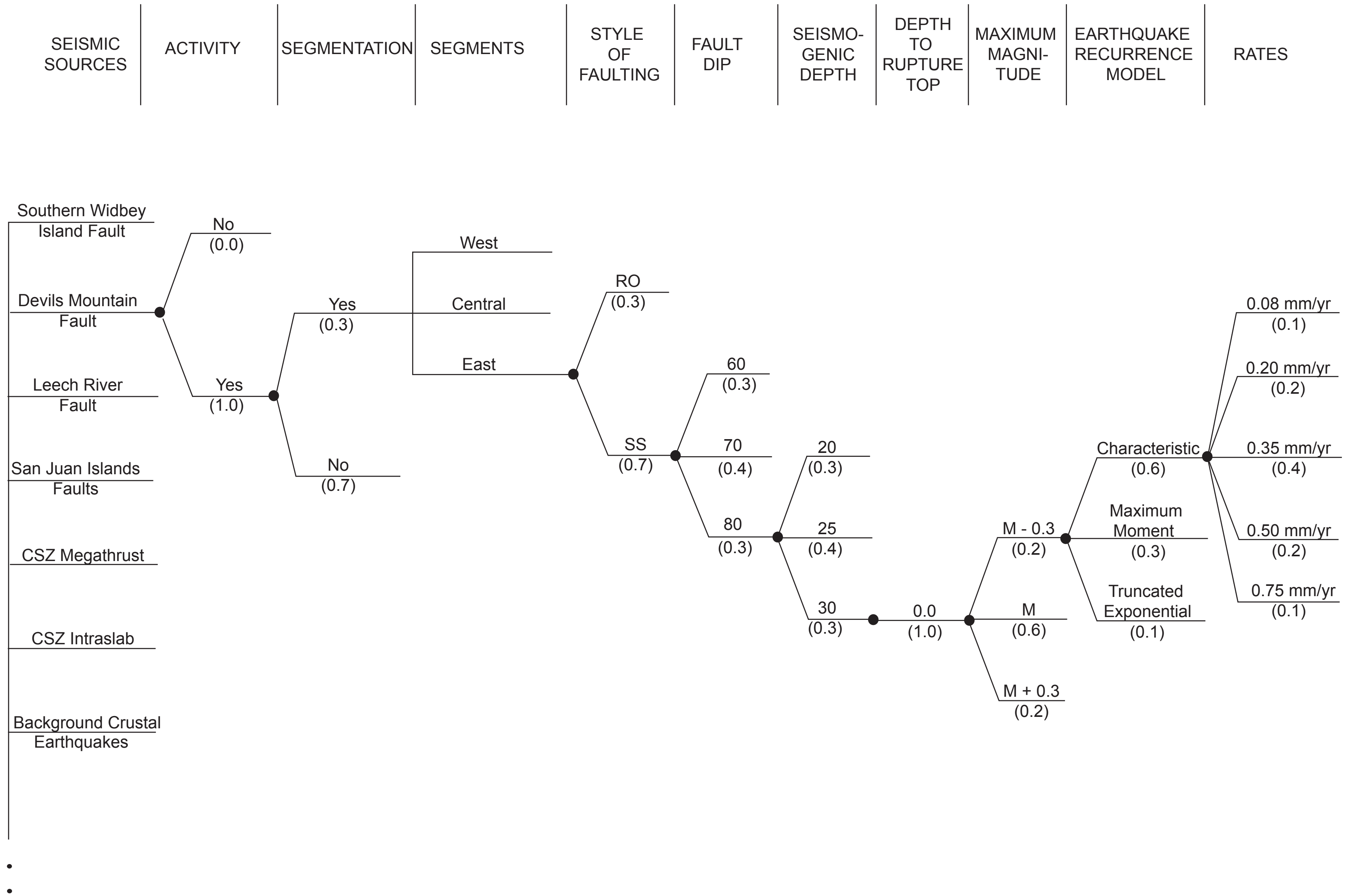

URS	Project No. 22240846 Trout Lake Dam, Washington	GENERALIZED SEISMIC SOURCE MODEL LOGIC TREE	Figure 4

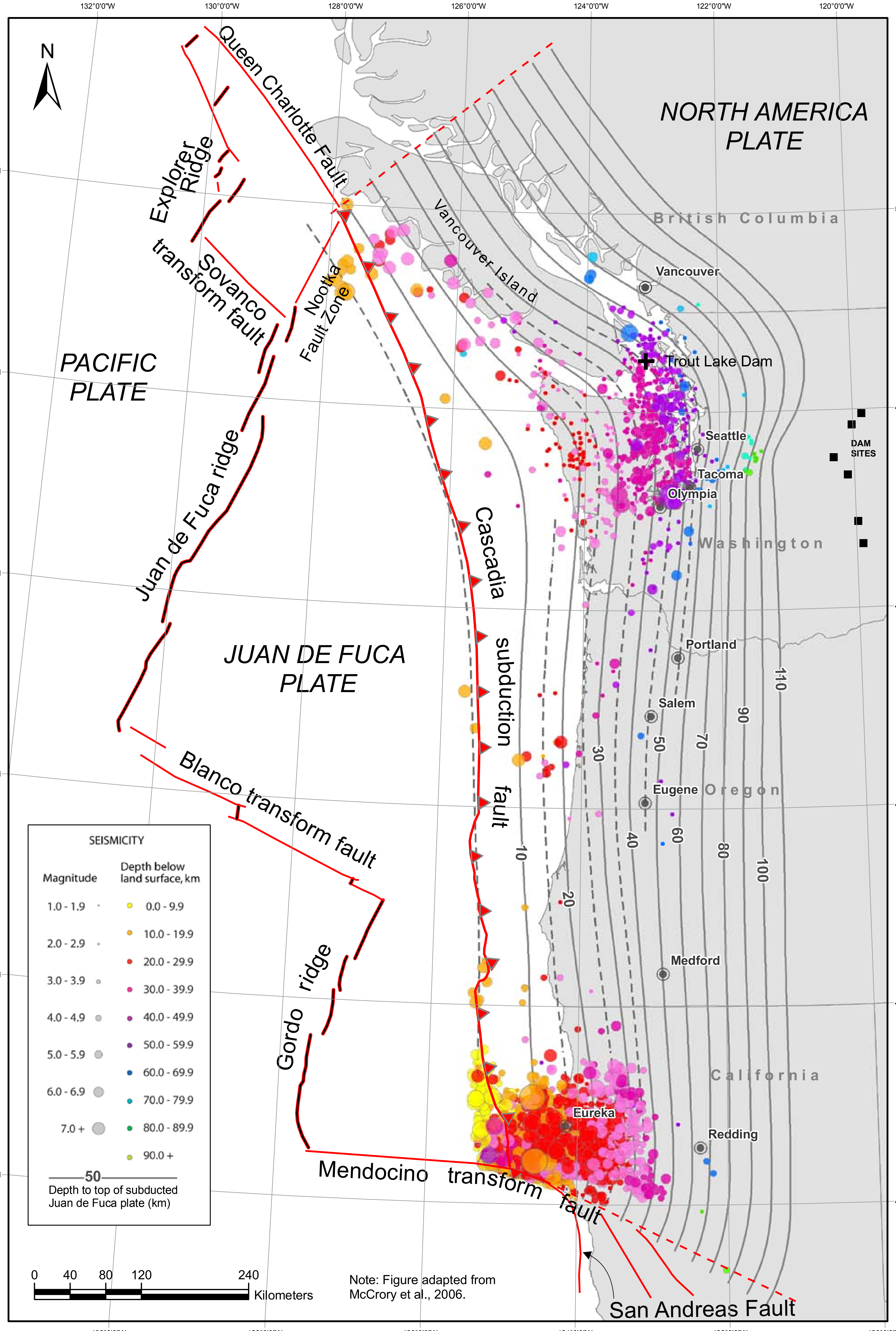

URS	Project No. 22240846	CSZ MODEL FROM MCCRORY ET AL. (2006)	Figure 5
	Trout Lake Dam Washington		

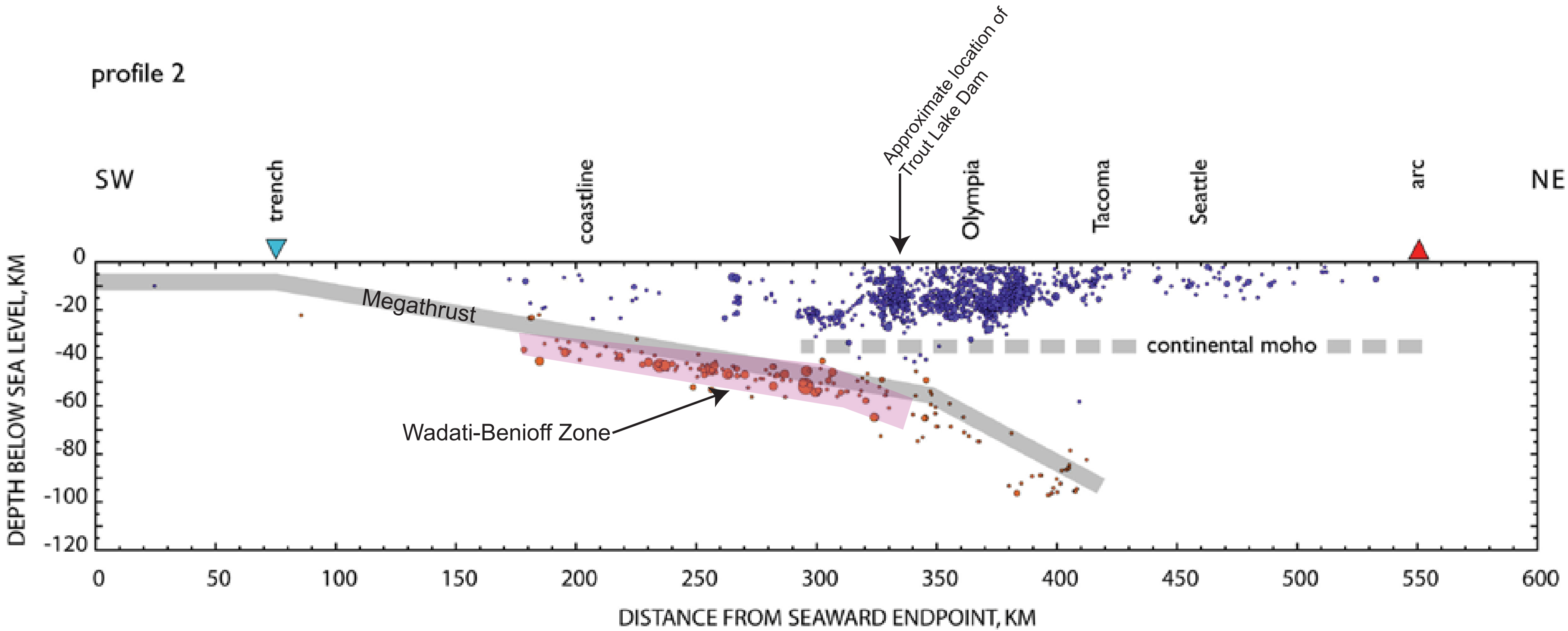

Source: McCrory *et al.* (2006)

Note: A 60-km wide swath of seismicity is projected onto the profile. Solid gray line denotes the location of the oceanic crust inferred from slab model; dashed gray line denotes approximate location of continental Moho. Blue circles denote hypocenters located above the modeled slab surface; orange circles denote hypocenters located below the surface.

URS	Project No. 22240846 Trout Lake Dam Washington	SCHEMATIC CROSS-SECTION THROUGH THE CSZ	Figure 6

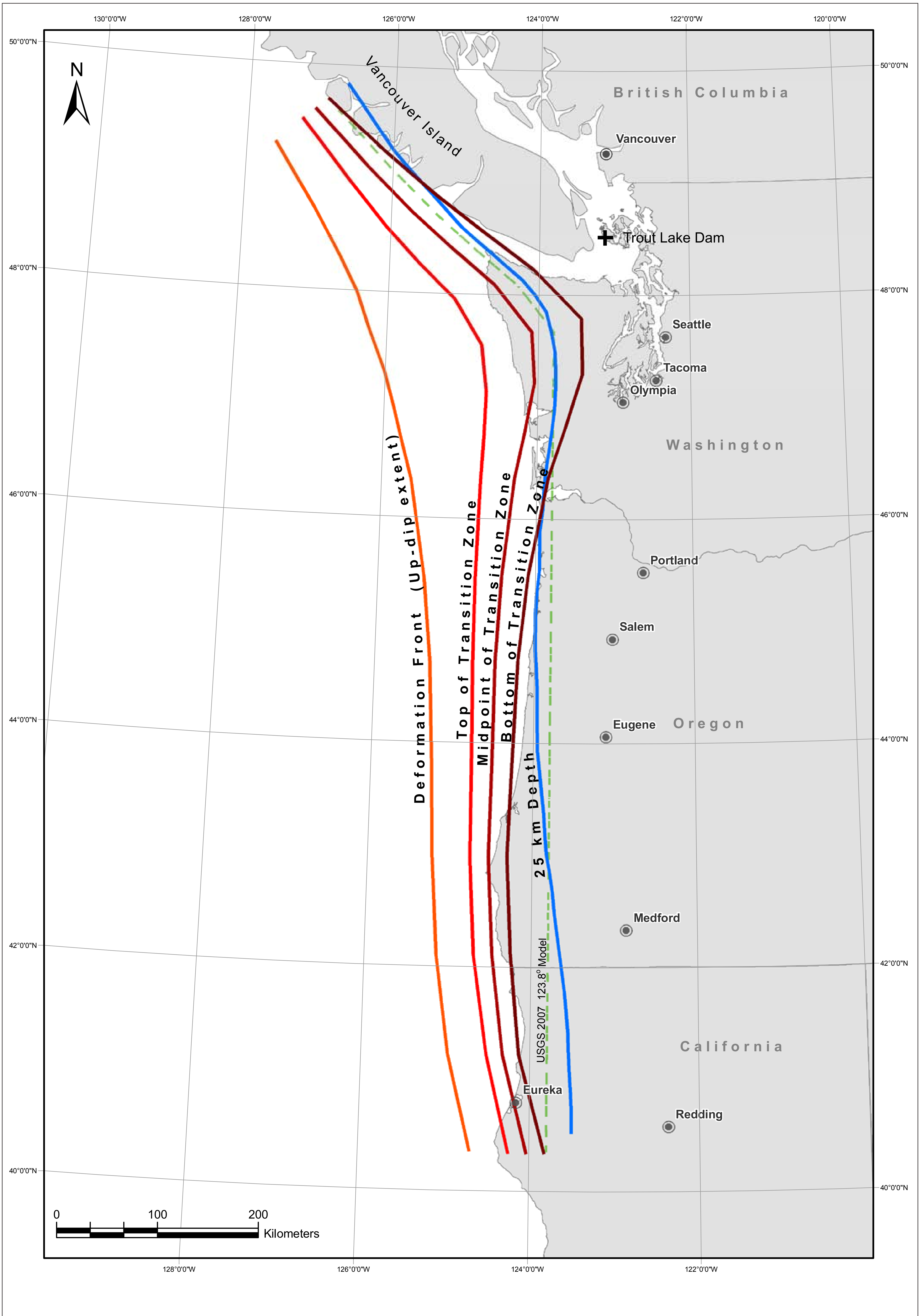

URS

Project No. 22240846

Trout Lake Dam
Washington

MODELED CSZ MEGATHRUST

Figure
7

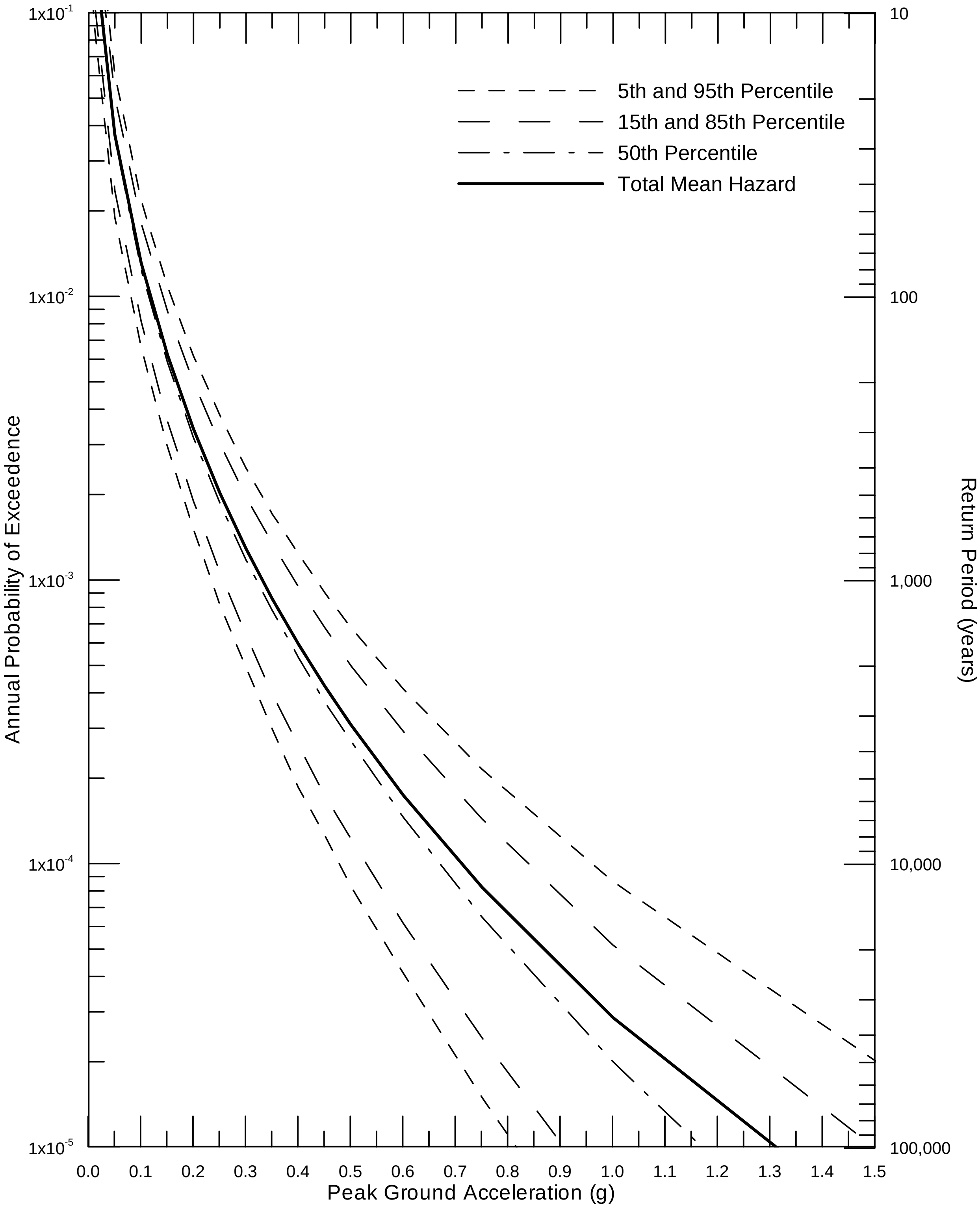

URS	Project No. 22240846 Trout Lake Dam Washington	SEISMIC HAZARD CURVES FOR PEAK HORIZONTAL ACCELERATION	Figure 8

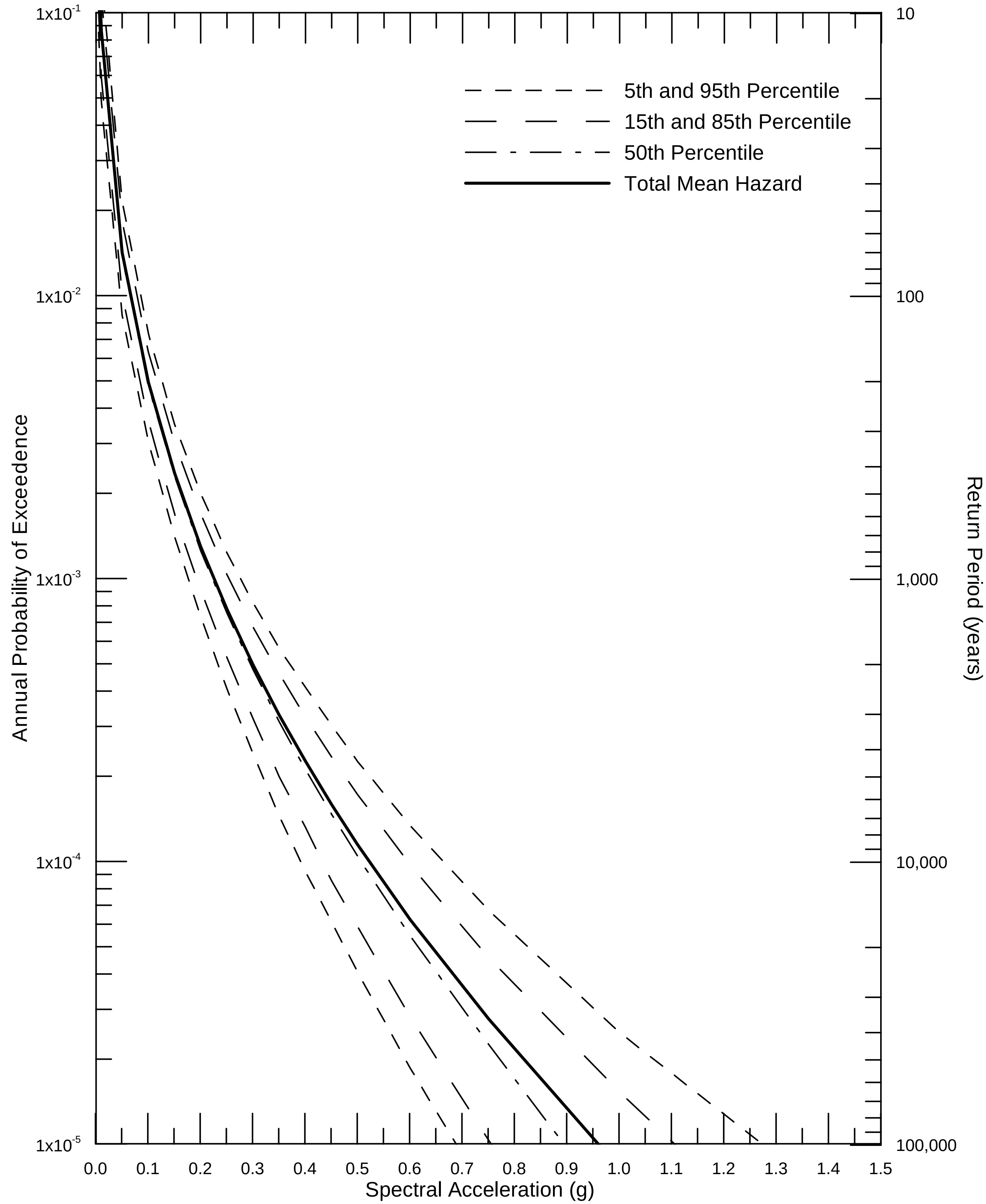

URS	Project No. 22240846 Trout Lake Dam Washington	SEISMIC HAZARD CURVES FOR 1.0 SEC HORIZONTAL SPECTRAL ACCELERATION	Figure 9

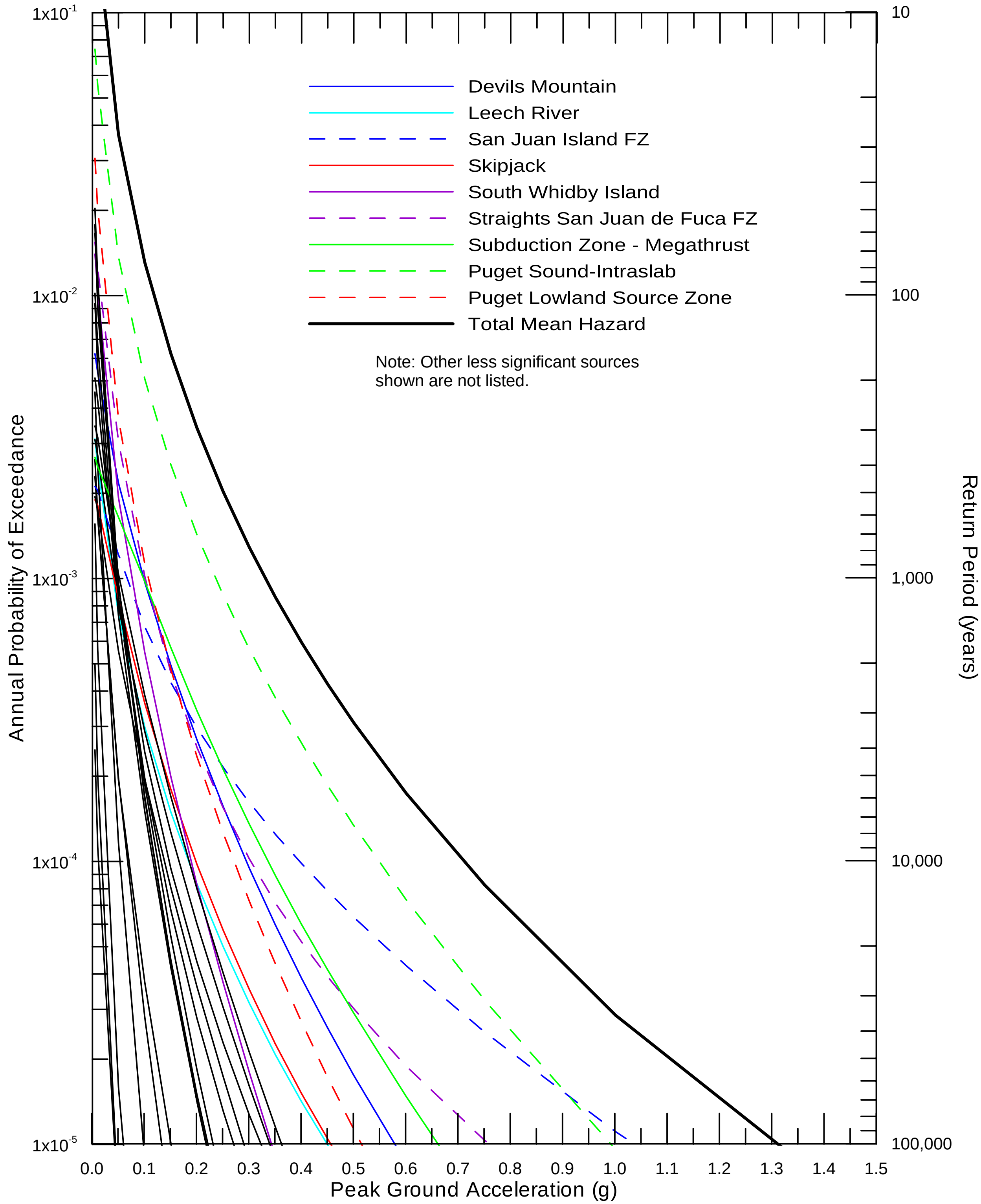

URS	Project No. 22240846	SEISMIC SOURCE CONTRIBUTIONS TO MEAN PEAK HORIZONTAL ACCELERATION HAZARD	Figure 10
	Trout Lake Dam Washington		

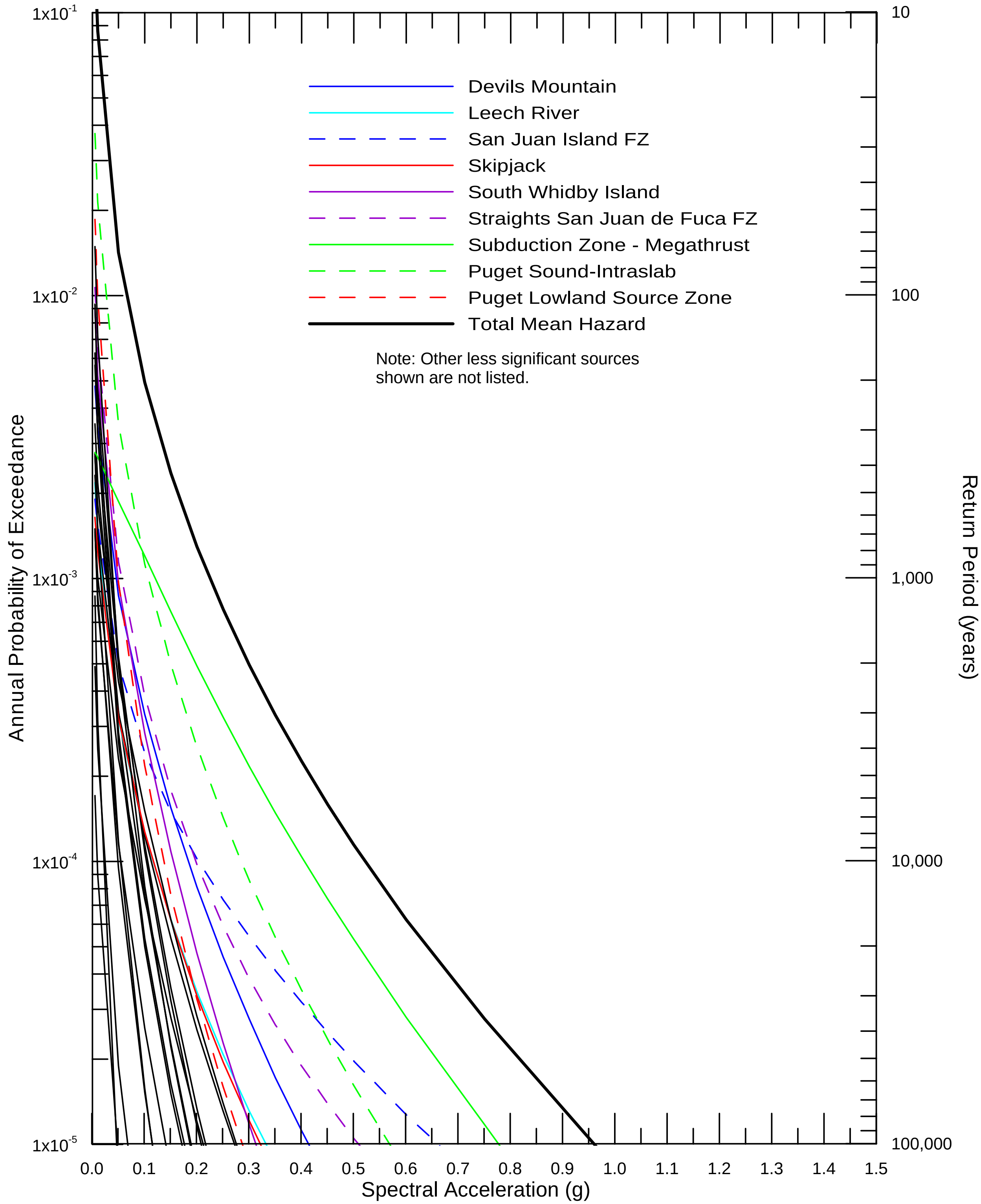

URS	Project No. 22240846 Trout Lake Dam Washington	SEISMIC SOURCE CONTRIBUTIONS TO MEAN 1.0 SEC HORIZONTAL SPECTRAL ACCELERATION HAZARD	Figure 11

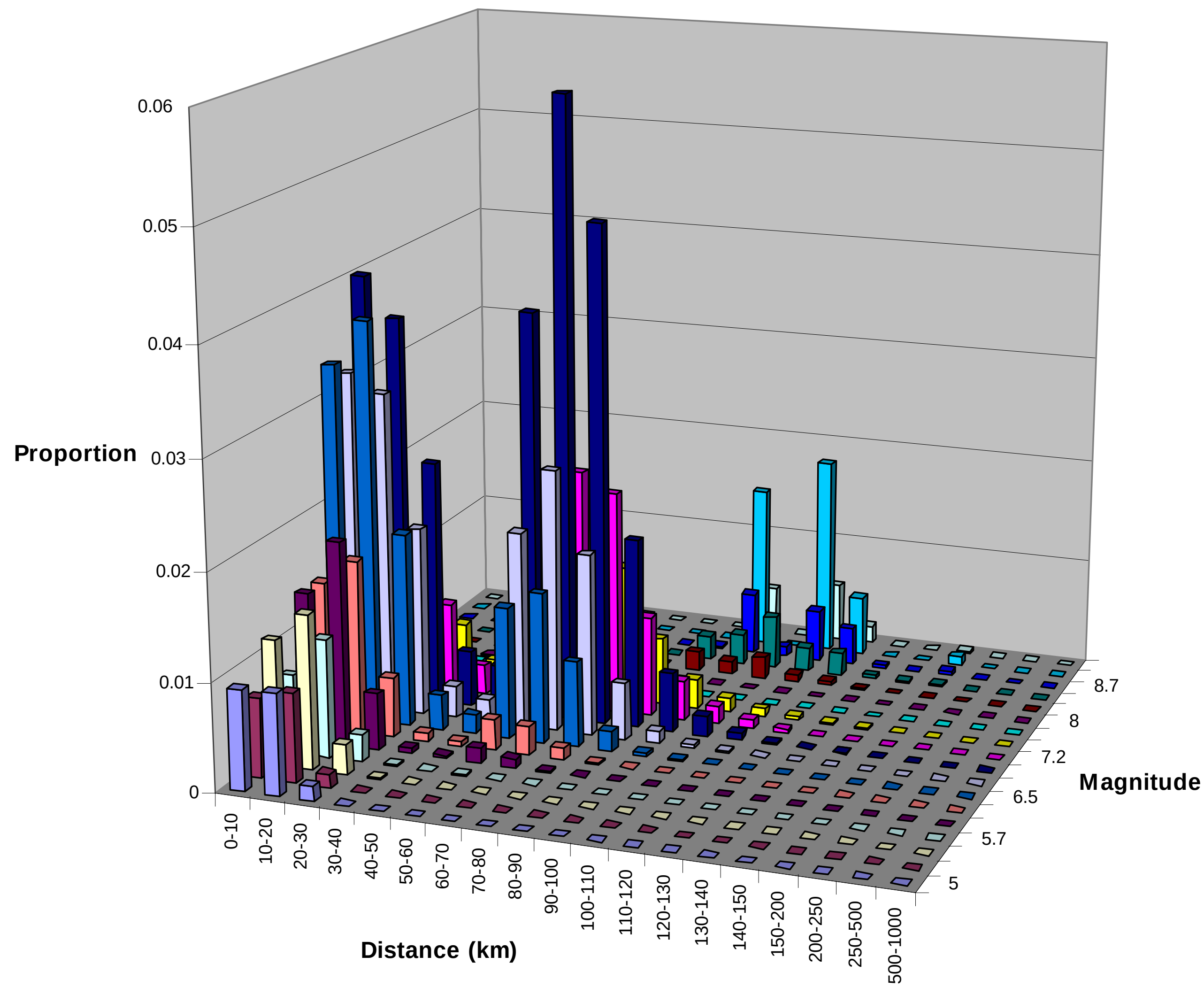

URS	Project No. 22240541 Trout Lake Dam Washington	MAGNITUDE AND DISTANCE CONTRIBUTIONS TO THE MEAN PEAK HORIZONTAL ACCELERATION HAZARD AT 3,000-YEAR RETURN PERIOD	Figure 12

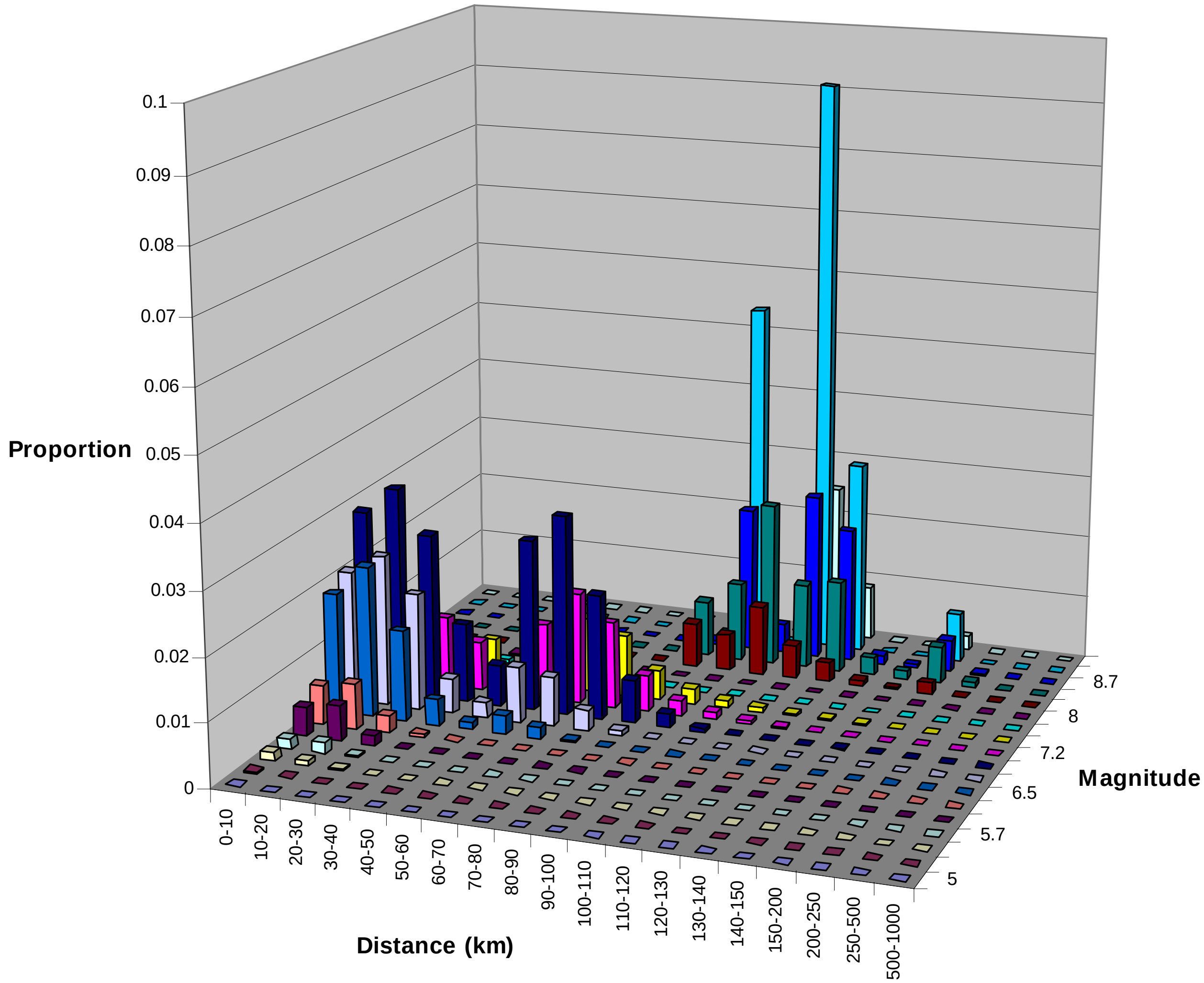

URS	Project No. 22240541 Trout Lake Dam Washington	MAGNITUDE AND DISTANCE CONTRIBUTIONS TO THE MEAN 1.0 SEC HORIZONTAL SPECTRAL ACCELERATION HAZARD AT 3,000-YEAR RETURN PERIOD	Figure 13

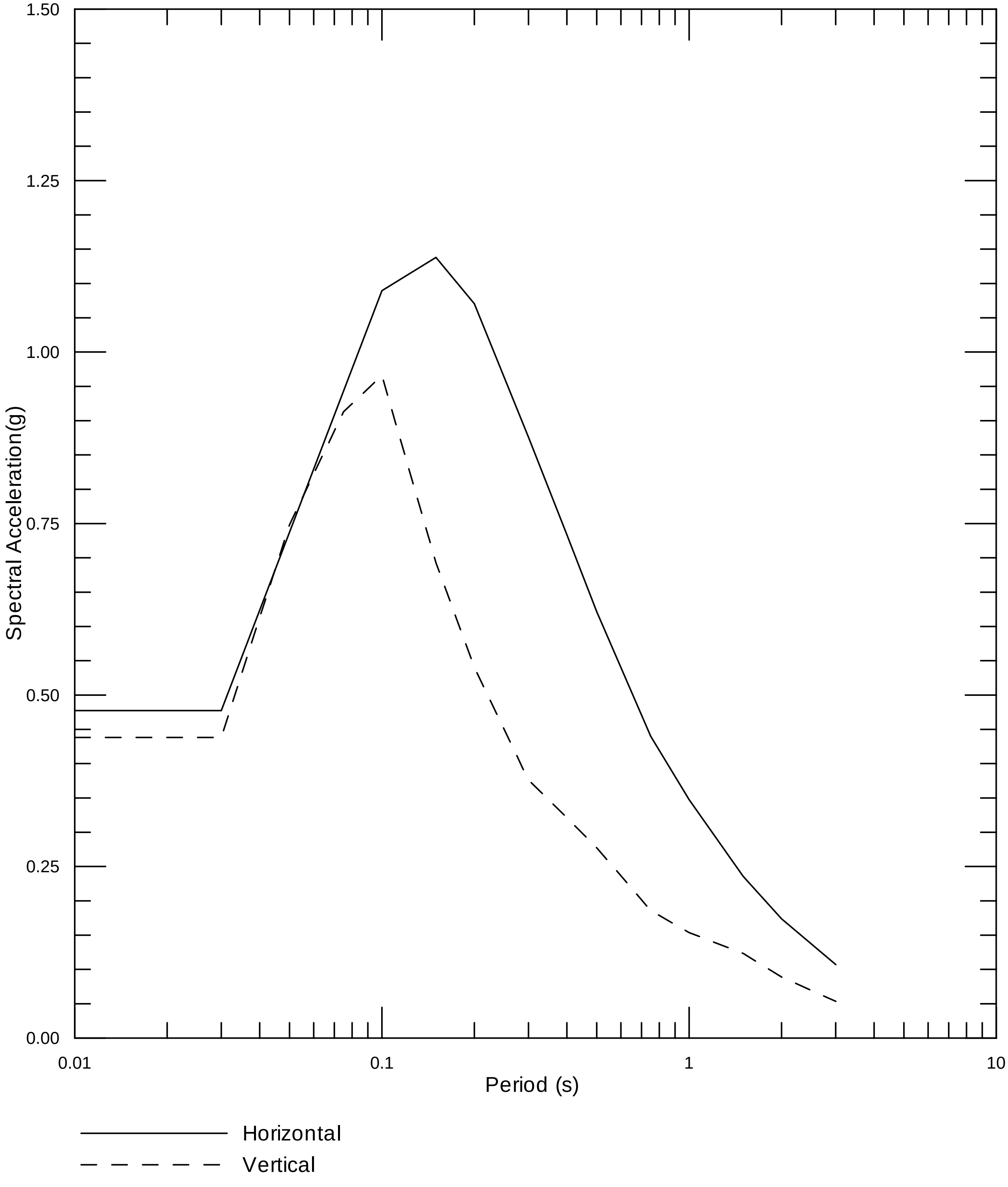

URS	Project No. 22240846	3,000-YEAR RETURN PERIOD 5%-DAMPED HORIZONTAL UHS	Figure 14
	Trout Lake Dam Washington		

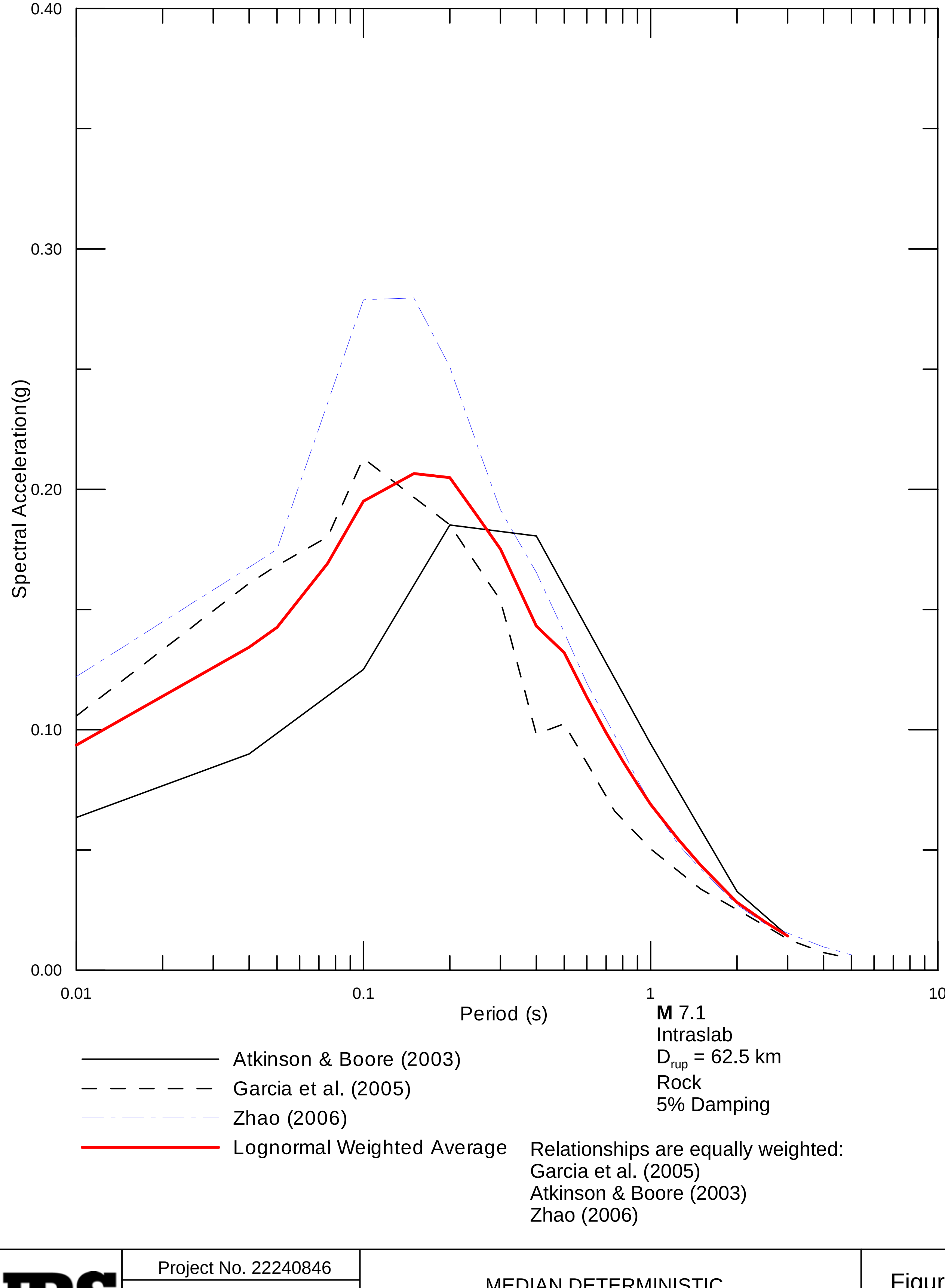

URS	Project No. 22240846 Trout Lake Dam	MEDIAN DETERMINISTIC SPECTRA FOR **M**7.1 INTRASLAB EVENT	Figure 15

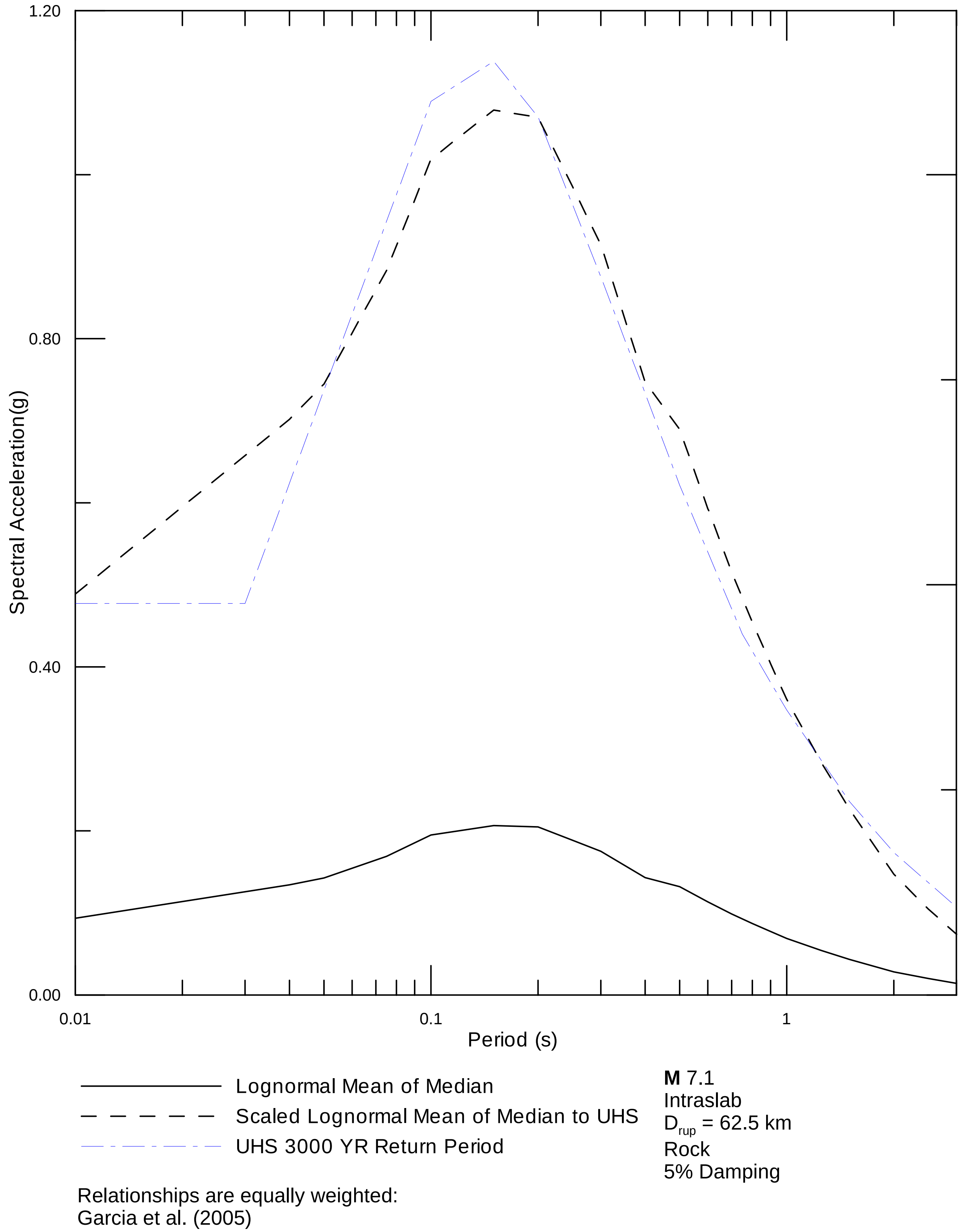

Relationships are equally weighted:
Garcia et al. (2005)
Atkinson & Boore (2003)
Zhao (2006)

URS	Project No. 22240846 Trout Lake Dam	MEDIAN DETERMINISTIC SPECTRA SCALED TO 3000-YR RETURN PERIOD UHS	Figure 16

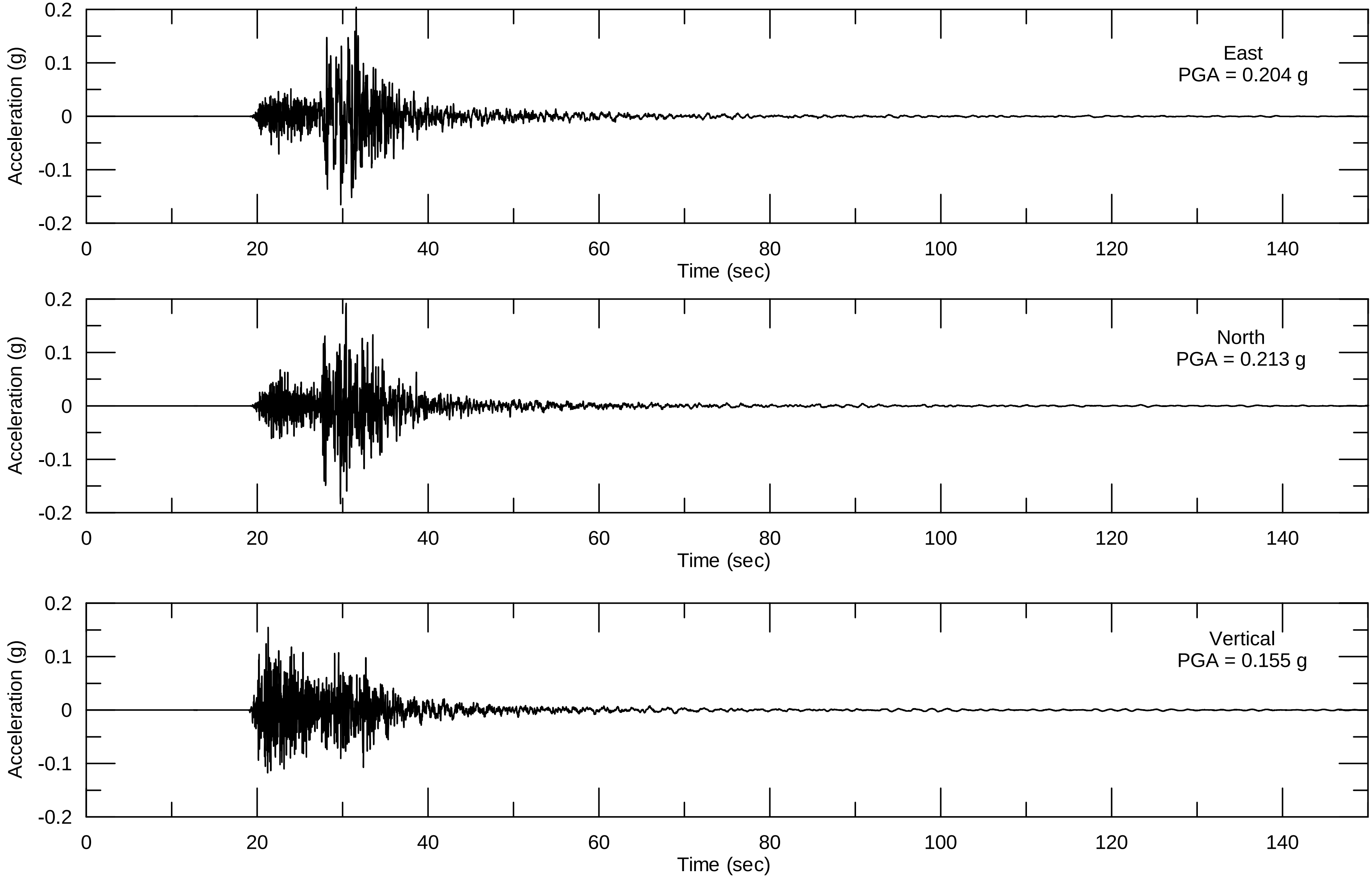

NEHRP Site Class = C
Vs30 = 1445 ft/s
Hypocentral Distance = 62 km

URS

Project No. 22240846

Trout Lake Dam

SEED TIME HISTORIES
2001 NISQUALLY EARTHQUAKE
PIERCE COUNTY EAST PRECINCT (PCEP)

Figure
17

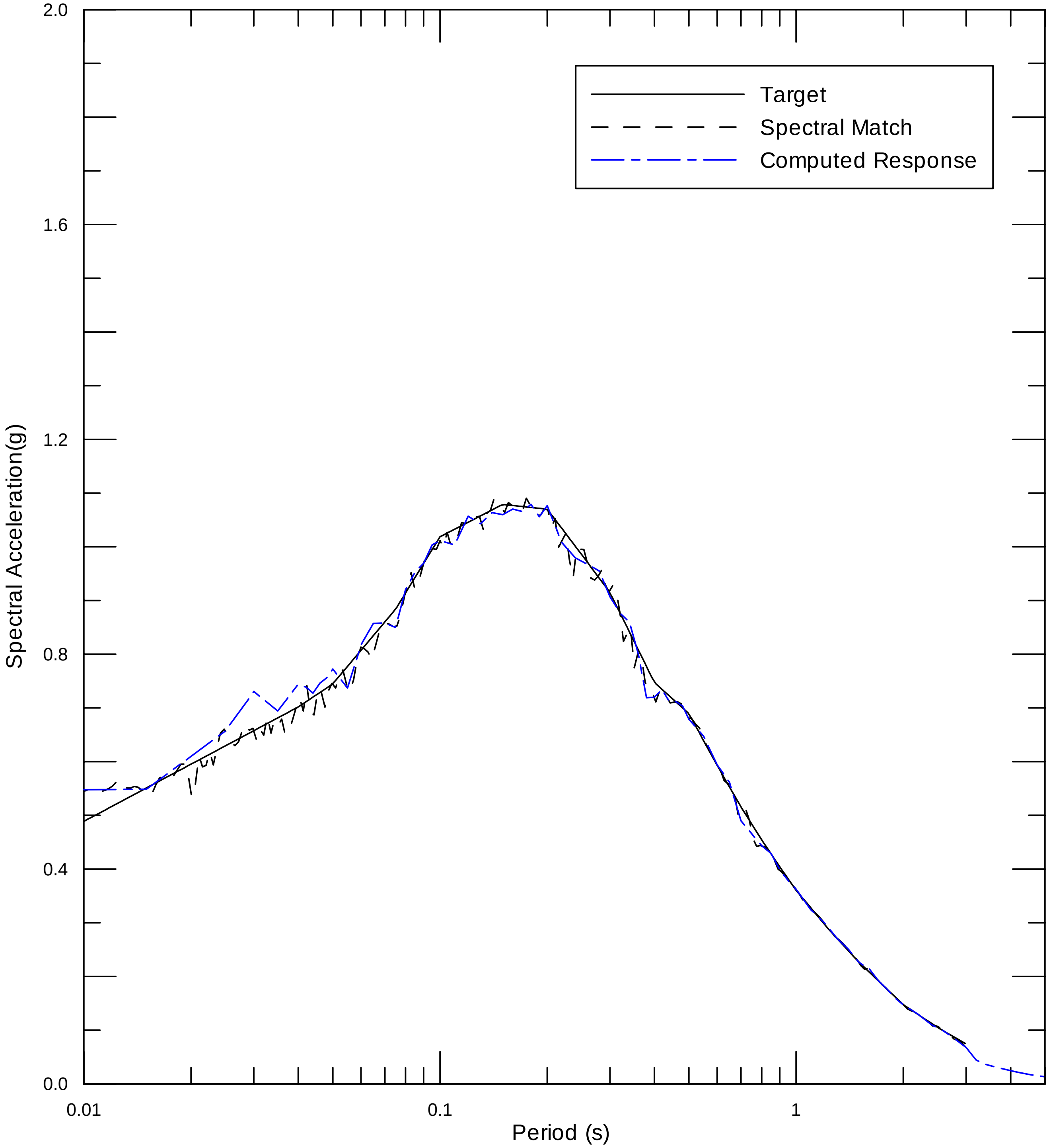

URS	Project No. 22240846 Trout Lake Dam	SPECTRAL MATCH TO HORIZONTAL DESIGN TARGET SPECTRUM 2001 NISQUALLY - PCEP (NORTH)	Figure 18

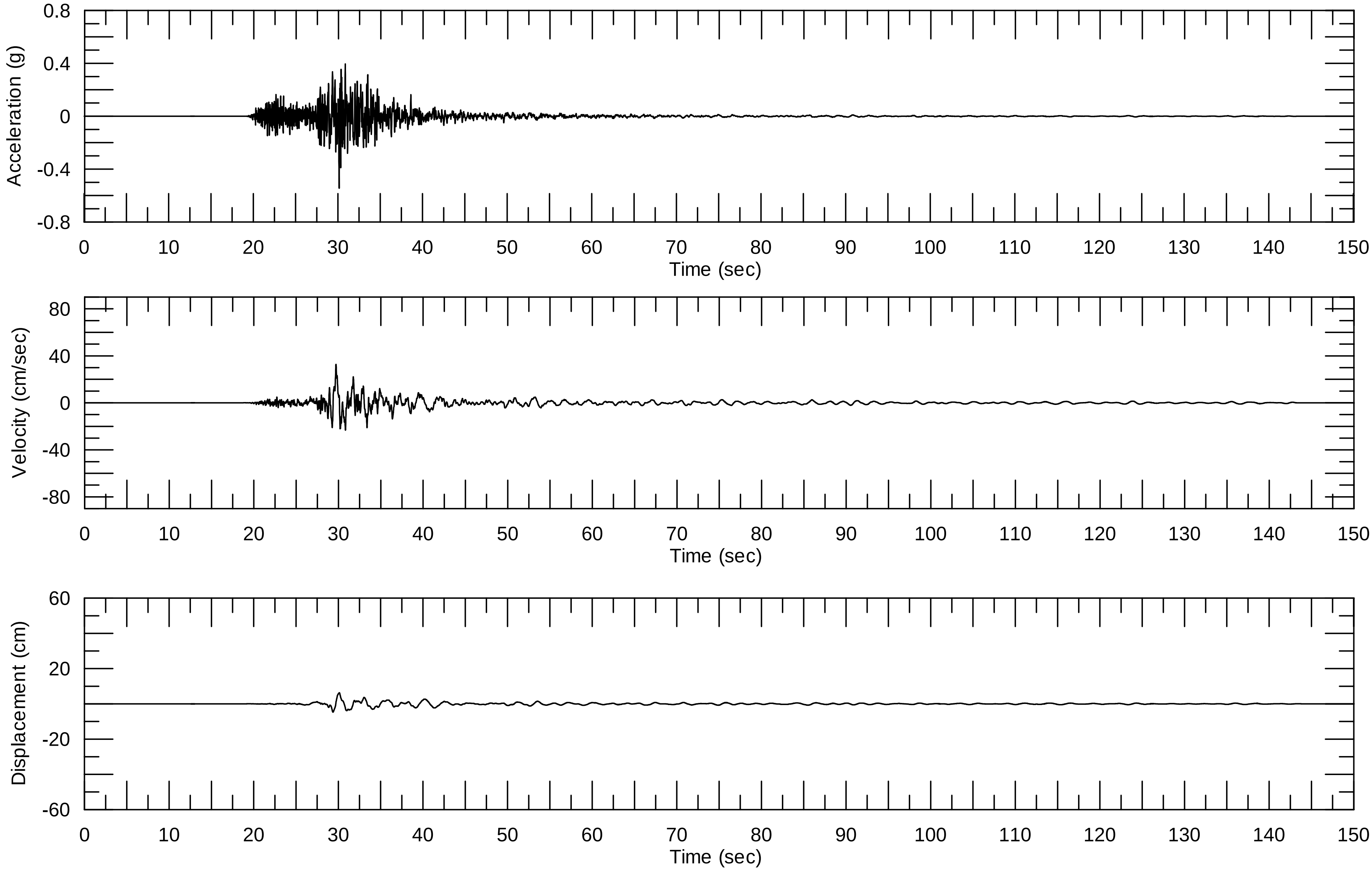

URS

Project No. 22240846

Trout Lake Dam

TIME HISTORIES SPECTRALLY MATCHED TO HORIZONTAL DESIGN TARGET SPECTRUM 2001 NISQUALLY - PCEP (NORTH)

Figure 19

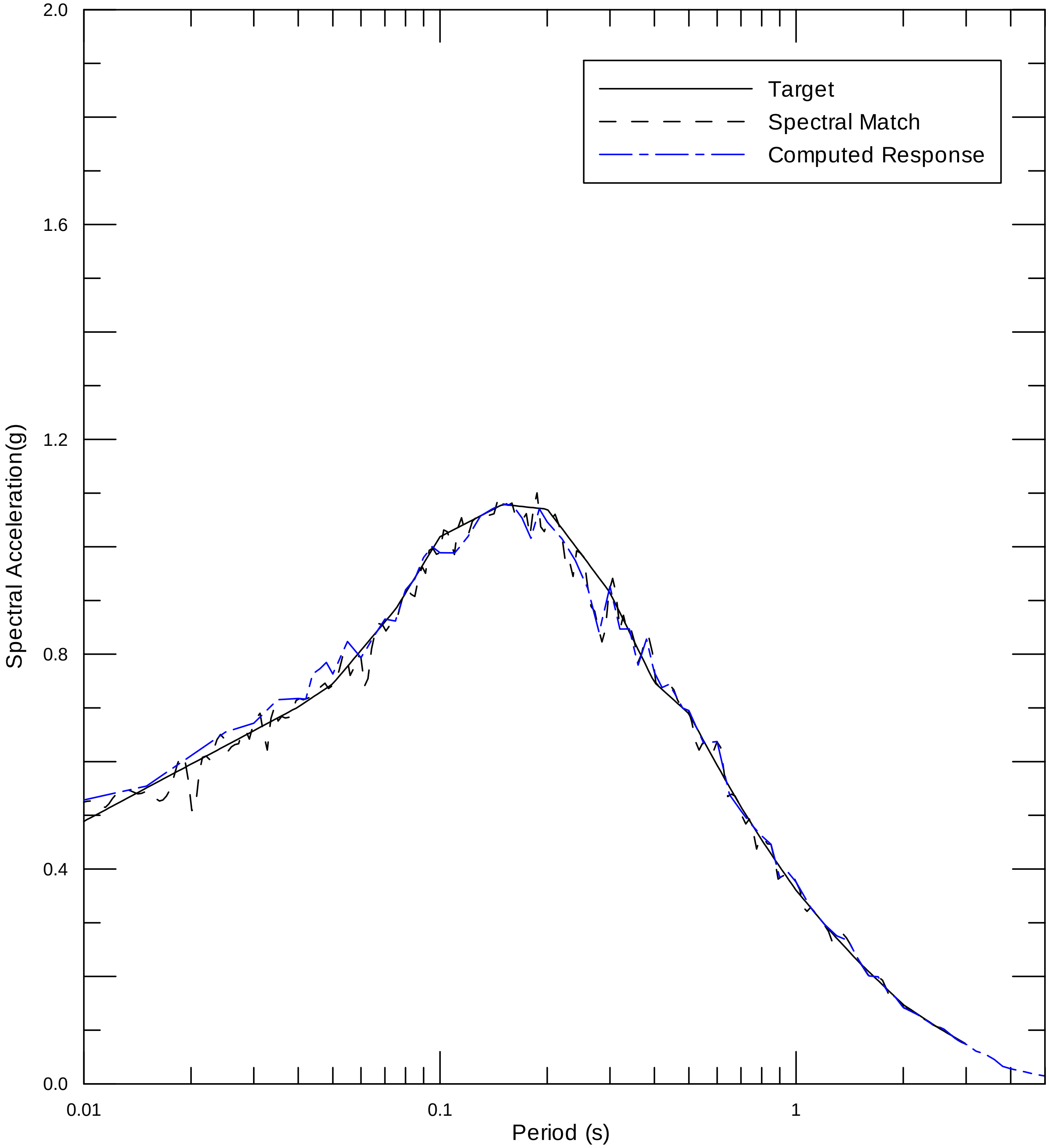

URS	Project No. 22240846 Trout Lake Dam	SPECTRAL MATCH TO HORIZONTAL DESIGN TARGET SPECTRUM 2001 NISQUALLY - PCEP (EAST)	Figure 20

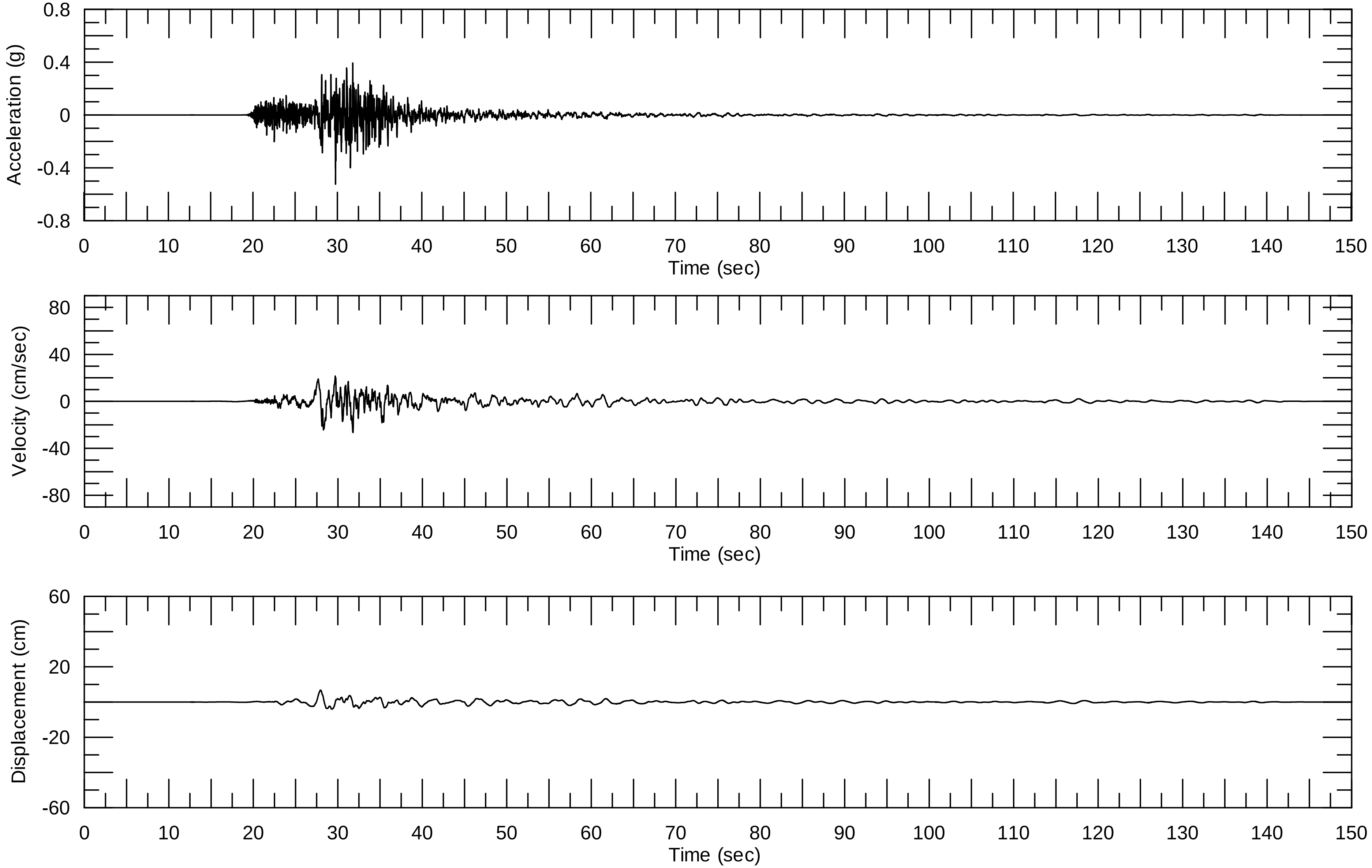

URS

Project No. 22240846

Trout Lake Dam

TIME HISTORIES SPECTRALLY MATCHED TO HORIZONTAL DESIGN TARGET SPECTRUM 2001 NISQUALLY - PCEP (EAST)

Figure 21

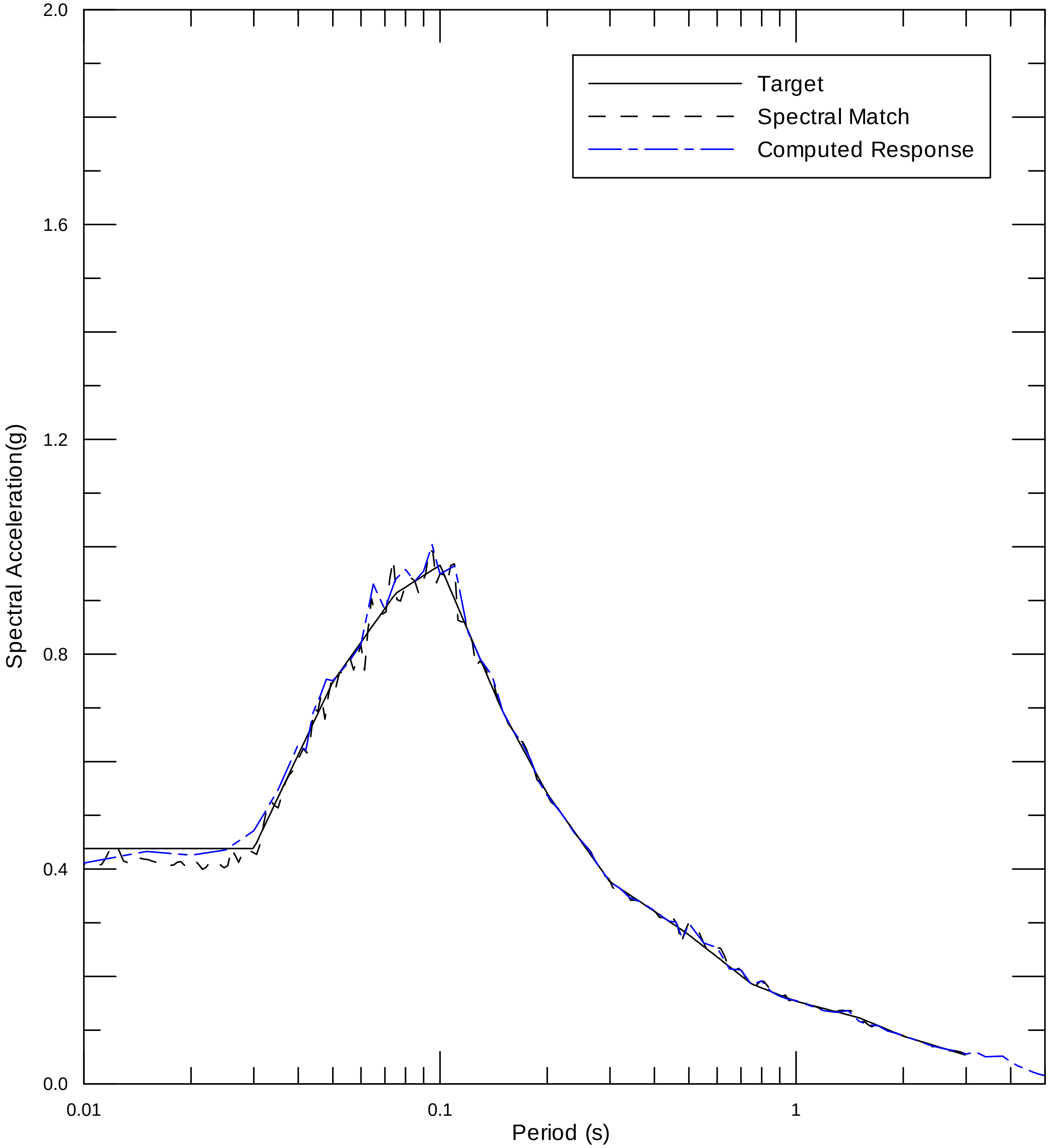

URS	Project No. 22240846 Trout Lake Dam	SPECTRAL MATCH TO VERTICAL DESIGN TARGET SPECTRUM 2001 NISQUALLY - PCEP (V)	Figure 22

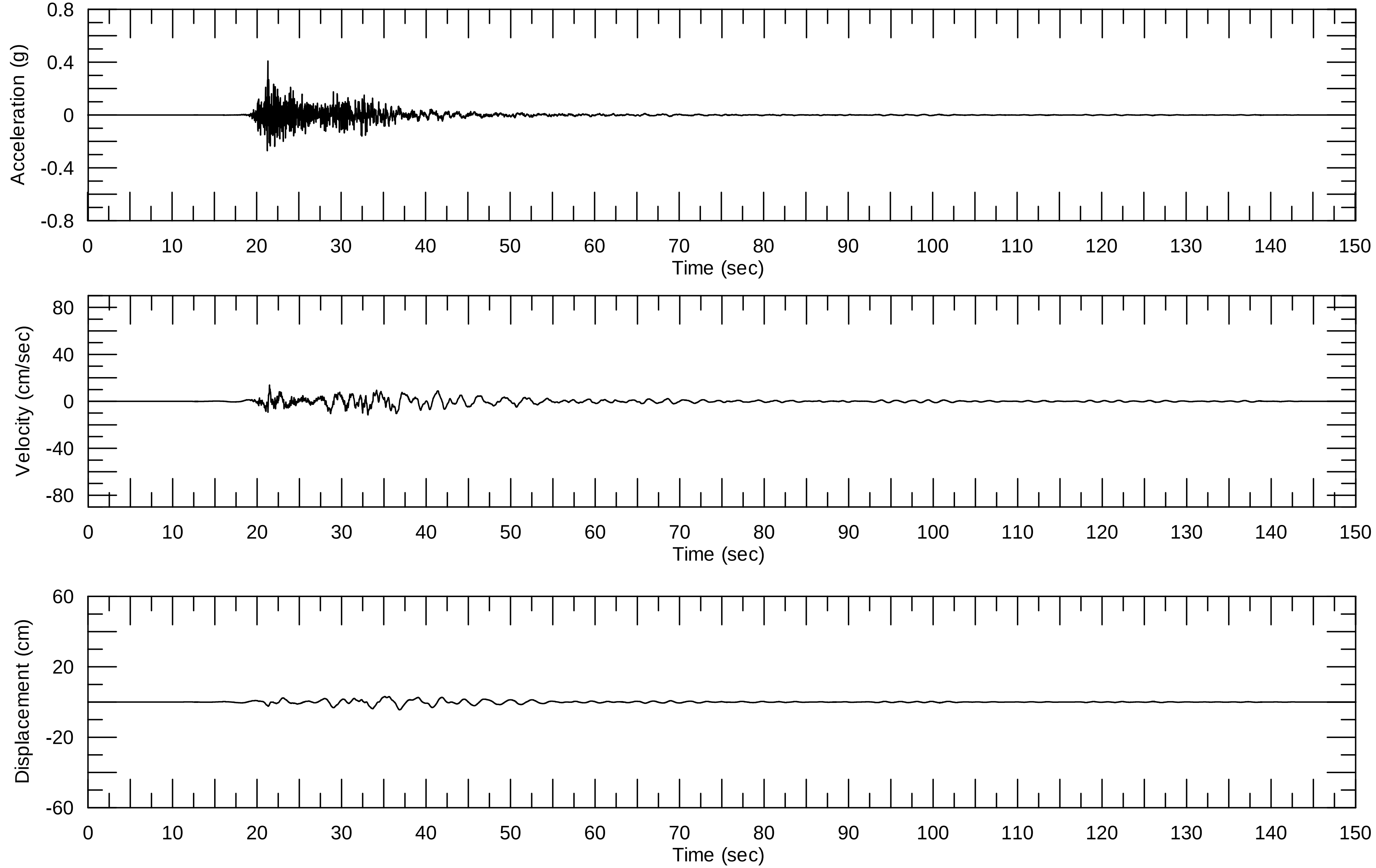

URS	Project No. 22240846 Lake Trout Dam	TIME HISTORIES SPECTRALLY MATCHED TO VERTICAL DESIGN TARGET SPECTRUM 2001 NISQUALLY- PCEP (V)	Figure 23

Appendix C

Photograph Log

TABLE OF CONTENTS

Photo No. 1 View dam from left abutment

Photo No. 2 View spillway from left abutment

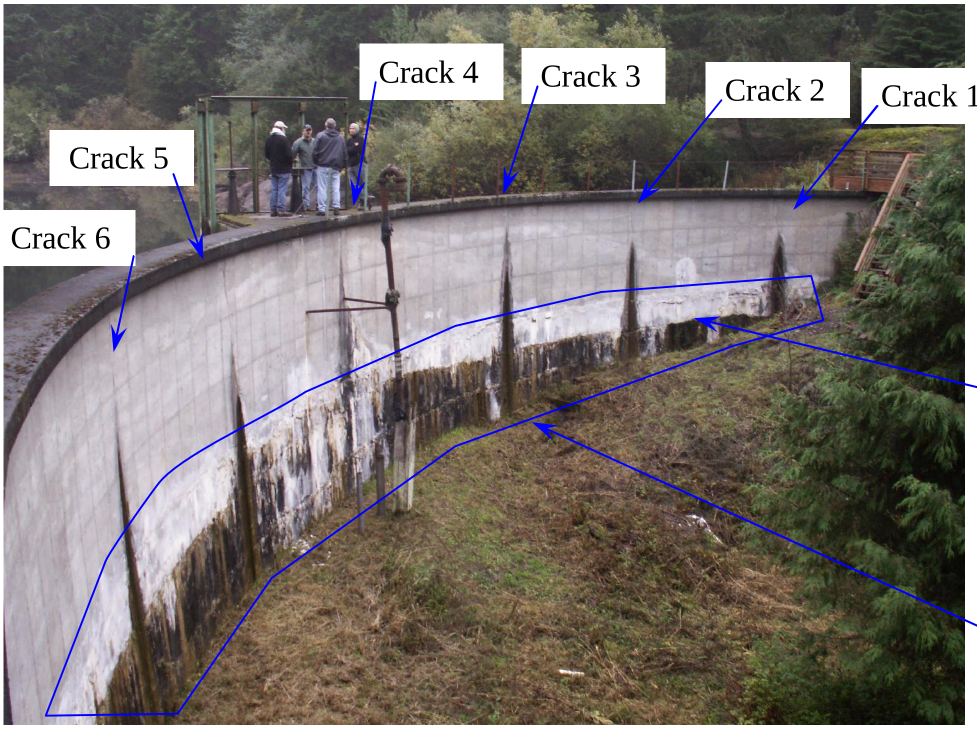

Photo No. 3 View of downstream side of dam from right abutment

Approximately top of original dam

The downstream face of the dam has a surface coat of concrete that has delaminating due to the seepage through the dam. This is not a structural concern regarding dam safety. See Photo No. 19 for close up view.

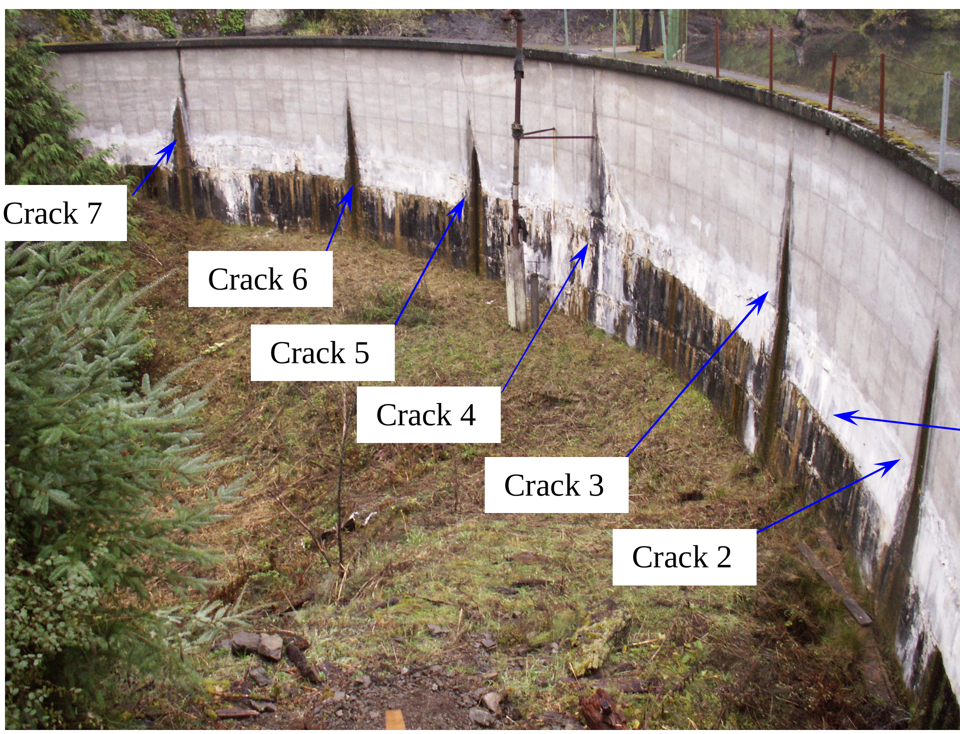

Approximately top of original dam

Photo No. 4 View of downstream side of dam from left abutment

Photo No. 5 View of crack 1 on crest of dam

Photo No. 6 View of crack 1 on downstream side of dam

Photo No. 7 View of crack 2 on crest of dam

Photo No. 8 View of crack 2 on downstream side of dam

Photo No. 9 View of crack 3 on crest of dam

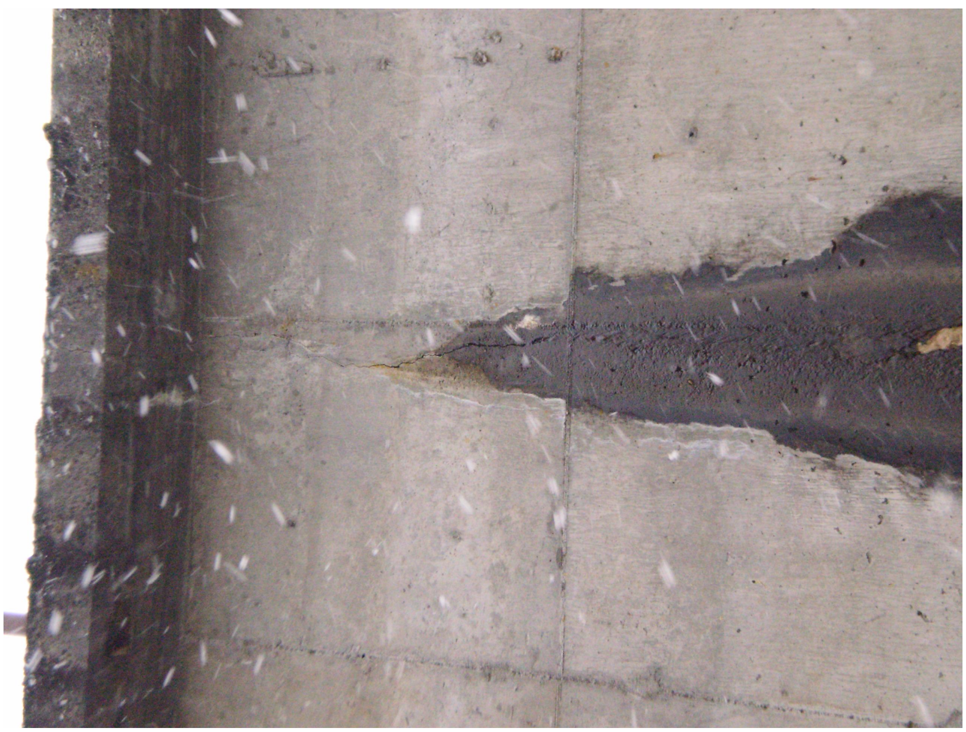

Photo No. 10 View of crack 3 on downstream side of dam

Photo No. 11 View of crack 4 on crest of dam

Photo No. 12 View of crack 4 on downstream side of dam

Photo No. 13 View of crack 5 on crest of dam

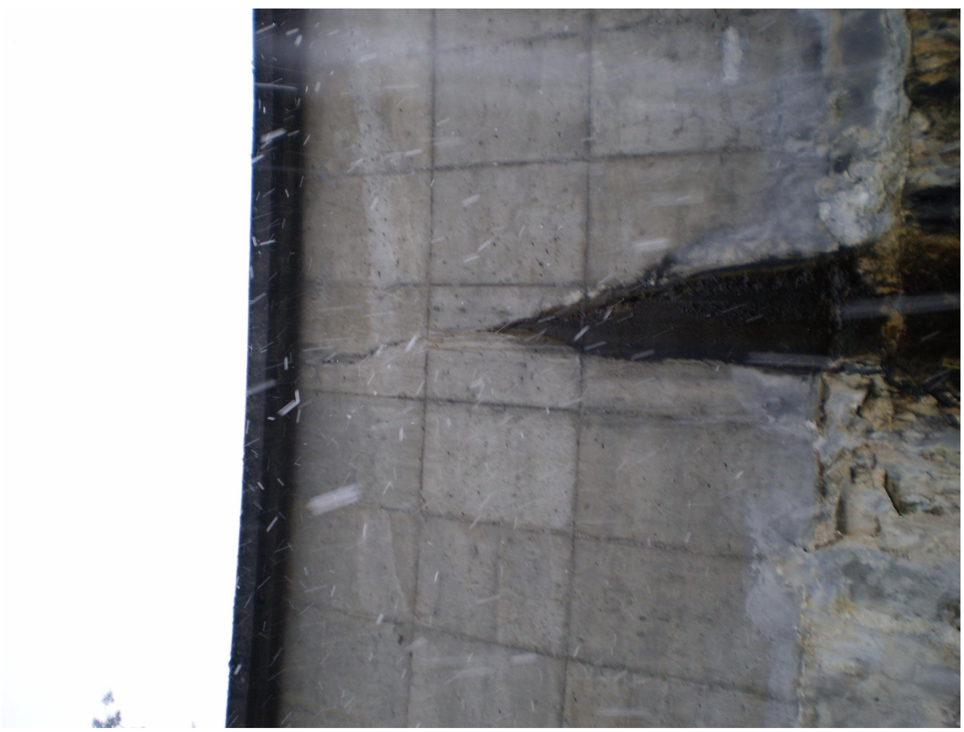

Photo No. 14 View of crack 5 on downstream side of dam

Photo No. 15 View of crack 6 on crest of dam

Photo No. 16 View of crack 6 on downstream side of dam

Photo No. 17 View of crack 7 on crest of dam

Photo No. 18 View of crack 7 on downstream side of dam

Photo No. 19 View of typical delaminating of patch concrete on downstream side of dam